POLITECHNIKA LUBELSKA

MONOGRAFIE

Oleksandra Hotra

Selected Issues on Temperature Sensors

Lublin 2013

Selected Issues on Temperature Sensors

Monografie – Politechnika Lubelska

Lublin University of Technology
Faculty of Electrical Engineering
and Computer Science
ul. Nadbystrzycka 38A
20-618 Lublin

Oleksandra Hotra

Selected Issues on Temperature Sensors

Politechnika Lubelska
Lublin 2013

Reviewers:
prof. dr hab. inż. Ryszard Romaniuk
prof. dr hab. inż. Waldemar Wójcik

Publication approved by the Rector of Lublin University of Technology

ISBN: 978-83-63569-29-7

Publisher: Lublin University of Technology
ul. Nadbystrzycka 38D, 20-618 Lublin, Poland
Realization: Lublin University of Technology Library
ul. Nadbystrzycka 36A, 20-618 Lublin, Poland
tel. (81) 538-46-59, email: wydawca@pollub.pl
www.biblioteka.pollub.pl
Printed by : TOP Agencja Reklamowa Agnieszka Łuczak
www.agencjatop.pl

Impression: 100 copies

Contents

Abbreviations and symbols

DTS	distributed temperature sensor
EDF	erbium-doped fibre
FBG	fibre Bragg grating
LC	liquid crystal
LED	light emitting diode
LPG	long period grating
OFT	optical fibre thermometer
OTDR	optical time-domain refractometry
PCF	photonic crystal fibre
PLCF	photonic liquid-crystal fibre
RTD	resistance temperature detector
SBS	stimulated Brillouin scattering
SMF	single mode fibre
TCR	temperature coefficient of resistance

ϑ	–	temperature in degrees Celsius
T	–	absolute temperature in kelvins

Chapter 2

α	–	temperature coefficient of resistance (TCR)
α_T	–	TCR of the thermistor
β	–	termistor coefficient (material constant)
ε	-	energy
$\varepsilon_{\vec{k}}$	–	dispersion
$\Delta\varepsilon_{\vec{k}}$	–	change of the charge carrier energy
γ	–	transfer coefficient of the former of supply voltage variable component
μ	–	chemical potential
μ*	–	reduced chemical potential
ρ	–	resistivity of the film material
σ		conductivity
τ	–	duration of the output pulse signal
τ_d	–	time difference between the charging and discharging time
τ_r	-	relaxation time of the charge carrier pulse
ϑ	–	temperature in degrees Celsius

$\Delta\vartheta$	–	interval of the temperature change
$\Delta_{\vartheta L}$	–	absolute equivalent error of the output voltage introduced by the lead wire resistances (in degrees centigrade)
$\Delta_{\vartheta n}$	–	absolute equivalent error of nonlinearity (in degrees Celsius)
ΔQ	–	amount of heat transferred to the system thin film-substrate of mass *m*
A, *B* and *C*	–	the constant coefficients of Pt RTDs
$A_{ik}^{(0)}(\vec{B})$	–	antisymmetric kinetic tensors
b	-	width of the conducting film
$\vec{B}$	–	induction of the magnetic field
C	–	capacitance
c	–	specific heat
d	–	thickness of the conducting film
e	–	charge of electron
$\vec{E}$	–	electric field intensity
ΔE	–	forbidden gap width
f_0	–	the Fermi-Dirac function
$g(\varepsilon)$	–	the density of the states
h	–	Planck’s constant
I	–	current
I_0	–	reference current
I_{out}	–	output current
$\vec{j}$	–	vector of the electric current density through the crystal
k	–	Boltzmann constant
$\vec{k}$	–	wave vector of the charge carriers
k_a	–	amplification coefficient of the voltage amplifier
k_b	–	transfer coefficient of the resistance bridge circuit
k_c	–	gain factor of the analogue-to-digital converter
K_{ef}	–	coefficient of efficiency
k_m	–	transformation coefficient of the microprocessor
k_n	–	quotient of the nominal value of the resistance of the resistor with positive TCR
k_v	–	coefficient of the supply voltage change of the resistance bridge circuit vs. the temperature
l	–	length of the conducting film
Δl	–	resistor’s length
m	–	mass
m^*	–	effective charge carrier mass
n_c	–	charge carrier concentration

n_i – the intrinsic charge carrier concentration
n_{sq} – the number of squares in the conducting film
p – pulse vector module
r – scattering factor
R_{ϑ} – resistance of the resistance temperature sensor at the temperature ϑ
$R_{\vartheta\max}$ – RTD resistance at the maximum measured temperature
$\Delta R_{\vartheta\, max}$ – maximum value of the resistance change of RTD
R_{∞} – resistance at $T\to\infty$
R_0 – resistance of the resistance temperature sensor at ϑ=0°C
R_{01}, R_{02} – resistances of the standard resistors
R_b – input resistance of the bridge circuit
R_D – forward resistance of the diode
R_L – lead wire resistance
δ_R - relative error of the resistance R
R_l – load resistance
R_{ONT} – ON resistance of the discharging transistor
R_{sq} – resistance of square in the conducting film
$S_{ik}^{(0)}(\vec{B})$ – symmetric kinetic tensors
ΔS – cross-section area
T_p period of the pulses of the triangle wave generator
$\nabla_{\vec{r}} T$ – temperature gradient
U_{ϑ} – variable component of the supply voltage (dependent on the output voltage of the supply unit and the temperature)
U_{al} – allowed voltage on spark-sensitive objects
U_D – voltage across the diode
$U_{\lim}$ – voltage limited by the spark protection circuit
$U_{\max}$ – maximum value of the voltage across the terminals of the RTD
U_{out} – output voltage
$U_{out\, max}$ – output voltage of the bridge circuit at the maximum temperature ϑ_{max}
U_s – supply voltage
$U_{s\, nom}$ – nominal supply voltage of the resistance bridge circuit at ϑ=0°C
$U_{st\, D}$ – stabilisation voltage of the Zener diode *D1*
Δ_{UL} – absolute error of the output voltage due to the influence of the lead wire resistances
Δ_{Un} – absolute error of nonlinearity of the resistance bridge output voltage

δ_{Un}	–	relative error of nonlinearity of the resistance bridge circuit output voltage
z	-	sign of the charge carriers
Z_{be}	–	large statistical sum for large non-equilibrium quantum ensemble with variable number of the particles

Chapter 3

ϑ_c	–	cold-junction temperature
ϑ_h	–	hot junction temperature
ϑ_1, ϑ_2	–	the initial and final values of the temperatures, respectively.
ϑ_{rj}	-	true values of the temperature of the thermocouple
$\Delta_{\vartheta c}$	–	absolute error of the compensation of the influence of the cold-junction temperature (in degrees centigrade)
a_{Lj}	–	additive coefficient of linearisation
$e(\vartheta)$	–	thermo-emf between the positive and negative legs of a thermocouple
$e(\vartheta_h)$	–	thermocouple emf at the hot-junction temperature ϑ_h
$e(\vartheta_c)$	–	thermocouple emf at the cold-junction temperature ϑ_c
e_1, e_2	–	the initial and final values of the thermo-emfs, respectively
e_{rj}	-	true values of the emf of the thermocouple
k_a	–	amplification coefficient of the amplifier
$k_b(\vartheta_c)$	–	coefficient of conversion of the bridge circuit dependent on the cold-junction temperature ϑ_c
k_c	–	conversion coefficient of the ADC
k_d	–	divider's voltage ratio of the voltage divider
k_{Lj}	–	multiplicative coefficient of linearisation
n	–	number of thermocouples
n_{ch}	–	number of the measured channels
$N_{j\ av}$	–	output average code of the microprocessor
N_ϑ	–	equivalent temperature code
I	–	current
I_0	–	reference current
I_{st}	–	stabilised current of the stabiliser
R_{eq}	–	equivalent resistance
R_b	–	input resistance of the bridge circuit
R_d	–	resistance of the calibration resistor
R_{out}	–	output resistance of the bridge circuit
U_a	-	output voltage of the amplifier
U_{be0}	–	base-emitter voltage of the transistor at 0°C,
ΔU_{be}	–	averaged value of the base-emitter voltage change of the

		transistor due to the temperature change of one degree Celsius
U_{D0}	–	voltage drop across the diode at 0°C
ΔU_D	–	change in the voltage across the diode due to the change in temperature of one degree Celsius,
U_c	–	compensating voltage
U_n	–	nominal value of the output voltage of the temperature-dependent voltage source (constant voltage component)
U_s	–	supply voltage
U_{sd}	–	output voltage of the temperature-dependent voltage source
U_{st}	–	current stabiliser output voltage
$U_{st\ nom}$	–	nominal output voltage of the stabiliser
ΔU_c	–	absolute value of the voltage change due to the change in the cold-junction temperature of one degree Celsius
Δ_{Uc}	–	absolute error of the compensation of the influence of the cold-junction temperature
U_v	–	variable voltage component of the output voltage of the temperature-dependent voltage source

Chapter 4

$\alpha_a(\omega)$	–	shift the absorption spectrum
α_T	–	thermal expansion coefficient of the core material
α_γ	–	constant that represents optical losses on the path between the sensing and reference interferometers
$\alpha_\gamma(z)$	–	Rayleigh scattering coefficient
$\alpha_{\gamma aS}$	–	the fibre attenuation coefficient for the anti-Stokes wavelength
$\alpha_{\gamma S}$	–	the fibre attenuation coefficient for the Stokes wavelength
$\Delta\alpha(z)$	–	differential attenuation of the Stokes and anti-Stokes backscattering along the cable
β	–	isothermal compressibility
β_λ	–	calibration factor of the blackbody optical fibre thermometer for a wavelength λ
ε	–	strain
γ	–	constant for a given DTS system
$\eta(V)$	–	the fraction of the integrated fundamental mode density contained in the core
κ	–	power splitting ratio of the input fibre coupler
λ	–	wavelength of light
λ_{aS}	–	measured anti-Stokes wavelength

λ_B	–	Bragg wavelength
λ_p	–	pump wavelength
λ_S	–	measured Stokes wavelength
ν	–	frequency
$\Delta\nu$	–	frequency shift
ν_B	–	Brillouin frequency shift
τ	–	input pulse width pulse of duration
τ_0	–	lifetime of fluorescence decay at a given wavelength
τ_1	–	lifetime of faster fluorescence decay component
ω	–	unchanged complex variable
ω'	–	changed complex variable
ξ	–	thermooptical coefficient
Λ	–	grating pitch of the index modulation
$\Delta\Phi_0$	–	phase difference between two successive beams transmitted from the Fabry-Perot interferometer
$\Delta\Phi_p$	–	phase shift induced by the temperature change
$\Delta\Phi_s$	–	total phase shift
ΔF	–	scanning a frequency range
A	–	fibre attenuation
A_p	–	constant
c	–	speed of light in vacuum
C_T	–	temperature coefficient of the Brillouin frequency shift
d	–	fibre core diameter
D	–	length of the optical pulse in the fibre
h	–	Planck's constant
$J(t)$	–	fluorescent radiation intensity at time t
$J_0(t)$	–	fluorescent radiation intensity at time t=0
k_B	–	Boltzmann's constant
k_{TS}	–	temperature sensitivity coefficient of a fibre Bragg grating sensor
$K_{a\lambda1}$	–	absorption coefficient of the sapphire fibre at wavelength λ_1
$K_{a\lambda2}$	–	absorption coefficient of the sapphire fibre at wavelength λ_2
L	–	length of the grating
L_p	–	length of the PLCF segment
m	–	the order of Bragg diffraction
$M_{e\lambda}$	–	output from the detector of the blackbody optical fibre thermometer
n	–	unperturbated value for the effective refractive index of fibre mode
n_{eff}	–	effective index of refraction in the core
n_g	–	group refractive index of the fibre core
Δn	–	refractive index change

Δn_{eff}	–	difference between the effective refractive indices of the fundamental mode and the second order mode
p	–	average photoelastic coefficient of the glass
P_0	–	peak power
p_{11}, p_{12}	–	Pockel's (photoelasticity) coefficients
p_e	–	photoelastic constant of the optical fibre
$P_{aS}(z,t)$	–	the power of the anti-Stokes backscatter
P_B	–	Brillouin power
P_{Is}	–	power incident on the sensing interferometer
P_{Rr}	–	power reflected from the reference interferometer
$P_S(z,t)$	–	the power of the Stokes backscatter
$r_\gamma(z)$	–	effective backscatter reflection coefficient per unit length
R	–	reflectance
R_B	–	reflectivity R_B of the "Bragg signal"
R_I	–	ratio of the intensities
$S_{\Delta T}$	–	temperature sensitivity
t	–	time
$t_{\lambda 1L}$	–	optical depth of the fibre for absorption coefficient $K_{a\lambda 1}$
$t_{\lambda 2L}$	–	optical depth of the fibre for absorption coefficient $K_{a\lambda 2}$
T_0	–	actual temperature of the blackbody optical fibre thermometer
T_b	–	estimated temperature of the blackbody optical fibre thermometer
T_f	–	temperature at which the density fluctuations are "frozen" in the material
T_{ref}	–	reference temperature
T_{ThR}	–	threshold optical power
V	–	the normalized frequency of the fibre
V_p	–	visibility of the interference pattern
z	–	the coordinate of the forward-propagating pulse during generation of the detected backscatter signal $P_\gamma(t)$
Δz	–	spatial resolution of OTDR meter

Chapter 5

α	–	concentration
λ	–	wavelength of light
λ_B	–	Bragg wavelength
λ_0	–	inversion wavelength
$\Delta\lambda$	–	width of the selective reflection band
τ_d	–	response time for the decay process
τ_r	–	response time for the rise process

θ	–	angle between the long axis L of individual molecule and the director's direction
θ_{in}	–	incident angle of light
$\varepsilon_{\mathrm{II}}$	–	dielectric permittivity in the direction parallel with respect to the director direction
$\varepsilon_{\perp}$	–	dielectric permittivity in the direction perpendicular with respect to the director direction
$\Delta\varepsilon$	–	dielectric anisotropy
μ_{II}	–	magnetic permeability in the direction parallel with respect to director
$\mu_{\perp}$	–	magnetic permeability in the direction perpendicular with respect to director
$\Delta\mu$	–	magnetic anisotropy
$\Gamma(T)$	–	intensity of the reflected beam
Γ_0	–	constant dependent on the attenuations
$\Psi(T)$	–	temperature-dependent total rotation
d	–	cell thickness
E	–	electric field strength
E_{cn}	–	threshold of the cholesteric-nematic transition
$E_{c'c}$	–	threshold of the focal-conic (texture) deformation
E_{nc}	–	threshold of the nematic-cholesteric transition
I	–	intensity of light (optical transmission)
I_{ph}	–	photodiode current
k	–	sensor sensitivity
K_1	–	splay elastic constant
K_2	–	twist elastic constant
K_3	–	bend elastic constant
l	–	length of the LC capsule
m	–	diffraction order
$\vec{n}$	–	director, unit vector
n	–	average refractive index
n_e	–	index of the extraordinary refraction
n_o	–	index of the ordinary refraction
Δn	–	optical anisotropy
p	–	pitch
p_c	–	critical value of the pitch
q	–	chirality
S	–	order parameter
T_c	–	clearing point temperature
T_i	–	liquid crystal-isotropic phase transition temperature
T_m	–	temperature of melting point of the crystalline solid

Chapter 6

μ	–	actual division ratio of the code-controlled voltage divider
μ_{aj}	–	division ratio of the auxiliary voltage divider
μ_{max}	–	the maximum code-controlled divider's voltage ratio (for the maximum code value)
τ	–	width of the output pulse of the code-pulse width converter
ω	–	angular frequency of the noise voltage
a_q	–	coefficient equal 0 or 1 depending on the connection of the appropriate resistors either to the common ground bus or to the output of the current-to-voltage converter, respectively
C	-	capacitance
e_{ni}	–	noise voltages in the *i*-th wire
I	–	current
I_c	–	compensating current
I_{in}	–	input current
$I_{l\,max}$	–	the maximum value of the input current
$k_{a\,j}$	–	value of the auxiliary divider's division ratio
K_n	–	noise reduction coefficient
K_r	–	lead wire error reduction ratio
N	–	numerical code
q	–	binary place of the bit in the binary output code
r_i	-	switch S_i on-state resistance
R_0	-	resistance of standard resistor
R_{im}	–	imitation resistance
$R_{im\,\mathrm{max}}$	–	the maximum imitation resistance
R_L	–	lead wire resistance
$\Delta_{R\mathrm{im\ n}}$	–	absolute error of the resistance imitator caused by noise
$\Delta_{Rim}(R_L)$	–	absolute error of the resistance imitator due to the resistance of connecting wire
R_{out}	–	output resistance of the resistive ladder of the code-controlled voltage divider
T_p		pulse repetition period
U_a	–	output voltage of the auxiliary voltage divider
$U_{a\,max}$	-	maximum output voltage of the differential amplifier
U_R	–	reference voltage

Introduction

Thermal sensors can be divided into heat flow sensors and temperature sensors (Fig. 1.1).

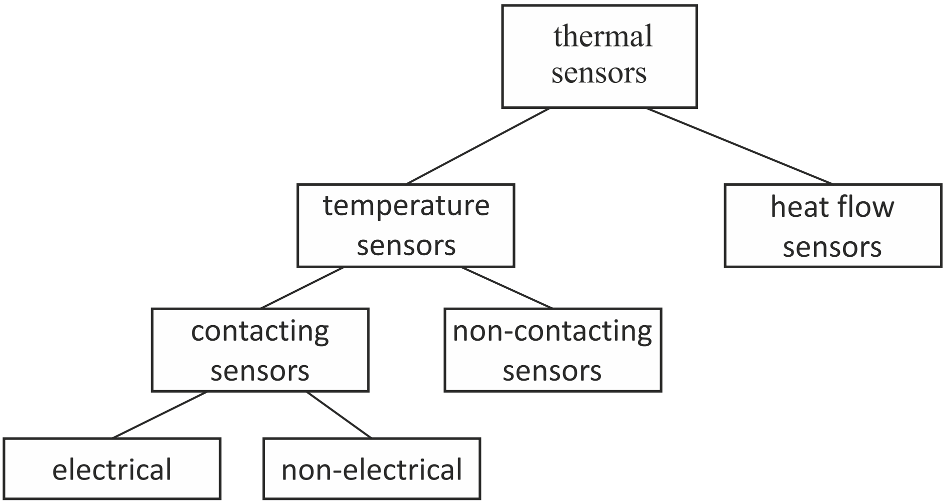

Figure 1.1. Classification diagram of thermal sensors

The heat flow sensors are beyond the scope of this book although these sensors also were the object of author's investigation. The elaborated designs of the heat flow sensors are characterised by advanced technology, relatively high sensitivity, high reproducibility of characteristics, and ease of operation and maintenance [110, 111, 247]. These sensors were employed for the measurements of heat fluxes of 10...10^4 W/m^2.

This book is focused on temperature sensors. Accordingly, the starting point should be a short introduction including the definition of temperature and the definition of sensor, as well as the classification of temperature sensors. The introduction also contains the rationale of the selection of the temperature sensors described in this book.

Temperature is one of the most frequently measured physical quantities. One can define ***temperature*** as the measure of internal energy (average kinetic energy of an atom or a molecule in a macroscopic amount of a substance) which characterises the amount of heat energy passed by an object. The temperature defines some properties of a substance. Depending on the temperature, there are such aggregate states of substance as gas, liquid, liquid crystal, and solid. A special state of matter is plasma.

During the XVIII and XIX centuries, three main temperature scales have been developed [220].

The ***Celsius temperature scale*** is based on 0 and 100°C for the freezing and the boiling points of water, respectively.

The ***Kelvin thermodynamic (absolute) temperature scale*** is based on the temperature of 273.16 K assigned to the triple point of water. The kelvin is the unit of temperature defined as 1/273.16 of the water triple point temperature. One kelvin is equal to one degree Celsius, so that the measured temperature intervals are the same on both the Kelvin and Celsius scales. The freezing point of water on the Kelvin scale is 273.15 K; thus, the conversion from degree Celsius to kelvin becomes $T=\vartheta+273.15$; T denotes the absolute temperature in kelvins, and ϑ denotes the temperature in degrees Celsius.

The ***Fahrenheit temperature scale*** is based on 32 and 212°F for the freezing and the boiling points of water, respectively; $\vartheta_F=1.8\vartheta+32$.

The ***International Temperature Scale*** of 1990 (ITS-90) is an internationally recognized temperature standard. Between 0.65 and 5 K, temperatures on the ITS-90 are defined in terms of the vapour pressure vs. temperature relationship for helium-3 and helium-4. Above 5 K, the ITS-90 assigns temperature values to sixteen fixed points.

Between the fixed points, the temperatures on the ITS-90 are obtained by interpolation using a helium gas thermometer in the range 3 K to 24.5561 K, a platinum resistance thermometer (PRT) in the range 13.8033 K to 1234.93 K, and an optical thermometer above 1234.93 K.

Some systems have suitable ***thermometric properties*** (i.e. which change with temperature), for example: electrical resistance, colour, transparency (opacity), etc. These thermometric properties are applied in different types of temperature sensors.

Let us define some terms that are used throughout this book.

Measured quantity is the physical quantity x_i that characterises the measured object (for example, the temperature of the object). In order to estimate the value of the quantity to be measured, the measuring process has to be performed.

Sensor (as a broader concept) is a device or an element that converts the input signal, quantity, property, or condition into the signal convenient for further conversion. The sensor can be a component of a measuring, regulating, or controlling device which converts some input quantity (for example, temperature) into a signal convenient for further measuring, transferring, storing, processing, or registration - usually into an electrical signal representing voltage, current, or charge (and as narrower concept some authors require sensor to output electrical signal). The advantages of the use of electrical quantities are the following: they are versatile (other quantities can be easily converted into electrical ones and vice versa), they can be transferred over long distances with high speed, converted into digital code, and allow high accuracy, sensitivity and fast performance. The output signal x_o is a function of the measured quantity x_i.

The transfer function $x_o=f(x_i)$ can be found experimentally using calibration, that is, for a given set of values x_i the respective values x_o are measured, and then the calibration equation is obtained. There are two kinds of sensors: direct and complex sensors (Fig. 1.2). A sensor is classified as a ***direct sensor*** if a direct energy conversion resulting in the output signal's generation or modification takes place (Fig 1.2a). However, in the case when it is impossible to convert the input quantity directly into electric one, the double conversion of the input quantity is performed (at first, the input quantity is converted into an intermediate nonelectrical quantity, and then the latter is converted into the electrical output quantity). A sensor that consists of one or more energy transducers and a direct sensor, is a ***complex sensor*** (Fig 1.2b).

A sensor is a component of a measuring system. The simplest measuring system consists of one sensor and one signal-processing device. The measurement system can include various devices for linearizating sensor's conversion characteristics, programmable amplifiers, A/D converters, etc.

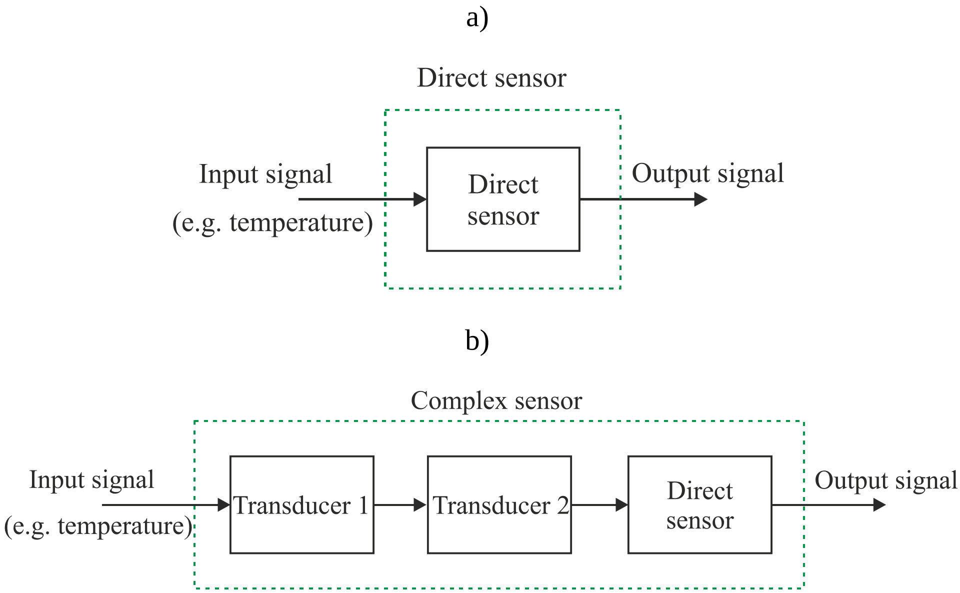

Figure 1.2. Schematic of (a) direct, and (b) complex sensor

Sensors can be classified into the following two types: active (self-generating) and passive (modulating). An ***active sensor*** converts the input energy into the output signal (without any supply from an additional energy source); most of the active sensors are direct sensors (for example, a thermocouple). A ***passive (parametric) sensor*** requires additional energy source (an excitation signal) to convert the input energy into the output signal (for example, a thermistor). Some authors, esp. in USA, call the self-generating sensors "passive" and modulating – "active" [186]; but the terms "self-generating" and "modulating" always mean the same.

Sensors can also be classified into absolute and relative. The sensor may produce a signal that relates to the absolute physical scale (an ***absolute sensor***), or to some special case (a ***relative sensor***). Relative temperature sensors measure the temperature difference between two objects one of which is a standard. A thermistor is an absolute sensor because its electrical resistance directly relates to the absolute temperature scale of Kelvin. A thermocouple is a relative sensor because its output signal should be referenced to a known baseline in order to relate to any particular temperature.

Depending on the structure design, a sensor can be ***external*** (when it is placed at the input of a device to give the information to the system about the outside quantities), or ***internal*** (***built-in***), inside the device (it can be the internal part of the device that produces a signal related to the state of the device).

As shown in Fig. 1.1, temperature sensors can be either ***contacting*** or ***non-contacting***. Contacting sensors contain a sensing element (e.g. a piece of material which responds to its temperature change, and is characterised by low specific heat capacity, small mass, high and predicted sensitivity), the leads (which are characterised by minimal heat conductance and resistance), and the housing which is characterised by high heat conductance, and is inert to humidity. The contacting sensors differ from non-contacting in the way of heat transfer from the object to the sensing element; the heat is transferred through physical contact, on contrary to non-contacting sensors for which the heat is transferred through thermal or optical radiation. The classification diagram of the contacting temperature sensors is given in Fig. 1.3; the sensors discussed in this book are within hatched areas. Other classes of the temperature sensors are not considered in this book, although the author would like to mention the thermosensitive integrated circuits (ICs); the principles of their design and results of their investigation are given in [73, 75]. These ICs provide relative temperature reading, and can be employed for temperature measurements over the narrow temperature range beginning from $\pm 1^{o}$C, within the temperature range $-50\ldots+120^{o}$C.

There are different classifications of the sensors depending on: sensor's material, sensor's conversion phenomena (for example: thermoelectric, thermooptic), operating principle (for example: thermoresistors, thermocouples, pyrometers), and the field of application.

Temperature sensors are widely used in different areas, e.g. industry, scientific investigations, space applications, medicine, etc. As reported in [293], slightly over 2 billion temperature sensors were fabricated in the year 2010, and the number is expected to reach three and a half billion by 2016, at an estimated CAGR (Compound Annual Growth Rate) of 10% from 2011 to 2016. Hence, the design of methods for improving accuracy of actual temperature measurement, and the design of the new temperature sensors is an up-to-date problem.

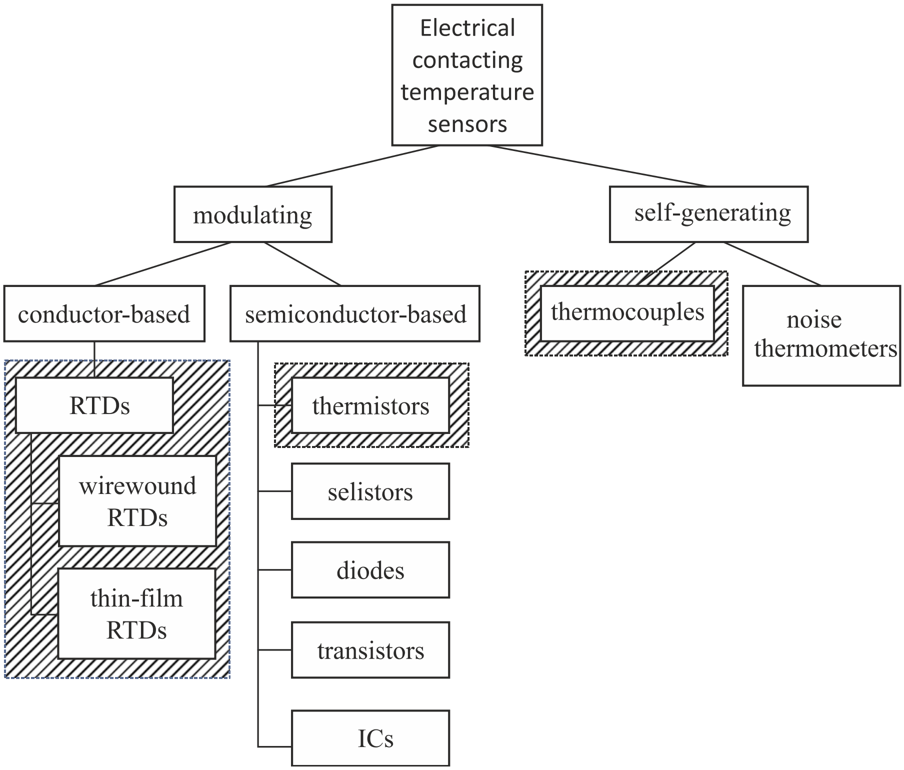

Figure 1.3. Classification diagram for contacting temperature sensors

Until now, there are no universal temperature sensors, which would meet all up-to-date requirements. Therefore, both traditional and new temperature measurement methods and temperature sensors are employed.

In industrial applications, such types of temperature sensors as thermocouples, resistance temperature detectors (RTDs) and thermistors are most frequently used. Thermocouples are still the most frequently employed type of temperature sensors. The use of each type of the aforementioned temperature sensors is related to the measurement task. The end-user chooses the temperature sensors considering the optimal parameters in given operating conditions. The selection of the best temperature sensor among the alternative sensors for a given application may be based on analytic hierarchy process method, considering appropriate criteria and subcriteria [6]. For temperature sensors, the criteria used as basis for comparison can be as follows: static criteria (maximum operating temperature, minimum operating temperature, temperature curve, maximum sensitivity region, self-heating issues, long term stability and accuracy, typical temperature coefficient, extension wires, long wire runs from sensor, measurement parameter, temperature measurement), dynamic characteristics (stimulation electronics required, typical output levels per degree Celsius, typical fast thermal time constant), environmental parameters (typical small size, noise immunity, fragility-durability characteristics, high thermal gradient environment, corrosion resistance), and other criteria (point or area measurement, manufacturing variances, standards, cost).

When comparing thermocouples, RTDs and thermistors, the wider operating temperature is exhibited by thermocouples, and the highest accuracy is offered by thermistors. High linearities are common for thermocouples and thermistors, the highest ruggedness is typical for thermocouples, and the response of the thermocouple is faster. The cost is lower for thermocouples (except for noble metal thermocouples) and thermistors. However, thermocouples require to compensate for the cold-junctions. Among different types of thermocouples, the K-type and J-type thermocouples are most commonly used; this may be related to their linearity and ability to provide a high output voltage over a given temperature range.

It should be noted that for a number of years there has been a trend towards a shift from thermocouples to RTDs. This can be explained by such advantages of RTDs over thermocouples as accuracy and stability. However, the main limitation of RTDs' use is that they cannot be employed in extremely high temperatures, as well as the high cost and time-consuming sensor maintenance and calibration. Also, the shift from the wirewound to the thin-film RTDs is observed.

The wide field of application of thermocouples, RTDs and thermistors results in the search for new methods of the accuracy improvement of the temperature measurement accomplished with them. The already well known, and the proposed by the author, methods of improvement in accuracy of temperature measurement with thermocouples and resistance temperature sensors, including thin-film thermoresistors, are described in Chapters 2 and 3. In order to understand the methods of improvement in temperature measurement accuracy, the basics on temperature sensors are given.

One of observed trends is the shift from contact temperature measurements to non-contact measurements. In this case, the fibre optic-based and the liquid crystal temperature sensors become an attractive choice because they can be employed in temperature measurements when the use of other types of sensors, such as thermocouples or RTDs, is not possible. Different types of fibre-optic temperature sensors, including photonic crystal fibre sensors with emphasis on their challenges and possibilities are described in Chapter 4. The known, and the proposed by the author, possibilities of application of liquid crystals in temperature sensors are presented in Chapter 5. The basics of liquid crystals are described for better understanding of both the sensor's operating and the predetermination of the parameters of liquid crystal material in order to apply it as the sensing element of the temperature sensor.

For temperature sensors, like for other types of sensors, a metrological instrumentation is required. In Chapter 6 some original solutions of a multi-range resistance standard and a multi-value resistance, voltage and current calibrator are given.

The author has narrowed the scope of the book to thermocouples and resistance temperature sensors, as the most widely used types of contact temperature sensors. Liquid crystal-based temperature sensors are also presented as attractive non-contact alternative sensors; other types of temperature sensors are omitted. The aforementioned types of temperature sensors are within the author’s field of interest, and new conceptions concerning these sensors are considered in this book.

The author hopes that this book will be useful for all who are in touch with the area of temperature measurements, including engineers, and the graduate and post-graduate students who are interested in the methods and devices for temperature measurement.

2. Resistance Temperature Sensors

2.1. Features of Resistance Temperature Detectors and thermistors as temperature sensors

Resistance temperature detectors (RTDs) and thermistors are the temperature sensors which change their electrical resistance with temperature.

The RTDs are made of the materials which are characterised by high values of electrical resistivity and temperature coefficient of resistance (TCR), as well by their high stability, high reproducibility of the electric resistance at certain temperatures, good stability of chemical and physical properties during heating, and insensitivity to operating conditions. Among the materials possessing the abovementioned properties and parameters, the following can be mentioned: platinum, copper, nickel, tungsten, and pure metals with small amount of alloying elements (e.g. rhodium-iron or platinum-cobalt). The platinum and copper RTDs are most commonly used [128, 235, 281]. In general, RTDs are employed over the wide temperature range from –260°C up to 850°C, and some of these RTDs are applied up to 1200 °C [13, 143, 220, 285].

In the range from 13.8033 K to 1234.94 K, the International Practical Temperature Scale is defined by means of a Standard Platinum RTD. This application is preferred because of platinum's features such as very high coefficient of resistivity, and very stable operation over a long period of time [235]. The TCR of Platinum RTD is high enough to result in sufficient measurable resistance changes with temperature.

Industrial Platinum RTDs do not correspond to Standard Platinum RTD qualities, but they meet the laboratory standard requirements and can be reproducible to a few tens of millikelvin over the range from −200 °C to about 600 °C. Industrial Platinum RTDs are applied not only in industrial processes, but also for testing and calibration purposes [63].

There are four tolerance classes of Industrial Pt100 RTDs (defined in IEC 60751:2008): AA, A, B and C (Fig. 2.1) [291].

The interpolation scheme for Industrial Platinum RTD, recognized in several international standards and corresponding national standards, is based on the Callendar–Van Dusen equation [63, 285].

The platinum RTD's transfer function, based on the Callendar-Van Dusen approximation over the temperature range from –200°C to 0°C, can be written as follows:

$$R_{\vartheta} = R_0\left[1 + A\vartheta + B\vartheta^2 + C(\vartheta - 100)\vartheta^3\right]. \tag{2.1}$$

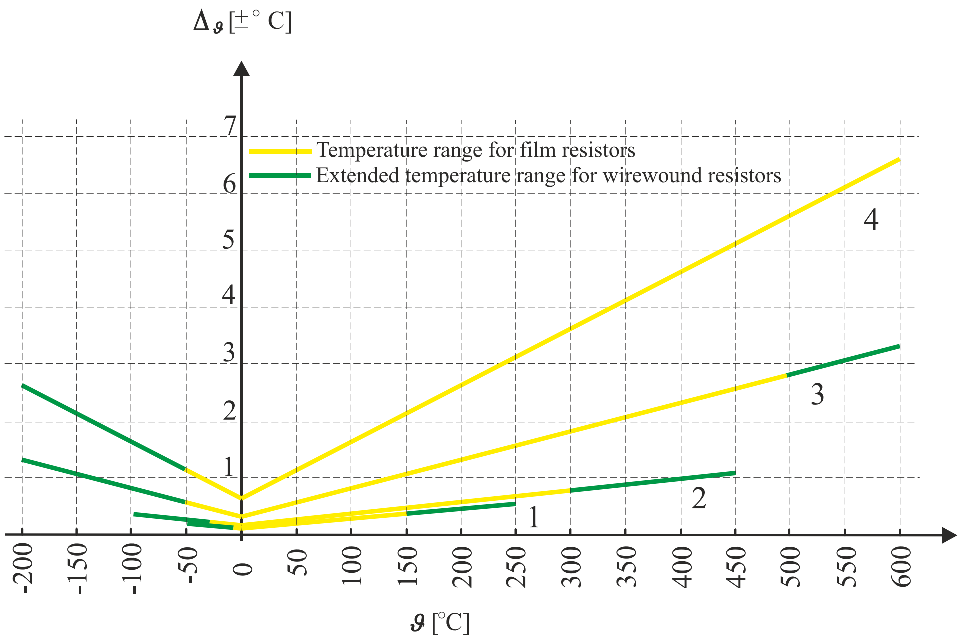

Figure 2.1. Tolerances Δ_ϑ for assembled Pt100 sensors (in compliance with IEC 60751:2008) for different classes: 1 – AA, 2 – A, 3 – B, 4 – C

Over the temperature range 0... 650 °C, the transfer function can be expressed by the following formula:

$$R_\vartheta = R_0\left(1 + A\vartheta + B\vartheta^2\right), \tag{2.2}$$

where R_ϑ is the resistance of the RTD at the temperature ϑ, R_0 is the base resistance at 0°C, and A, B and C are the constant coefficients. For a standard Pt RTDs, the coefficients A, B, and C are given in Table 2.1. In some particular cases these coefficients can be obtained for each individual RTD; for example, by measuring the resistance at different temperatures the coefficients A, B, and C can be determined using the regression analysis [171, 176, 292].

Different constructions of RTDs are applied; all these designs provide a strain-free sensing element by eliminating the constraints of a normalised winding mandrel and its overcoating. For example, one of the common RTD designs is the wirewound element made by winding platinum wire around a mandrel (Fig. 2.2). The mandrel is made of an electrically non-conductive material. The sensing element is connected with lead wires. It is overcoated with a nonconductive protective coating (e.g. ceramic cement, or glassy coating).

Table 2.1. Callendar-Van Dusen coefficients corresponding to common Pt RTDs

Standard	Temperature coefficient of resistance, α	A	B	C
	$[°C]^{-1}$	$[°C]^{-1}$	$[°C]^{-2}$	$[°C]^{-4}$
DIN 43760	0.003850	$3.9080 \cdot 10^{-3}$	$-5.8019 \cdot 10^{-7}$	$-4.2735 \cdot 10^{-12}$
American	0.003911	$3.9692\ 10^{-3}$	$-5.8495 \cdot 10^{-7}$	$-4.325 \cdot 10^{-12}$
ITS-90	0.003926	$3.9848 \cdot 10^{-3}$	$-5.870 \cdot 10^{-7}$	$-4.0000 \cdot 10^{-12}$
IEC 60751:2008	0.003851	$3.9083 \cdot 10^{-3}$	$-5.775 \cdot 10^{-7}$	$-4.183 \cdot 10^{-12}$

Another design includes the coil of fine platinum wire assembled into small holes in a cylindrical ceramic mandrel. The ceramic powders support the coils in the mandrel bores and hold them firmly in place with minimum strain. These constructions are characterised by the reduced influence of the strain on the resistance, very high accuracy and stability, necessary for the use in secondary temperature standards and docile industrial applications (with little or no vibration or shock). The ceramic materials that allow for the achievement of higher stability of the sensing coil, resulting in accuracies of 0.03°C after thousands of hours at temperatures of 500°C are also reported [220].

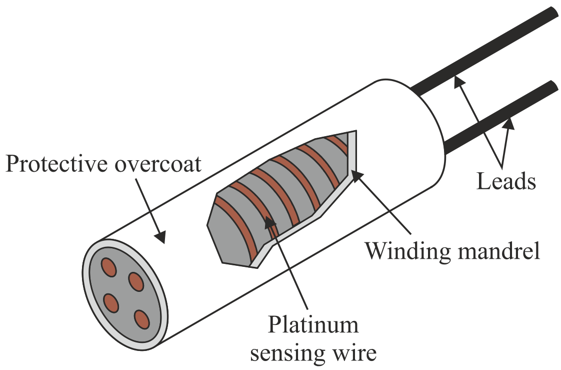

Figure 2.2. Wirewound RTD

The drawbacks of the platinum RTDs are: a considerably high level of contamination in platinum from metal vapours (especially by iron) at high temperatures, and a relatively low chemical stability of platinum in the reducing atmosphere, resulting in its fragility, and instability of parameters.

Because of the low cost and fairly high stability against the corrosion, the copper is widely used in RTDs over the temperature range −50...+180°C. The TCR of copper is nearly 0.00427 1/°C. The relationship between the resistance and the temperature for copper is fairly linear within 0.1°C at temperatures less than 200°C [36]:

$$R_{\vartheta} = R_0 \left(1 + \alpha_{Cu} \vartheta\right), \qquad (2.3)$$

where α_{Cu} is temperature coefficient of resistance (TCR) for copper.

The drawback of the copper RTDs is high oxidation during the heating; that limits their application to the above-mentioned narrow temperature range in the environments with low humidity and without aggressive gases.

Nickel is characterised by high resistivity and TCR value (near 0.00672 1/°C). Nickel is sensitive, quite repeatable, and less expensive than platinum, but the resistance change with temperature is nonlinear and sensitive to strain [36].

Tungsten RTDs are usually employed for temperatures over 600°C. The use of the refractory metals such as tungsten, molybdenum, tantalum and niobium is limited because under the temperature influence they become fragile, and therefore very sensitive to mechanical vibrations.

Metallic alloys, which exhibit electrical resistivity higher than pure metals, have not been applied as materials for sensing elements of RTDs because of a relatively low TCR, the value of which considerably depends on the qualitative and quantitative composition of alloy-forming elements.

Germanium RTDs have been recognized as secondary standard thermometers and are applied for temperature measurement over the range from −272°C to −173 °C.

For cryogenic applications, the germanium RTDs (−272 °C ÷ −243 °C) and the rhodium-iron RTDs (−272 °C ÷ −190 °C) are employed. Rhodium-iron RTDs are applied not only in low temperatures, but also up to temperatures as high as 500 °C, and are characterised by high stability. In consequence, they are used for high precision, accurate temperature measurements over a wide temperature range.

Platinum-cobalt RTDs (0.5 wt % Co) have similar low temperature behaviour as the Rhodium-iron RTDs [272].

The parameters of the widely applicable RTD materials are given in Table 2.2 [294].

The main causes of the errors of the RTDs are the following: inaccuracy of the resistance adjustment R_0 at 0°C and deviation of the ratio of the resistance R_{100} (at 100°C) to the resistance R_0 from the nominal ratio value, time instability of these parameters, additional heating caused by operating current flow, the influence of the lead wire resistance between the measuring circuit and RTD, etc.

Table 2.2. Parameters of materials for RTD

Material	Temperature coefficient of resistance	Law	Resistivity	Temperature range	Stability
	[°C^{-1}]	-	[Ω/cmf*]	[°C]	-
Platinum (Pt)	0.00375 0.00385 0.003911 0.003926	Quadratic or cubic	59	–260…1200	high
Nickel (Ni)	0.00618 0.00672	Quadratic or cubic	36	–260…1200	medium
Copper (Cu)	0.00427	Linear	9.26	–200… 200	medium
Balco iron-nickel alloy	0.0052 0.00518 0.00527	Quadratic or cubic	120	–200 …204	medium
Rhodium-iron Rh5%Fe	0.004	Quadratic		–272… 400	high

* - cmf = "circular - mil - foot" is a unit of volume. Typically, it is used to compare resistivities of wires in form of a conductor which is 1 foot in length and has a cross-sectional area of 1 circular mil.

The response time of RTD, in general, is from 0.5 to 5 seconds or more, and is related to thermal conductivity which is essential for bringing the device into thermal equilibrium with its environment. The response time is longer for a "free air" condition (or its equivalent) because of poor thermal conductivity. The shorter response time is for an "oil bath" condition (or its equivalent) because of better thermal contact. For various applications, different response times of RTDs are required [46].

The application of the thin-film technology in the RTD manufacturing offers new possibilities: it allows obtaining different film materials with certain properties, and simplifies the manufacturing technology of the RTDs based on these materials. The film metal-insulator-metal structures can be obtained directly on the measuring surface by vacuum evaporation. This leads to the minimization of the measurement error caused by the imperfections of the heat contact between the sensing element and the surface. If a thin film platinum

RTD is bonded to a substrate material, then it can measure the temperature in a very local area. Such benefits of the thin film RTD like the small overall size and good thermal contact, result in the fast response of the RTD. The devices created using the thin-film technology are smaller, less expensive, more rugged mechanically, more reliable, less power consuming, and exhibit a faster response time in comparison with the wirewound RTDs. Because of the abovementioned advantages of the thin film RTDs, they are often employed for temperature measurement and control [218, 220].

Thin film RTDs are usually made of platinum or its alloys (thickness from 1 to 2 μm), and are deposited on a suitable substrate (such as a micromachined silicon membrane). The trimming of the length of the film allows obtaining precise resistance values. The use of the adjustment of the thickness and other dimensions of the film enable the achievement of much higher resistances. The film is protected from mechanical strains and environmental conditions by a thick (10 μm) protective coating. For example, for platinum film this coating can be made of epoxy or glass. The coating acts as a strain relief for the external lead wires which may be attached by soldering, crimping, brazing or welding. In order to ensure a sufficiently large length-to-width ratio for the sensor, the RTDs are often fabricated in a serpentine shape (Fig. 2.3) [220].

For a rectangular-shaped conductive film of the length l, width b and thickness d, the resistance R is equal to:

$$R = \rho \frac{l}{b \cdot d}, \tag{2.4}$$

where ρ is the resistivity of the film material.

For $l=b$ (a square shape), the resistance formula is the following:

$$R_{sq} = \frac{\rho}{d}. \tag{2.5}$$

If $l/b=n_{sq}$ (n_{sq} is the number of the squares), then

$$R = R_{sq} \cdot n_{sq}. \tag{2.6}$$

The TCR values of the film RTDs are lower, and the temperature ranges are narrower than for their wirewound counterparts. This can be explained by the difference between the coefficients of linear expansion of the substrate and the metal film that causes a plastic deformation of the film due to remarkable increase (or decrease) in temperature. In order to eliminate this undesirable phenomenon, the multilayer structures consisting of one thermosensitive layer, and a number of intermediate layers which ensure strong mechanical contact, are used. For ensuring a high level of stabilisation of the electro-physical properties of the film RTDs, the thermal aging in vacuum under the conditions of cyclic temperature changes is applied.

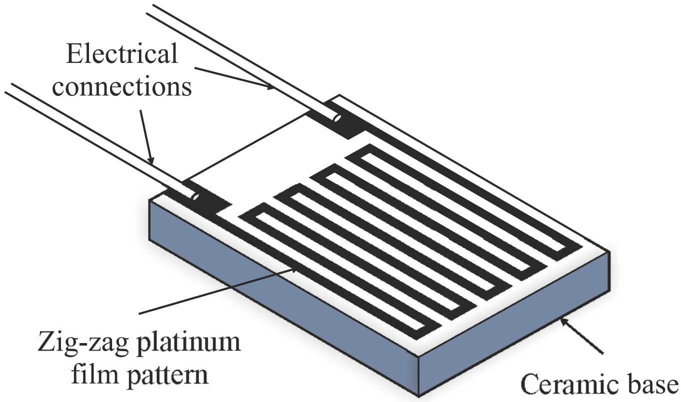

Figure 2.3. Exemplary thin-film RTD design

The manufacturing process involved with the thin-film RTDs consists of developing the sensitive element configuration, mask making, deposition of the active thin-film layer, and calibration.

In order to obtain higher nominal resistance values, it is necessary to minimize both the resistor's width (which is limited by technological possibilities), and the resistor's thickness (which should be no less than the limits of its homogeneity, i.e. near 20 nm). Also, the upper limit of the thickness is determined (d_{max} = 0.5 μm) by the difficulties in the protection of the resistor's ends during the technological process of manufacturing the thin-film RTD. The best method to ensure high nominal resistance of thin-film RTDs is the use of resistive materials which exhibit high TCR values.

In [152] it was demonstrated that for thin film Pt RTDs, the TCR increased with: a decrease in film thickness, a narrower pattern line width, and an increase in annealing temperature. The highest obtained TCR value for thin film Pt RTDs was 3.53×10^{-3} 1/°C for RTD with 1 mm line width, and after thermal treatment at 700°C. In [37] it was shown that for Pt RTDs fabricated on the $MgO/SiO_2/Si$ substrates, the TCR increases to the value 3.927×10^{-3} 1/°C. Such RTDs exhibit a remarkable dispersion of resistance and linearity with temperature, similarly to the inherent characteristics of Pt RTDs over a wide temperature range.

During the fabrication of the copper film RTDs on the glass ceramic substrate, the intermediate adhesion of the TiW layer is used to increase the stability of R_0, and to ensure the high adhesion of the thermosensitive copper layer to the glass ceramics.

The thicknesses of the adhesive and protective layers are tailored to ensure the required adhesion, as well as the lowest shunting of the thermoresistive layer, and to prevent the oxidation. Such thin-film RTDs are characterised by high reproducibility of the temperature characteristics, and the TCR is equal to 3.22×10^{-3} 1/°C [26].

Making the choice of the material of the substrate for a thin-film RTD, the heat exchange between the RTD and the surrounding environment, described by the equation (2.7), should be considered:

$$\Delta Q = cm\Delta\vartheta\,, \tag{2.7}$$

where ΔQ is the amount of heat transferred to the system thin film-substrate of mass m; c is the specific heat, and $\Delta\vartheta$ is the interval of the temperature change. Knowing the heat transfer parameters is important for an assessment of the thermal inertia of the film resistor.

Under operating conditions, the heat transfer between the RTD and its ambient can be described by three processes: the heat losses due to the heat conductance of the substrate material, the forced convection, and the radiation.

The Ni-Fe and Ni-Co alloys are used for the film RTD; e.g. the TCR of the permalloy (Ni 80% - Fe 20%) is approximately the same as that of platinum, and its maximum value is observed within the film thickness range from 60 nm to 80 nm (for platinum, the maximum TCR is reached at the thickness of 350 nm). Hence, the use of permalloy allows considerable reducing of the RTD's square.

The nominal resistance is the prespecified resistance value at a given temperature. Most standards, including IEC 60751, use the temperature 0ºC as the reference point. The recommended IEC standard is 100 Ω at 0ºC, but other nominal resistances such as 50, 200, 400, 500, 1000 and 2000 Ω, are also allowed.

In order to register the resistance change, the RTDs require an external current source. The current should be kept low (1–5 mA) in order to minimize the self-heating effect. The minimization of the self-heating can be achieved either by the pulse current supply of the bridge circuit to which the RTD is connected, or by using a higher value of the RTD's resistance [235].

The thermistors are semiconductor transducers that are manufactured mainly by the methods of powder metallurgy; the fabricated shapes are rods, disks, beads, wafer thin plates, etc.; the size varies from 1-10 μm to 1-2 cm.

The sensitivity of thermistors is very high. The resistance of a thermistor may change by five orders of magnitude in the sensor's useful temperature range. The TCRs of the thermistors are high (tens of times higher than for metal transducers).

The thermistors with negative TCRs are made from the mixture of polycrystalline oxides of transition metals (e.g.: MnO, CoO, NiO, CuO) doped with Ge and Si, $A^{III}B^{V}$ semiconductors, glass semiconductors and other materials.

Let us consider the thermistors with high negative temperature coefficient of resistance. The relationship between temperature and thermistor's resistance can be described as follows:

$$R = R_\infty \exp\left(\frac{\beta}{T}\right), \tag{2.8}$$

where R is the thermistor's resistance, R_∞ is the thermistor's resistance at $T \to \infty$ (it can exhibit a weak temperature dependence), β is the thermistor coefficient (material constant), and T is the temperature in kelvins. The β and R_∞ are the main parameters of the thermistor.

The TCR of the thermistor is described as:

$$\alpha_T = \frac{d(\ln R)}{dT} = -\frac{\beta}{T^2}\,. \tag{2.9}$$

The efficiency of operating, and the sensitivity of thermistors depend on their main parameters and the TCR. In order to achieve high sensitivity, high values of the parameters β and α_T are required.

To understand the nature of the parameters β, and R_∞, the elements of the kinetic theory based on the large statistical sum Z_{be} for large non-equilibrium quantum ensemble with variable number of particles should be discussed. This conception is an alternative to the classical kinetic theory based on the kinetic Boltzmann equation [30].

Taking into account the spin degeneracy, the statistical sum of such ensemble [28] is equal to:

$$Z_{be} = \prod_{\vec{k}} \left[1 + \exp\left(\frac{\mu + \Delta\varepsilon_{\vec{k}} - \varepsilon_{\vec{k}}}{kT}\right)\right]^2, \tag{2.10}$$

where $\vec{k}$ is the wave vector of the charge carriers (it is a counterpart of the quantum number), $\varepsilon_{\vec{k}}$ is the dispersion, μ is the chemical potential, k is Boltzmann constant, and $\Delta\varepsilon_{\vec{k}}$ is the change of the charge carrier energy under the disturbances which interfere with the state of the crystal's thermodynamic equilibrium. At the absence of such disturbances $\Delta\varepsilon_{\vec{k}} = 0$, and the charge carrier gas transforms into the large quantum ensemble of particles.

For the charge carrier gas in the non-equilibrium state, the transfer of the electricity and the heat transfer are described by the generalized equation of the electric and heat conductivity.

Let us consider the generalized equation of the electric conductivity for the isotropic conductive crystals. In such crystals, there are both the electric field intensity $\vec{E}$ and the temperature gradient $\nabla_{\vec{r}} T$, and the crystals are immersed in the magnetic field $\vec{B}$. For crystals of large statistical sum, this equation can be written as:

$$\vec{j} = en\left[S_{ik}^{(0)}(\vec{B}) + A_{ik}^{(0)}(\vec{B})\right]\vec{E} - en_c\left(\frac{k}{ze}\right)\left[S_{ik}^{(1)}(\vec{B}) + A_{ik}^{(1)}\right]\nabla_{\vec{r}} T\,, \qquad (2.11)$$

where $\vec{j}$ is the vector of the electric current density through the crystal, and $S_{ik}^{(0)}(\vec{B}), A_{ik}^{(0)}(\vec{B})$ are the symmetric and antisymmetric kinetic tensors, respectively [29].

The nature of these tensors depends on the charge carrier dispersion law and the scattering mechanisms; $z = \pm 1$ is the sign of the charge carriers, and n_c is the charge carrier concentration.

$$n = \int_0^\infty G(\varepsilon)\left(-\frac{\partial f_0}{\partial \varepsilon}\right)d\varepsilon\,, \qquad (2.12)$$

where $f_0 = \left[\exp\left(\frac{\varepsilon_{\vec{p}} - \mu}{kT} + 1\right)\right]^{-1}$ is the Fermi-Dirac function,

$$G(\varepsilon) = \int_0^\varepsilon g(\varepsilon)d\varepsilon\,, \qquad (2.13)$$

where

$$g(\varepsilon) = \frac{2}{h^3}\oint \frac{dS}{\left|\nabla_p \varepsilon_p\right|} \qquad (2.14)$$

is the density of the states.

In the formula (2.14) the surface integral is taken over the energy surface defined by the dispersion law $\varepsilon_{\vec{p}} = \varepsilon(\vec{p})$, where $\vec{p} = \hbar\vec{k}$.

In the absence of the magnetic field and temperature gradient, for isotropic crystals the equation (2.11) can be rewritten as:

$$\vec{j} = en_c S^{(0)}(0)\vec{E} = en_c\langle u\rangle\vec{E}\,, \qquad (2.15)$$

where the average mobility <*u*> equals:

$$\langle u\rangle = \frac{\int_0^{\infty} G(\varepsilon)u(\varepsilon)(-\frac{\partial f}{\partial\varepsilon})d\varepsilon}{\int G(\varepsilon)(-\frac{\partial f_0}{\partial\varepsilon})d\varepsilon} . \qquad (2.16)$$

The scattering function $u(\varepsilon)$ in (2.16) is expressed in the same unit as the charge carrier mobility. For the crystals that obey the isotropic dispersion law $\varepsilon_{\vec{p}} = \varepsilon(|\vec{p}|) = \varepsilon(p)$, this function can be determined by the following formula [31]:

$$u(\varepsilon) = \frac{e\tau_r}{p}\left(\frac{d\varepsilon}{dp}\right), \qquad (2.17)$$

where τ_r is the relaxation time of the charge carrier pulse during their scattering on the crystal lattice's defects, and p is the pulse vector module.

The scattering function $u(\varepsilon)$ is described by the following formula:

$$u(\varepsilon) = u_0^{(r)}(T)\,p^{(2r-3)}\left(\frac{d\varepsilon}{dp}\right)^2, \qquad (2.18)$$

where the scattering factor r and the temperature function $u_0^{(r)}(T)$ depend on the nature of the crystal and on the scattering mechanisms.

For crystals which obey the parabolic dispersion law: $\varepsilon = \frac{p^2}{2m^*}$ (m^* is the effective charge carrier mass) the scattering function (2.18) can be rewritten as:

$$u(\varepsilon) = u_0^{(r)}(T)\left(\frac{\varepsilon}{kT}\right)^{r-1/2}. \qquad (2.19)$$

In the case of the scattering of charge carriers by acoustical phonons, the scattering factor r equals to 0 and the temperature function is $u_0^{(0)}(T) \sim T^{-3/2}$. If the charge carriers are scattered by the optical phonons above the Debye temperature, $r = 1$ and the temperature function is $u_0^{(1)}(T) \sim T^{-1/2}$. For the charge carriers scattered by the ionized dopants in the crystal, $r = 2$ and the temperature function is $u_0^{(2)}(T) \sim T^{3/2}$.

If a complex scattering occurs, then the superposition of a few scattering mechanisms is characterised by the factors r_1, r_2, ... r_i, and the generalized scattering function is the following:

$$\frac{1}{u} = \frac{1}{u^{(r_1)}} + \frac{1}{u^{(r_2)}} + \ldots + \frac{1}{u^{(r_i)}} . \qquad (2.20)$$

For the parabolic dispersion law:

$$G(\varepsilon) = \frac{8}{3\sqrt{\pi}} \left(\frac{2\pi m^* kT}{h^2}\right)^{3/2} \varepsilon^{3/2} . \qquad (2.21)$$

According to (2.12) and (2.16):

$$n = \frac{8}{3\sqrt{\pi}} \left(\frac{2\pi m^* kT}{h^2} \right)^{3/2} F_{3/2}(\mu^*) , \qquad (2.22)$$

$$\langle u \rangle = u_0^{(r)}(T) \frac{F_{r+1}(\mu^*)}{F_{3/2}(\mu^*)} , \qquad (2.23)$$

where $\mu^* = \dfrac{\mu}{kT}$ is the reduced chemical potential, and $F_r(\mu^*) = \int\limits_0^\infty x^r \left(-\dfrac{\partial f_0}{\partial x}\right) dx$ is the Fermi integral.

The formulae (2.15) and (2.16) describe the average value of the charge carrier mobility (we will consider u_n or u_p for the n-type and p-type conductivity, respectively). The generalized equation of the electric conductivity (2.15) can be rewritten as follows:

$$\vec{j} = en_c u_n \vec{E} = \sigma_n \vec{E} , \qquad (2.24)$$

where σ_n is the conductivity of the crystal. In the case of the complex electric conductivity, the equation (24) can be expressed as follows:

$$\vec{j} = (enu_n + epu_p)\vec{E} = (\sigma_n + \sigma_p)\vec{E} = \sigma\vec{E} . \qquad (2.25)$$

The resistance of the semiconductor resistor is equal to:

$$R = \frac{1}{\sigma} \cdot \left(\frac{\Delta l}{\Delta S} \right) , \qquad (2.26)$$

where Δl is the resistor length, and ΔS is the cross-section area.

The intrinsic conductivity of semiconductor resistors is equal to:

$$\sigma_i = en_i u_n + en_i u_p = en_i u_n \left(1 + \frac{u_p}{u_n} \right) , \qquad (2.27)$$

where $n_i = (2\pi)^3 (m_n^* m_p^*)^{3/2} T^{3/2} \exp\left(-\frac{\Delta E}{2kT}\right)$ is the intrinsic charge carrier concentration, ΔE is the forbidden gap width, and (u_p/u_n) is a constant.

Within the area of the intrinsic conductivity when $u_0^{(0)}(T) \sim T^{-3/2}$, the most probable is the scattering of the charge carriers by acoustical phonons of the crystal lattice. Then the conductivity of the semiconductor crystals can be described as follows:

$$\sigma_i = \left[e(2\pi)^3 (m_n^* m_p^*)^{3/2} T^{3/2} u_n \left(1 + \frac{u_p}{u_n}\right)\right] e^{-\frac{\Delta E}{2kT}} = \sigma_0 \exp\left(-\frac{\Delta E}{2kT}\right). \quad (2.28)$$

According to (2.26), the resistance of the semiconductor resistor is equal to:

$$R = \frac{1}{\sigma_0}\left(\frac{\Delta l}{\Delta S}\right) e^{\frac{\Delta E}{2kT}} = R_\infty e^{\frac{\Delta E}{2kT}}. \quad (2.29)$$

Comparing the formula given above with the formula describing the temperature dependence of the thermistor's resistance, one can obtain:

$$R_\infty = \frac{1}{\sigma_0}\left(\frac{\Delta l}{\Delta S}\right) \quad (2.30)$$

where R_∞ depends on the composition and the size of the thermistor. $\beta = \Delta E / 2k$ is proportional to the forbidden gap width. In order to manufacture the high TCR thermistors, the semiconductor materials with large forbidden gap width are the right choice.

Thermistors are not standardised. Therefore, the design, construction, and characteristics of thermistors can vary for different manufacturers.

The benefits of thermistors are small sizes, small inertness, simplicity, and possibility of operating in different climatic conditions at considerable mechanical loads. In comparison with metallic resistors, their accuracy is lower, and their temperature vs. resistance characteristics is typically nonlinear; the stability of their parameters is not high because of aging effects.

The bulk sensing elements should be mounted strain-free because the semiconductors exhibit piezoresistivity. This involves the reduction of the thermal attachments to the measuring object. That, in turn, means that the self-heating effect should be considered unless the power supplied to the sensor is kept extremely low [272].

2.2. Circuit design methods for the accuracy improvement of the temperature measurement with resistance temperature sensors

Since RTDs are widely used for temperature measurements, the development of the methods for improving the accuracy of the temperature measurement with an RTD is a topical issue. The improvement of the temperature measurement accuracy can be achieved by the linearization of the transfer function of RTDs, the compensation of the lead wire resistance, and the increase in linearity of the thermoresistive measuring bridge circuits. In the following section, some methods for the improvement of the temperature measurement accuracy are considered.

2.2.1. Linearization of the transfer function of platinum thin film RTDs

As it was mentioned above, the platinum resistance thermometers (PRTs) are widely used for accurate temperature measurements because of the lowest achievable uncertainty over a wide temperature range. The PRTs are applied in industrial process control, and in testing and calibration laboratories [63].

Platinum RTDs are more linear devices than thermocouples, but they exhibit a non-linearity of the second order, approximately 0.38% per 100°C, which cannot be neglected [251].

For linearization of the transfer function of the resistive transducers used as primary temperature transducers, both analogue and digital methods are applied. The analogue methods can be utilized for different types of the secondary measuring devices. The digital methods of the linearization are employed only for digital secondary measuring devices based on the elements of the microprocessor technique [289].

The linearization circuit transforms the nonlinear resistor’s resistance vs. temperature change relationship into a linear voltage vs. temperature one. To evaluate the accuracy of such transformation, the following factors should be considered: the circuit itself, the values of circuit elements, and the linearized temperature range [243].

In the case of quadratic nonlinearity, the feedback techniques of linearization can be utilized [249]. In this case, the high-ohmic RTDs are employed and the error of nonlinearity within 0.1°C over the range −75..235°C is ensured.

There are analogue methods of the linearization that minimize the nonlinearity up to 0.11% over the range 100..800°C for calibration at the midpoint and at the endpoint of the range [251].

For converting the resistance of the RTDs into the voltage, the unbalanced resistance bridge circuits are employed [236].

If an RTD is described by a nonlinear transfer function (2.2), the output signal of the resistance bridge circuit can be expressed by the following equation:

$$U_{out1} = U_s k_b R_0 \left(A\vartheta + B\vartheta^2\right), \tag{2.31}$$

where U_s is the supply voltage of the resistance bridge circuit, k_b is the transfer coefficient of the resistance bridge circuit, and R_0 is the resistance of the RTD at ϑ = 0°C; *A* and *B* are the constant coefficients of Pt RTDs.

In this case, the absolute error of nonlinearity of the resistance bridge output voltage expressed by the change in the output voltage is equal to:

$$\Delta_{Un1} = U_s k_b R_0 B\vartheta^2 . \tag{2.32}$$

One of the methods for reducing the nonlinearity by the compensation of the quadratic component of the resistance bridge output voltage involves the change in the supply voltage of the resistance bridge circuit according to the change in the measured temperature. Then, the supply voltage of the resistance bridge circuit is determined by the following expression:

$$U_s = U_{snom}\left(1 + k_v\vartheta\right), \tag{2.33}$$

where U_{snom} is the nominal supply voltage of the resistance bridge circuit at ϑ = 0°C, and k_v is the coefficient of the supply voltage change vs. temperature.

Then, the output voltage of the resistance bridge circuit can be written as follows:

$$U_{out2} = U_{snom} k_b R_0 \left(A\vartheta + B\vartheta^2 + k_v A\vartheta^2 + k_v B\vartheta^3\right). \tag{2.34}$$

From the analysis of the expression (2.34) one can see that for the compensation of the quadratic component of the resistance bridge output signal $\left(B\vartheta^2 + k_v A\vartheta^2\right)$, the following equality must be met:

$$B\vartheta^2 = -k_v A\vartheta^2 . \tag{2.35}$$

Then the coefficient of the supply voltage change of the resistance bridge circuit should be equal to:

$$k_v = -\frac{B}{A} . \tag{2.36}$$

The absolute error of nonlinearity of the resistance bridge output voltage at partial compensation is determined by the following expression:

$$\Delta_{U\,n2} = U_{s\,nom} k_b R_0 k_v B\vartheta^3 = -U_{s\,nom} k_b R_0 \frac{B^2}{A}\vartheta^3 . \qquad (2.37)$$

The relative error of nonlinearity is equal to:

$$\delta_{U\,n2} = \frac{\Delta_{U\,n2}}{U_{out2}} = -\frac{B^2}{A^2}\vartheta^2 . \qquad (2.38)$$

The relative error due to the nonlinearity of the resistance bridge output voltage over the measured temperature range 0...800°C for a partially compensated bridge circuit with a Pt RTD (curve 1) but without calibration at the endpoint of the range, is shown in Fig. 2.4. For comparison, the corresponding dependence of the relative error of nonlinearity without compensation (curve 2) is also presented in Fig. 2.4.

The efficiency of the method described above can be evaluated comparing the absolute errors of the nonlinearity of the output voltage for the resistance bridge circuit both with and without compensation. It is reasonable to introduce the coefficient of compensation efficiency K_{ef} (expressed in decibels, dB):

$$K_{ef} = 20\lg\left|\frac{\Delta_{U\,n1}}{\Delta_{U\,n2}}\right| = 20\lg\left|\frac{B\vartheta^2}{B\vartheta^2 + k_v A\vartheta^2 + k_v B\vartheta^3}\right| . \qquad (2.39)$$

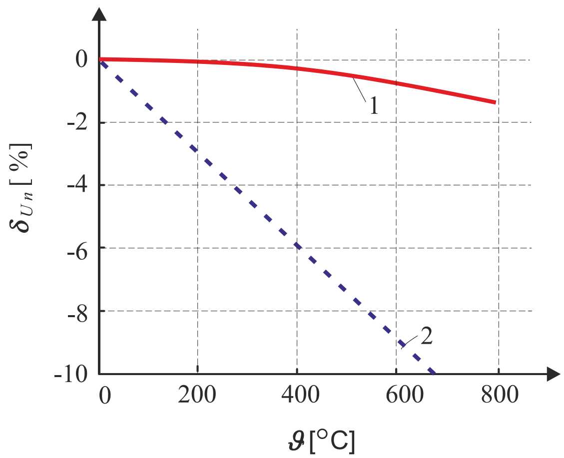

Figure 2.4. Relative error due to the nonlinearity of the output voltage of the resistance bridge circuit plotted against the temperature, for partial compensation (1) and without compensation (2)

The coefficient of compensation efficiency vs. temperature relationship for the case of the partial compensation is plotted in Fig. 2.5.

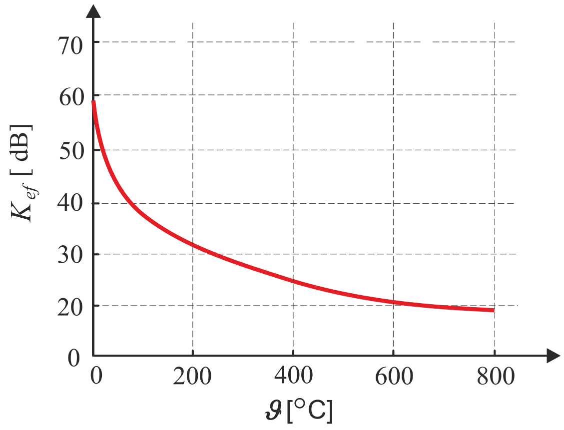

Figure 2.5. The coefficient of compensation efficiency vs. temperature relationship for partial compensation

From the graph of this relationship it is clear that the considered method provides the drop in the value of the coefficient of compensation efficiency from 60 to 19 dB for the temperature change from 0 up to 800°C. When the temperature increases, the coefficient of the efficiency decreases.

The efficiency of determining certain values of the measured temperature ϑ_i can be improved if the following condition is met:

$$B\vartheta_i^2 + k_v A\vartheta_i^2 + k_v B\vartheta_i^3 = 0\,. \tag{2.40}$$

In order to meet this condition, the calibration in the points ϑ_i should be done.

The graph of the relative error of nonlinearity of the output voltage of the resistance bridge circuit after calibration at the points ϑ_i =200, 400, 600, and 800°C over the range 0..800°C is given in Fig. 2.6a, and after calibration at the points ϑ_i =300 and 400°C over the range 0..400°C is given in Fig. 2.6b.

The analysis of the plots depicted in Fig. 2.6 has shown that in the case of the calibration performed at the endpoint of the range (800°C), the relative error of nonlinearity of the bridge output voltage is less than 0.4%, and for the calibration at the point 400°C it is less than 0.1% over the range 0..500°C. In the case of the calibration at the point 300°C, the relative error of nonlinearity is less than 0.05% over the range 0..350°C.

The temperature dependencies of the coefficient of compensation efficiency K_{ef} at different ϑ_i are plotted in Fig. 2.7.

In order to form the temperature-dependent component of the supply voltage, the additional film RTD placed together with the main RTD can be employed. Alternatively, in order to form the variable component of the supply voltage, the output voltage of the resistance bridge circuit or the voltage across the RTD can be used.

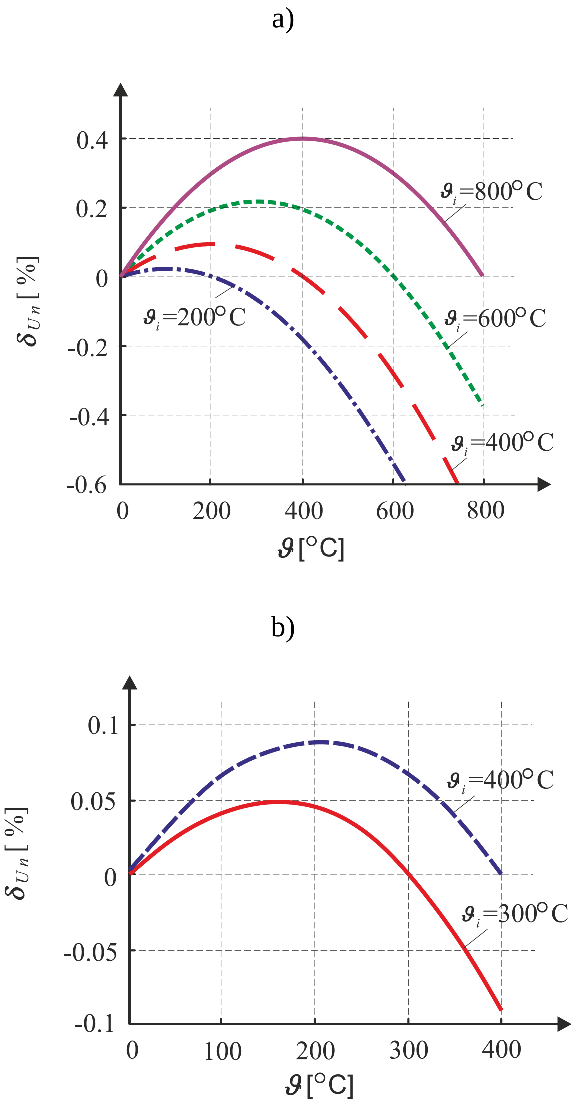

Figure 2.6. The plot of the relationship of the temperature vs. the relative error of nonlinearity of the bridge circuit output voltage after calibration at the points ϑ_i: a) 200, 400, 600 and 800°C, b) 300 and 400°C

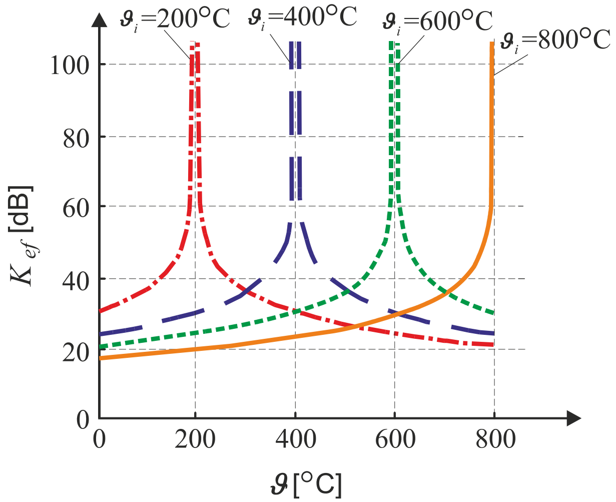

Figure 2.7. Temperature dependencies of the coefficient of compensation efficiency after calibration at the points ϑ_i

The schematic diagram of the temperature-to-voltage converter with the linearization of the transfer function of the RTD is given in Fig. 2.8. It consists of the unbalanced resistance bridge circuit constructed using film technology, the supply unit, the former of supply voltage variable component, and the voltage summator.

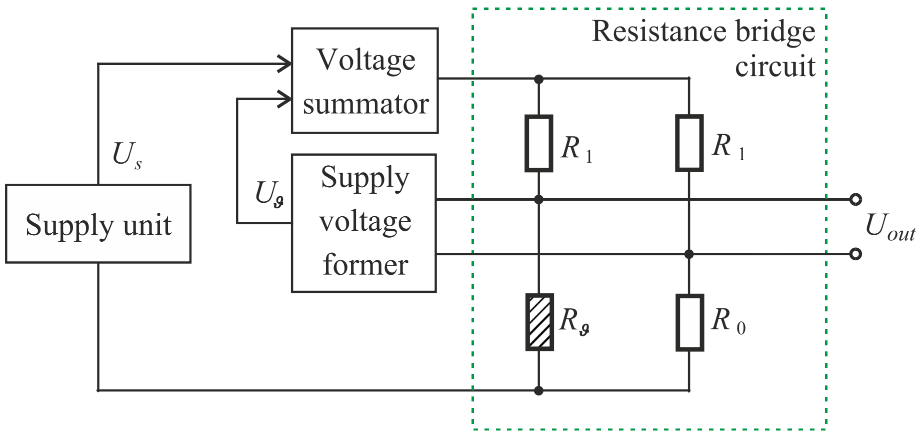

Figure 2.8. Schematic diagram of the temperature-to-voltage converter with the linearization of the transfer function

The resistance bridge circuit consists of the resistors R_ϑ (hatched in Fig.2.8 and throughout the rest of this chapter), R_0 and (two) R_1. The output voltage of resistance bridge circuit is described by the following expression:

$$U_{out} = (U_s + U_\vartheta) k_b\,, \tag{2.41}$$

where U_s is the output voltage of the supply unit, and U_ϑ is the variable component of the supply voltage (dependent on the output voltage of the supply unit and the temperature).

The transfer coefficient of the resistance bridge circuit is expressed as:

$$k_b = \left(\frac{R_\vartheta}{R_1 + R_\vartheta} - \frac{R_0}{R_1 + R_0} \right). \tag{2.42}$$

The output voltage of the resistance bridge circuit U_{out} is put on the input of the supply voltage former of the variable component U_ϑ, which in turn is added to the supply unit voltage U_s. The formula for the output voltage of the resistance bridge circuit can be written as:

$$U_{out} = \frac{U_s \cdot k_b}{1 - \gamma \cdot k_b}\,, \tag{2.43}$$

where γ is the transfer coefficient of the former of supply voltage variable component.

The absolute error of nonlinearity of the resistance bridge output voltage is determined by the formula:

$$\Delta_{Un} = \frac{U_s \cdot k_b}{1 - \gamma \cdot k_b} - \frac{U_{out\max}}{\vartheta_{\max}} \cdot \vartheta\,. \tag{2.44}$$

The absolute equivalent error of nonlinearity in degrees Celsius is expressed by the following equation:

$$\Delta_{\vartheta n} = \frac{U_s \cdot k_b \cdot \vartheta_{\max}}{(1 - \gamma \cdot k_b) \cdot U_{out_{\max}}} - \vartheta\,. \tag{2.45}$$

The relationships between the error $\Delta_{\vartheta n}$ and the temperature for different values of γ at U_s=6 V, R_1=10 kΩ, and R_0=100 Ω over the temperature ranges 0..800°C, 0..400°C and 0..200°C are graphed in Figs. 2.9, 2.10, and 2.11, respectively.

In order to form the temperature-dependent component of the supply voltage, the output voltage of the resistance bridge circuit, multiplied by the coefficient γ and summed with the output voltage of the supply unit was used. The nonlinearity errors of the temperature-voltage conversion are less than 0.7°C over the range 0..800°C at γ=5.55, less than 0.07°C over the range 0..400°C at γ=5.14, and less than 0.01°C over the range 0..200°C at γ=4.96.

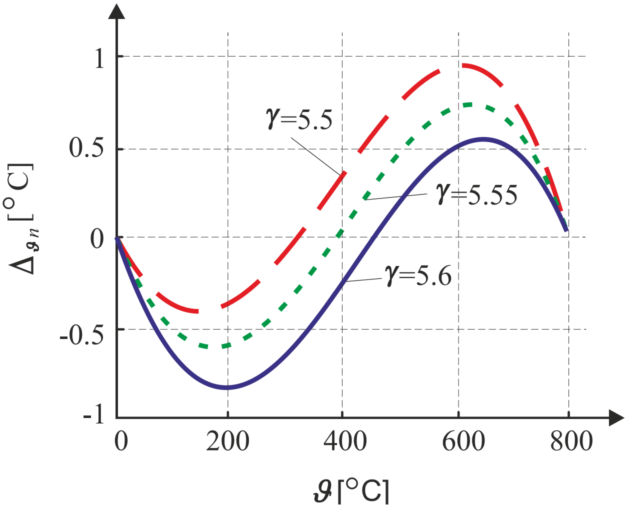

Figure 2.9. The absolute equivalent error of nonlinearity vs. temperature for different values of the transfer coefficient γ of the former of supply voltage variable component

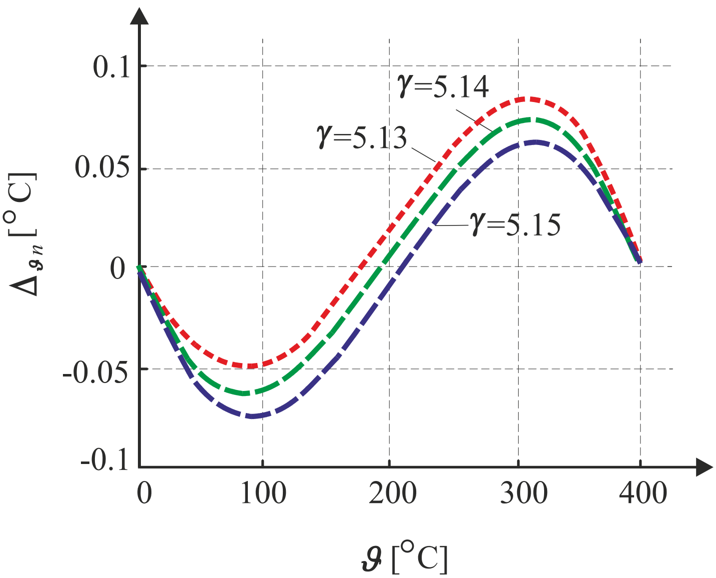

Figure 2.10. The absolute equivalent error of nonlinearity vs. temperature (cont.)

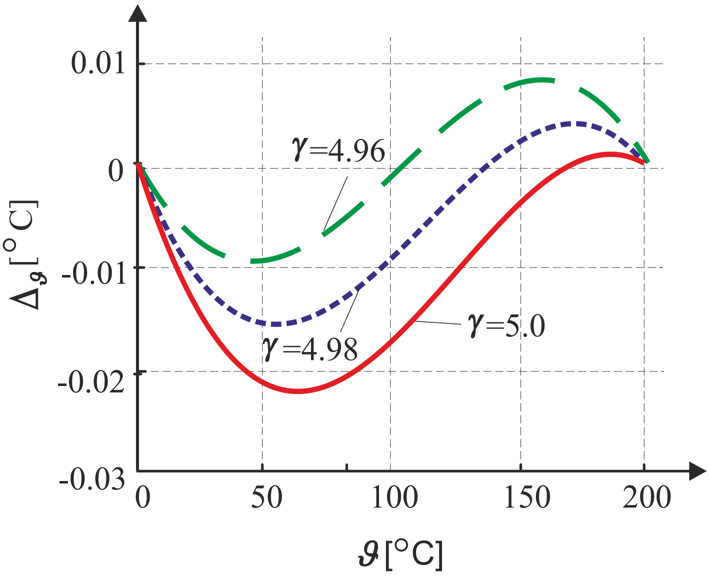

Figure 2.11. The absolute equivalent error of nonlinearity vs. temperature (end)

2.2.2. Compensation of lead wire resistance

In temperature measurements with RTDs, the unbalanced resistance bridge circuits are usually employed. However, such circuits have the following drawbacks:

1. The output characteristic of the resistance bridge circuit is nonlinear,
2. The lead wire resistance adds to the RTD resistance and causes considerable errors.

In the case of two-wire connection of the Pt100 RTD, the additional error introduced by the influence of lead wire resistance of 1 Ω results in the additive error of 5°C. In practice, especially for remote measurements when the RTD and the secondary measuring transducer are placed far from each other, the lead wire resistance can be 5-10 Ω [219]. Another factor that influences the error is the change of the lead wire resistance due to the change in the ambient temperature [234].

There are three methods of the RTD connection to the secondary measuring transducer: two-wire, three-wire, and four-wire connection. The two-wire connection is the most simple and economic method, but it is not adequate because the resistances of the wires add to the RTD resistance. The three-wire connection is the most frequently used one. For this method, the voltage source is connected to one of the wires, and the other two wires are connected in series in the opposite arms of the resistance bridge circuit, and compensate each other.

The four-wire connection is the most accurate but not economic, and the difficulties concerning the additional lead wire appear [219, 235].

In [234] it is proposed to use the additive resistor made of the same material, and of the same resistance value as the lead wires R_{L1}, R_{L2} for the compensation of the lead wire influence on the two-wire RTD connection (Fig. 2.12).

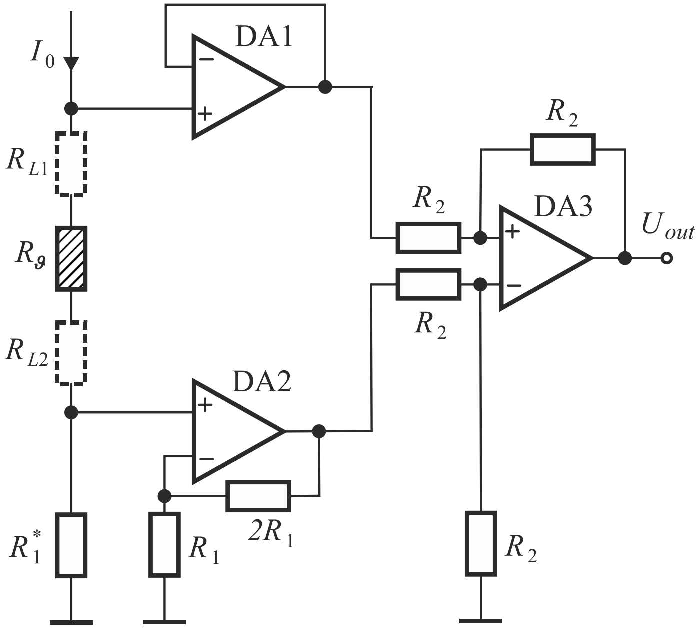

Figure 2.12. Schematic diagram of the compensation circuit for two-wire RTDs [234]

If $R_1^*=R_{L1}=R_{L2}$, then the output voltage of the compensation circuit equals:

$$U_{out} = I_0 R_\vartheta , \tag{2.46}$$

where I_0 is the reference current, and R_ϑ is the RTD resistance.

In order to take into account the ambient temperature influence on the lead wire resistance, an additive resistance should be placed in the same operating conditions as the lead wires. In some cases it cannot be realised, and the stability in the wide range of the operating temperature of the lead wires is not achieved.

The circuit topologies alternative to conventional bridge, aimed at converting the sensing resistance deviation using a pulse width circuit [151] or time interval [133, 213] have been reported. Such converters easily provide digital equivalent output, and they can be applied for lead wire compensation [139, 181]. The compensation method using the additional diodes, the conventional timer IC555 and the digital storage oscilloscope (DSO) is rather simple (Fig. 2.13) [182].

In order to eliminate the effects of lead resistance and compensate the effects of ambient temperature variation in the remote measurements, two additional diodes (made from two identical *n-p-n* transistors on LM389 used as diodes), are placed at approximately the same ambient temperature.

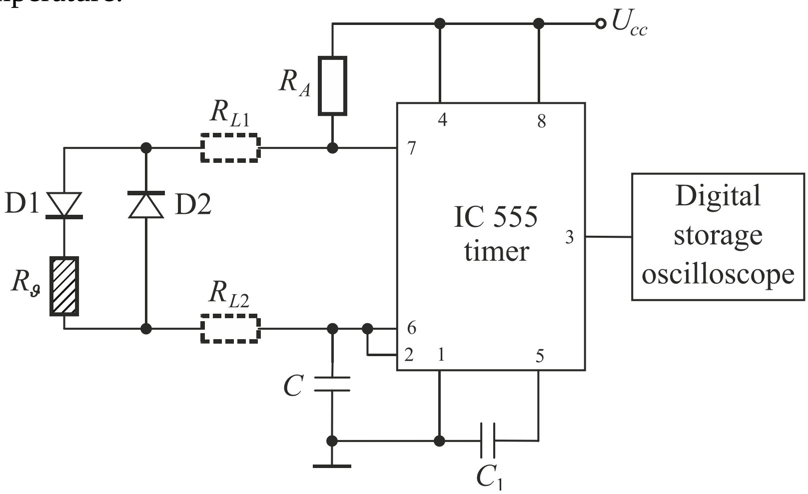

Figure 2.13. Lead wire resistance compensation circuit with digital storage oscilloscope [182]

The time difference τ_d between the charging and discharging time can be written as follows:

$$\tau_d = K\left(R_\vartheta + R_A + R_{D1} - R_{D2} - R_{ONT}\right)\cdot C\,, \tag{2.47}$$

where $K = \ln\dfrac{2U_{cc} - 3U_{D1}}{U_{cc} - 3U_{D1}} \approx \ln\dfrac{2U_{cc} - 3U_{D2}}{U_{cc} - 3U_{D2}}$; R_{D1} and R_{D2} are the forward resistances of the diodes $D1$ and $D2$; U_{D1} and U_{D2} are the voltages across the diodes $D1$ and $D2$; R_{ONT} is the ON resistance of the discharging transistor of the timer, and C is the capacitance of the capacitor.

The differential resistance (R_{D1} - R_{D2}) tends to zero because the diodes are adapted from an identical transistor pair from LM389. The resistance R_A was adjusted so that the impact of the in-built transistor's ON resistance (R_{ONT}) on the measurements can be minimized. The time difference τ_d obtained from the two measured pulse widths, changes linearly with the sensor resistance R_ϑ and is independent from the lead resistances R_{L1} and R_{L2}. The digital storage oscilloscope is applied both for the display of the output waveform and for the measurement of the pulse widths.

The drawback of that circuit is the difficulty of placing the additional diodes close to the RTD.

To eliminate the influence of the connection wire resistances on the transfer accuracy, and to ensure the transfer function linearity, the measuring circuits and the current stabiliser with four-wire connection of the primary RTD are employed (Fig. 2.14) [235].

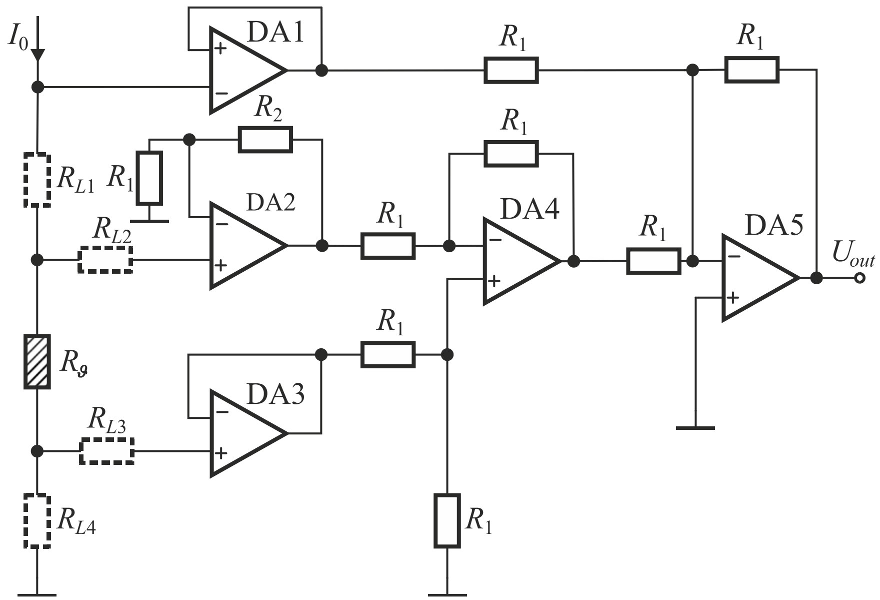

Figure 2.14. Lead wire resistance compensation circuit for four-wire RTD connection [235]

If $R_{L1}=R_{L4}$, then the output voltage equals:

$$U_{out} = 2 \cdot I_0 \cdot R_\vartheta \,. \qquad (2.48)$$

It can be seen that the output voltage is independent of the lead wire resistances, and depends only on R_ϑ, if I_0 is constant. However, the circuit presented above does not compensate for the initial resistance of the RTD at 0°C.

For many objects where the connection wires are already installed, it is difficult to replace the three-wire connection circuit of the RTDs with four-wire connection. That is why compensation circuits for three-wire connections should be applied. The compensation circuit for three-wire RTDs is shown in Fig. 2.15 [219].

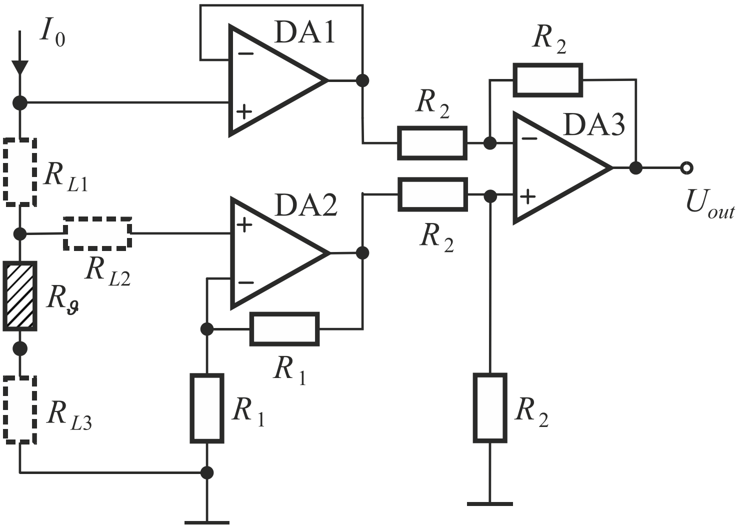

Figure 2.15. Lead wire resistance compensation circuit for three-wire RTD connection [219]

The output voltage equals:

$$U_{out} = 2I_0(R_\vartheta + R_L) - I_0(R_\vartheta + 2R_L) = I_0 R_\vartheta . \tag{2.49}$$

As it can be seen from the expression above, the output voltage depends only on the resistance R_ϑ of the RTD.

The more simple compensation circuit that additionally ensures the spark protection, is presented in Fig. 2.16 [99].

The RTD resistance R_ϑ is connected directly with the three lead wires R_{L1}, R_{L2} and R_{L3}, and indirectly to the standard resistor R_{01} (through R_{L2}), the inputs of the resistance change transducer (through R_{L1} and R_{L3}), and the output of the current stabiliser which forms the reference current I_{01} (through R_{L3}).

The spark protection circuit is applied for preventing the sparks at the terminals of RTD in explosive environments. It limits the maximum allowed voltage (or current) which can appear between the supply of the resistance change transducer and the terminals of the RTD.

The maximum voltage across the terminals of the RTD should satisfy the following condition:

$$|U_{\max}| < |U_{\lim}| < |U_{al}| , \tag{2.50}$$

where $U_{\max}$ is the maximum value of the voltage at the terminals: $U_{\max} = I_{01}(R_{\vartheta\max} + R_{01})$, $R_{\vartheta\max}$ is the RTD resistance at the maximum measured temperature, R_{01} is the resistance of the standard resistor, U_{lim} is the voltage limited by the spark protection circuit, and U_{al} is the allowed voltage on some spark-sensitive objects.

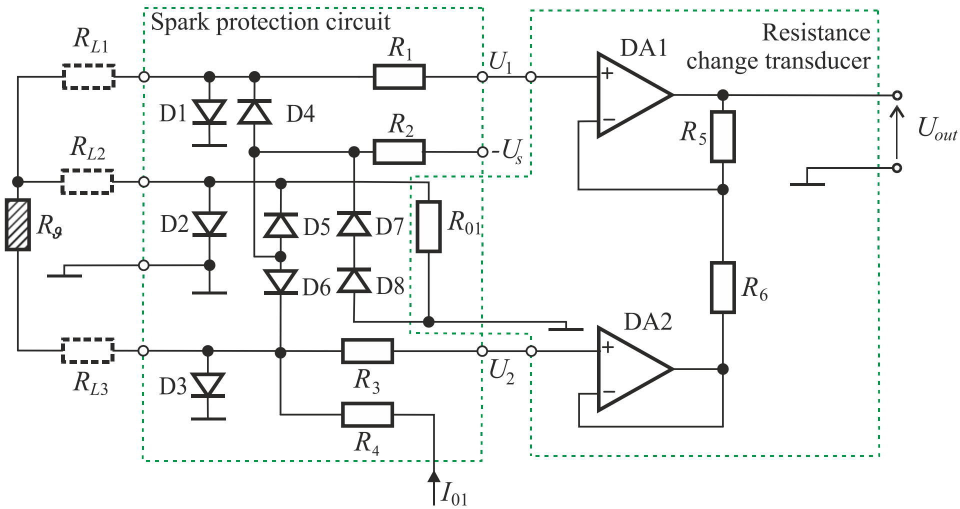

Figure 2.16. Schematic of the circuit for compensating the influence of lead wire resistances, supplied with a spark protection circuit

The semiconductor diodes D1…D8 are used for voltage limitation in the spark protection circuit. The positive voltage is limited by the diodes D1…D3 connected between the lead wires and the common bus grounded at the object. The negative voltage is limited by the diodes D4…D6 connected to the lead wires and the diodes D7…D8, which together with the resistor R_2 form the negative bias voltage, able to satisfy the following condition:

$$U_{\lim} > I_{01}\left(R_{9\max} + R_{01} + R_{L2} + R_{L3}\right). \tag{2.51}$$

The current in the lead wires is limited by the resistors R_1, R_3 and R_4. The spark protection circuit should be made as a monolithic block. The standard resistor R_{01} is placed inside the monolithic block, made in hybrid film technology, to exclude the possibility of supplying a high voltage on the RTD resistance R_9 through the lead wire R_{L2}.

In order to reduce the influence of the reverse currents of the diodes on the measurement accuracy, the diodes with minimum reverse currents should be selected.

The resistance change transducer consists of the differential amplifiers DA1 and DA2, the resistors R_5 and R_6 of the negative feedback paths, and a standard resistor R_{01} inserted in the spark protection circuit to ensure the spark protection.

The lead wire resistance R_{L1} in series with the resistor R_1 is connected with the circuit of high-ohmic input of the amplifier DA1, and in consequence does not influence the measurement result. The resistances of lead wires R_{L2} and R_{L3} add to the resistances of the standard resistor R_{01} and the RTD resistance R_ϑ, respectively.

The current I_{01} is fed into the input of the spark protection circuit and flows through the resistor R_4, the lead wire R_{L3}, the primary transducer of the resistance R_ϑ, and the lead wire R_{L2}, into the standard resistor R_{01}.

In this case, the signals put on the non-inverting inputs of the differential amplifiers DA1 and DA2 are as follows:

$$U_1 = -I_{01}(R_{01} + R_{L2}), \tag{2.52}$$

$$U_2 = -I_{01}(R_{01} + R_{L2} + R_\vartheta + R_{L3}). \tag{2.53}$$

Then the output voltage of the differential amplifier DA1 can be expressed as follows:

$$U_{out} = I_{01}\left(R_\vartheta \cdot \frac{R_5}{R_6} + R_{L3} \cdot \frac{R_5}{R_6} - R_{01} - R_{L2} \right). \tag{2.54}$$

It can be seen that full compensation of the influence of the lead wire resistances on the measurement error occurs when the following equality is satisfied:

$$R_{L2} = R_{L3} \cdot \frac{R_5}{R_6}. \tag{2.55}$$

If $R_{L2} = R_{L3}$, then for full compensation of the influence of the lead wires, the resistances of the resistors R_5 i R_6 should be equal. In consequence, the output voltage of the amplifier DA1 can be expressed as:

$$U_{out} = I_{01}(R_\vartheta - R_{01}). \tag{2.56}$$

Substituting $R_\vartheta = R_0 + R_0\alpha\vartheta$, one can obtain:

$$U_{out} = I_{01}(R_0 + R_0\alpha\vartheta - R_{01}), \tag{2.57}$$

where α is the TCR, ϑ is the measuring temperature, and R_0 is the resistance of RTD at ϑ=0°C.

The resistance of the standard resistor R_{01} is matched equal to the resistance R_0. In this case, the output voltage equals:

$$U_{out} = I_{01}R_0\alpha\vartheta. \tag{2.58}$$

If the lead wires resistances are not equal ($R_{L2} \neq R_{L3}$), the measurement error appears. The relative error is expressed as follows:

$$\delta_{RL} = \frac{\left| R_{L2} - R_{L3} \right|}{\Delta R_{\vartheta\,\max}}, \qquad (2.59)$$

where $\Delta R_{\vartheta\, max}$ is the maximum value of the resistance change of RTD.

2.2.3. Resistance temperature transducer with lead wire compensation

Let us consider the resistance temperature transducer based on the abovementioned compensation circuit shown in Fig. 2.16; the schematic diagram of the resistance temperature transducer is given in Fig. 2.17. The transducer consists of the RTD (R_{ϑ}), the compensation circuit, the current stabiliser, the wide-band pulse transducer, the galvanic isolation device, the pulse width-to-voltage converter, the voltage-to-current converter, and the supply unit [99].

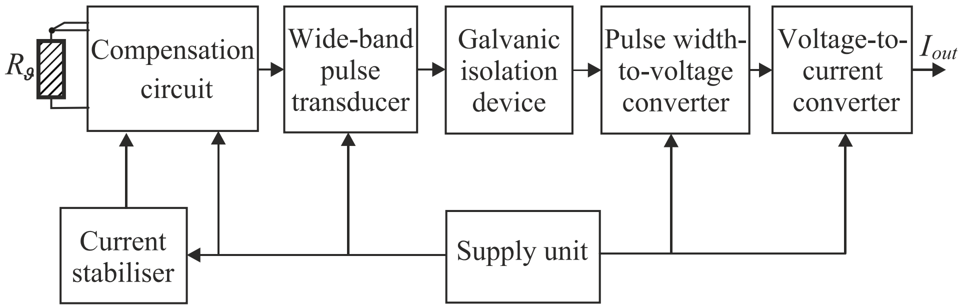

Figure 2.17. Schematic diagram of the resistance temperature transducer

The reference current I_{01} is formed by the current stabiliser; the schematic of the stabiliser is given in Fig. 2.18. The current stabiliser consists of the parametric voltage stabiliser based on the Zener diode D1 and the resistor R_1, the differential amplifier DA1, the standard resistor R_{02}, and the output cascade based on the MOS transistor Q1.

The output current of the current stabiliser can be expressed as:

$$I_{01} = \frac{U_{stD}}{R_{02}}, \qquad (2.60)$$

where U_{stD} is the stabilisation voltage of the Zener diode D1, and R_{02} is the resistance of the standard resistor.

By choosing an operational amplifier with low input currents, and the use of the MOS transistor in the output cascade, the equality of the currents $I_{01} = I_0$ is ensured. This improves the temperature and time stability of the output current I_{01}.

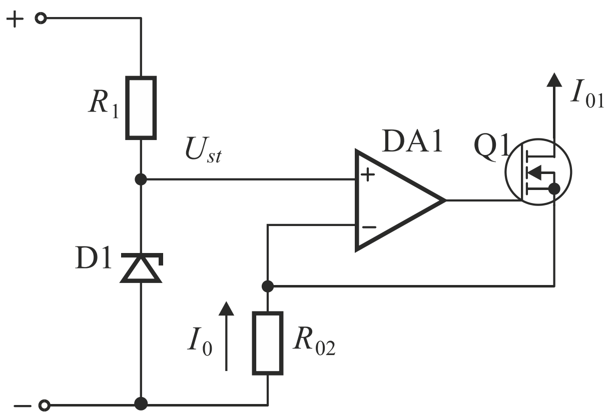

Figure 2.18. Schematic of the current stabiliser [99]

The output signal of the resistance change transducer U_{out1} is set on the input of the wide-band pulse transducer shown on the schematic diagram in Fig. 2.19. The wide-band pulse transducer consists of the integrator comprising the differential amplifier DA1 with the *RC*-element, the comparing circuit, the triangle wave generator, the switch and the current stabiliser.

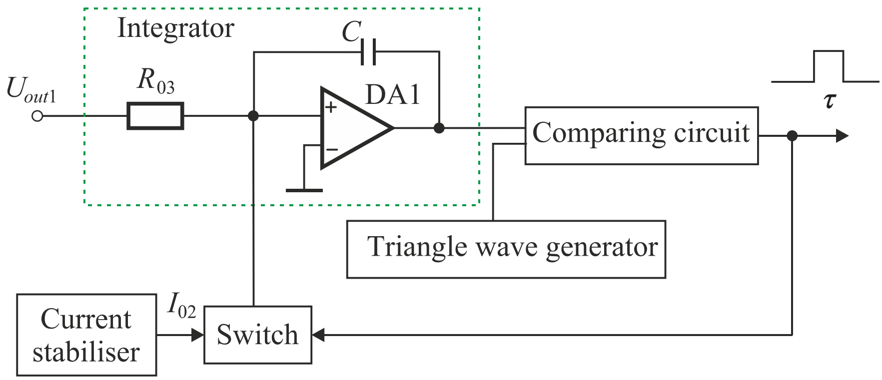

Figure 2.19. Schematic diagram of the wide-band pulse transducer [99]

The input voltage of the wide-band pulse transducer is integrated by the integrator and put to the input of the comparing circuit. The output voltage of the triangle wave generator is set to another input of that circuit. In consequence, at the output of the comparing circuit the pulse signal of the duration τ is formed, which in turn is put on the input of the switch. The switch connects the output of the current stabiliser to the input of the integrator for the time interval τ.

If the output voltage changes, then the output impulse duration τ can be determined if the following equality holds true:

$$\int_0^{T_p} \frac{U_{out1}}{R_{03}} dt = \int_0^{\tau} I_{02} dt, \tag{2.61}$$

where T_p is the period of the pulses of the triangle wave generator, and I_{02} is the output current of the current stabiliser.

The duration of the output pulse signal τ can be expressed as:

$$\tau = \frac{U_{out1} T_p}{R_{03} I_{02}}. \tag{2.62}$$

Substituting (2.58) into (2.62), the following expression can be obtained:

$$\tau = \frac{I_{01} R_0 \alpha \vartheta T_p}{R_{03} I_{02}}. \tag{2.63}$$

In order to ensure the galvanic separation between the input and output of the resistance temperature transducer, the impulse signal τ is transferred through the galvanic isolation device to the control input of the pulse width-to-voltage converter.

The schematic diagram of the pulse width-to-voltage converter is given in Fig. 2.20. The pulse width-to-voltage converter consists of the integrator based on the differential amplifier DA1 with the parallel *RC*-circuit placed in the feedback path, the switch, the current stabiliser and the output RC filter.

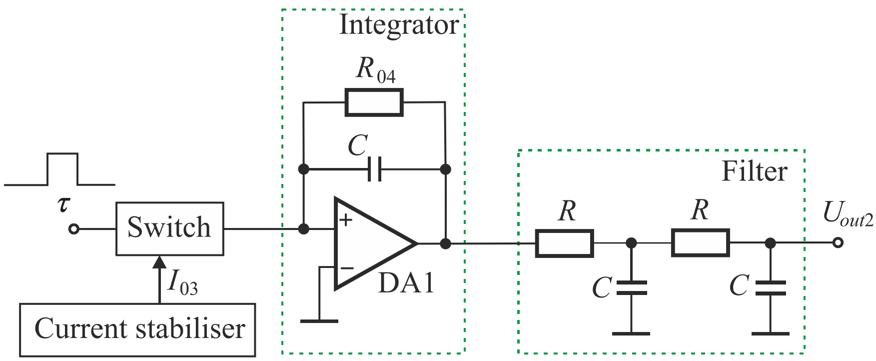

Figure 2.20. Schematic diagram of the pulse width-to-voltage converter [99]

The switch puts the reference current of the current stabiliser to the input of the integrator during the time τ. The integrator operates in the mode of the active filter, and averages the input current signal. The integrator also converts the current into the voltage. In order to reduce the integrator output voltage pulsation, the additional output RC-filter is employed.

The output voltage of the pulse width-to-voltage converter equals:

$$U_{out2} = \frac{\tau}{T_p} I_{03} R_{04}, \qquad (2.64)$$

where I_{03} is the output current of the current stabiliser, and R_{04} is the resistance of the feedback path resistor of the integrator.

After substituting τ from (2.63) into (2.64), the expression for the output voltage of the pulse width-to-voltage converter can be obtained:

$$U_{out2} = \frac{I_{01} I_{03}}{I_{02}} \cdot \frac{R_{04}}{R_{03}} \cdot R_0 \alpha \vartheta. \qquad (2.65)$$

The output voltage of the pulse width-to-voltage converter is applied to the input of the voltage-to-current converter. The schematic diagram of the voltage-to-current converter based on the differential amplifier DA1 is show in Fig. 2.21.

The output current of the transducer is defined by the resistance of the resistor R_{05} and flows to the output through the transistor Q1. The load resistance R_l is connected between the drain of the output transistor Q1 and the supply bus.

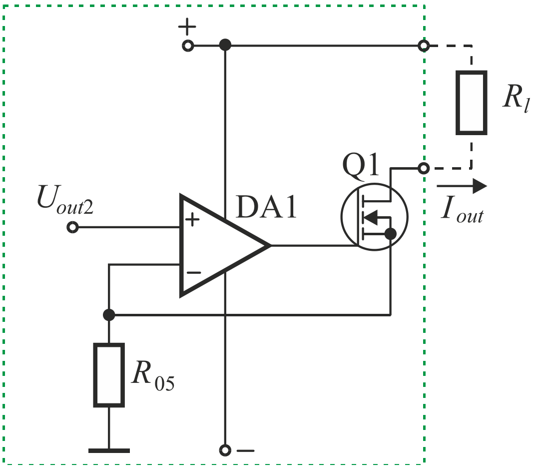

Figure 2.21. Schematic diagram of the voltage-to-current converter

The generalized transfer function of the resistance temperature transducer can be expressed as follows:

$$I_{out} = \frac{U_{out2}}{R_{05}} = \frac{I_{01} I_{03}}{I_{02}} \cdot \frac{R_{04}}{R_{03}} \cdot \frac{R_0 \alpha \vartheta}{R_{05}}. \tag{2.66}$$

It can be seen that the range of the output current signal depends on the choice of the resistance values of the resistors R_{03} … R_{05} and the range of the measured temperature. The relationship between the output current I_{out} and the resistance change of RTD is linear.

The supply unit provides the temperature measuring device with the required supply voltages, and ensures the galvanic separation of the input and the output of the transducer.

The considered scheme with current stabiliser for the measurement of the resistance of the RTD ensures the linearity of the transfer function. The requirements for the lead wires are lesser because it is only required to provide the equality of the resistances of two lead wires $R_{L2} = R_{L3}$, but not to adjust the resistances of the lead wires to a given value.

2.2.4. Improvement of the linearity of the measuring resistance bridge circuits

One of the drawbacks of the resistance bridge circuits is the nonlinear dependency of the output voltage on the resistance change of the resistor in the measuring arm. In order to reduce the nonlinearity of the resistance bridge circuits, the temperature dependent resistors with both positive and negative values of TCRs can be applied [23, 103]. The schematic of the measuring bridge and the arrangement details of the construction made with thin-film technology are shown in Fig. 2.22. It can be seen that the resistors R_2 and R_3 are made of the double layers R_{21}, R_{22}, and R_{31}, R_{32}, respectively. The TCR of the resistors R_1, R_{21}, and R_{31} is positive; the TCR of the resistors R_{22}, R_{32}, and R_4 is negative.

The resistances of the resistors R_1 and R_4 could be calculated as follows:

$$R_1 = R_0 (1 + \alpha \vartheta), \tag{2.67}$$

$$R_4 = R_0 (1 - \alpha \vartheta), \tag{2.68}$$

where R_0 is the nominal resistance of the resistors R_1 and R_4 at 0 °C.

The resistances of the resistors R_2 and R_3 can be expressed as:

$$R_2 = \frac{R_{21}(1+\alpha\vartheta) \cdot R_{22}(1-\alpha\vartheta)}{R_{21}(1+\alpha\vartheta) + R_{22}(1-\alpha\vartheta)}, \tag{2.69}$$

and

$$R_3 = \frac{R_{31}(1+\alpha\vartheta) \cdot R_{32}(1-\alpha\vartheta)}{R_{31}(1+\alpha\vartheta) + R_{32}(1-\alpha\vartheta)}, \tag{2.70}$$

where R_{21}, R_{22} are the resistances of the resistors R_{21} and R_{22} at 0°C, respectively; R_{31}, R_{32} are the resistances of the resistors R_{31} and R_{32} at 0°C, respectively; ϑ is the measured temperature in degrees Celsius.

a)

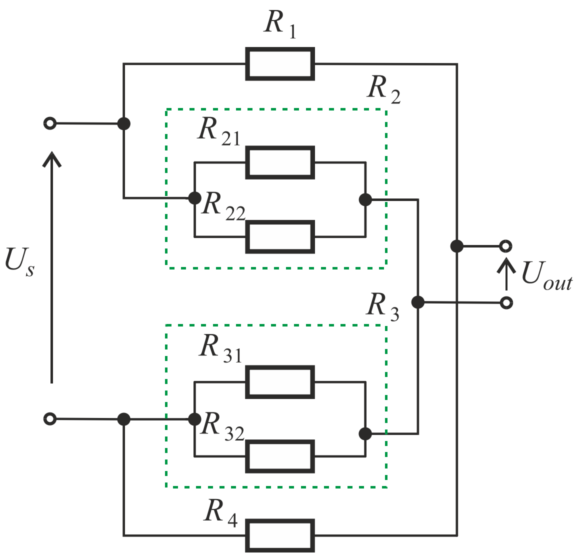

b)

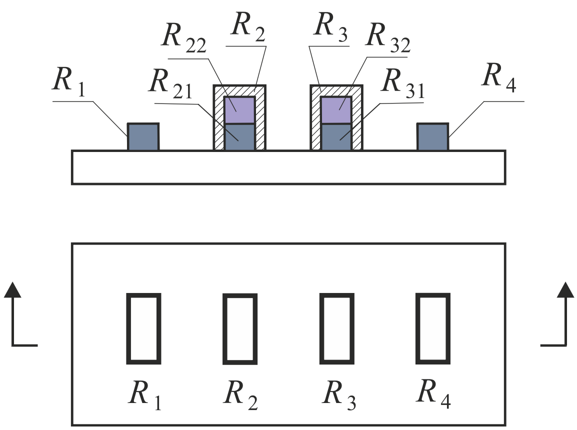

Figure 2.22. Double-layer thin-film RTD: a) principal schematic, b) arrangement details [103]

Let us discuss the accuracy of the formation of the R_2 and R_3 resistances giving the resistor R_2 as the example.

If the nominal resistances of the resistors R_{21}=R_{22}= 2R_{20}, then R_2 is described as:

$$R_2 = R_{20}(1-\alpha\vartheta)^2 . \tag{2.71}$$

The parallel connection of the resistors with different signs of TCRs does not ensure a high temperature stability of the resistance R_2, which sharply falls off with the increase of either the temperature or the values of TCR of the resistors (Fig. 2.23).

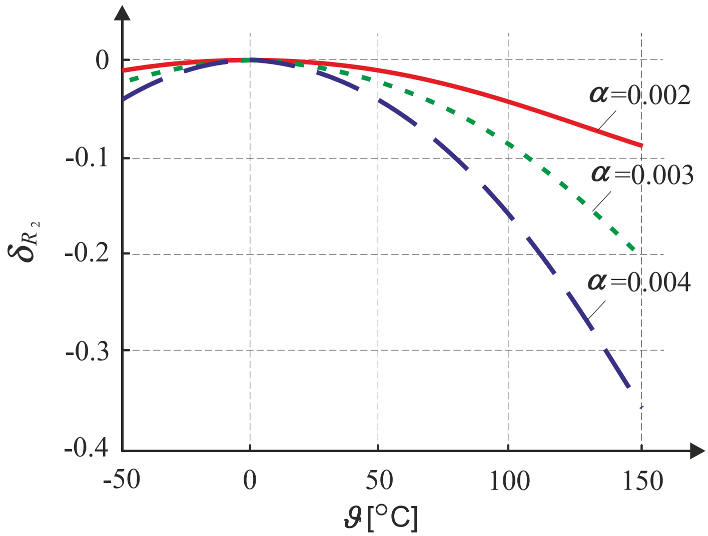

Figure 2.23. The relationship between the temperature and the relative error of the resistance R_2 for different values of TCR

In order to reduce the resistance error, different nominal values of the resistance of the resistors at 0°C should be matched. In this case, the inequality R_{21} < R_{22} should be satisfied. The nominal resistance values of the resistors R_{21} and R_{22} can be calculated as:

$$R_{21} = k_n R_{20}, \tag{2.72}$$

$$R_{22} = \frac{k_n}{k_n - 1} R_{20}, \tag{2.73}$$

where k_n is the quotient of the nominal value of the resistance of the resistor with positive TCR and the equivalent value of the resistance of the resistor R_2; R_{20} is the nominal equivalent resistance of the resistor R_2.

The temperature dependence of the resistance of the resistor R_2 is described by the following expression:

$$R_2 = \frac{k_n R_{2n}\left(1-\alpha^2\vartheta^2\right)}{k_n+\left(k_n-2\right)\alpha\vartheta}. \qquad (2.74)$$

As it can be seen from the dependencies presented in Figs. 2.24 and 2.25, the maximum value of the relative error δ_{R_2} over the temperature range –50…150°C does not exceed 0.05 for k_n=1.4 and α≤0.002.

In the case when the equality R_{30}= R_{20} is true, the output voltage of the resistance bridge circuit can be expressed as follows:

$$U_{out} = U_s \cdot \left(\frac{R_3}{R_2+R_3} - \frac{R_4}{R_1+R_4}\right) = \frac{U_s\alpha\vartheta}{2}. \qquad (2.75)$$

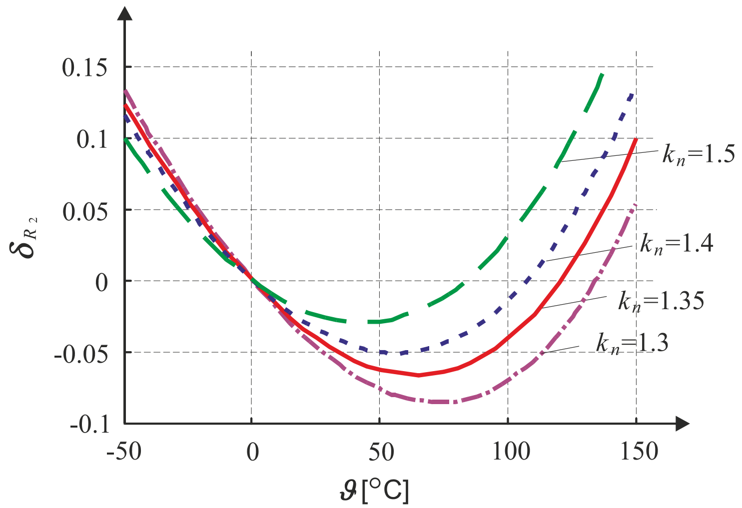

Figure 2.24. Temperature dependencies of the relative error of the resistance R_2 at α=0.004 for different values of the coefficient k_n

When analyzing the expression given above, it can be easily noticed that the output voltage of the resistance bridge circuit is a linear function of temperature measured.

The resistance bridge circuit based on the two-layer film structures can be applied for: design of temperature sensors for non-aggressive environments, compensation of the cold-junction temperature influence, and temperature compensation of an e.m.f. change of a reference cell. The application of the measuring bridge in the chemically active environments requires the protection – of both the substrate and the resistors deposited on it – by chemically stable, electrically isolating and heat conducting covers, or by other construction methods.

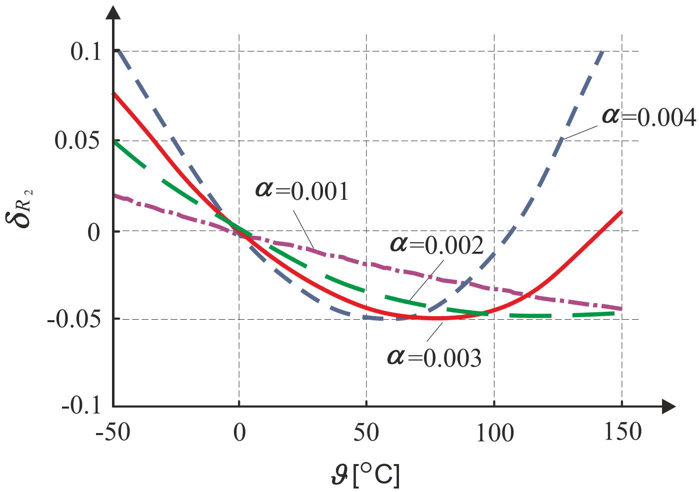

Figure 2.25. Temperature dependencies of the relative error at k_n=1.4 for different values of TCR

The temperature measuring device that consists of the resistance bridge circuit and the secondary transducer is shown in Fig. 2.26. The resistance bridge circuit is connected to the secondary transducer by two pairs of lead wires: R_{L1}, R_{L2}, and R_{L3}, R_{L4}. The secondary transducer consists of a galvanically separated, controlled voltage stabiliser, an amplifier of the resistance bridge circuit output signal, a microprocessor, a control device, an indicator device, and a power supply unit.

In order to reduce the influence of the measuring current of the primary transducer on the accuracy of the measurement, the resistance bridge circuit is supplied by the signal from the microprocessor only when measurements are performed. If the resistance of the lead wires is taken into account, the output voltage of the measuring bridge can be described by the following expression:

$$U_{out} = \frac{U_s R_b}{2(R_{L1} + R_{L2} + R_b)} \cdot \alpha \vartheta, \tag{2.76}$$

where $R_b = \dfrac{(R_1 + R_4)(R_2 + R_3)}{R_1 + R_4 + R_2 + R_3}$ is the input resistance of the bridge circuit.

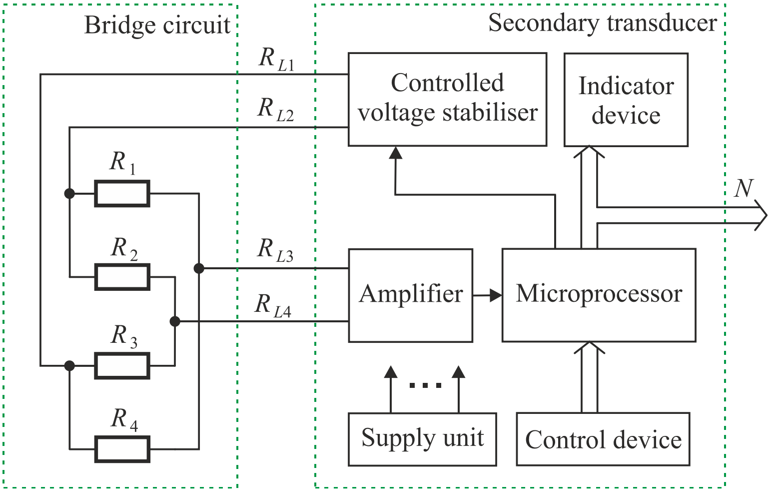

Figure 2.26. Schematic diagram of the temperature measuring device

The lead wire resistances R_{L3}, R_{L4} are connected to the high input resistances of the operational amplifier, and in consequence do not influence the accuracy of the output voltage formation. The absolute error of the output voltage due to the influence of the lead wire resistances can be expressed as:

$$\Delta_{UL} = \frac{U_s}{2}\left(\frac{R_b \alpha \vartheta}{R_{L1} + R_{L2} + R_b} - 1\right). \tag{2.77}$$

The absolute equivalent error of the output voltage $\Delta_{\vartheta L}$ introduced by the lead wire resistances, expressed in degrees Celsius, is equal to:

$$\Delta_{\vartheta L} = \frac{\Delta_{UL} \cdot \vartheta_{\max}}{U_{out\max}}, \tag{2.78}$$

where $U_{out\max}$ is the output voltage of the bridge circuit at the maximum temperature ϑ_{max}.

The relationships between the absolute equivalent error of the output voltage introduced by the lead wire resistance and the temperature for different nominal resistances R_0 and lead wire resistances $R_L = R_{L1}+R_{L2}$, are shown in Fig. 2.27.

From Fig. 2.27 it can be seen that the influence of the lead wire resistance on the measurement accuracy decreases with the increase in the nominal resistance R_0.

The output voltage of the resistance bridge circuit is applied to the input of the amplifier of the resistance bridge circuit output signal. The output voltage of the amplifier is passed to the input of the analogue-to-digital converter of the microprocessor. After processing the data, the microprocessor returns the measurement result to the indicator device in the form of a numerical code $N(\vartheta)$:

$$N(\vartheta) = \frac{U_s R_b}{2(R_{L1} + R_{L2} + R_b)} \cdot \alpha\vartheta \cdot k_a \cdot k_c \cdot k_m , \tag{2.79}$$

where k_a is the amplification coefficient of the amplifier of the output signal of the resistance bridge circuit, k_c is the gain factor of the analogue-to-digital converter, and k_m is the transformation coefficient of the microprocessor.

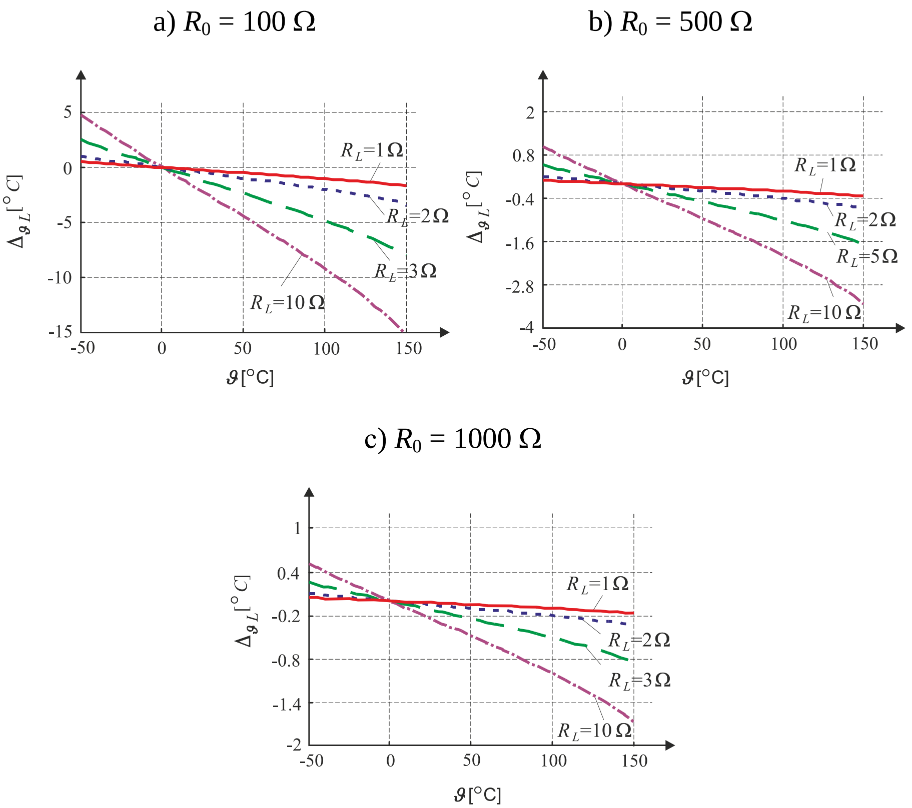

Figure 2.27. Graph dependencies of the absolute equivalent error of the output voltage introduced by lead wire resistance on the temperature, for different nominal resistances R_0: a) R_0 = 100 Ω, b) R_0 = 500 Ω, c) R_0 = 1000 Ω, and various lead wire resistances R_L

For $\dfrac{U_s R_b}{2(R_{L1} + R_{L2} + R_b)} \cdot \alpha \cdot k_a \cdot k_c \cdot k_m = 1$, the output code is equal numerically to the measured temperature.

The total error of the temperature measurement includes the errors of: the measuring bridge, the amplifier of the resistance bridge circuit output signal, and the analogue-to-digital converter. By choosing the coefficient k_m, one can compensate for the multiplicative errors of some units and for the error introduced by the lead wire resistance.

Summary

RTDs are among the most widely used temperature sensors. They are characterised by high accuracy and stability, and exhibit the transfer function closest to linear function.

The resistance temperature sensors based on thin films are smaller, less expensive, more reliable, less power consuming, and have a faster response time than the wirewound RTDs. The thin film RTDs can be employed for surface temperature measurements, but they are less reliable than the wirewound RTDs.

In order to linearize the transfer function of the platinum RTD, both the analogue and digital methods are applied; the analogue methods are more common. In the case of analogue linearization, the bridge circuit should be supplied by the voltage consisting of both the constant and the variable component. The variable component is a function of the temperature to be measured. In consequence, the quadratic component of the RTD transfer function is fully compensated; however, the additive cubic component still appears. In order to reduce this component, the calibration at certain points is required. For example, for platinum RTD, after the calibration at the point 400°C, the error of nonlinearity does not exceed 0.1% over the temperature measurement range 0..500°C.

In the case of the employment of the resistance bridge circuits for RTD output signal measurement, the nonlinearity of the bridge circuit and the resistances of lead wire connections can considerably influence the measurement results. In order to decrease the influence of the resistances of the three-wire connection of RTDs, the circuit of the thermoresistive transducer based on a current stabiliser is proposed. The transfer function of the output voltage of the proposed thermoresistive transducer is linear with respect to the change of the RTD resistance. In order to compensate the influence of the connection wires, the only condition to be fulfilled is that the resistances of the two wires should be equal.

The improvement of the linearity of the bridge measuring circuits is possible using the double-layer film structures based on the temperature dependent resistors with opposite sign of TCR. For example, for thin film structures with α_1=0.002 and α_2=-0.002 and nominal resistances 140 and 350 Ω, respectively, the maximum value of the relative error of nonlinearity of the bridge circuit over the temperature range –50…150°C does not exceed 0.05.

3. Thermocouples

3.1. Features of thermocouples as temperature sensors

Thermocouples are typical self-generating transducers. A thermocouple consists of two dissimilar materials that are joined together at one end by welding or soldering.

The operating principle of a themocouple is based on the Seebeck effect. The essence of the Seebeck effect is the generating of the thermo-emf in the circuit which consists of two dissimilar conductors or semiconductors, if a temperature difference between the place of electrode connection (hot junction) and the place of the cold junction is created.

A thermocouple can measure the temperature difference between two junctions, but not the absolute temperature value. The cold junction (reference) is maintained at a known (reference) temperature, while the other end remains attached to an object to be measured. Thermocouple Reference Tables (e.g. provided by National Institute of Standards and Technology) contain the data for various types of thermocouples. In the appropriate table, one can find the temperature of the hot (measuring) junction, corresponding to the measured output voltage of the thermocouple when the temperature of the cold junction is kept at zero degrees Celsius (melting ice-bath reference). Many years ago, the ice-bath reference was established as the standard for thermocouple applications [259]. In the case of any deviation of the cold-junction temperature from zero degree Celsius, the measured thermo-emf value $e(\vartheta)$ should be corrected for the value corresponding to this deviation.

The cold-junction temperature is measured with other types of temperature sensors such as RTDs, integrated circuit (IC) sensors, or thermistors [57, 245]. The calibrated platinum RTDs are applied for high accuracy measurements over the widest temperature range, but they are expensive. For less accurate measurements, thermistors and silicon temperature-sensing ICs are employed, because of lower prices compared to RTDs. The benefit of thermistors in comparison with silicon ICs is that thermistors can be applied over a wider range of operating temperature. The advantage of the temperature-sensing ICs is better linearity with respect to thermistors.

The type of the temperature sensor for cold-junction temperature measurement should be selected according to the requirements valid under given conditions. One should choose the optimal combination of accuracy, temperature range, linearity and cost [286].

The thermo-emf $e(\vartheta)$ that appears between the positive and negative legs of a thermocouple, is a function of the temperature difference between the hot and cold junctions:

$$e(\vartheta) = f\left(\vartheta_h - \vartheta_c\right) = f(\vartheta_h) - f(\vartheta_c), \tag{3.1}$$

where ϑ_h is the hot-junction temperature, and ϑ_c is the cold-junction temperature.

Thermocouples have many benefits, and currently they are the most widely employed sensors for temperature measurement both in industrial and scientific applications. The measurement range of thermocouples covers the temperature interval from –270°C to 3000°C. Thermocouples are the best choice for many kinds of the measuring equipment because of their advantages: they exhibit long-term stability, repeatability, high reliability, and long usability period. Simplicity, small sizes, compactness, ruggedness and low cost are the additional merits of thermocouples. Typical response time for thermocouples is of the order of tenths of a second which in most applications is convenient. One can also note the following drawbacks of thermocouples: the need of the reference temperature, limited accuracy and sensitivity but for many applications, these thermocouple parameters are suitable [49, 97, 160, 164, 185, 188, 220, 232].

There are many types of thermocouples [156]. The parameters of the commonly used thermocouple types are tabulated in Table 3.1.

Table 3.1. Parameters of commonly used types of thermocouples

Type	Composition of positive leg A	Composition of negative leg B	Temperature range	Sensitivity within a specified range
			[°C]	[µV/°C]
B	platinum–rhodium Pt-30% Rh	platinum–rhodium Pt-6% Rh	0 to 1820	10-14 (1000-1800°C)
E	Chromel Ni-Cr alloy (90.5% Ni + 9.5% Cr)	Constantan Cu-Ni alloy (55% Cu + 45% Ni, Mn, Fe)	–270 to 1000	59-81 (0-600°C)
J	Iron Fe	Constantan Cu-Ni alloy (55% Cu + 45% Ni, Mn, Fe)	–210 to 1200	50-64 (0-800°C)
K	Chromel Ni-Cr alloy (90.5% Ni +9.5% Cr)	Alumel Ni-Al alloy (94.5% Ni + 5.5% Al, Si, Mn, Co)	–270 to 1372	35-42 (0-1300°C)

N	Nicrosil Ni-Cr-Si alloy (83.49% Ni +13.7% Cr + 1.2% Si+ 0.15% Fe + 0.05% C + 0.01% Mg)	Nisil Ni-Si- Mg alloy (94.98% Ni + 0.02% Cr + 4.2% Si + 0.15% Fe + 0.05% C + 0.05% Mg)	–270 to 1300	26-39 (0-1300°C)
R	platinum–rhodium (87%Pt + 13%Rh)	Platinum Pt	–50 to 1768	10-14 (600-1600°C)
S	platinum–rhodium (90%Pt-10% Rh)	Platinum Pt	–50 to 1768	10-14 (600-1600°C)
T	Copper Cu	Constantan Cu-Ni alloy (55% Cu + 45% Ni, Mn, Fe)	–270 to 400	40-60 (0-400°C)
L	Chromel Ni-Cr alloy (90.5% Ni +9.5% Cr)	Copel (56% Cu + 44% Ni)	–200 to 900	64-88 (0-600°C)

The most widely applied is the K-type thermocouple because it covers the widest temperature measurement range from –270 to 1372°C. The average sensitivity of the K-type thermocouple is approximately 41 μV/°C. The K-type thermocouple is resistant to oxidation (especially above 500°C) but unsuitable for operation in reducing or sulphurous conditions [143].

The E-type thermocouple operates in oxidizing or inert atmospheres over the temperature range from –270 to 870 °C. The E-type thermocouple exhibits the highest sensitivity: it is resistant to oxidation and to moisture corrosion.

The J-type thermocouple can be used in vacuum, in reducing or inert atmosphere, but it is unsuitable for the moist or sulphurous conditions, because it oxidises above 540°C.

It is shown in [185] that the N-type thermocouple is the best type for routine temperature measurements and control over the temperature range from –40°C to 1200°C because of its high sensitivity, stability at high temperatures, and its resistance to high temperature oxidation.

For the precise temperature measurement and monitoring at high temperatures, different thermocouples with the electrodes made of platinum, and platinum-rhodium alloys, are most frequently employed. Such thermocouples have been utilized as a secondary reference standard over the temperature range from 0 to 1400°C. The S-type thermocouple was formerly used in defining the International Practical Temperature Scale of 1968 in the range from 630 to 1064°C, because it exhibits good thermal stability. The S-type and R-type thermocouples are usually employed to provide temperature measurements up to 1400°C. The wide use of the S-type thermocouples in industry is due to their ability to carry out simple and accurate temperature measurements [1, 150]. Comparing the linearity of the K-type thermocouple and the S-type thermocouple with other thermocouple types, it turns out that the former is the most linear, while the latter is the least linear one.

The B-type thermocouples are usually applied over the temperature range from 800 to 1700°C.

The noble metal thermocouples can be used as a substandard for routine measurements and calibration. The Pt/Au thermocouple can be employed over the temperature range up to 1000°C, and has a sensitivity of 25 μV/°C at 900°C. The Pt/Pd thermocouple can be applied in the temperature range up to 1500°C, and is characterised by rather low sensitivity (19 μV/°C at 1000°C). The thermoelectric properties of Pt/Pd thermocouples are better than corresponding properties of Pt-10% Rh/Pt thermocouples, at least up to 1060°C. These two types of thermocouples exhibit good repeatability. It was proved that the stability and repeatability of the noble metal thermocouples could be improved after annealing at 950°C for 300 h. It should be pointed out that the pure element thermocouples are more homogenous than alloyed thermocouples made of alloys [1, 130, 185].

Now let us consider the possible reasons for the thermoelectric instability of thermocouples. The main reason is related to the variations in composition of the thermoelectric alloys. The contaminations, oxidation and vaporization of the thermocouple electrodes materials result in the instability of thermocouples. In recent years, and up to present time, the thermocouples with electrodes of pure-metals are still designed and investigated. The advantages of the thermocouples with electrodes of pure metals, compared to thermocouples with electrodes made of alloys, are that pure metals have the merits of accuracy and stability. This is due to their thermoelectric uniformity, the constant composition of the electrodes (the selective oxidation of the components of the alloy or mutual diffusion are eliminated). In order to achieve good interchangeability of the thermocouples, it is recommended to use thermocouple electrodes made of high-purity metals, for which the deviations of the thermo-emf function $e(\vartheta)$ from the standardized values are small [197].

3.2. Improvement of accuracy in temperature measurement with thermocouples

The thermocouples are widely used for measuring temperature. However, some demerits should be considered when the temperature measurements with thermocouples are to be performed. The cold-junction temperature has a considerable impact on the measurement results. In many cases, the application of the melting ice-bath in order to keep cold junction at zero degree Celsius is impractical. If the cold junction is not kept at 0°C, the temperature of this junction should be known for determining the actual hot-junction temperature. In this case, the cold-junction compensation is required, i.e. the compensation of the shift of the output voltage of the thermocouple due to the voltage shift produced because of nonzero cold-junction temperature. The relationships between the thermo-emf of the various types of thermocouples and the measured temperatures are nonlinear. Errors up to 5% can be caused by the nonlinearity of a thermocouple [232]. When using a resistance temperature sensor for cold-junction compensation, the error to be compensated for is a function of both thermocouple nonlinearity and the variation in ambient temperature [280].

3.2.1 Analysis of the compensation schemes of the cold-junction temperature

The cold-junction temperature influences the measurement accuracy, especially in measurements of low temperatures. In order to compensate the cold-junction temperature influence, either the thermostatting of the cold junction or compensating electronic circuits are applied [96, 164].

Compensation methods can be divided into broad categories of analogue and digital. Digital methods require an additional measuring channel and expensive compensation sensors of high accuracy [164, 259]. In the case of an analogue compensation, various types of secondary measuring devices can be employed. An analogue compensating circuit forms a voltage equal to the thermo-emf of the thermocouple at a nonzero cold-junction temperature but with the sign opposite to this emf.

The cold-junction compensation is based on summing up the compensating voltage with the output voltage of the thermocouple, so that the cold junction appears to be at 0°C, no matter what the actual cold-junction temperature may be. In order to form the compensating voltage, temperature dependent bridge circuits are employed. In these circuits, the resistance temperature sensors are connected either in one or in two arms of the bridge [147, 178, 188]. The compensating voltage can be expressed by the formula:

$$U_c = U_s k_b(\vartheta_c), \tag{3.2}$$

where U_s is the supply voltage of the bridge circuit, and $k_b(\vartheta_c)$ is the transfer coefficient of the bridge circuit, which depends on the cold-junction temperature ϑ_c.

In [277] the following bridge compensating circuit is described. A resistive KTY silicon temperature sensor with a positive TCR is connected in one bridge arm, and also two additional resistors are connected: one in parallel, and the other in series with the KTY sensor. As the KTY silicon resistive sensor is high-ohmic one, an additional operational amplifier is applied. For the ambient temperature changes within the range from –20°C to 70°C, the accuracy better than 0.5°C is achieved.

The bridge circuits can be fed from a constant voltage/current source, and galvanically separated from the rest of the thermocouple measuring device (Fig. 3.1) [96].

The formulas for the output compensating voltage of the circuits depicted in Fig. 3.1 (for the schematics (a), (b), and (c), respectively) can be expressed as follows:

(circuit a)
$$U_c = U_s\left(\frac{R_\vartheta}{R_\vartheta + R_1} - \frac{R_3}{R_2 + R_3}\right), \tag{3.3}$$

(circuit b)
$$U_c = \frac{U_s R_b}{R_b + R_d}\left(\frac{R_\vartheta}{R_\vartheta + R_1} - \frac{R_3}{R_2 + R_3}\right), \tag{3.4}$$

(circuit c)
$$U_c = \frac{I_0 R_b R_d}{R_b + R_d}\left(\frac{R_\vartheta}{R_\vartheta + R_1} - \frac{R_3}{R_2 + R_3}\right), \tag{3.5}$$

where I_0 is the value of the reference current from a constant current source; R_1, R_2, and R_3 are the resistances of the temperature-independent resistors of the bridge circuit, R_ϑ is the resistance of the resistance temperature sensor of the bridge circuit, and R_d is the resistance of the calibration resistor.

The R_b resistance is the input resistance of the bridge circuit, and can be calculated from the formula:

$$R_b = \frac{(R_1 + R_\vartheta)(R_2 + R_3)}{R_1 + R_2 + R_3 + R_\vartheta}. \tag{3.6}$$

Usually, as the resistance temperature sensor R_ϑ in the compensating circuit an RTD Cu100 type is employed. The resistance of such resistor is expressed by the formula (2.3).

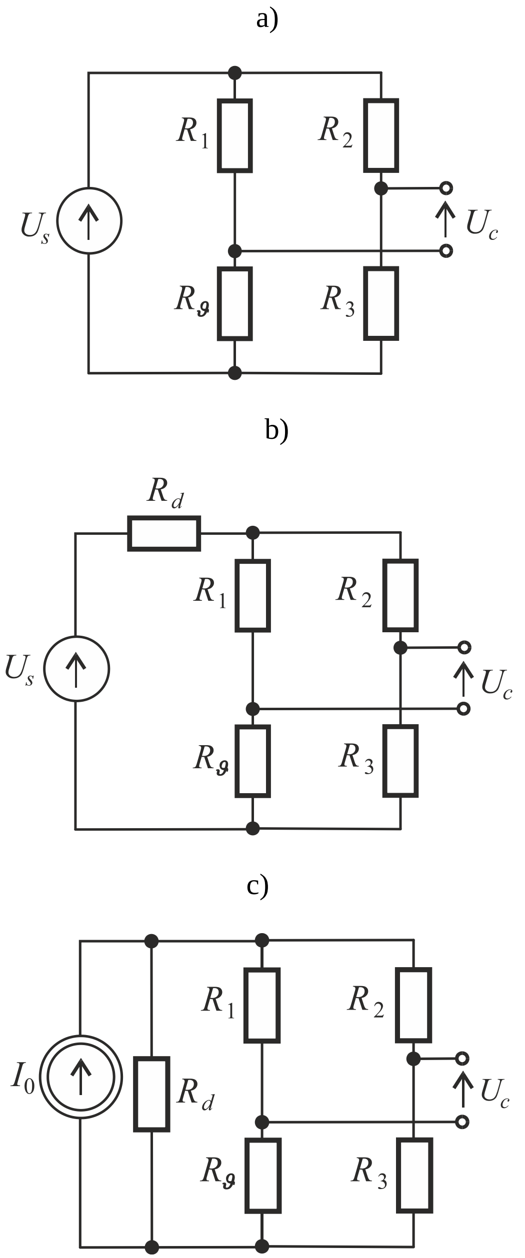

Figure 3.1. Schematics of compensating circuits fed from: (a) constant voltage source, (b) constant voltage source connected in series with calibration resistor, (c) constant current source connected in parallel with calibration resistor [96]

The resulting value of the compensating voltage U_c for the maximum cold-junction temperature is set by choosing the parameters of the supply source and the resistance R_d. In order to improve the accuracy of the compensation of the influence of the cold-junction temperature, the equality of the cold-junction temperature and the temperature of the sensor of resistance R_ϑ should be provided.

The absolute error of the compensation of the influence of the cold-junction temperature can be expressed as follows:

$$\Delta_{Uc} = U_c - e(\vartheta_c), \tag{3.7}$$

where $e(\vartheta_c)$ is the thermocouple emf at the cold-junction temperature ϑ_c, which is determined in compliance to IEC 584-1 [284, 287].

The absolute error of the compensation of the influence of the cold-junction temperature for a given temperature range $\vartheta_1 ... \vartheta_2$, expressed in degrees centigrade, is equal to:

$$\Delta_{\vartheta c} = \frac{[U_c - e(\vartheta_c)](\vartheta_{c2} - \vartheta_{c1})}{e(\vartheta_{c2}) - e(\vartheta_{c1})}, \tag{3.8}$$

where $e(\vartheta_{c1})$, $e(\vartheta_{c2})$, ϑ_{c1}, ϑ_{c2} are either initial or final values of the interval of the thermo-emfs and the temperatures, respectively.

The relationships between the absolute error of the compensation of the influence of the cold-junction temperature and temperature, for the given compensating circuits (Fig. 3.1) containing a Cu100 RTD as the R_ϑ, and the resistances of the arms equal to: $R_1=R_2=R_3=100\ \Omega$, for various types of thermocouples are graphed in Fig. 3.2 [96].

As it can be seen from the plots depicted in Fig. 3.2, the minimum error values are obtained for the compensating circuit driven by a constant voltage source connected in series with a calibration resistor (Fig. 3.1b).

The resistors R_1 and R_2 of the compensating circuit considerably influence the compensation accuracy. The relationships between the absolute error of the compensation of the influence of the cold-junction temperature, and the temperature measured using the K-type thermocouple, for a compensating circuit which contains a constant voltage source and a calibration resistor, are graphed in Fig. 3.3 for different R_1 and R_2 resistor values. From the graphs presented in Fig. 3.3 it can be seen that the accuracy of compensating voltage increases as the R_1 and R_2 resistor values increase. The maximum accuracy is attained for $R_1=R_2=10000\ \Omega$. The further increase in the R_1 and R_2 resistor values has no impact on the (constant) effectiveness of the compensating circuit; consequently, no essential gain in accuracy is observed.

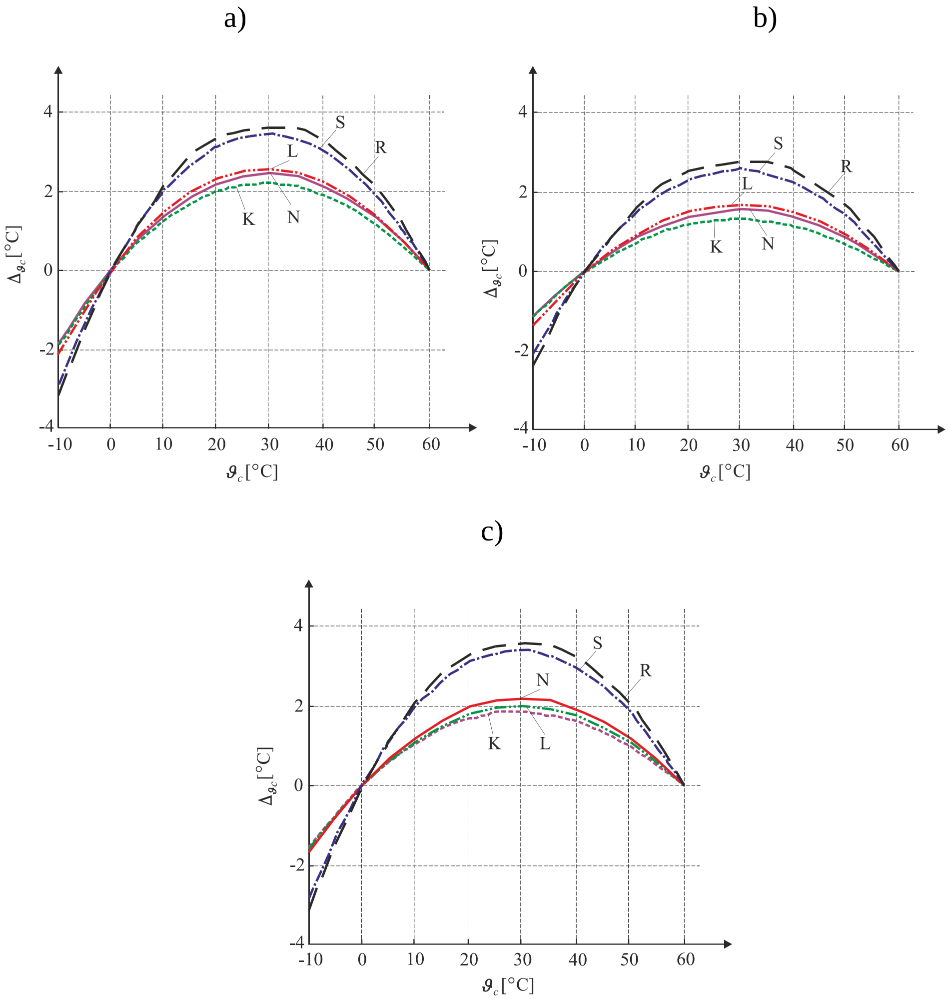

Figure 3.2. Relationships between the absolute error of the compensation of the influence of the cold-junction temperature and the cold-junction temperature, plotted for the compensating circuits with: a) a constant voltage source (cf. Fig. 3.1a); b) constant voltage source and calibration resistor (cf. Fig. 3.1b); c) current source (cf. Fig. 3.1c) for various types of thermocouples

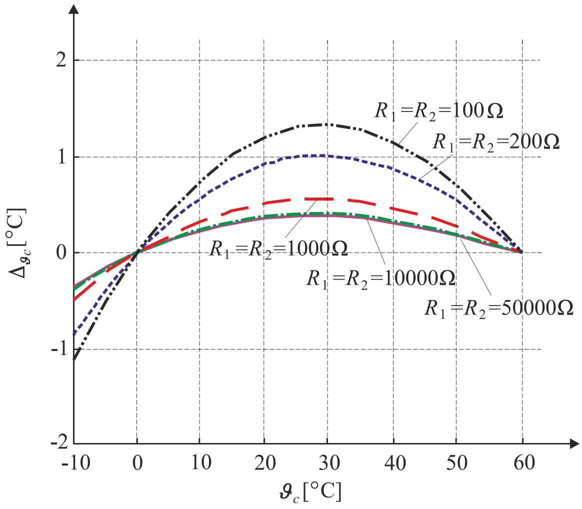

Figure 3.3. Relationships between the absolute error of the compensation of the influence of the cold-junction temperature and the cold-junction temperature, for different values of R_1=R_2

Within the narrow range of the cold-junction temperature variations, the shift of the characteristics of the circuit at the endpoints of the aforementioned range can improve the effectiveness of the compensating circuit [96]. At the upper range limit, the compensating voltage can be adjusted by changing the supply source voltage or the resistor value R_d; at the lower range limit, it can be adjusted by changing the resistor value R_3. The relationships between the absolute error of compensation and the cold-junction temperature over the temperature range from 10 to 50°C, for compensating circuits with a constant voltage source and a calibration resistor (Fig. 3.1b), for various types of thermocouples with shifted characteristics are depicted in Fig. 3.4. From Fig. 3.4 it can be seen that for the shifted characteristics of the compensating circuit, the absolute error over the cold-junction temperature variation range from 10 to 50°C does not exceed 0.2°C for the thermocouples of K-, N- and L-types at R_1= R_2 =1000 Ω.

a)

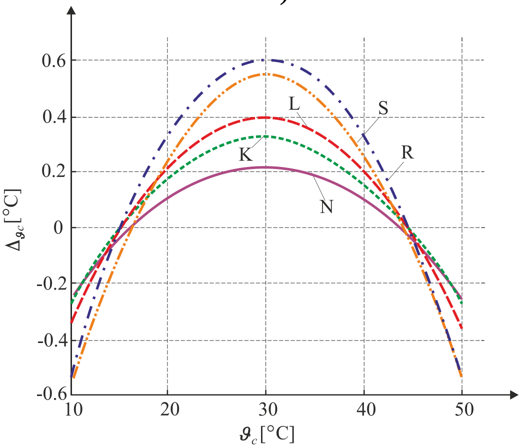

b)

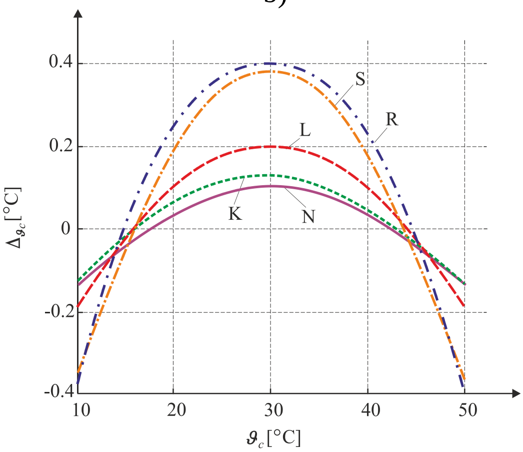

Figure 3.4. Relationships between absolute error of the compensation of the influence of the cold-junction temperature and the cold-junction temperature, for various types of thermocouples, using the shift of the output characteristics at different values of $R_1 = R_2$ (R_1 and R_2 are the resistances of the upper arms of the bridge circuit): a) $R_1 = R_2 = 100\ \Omega$; b) $R_1 = R_2 = 1000\ \Omega$

3.2.2. Thin film compensating circuit

In order to compensate the cold-junction temperature influence, the compensating circuit should be placed close to the cold junction. The equality of the temperatures of the cold junction and the temperature-dependent components of the compensating circuit should be achieved. The application of the thin film technology to the manufacturing process of the temperature-dependent resistance bridge circuits considerably increases the accuracy of the equalisation of the temperatures of the cold junction and the temperature-dependent resistors; it also ensures the required TCR value of the temperature-dependent resistors. In consequence, the temperature measurement accuracy increases.

The scheme of the cold-junction temperature compensating circuit made in thin film technology, and its connection to the thermocouple, is shown in Fig. 3.5 [24].

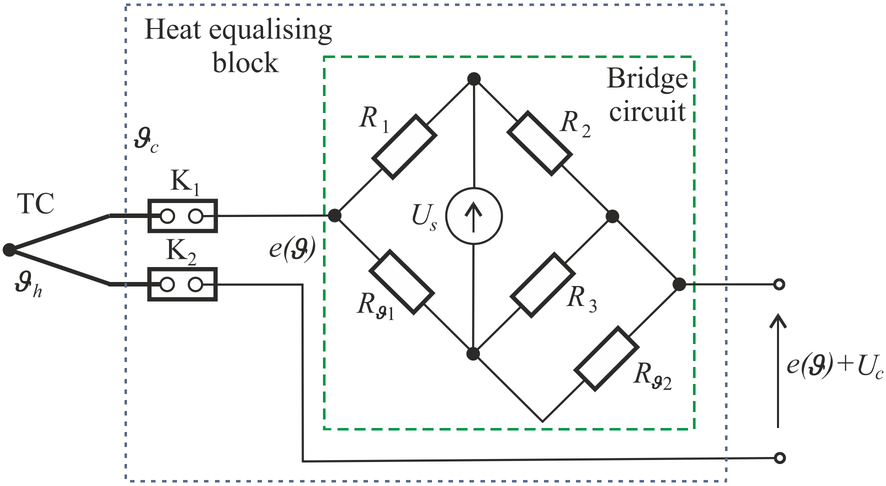

Figure 3.5. Scheme of the cold-junction temperature compensation circuit made by thin film technology, and its connection to the thermocouple

The compensation bridge consists of the resistors R_1, R_2, R_3, and $R_{\vartheta 1}$. The additional resistor $R_{\vartheta 2}$ is connected in parallel to the resistor R_3, in order to obtain the required nonlinearity limit of the transfer characteristics. The bridge compensating circuit is made of the shifted double-layer resistive film structure on the dielectric substrate (Fig. 3.6). The resistance temperature sensors $R_{\vartheta 1}$ and $R_{\vartheta 2}$ are made of the resistive film layers with positive (R_1) and negative (R_2) TCR, respectively. The resistors R_1, R_2, R_3 are made with the shifted double-layer resistive film (Fig. 3.6). For equalising the temperatures of the bridge compensating circuit and the cold junction, the heat equalising blocks are applied. These thermal conducting blocks are comb-shaped copper plates, and should be arranged in an interdigitated structure, with the plates spaced a few millimetres apart from each other (Fig. 3.7) [24].

The thermocouple output voltage is summed with the output voltage of the compensating circuit U_c, which is expressed as follows:

$$U_c = U_s \left(\frac{R_{\vartheta 1}}{R_1 + R_{\vartheta 1}} - \frac{R_{eq}}{R_2 + R_{eq}} \right), \tag{3.9}$$

where U_s is the supply voltage of the bridge compensating circuit, and R_{eq} is the equivalent resistance for the resistors $R_{\vartheta 2}$ and R_3 in parallel.

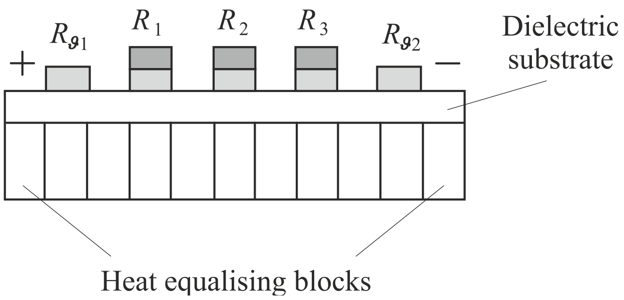

Figure 3.6. Arrangement of the thin film resistors in the bridge compensating circuit [24]

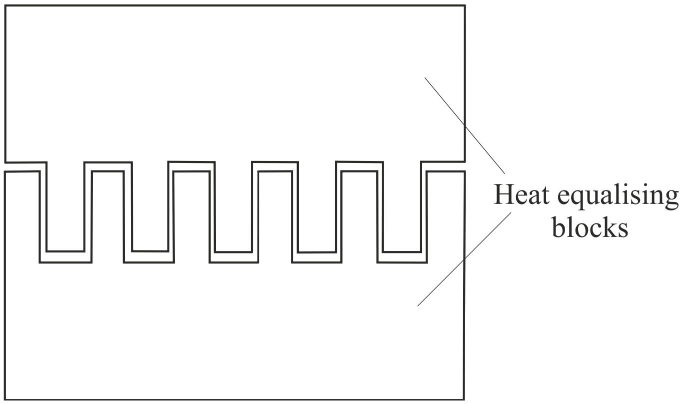

Figure 3.7. Heat equalising blocks of the bridge compensating circuit [24]

From the analysis of the expression (3.9) it can be seen that the required value of the compensating voltage for the maximum value of the cold-junction temperature can be adjusted by setting a proper value of the supply voltage. The acceptable nonlinearity limit is set by the values of resistances of the resistors of the bridge circuit.

In order to balance the bridge circuit at ϑ=0°C, the resistances of the resistor $R_{\vartheta 1}$ and the equivalent resistance R_{eq} at ϑ=0°C should be equal.

The graphs of the relationships between the absolute errors due to the influence of the cold-junction temperature and the cold-junction temperature for K-type thermocouple, calculated using the equation (3.8) for different resistances of the resistors R_1 and R_2, are shown in Fig. 3.8. The values of the resistance of the temperature-dependent resistor $R_{\vartheta 1}$ and the equivalent resistance R_{eq} were assumed to be 100 Ω at ϑ=0°C: the TCR of the temperature-dependent resistors was chosen to be 0.0043 Ω/°C.

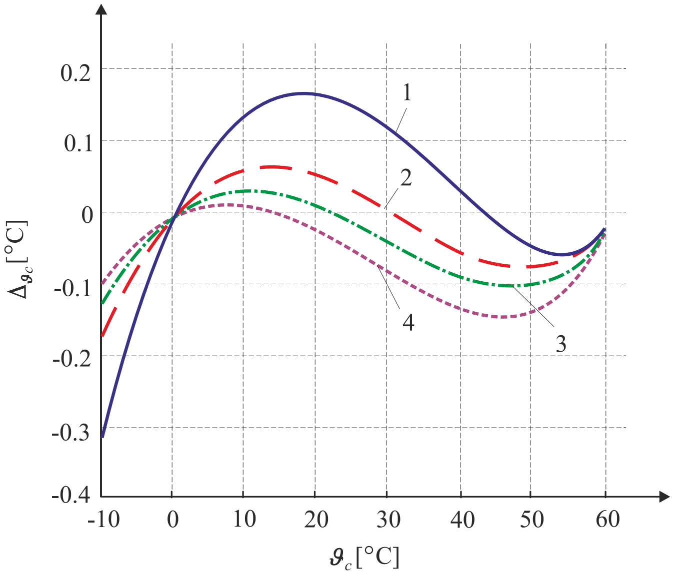

Figure 3.8. Plots of the relationship of the absolute error due to the influence of the cold-junction temperature vs. cold-junction temperature, for different values of R_1=R_2: 1) R_1=R_2=100 Ω, 2) R_1=R_2=200 Ω, 3) R_1=R_2=250 Ω, 4) R_1=R_2=300 Ω

From the analysis of the plots it can be seen that the minimum error is attained for the resistances value R_1= R_2=250 Ω, and is less than 0.15°C.

The improvement in the accuracy is possible by means of shifting of the characteristics of the conversion function, changing the supply voltage U_s and the value of the resistance R_3. The relationships between the absolute error of the compensation of the influence of the cold-junction temperature and cold-junction temperature, for different values of U_s and R_3, are plotted in Fig. 3.9. After shifting the characteristics of the conversion function of the compensating circuit, the absolute error of the compensation of the influence of the cold-junction temperature less than 0.1°C (the curve plotted for R_1=R_2=200 Ω, Fig. 3.9) can be achieved.

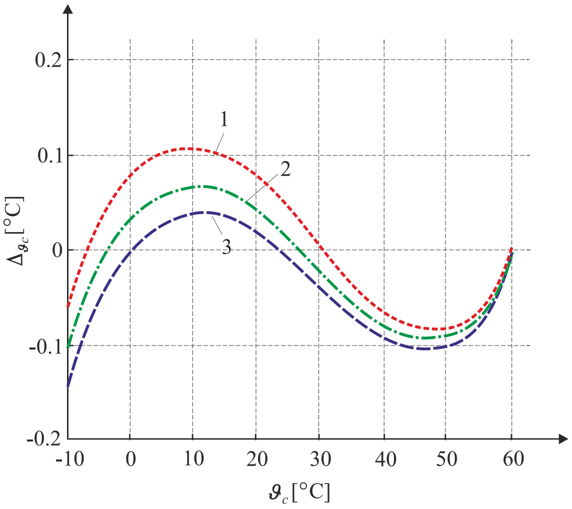

Figure 3.9. Plots of the relationship of the absolute error due to the influence of the cold-junction temperature vs. cold-junction temperature, for different values of U_s and R_3: 1) U_s=30.34 mV; R_3=199.8 Ω, 2) U_s =30.36 mV; R_3=199.9 Ω, 3) U_s =30.37 mV; R_3=200 Ω

3.2.3. Compensating circuits with temperature-dependent voltage source

The improvement in the accuracy of reproducibility of the thermo-emf of the thermocouples over a wide range of cold-junction temperature changes can be obtained using the temperature-dependent voltage source for bridge circuit supply. The output voltage U_{sd} from the temperature-dependent voltage source can be expressed as:

$$U_{sd} = U_n + \Delta U_c \cdot \vartheta_c , \tag{3.10}$$

where U_n is the nominal value of the output voltage at the cold-junction temperature ϑ_c=0°C, ΔU_c is the absolute value of the voltage change due to the change in the cold-junction temperature of one degree Celsius, and ϑ_c is the thermocouple cold-junction temperature.

The compensating voltage can be expressed as:

$$U_c = \left(U_n + \Delta U_c \cdot \vartheta_c\right) \cdot k_b(\vartheta_c) = U_n \cdot k_b(\vartheta_c) + \Delta U_c \cdot \vartheta_c \cdot k_b(\vartheta_c) , \tag{3.11}$$

where $k_b(\vartheta_c)$ is the transfer coefficient of the bridge circuit which depends on the cold-junction temperature.

From the analysis of the equation (3.11), it can be seen that the second term constitutes an additional nonlinear component of the voltage compensation equation compared with (3.2); hence, the equation (3.11) allows reproducing the value of thermo-emfs of thermocouples, affected by the cold-junction temperature change, with higher accuracy.

In order to design a temperature-dependent voltage source, different resistive or semiconductor thermocouple electrodes can be applied. The simplest method is to employ semiconductor diodes [21, 96].

The compensating circuit composed of a bridge and the temperature-dependent voltage source containing a semiconductor diode D1 and the resistor R_1, is shown in Fig. 3.10. The resistor R_1 is applied for setting a required temperature-dependent voltage drop across the diode D1. The equality of the temperatures of the cold-junction, the semiconductor diode D1 and the resistance temperature sensor R_ϑ can be achieved by various device design techniques.

The output voltage U_{sd} of the temperature-dependent voltage source can be expressed as:

$$U_{sd} = U_s - U_{D0} + \Delta U_D \cdot \vartheta_c, \tag{3.12}$$

where U_s is the supply voltage of the temperature-dependent voltage source, U_{D0} is the voltage drop across the diode at 0°C, ΔU_D is the change in the voltage across the diode due to the change in temperature of one degree Celsius, and ϑ_c is the temperature of the thermocouple cold junction, the semiconductor diode D1 and the resistance temperature sensor R_ϑ.

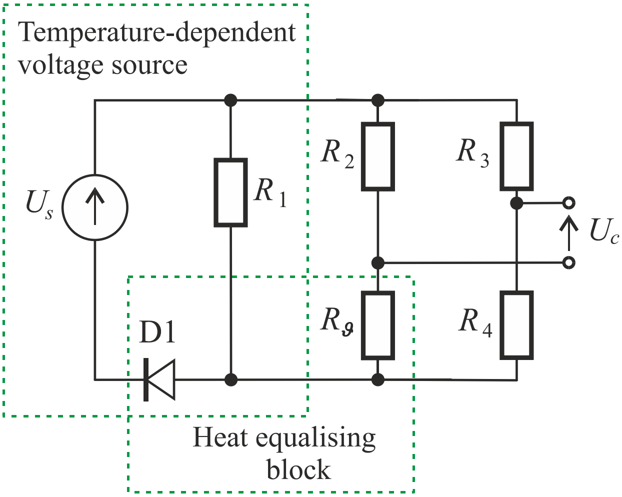

Figure 3.10. Compensating circuit with the temperature-dependent voltage source with semiconductor diode

The optimal values of the supply voltage U_s of the temperature-dependent voltage source, and the resistances of the resistors R_2, R_3, R_4 for various types of thermocouples are given in Table 3.2.

Table 3.2. Optimal values of the elements of the compensating circuit with a temperature-dependent voltage source containing a semiconductor diode (Fig. 3.10) for various types of thermocouples

Thermocouple type	L-type	K-type	R-type	S-type	N-type
U_s [V]	2.235	3.514	1.367	1.498	3.178
R_2 [kΩ]	10	30	51	60	40
R_3 [kΩ]	10	30	51	60	40
R_4 [Ω]	100	100	99.98	99.98	100

The relationships between the absolute error of the compensation of the influence of the cold-junction temperature and the cold-junction temperature, calculated from equation (3.8) for various types of thermocouples over the range –10 … 60°C, are depicted in Fig. 3.11.

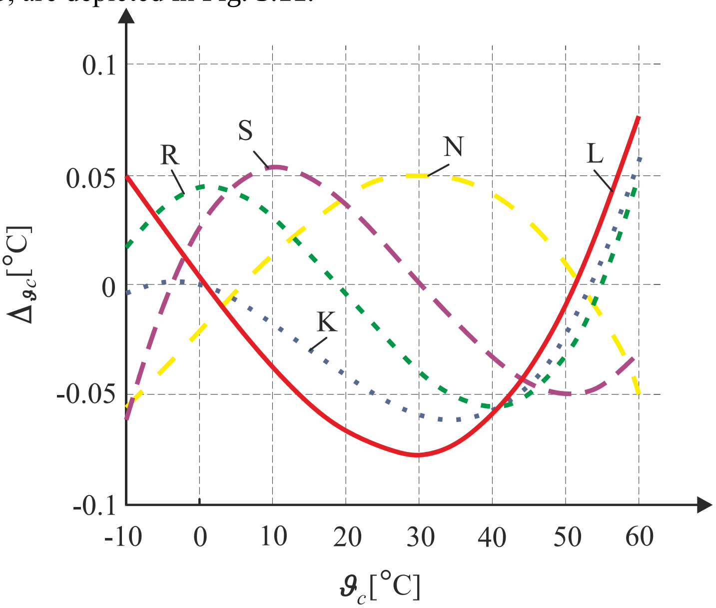

Figure 3.11. Relationships between the absolute error of the compensation of the influence of the cold-junction temperature and the cold-junction temperature, for the various types of thermocouples

From the graphs depicted in Fig. 3.11, it can be seen that for various types of thermocouples the absolute error of the compensation of the influence of the cold-junction temperature is less than 0.1°C.

The reduction of the resistances of the resistors R_2 and R_3 of the bridge circuit is achievable by using an additional resistor R_d, connected in series with the bridge circuit [96]. For that bridge circuit, the optimal values of the supply voltage of the temperature-dependent voltage source and of the resistances of the resistors R_2, R_3 and R_4 for various types of thermocouples, are given in Table 3.3.

From the graphs plotted in Fig. 3.12, it can be seen that in this case the absolute error of the compensation of the influence of the cold-junction temperature is less than 0.06°C for various types of thermocouples.

Taking into consideration all aspects presented above, the following conclusion can be drawn: the compensating circuit with a temperature-dependent voltage source containing a semiconductor diode provides the absolute error of the compensation of the influence of the cold-junction temperature less than 0.1°C for various types of thermocouples.

Table 3.3. Optimal values of the elements for compensating circuit with a temperature-dependent voltage source containing a semiconductor diode and additional resistor R_d, for various types of thermocouples

Circuit parameter	Thermocouple type				
	L-type	K-type	R-type	S-type	N-type
U_s [V]	1.50	1.675	1.15	1.19	1.565
R_2 [Ω]	100	100	100	100	100
R_3 [Ω]	100	100	100	100	100
R_4 [Ω]	100	99.99	99.99	99.99	100.02
R_d [kΩ]	1.191	2.45	8.416	8.936	3.326

For designing a temperature-dependent voltage source, transistors can also be applied [20, 104]. Then, the compensating circuit consists of the galvanically separated temperature-dependent voltage source, and the resistance bridge circuit (Fig. 3.13).

The temperature-dependent voltage source is fed from an external AC power source through the isolation transformer. The rectified alternating voltage is set on the capacitor C_1, and is stabilised by the current stabiliser DA2. The resistors R_1 and R_2 are employed for the regulation of the stabiliser output voltage, in order to ensure the required accuracy of the compensating voltage formed within the circuit for various types of thermocouples.

The value of the current stabiliser output voltage is equal to:

$$U_{st} = U_{st\,nom} + R_1\left(I_{st} + \frac{U_{st\,nom}}{R_2}\right), \tag{3.14}$$

where I_{st} is the stabilised current of the stabiliser DA2, and $U_{st\ nom}$ is the nominal output voltage of the stabiliser DA2.

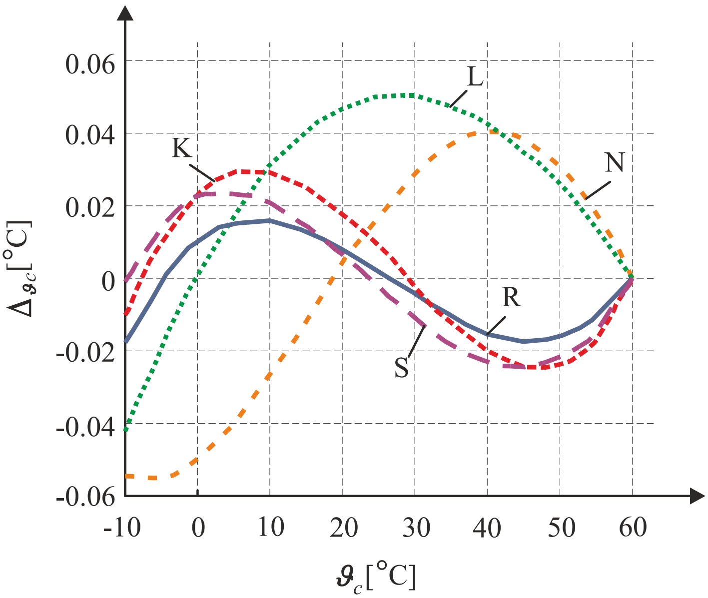

Figure 3.12. Relationships between the absolute error of the compensation of the influence of the cold-junction temperature and the cold-junction temperature for various types of thermocouples

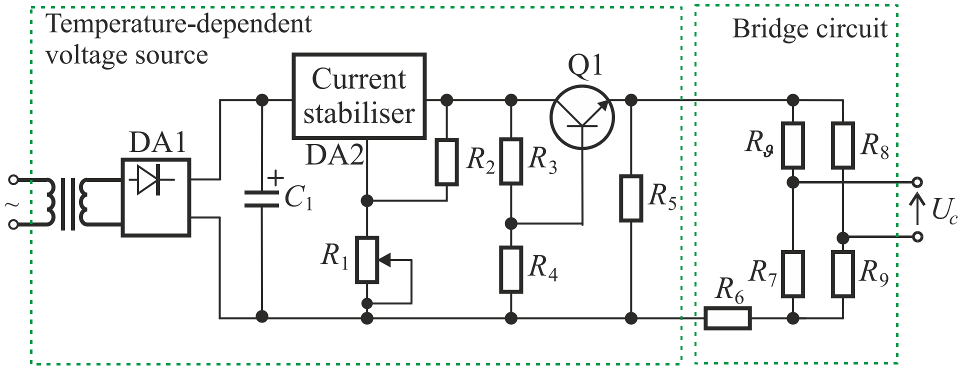

Figure 3.13. Compensating circuit comprising a temperature-dependent voltage source based on a transistor

The required relationship between the output voltage of the temperature-dependent voltage source and temperature is ensured by the temperature dependence of the base-emitter voltage of the transistor Q1, and can be expressed as follows:

$$U_{sd} = k_d U_{st} - U_{be0} + \Delta U_{be} \vartheta_c , \tag{3.15}$$

where U_{be0} is the base-emitter voltage of the transistor Q1 at 0°C, ΔU_{be} is the averaged value of the base-emitter voltage change due to the temperature change of 1°C, and $k_d = \dfrac{R_4}{R_3 + R_4}$ is the divider's voltage ratio of the voltage divider built with the resistors R_3 and R_4.

The compensating voltage U_c is equal to:

$$U_c = \frac{U_{sd} R_b}{R_6 + R_b} \left(\frac{R_\vartheta}{R_7 + R_\vartheta} - \frac{R_8}{R_8 + R_9} \right), \tag{3.16}$$

where $R_b = \dfrac{(R_7 + R_\vartheta)(R_8 + R_9)}{R_7 + R_8 + R_9 + R_\vartheta}$ is the input resistance of the resistance bridge circuit.

The required accuracy of the compensating voltage is achieved by choosing the values of U_{st}, U_{be0}, ΔU_{be} and R_6. The resistor R_5 is applied for setting the U_{be0}, and ΔU_{be} values.

The resistance values of the resistors of the bridge circuit for various types thermocouples types were chosen to be equal: $R_7=R_8=R_9=R_0$, where R_0 is the resistance of the resistance temperature sensor at 0°C.

Then, the expression (3.16) is transformed into the following one:

$$U_c = \frac{U_{sd} \cdot \alpha \vartheta_c R_0}{R_6 (4 + \alpha \vartheta) + 2R_0 (2 + \alpha \vartheta_c)} . \tag{3.17}$$

The optimal values of the supply voltage of the stabiliser and the resistance of the resistor R_6 for various types of thermocouples are given in Table 3.4.

Table 3.4. Supply voltage of the stabiliser and the resistance values of the resistor R_6 for various types of thermocouples

Circuit parameter	Thermocouple type				
	L-type	K-type	R-type	S-type	N-type
U_{st} [V]	1.6	1.9	1.2	1.25	1.7
R_6 [kΩ]	1.465	3.218	10.56	11.3	4.145

The relationships between the absolute error of the compensation of the influence of the cold-junction temperature and the cold-junction temperature, for various types of thermocouples are plotted in Fig. 3.14.

From the analysis of these relationships, it can be seen that for the latter compensating circuit (Fig. 3.13) the absolute error of the compensation of the influence of the cold-junction temperature is less than 0.07 °C for various types of thermocouple.

The same results were obtained for the compensating circuit with temperature-dependent supply source based on a transistor, described in [104].

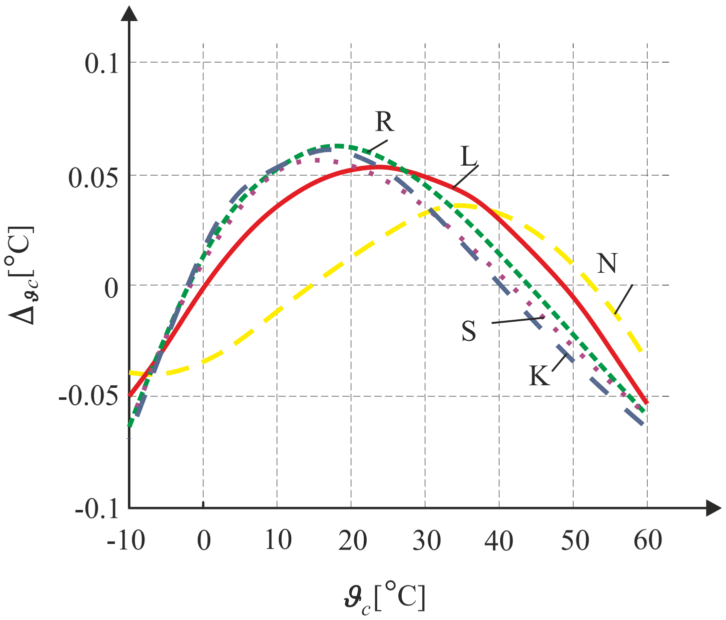

Figure 3.14. Relationships between the absolute error of the compensation of the influence of the cold-junction temperature and the cold-junction temperature for various types of thermocouples

The reproducing accuracy of the voltage U_c depends on the equality of temperatures of the cold-junction and the temperature-dependent elements (the semiconductor transistor Q1 and the resistor R_ϑ). In order to ensure the equality of the temperatures of Q1, R_ϑ, and the contact elements K_1 and K_2 with which the cold junction terminals are connected, all these components should be placed on heat equalising block, and put in the thermostat. The scheme of the arrangement of the components and the thermocouple connection is given in Fig. 3.15.

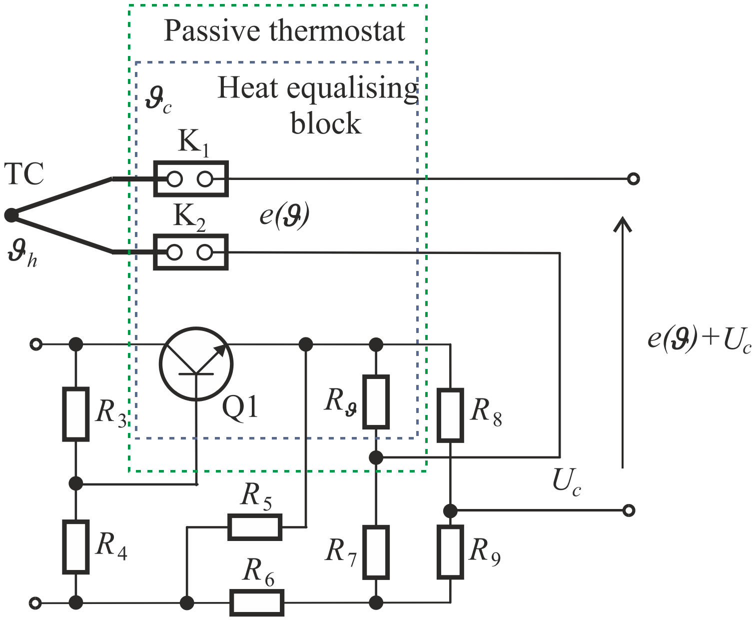

Figure 3.15. Scheme of the temperature-dependent element emplacement and thermocouple connection

In order to improve the heat contact, a caseless-type transistor Q1 and a thin film resistor R_ϑ can be applied. They can be placed on the contact elements K_1 and K_2.

The temperature-dependent voltage source based on an operational amplifier and a resistance temperature sensor [100] allows performing an independent regulation within wide range of both the nominal voltage U_n values, and the values of voltage changes due to the changes in the cold-junction temperature ΔU_c. Thus, the compensating voltage for various types of thermocouples can be formed with higher accuracy. The schematic diagram of the compensating circuit composed of the temperature-dependent voltage source, the temperature-dependent resistance bridge circuit, and the heat equalising block, is shown in Fig. 3.16.

The current I_0 from the current stabiliser flows through the resistors R_1 and $R_{\vartheta 1}$, and forms the temperature-dependent voltage, which is equal to:

$$U = I_0\left(R_1 + R_{\vartheta 1}\right). \tag{3.18}$$

The temperature-dependent voltage U is amplified in the non-inverting operational amplifier DA1 circuit, the gain k_a of which is expressed as follows:

$$k_a = \frac{R_2 + R_3}{R_3}. \tag{3.19}$$

The output voltage of the temperature-dependent voltage source U_{sd} consists of the constant voltage component, which is equal to the nominal value of the output voltage U_n at the cold-junction temperature ϑ_c=0°C and the variable voltage component $U_v = \Delta U_c \vartheta_c$:

$$U_{sd} = U_n + U_v. \tag{3.20}$$

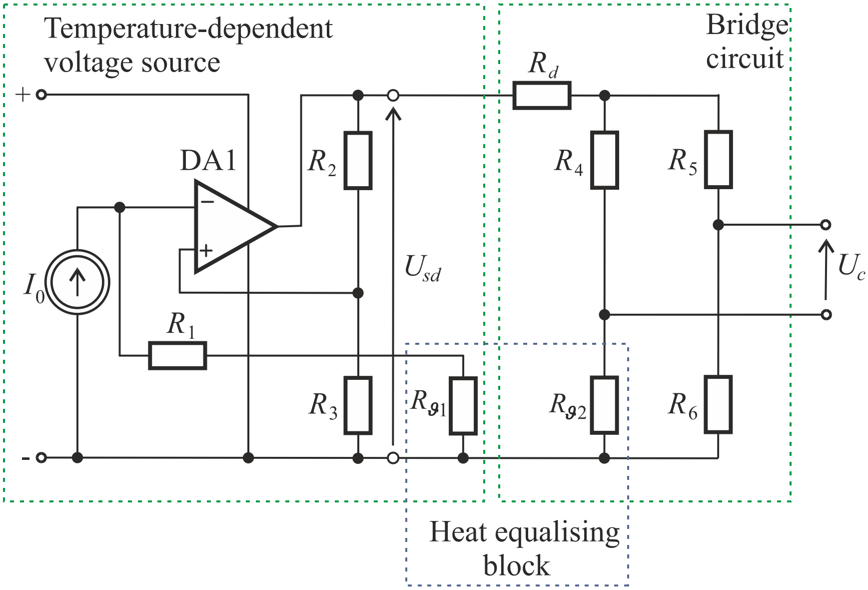

Figure 3.16. Compensating circuit with a temperature-dependent op-amp-based voltage source with a resistance temperature sensor

The constant voltage component is determined by the resistance values of the resistor R_1 and the resistance temperature sensor R_ϑ at 0°C; it is equal to:

$$U_n = I_0(R_1 + R_0) \cdot k_a, \tag{3.21}$$

where R_0 is the resistance of the resistor $R_{\vartheta 1}$ at 0°C.

The variable component of the output voltage of the temperature-dependent voltage source is determined by the change of the value of $R_{\vartheta 1}$ with cold-junction temperature, and is expressed as follows:

$$U_v = I_0 R_0 \alpha \vartheta_c k_a, \tag{3.22}$$

where α is the TCR of the RTD resistor $R_{\vartheta 1}$, and ϑ_c is the cold-junction temperature.

The compensating voltage, i.e. the output voltage of the bridge circuit based on the resistors R_d, R_4, $R_{\vartheta 2}$, R_5 and R_6, is equal to:

$$U_c = U_{sd} \frac{R_b}{R_d + R_b} \cdot \frac{\alpha \vartheta_c}{2(2 + \alpha \vartheta_c)}, \tag{3.23}$$

where $R_b = \dfrac{(R_4 + R_{\vartheta 2})(R_5 + R_6)}{R_4 + R_5 + R_6 + R_{\vartheta 2}}$ is the input resistance of the resistance bridge circuit.

Substituting (3.21) and (3.22) into (3.23), the following expression is obtained:

$$U_c = I_0(R_1 + R_0) \cdot k_a \frac{R_b}{R_d + R_b} \cdot \frac{\alpha \vartheta_c}{2(2 + \alpha \vartheta_c)} + I_0 R_0 k_a \frac{R_b}{R_d + R_b} \cdot \frac{(\alpha \vartheta_c)^2}{2(2 + \alpha \vartheta_c)}. \tag{3.24}$$

From the analysis of the expression (3.24) it can be seen that the second term constitutes the additional nonlinearity which improves the reproducing accuracy of the thermo-emf of the cold junction. The optimal values of the nominal supply voltage and the temperature-induced change in the output voltage can be determined for various thermocouples by choosing the appropriate values of the resistor R_1 and the gain of the operational amplifier; the k_a value is set with the resistors R_2 and R_3.

The heat equalising block is applied for equalising the temperature difference between the cold junction of the thermocouple and the resistance temperature sensors $R_{\vartheta 1}$ and $R_{\vartheta 2}$.

The compensation effectiveness for the L-type, K-type, S-type, R-type and N-type thermocouples was investigated. As the result of the investigations, some component values of the compensating circuit (Table 3.5) at which the optimal values of the compensating voltage can be achieved were determined.

Table 3.5. Optimal values of the compensating circuit components obtained using the formulas (3.8) and (3.24)

Thermocouple type	R_1 [Ω]	R_2 [Ω]	R_d [Ω]	R_3 [Ω]	I_0 [mA]
L-type	110	3600	1500	1000	0.9816
K-type	159	3600	2500	1000	0.8037
R-type	15	3600	1427	1000	0.1425
S-type	30	3300	1482	1000	0.1434
N-type	130	3600	1311	1000	0.3234

The relationships between the absolute error of the compensation of the influence of the cold-junction temperature and the cold-junction temperature for various types of thermocouples are plotted in Fig. 3.17.

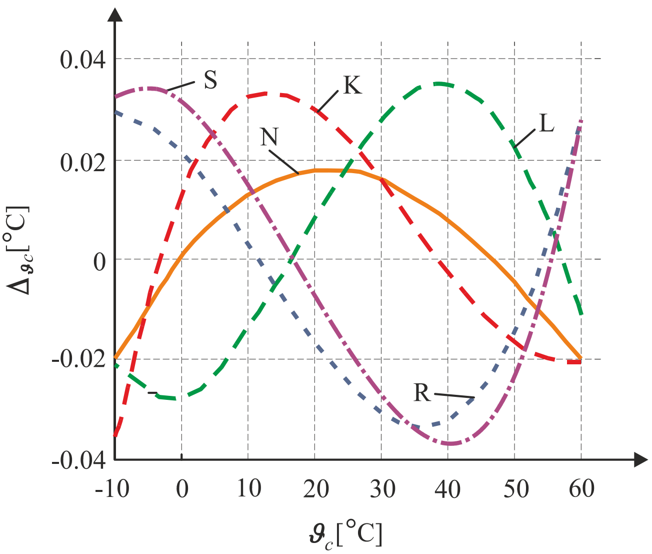

Figure 3.17. Relationships between the absolute error of the compensation of the influence of the cold-junction temperature and the cold-junction temperature for various types of thermocouple

From the analysis of the plots in Fig. 3.17 it can be seen that the absolute error of the compensation of the influence of the cold-junction temperature is less than 0.04 °C for L-type, K-type, R-type and S-type thermocouples, and does not exceed 0.02 °C for the N-type thermocouple.

In order to supply a temperature-dependent voltage source based on an operational amplifier, a voltage source can be employed [100]. In this case, the resistor R_z is connected between the positive terminal of the supply voltage source and the resistor R_1, in order to feed the operating current through the resistors R_1 and $R_{\vartheta 1}$.

The constant component of the output voltage of the temperature-dependent voltage source is equal to:

$$U_n = \frac{U_s \cdot (R_1 + R_0)}{R_z + R_1 + R_0} \cdot k_a , \tag{3.25}$$

where U_s is the supply voltage of the temperature-dependent voltage source.

If the condition $R_2+R_{\vartheta 1} << R_1$ is met, the temperature-induced change in the output voltage can be expressed as:

$$\Delta U_c = \frac{U_s \cdot R_0 \cdot \alpha \cdot \vartheta_c}{R_z + R_1 + R_0} \cdot k_a . \tag{3.26}$$

The compensation voltage of the compensating circuit with temperature-dependent voltage source based on operational amplifier and containing a resistance temperature sensor, is equal to:

$$\begin{aligned} U_c = {} & \frac{U_s \cdot \left(R_1 + R_0\right)}{R_z + R_1 + R_0} \cdot k_a \cdot \frac{R_b}{R_d + R_b} \cdot \frac{\alpha \vartheta_c}{2(2 + \alpha \vartheta_c)} + \\ & + \frac{U_s \cdot R_0}{R_z + R_1 + R_0} \cdot k_a \cdot \frac{R_b}{R_d + R_b} \cdot \frac{\left(\alpha \vartheta_c\right)^2}{2(2 + \alpha \vartheta_c)} \end{aligned} . \tag{3.27}$$

Some component values of the compensating circuit at which the optimal values of the compensating voltage can be achieved, are presented in Table 3.6 [100].

Table 3.6. Optimal values of the compensating circuit components obtained using the formula (3.8) and (3.27)

Thermocouple type	R_z	R_1	R_2	R_d	R_3	U
	[Ω]	[Ω]	[Ω]	[Ω]	[Ω]	[V]
L-type	4557	95.5	3600	1500	1000	5.0
K-type	6185	159	3600	2500	1000	5.0
R-type	34900	15	3600	1429	1000	5.0
S-type	34700	30	3300	1483	1000	5.0
N-type	15215	130	3600	1310	1000	5.0

The relationships between the absolute error of the compensation of the influence of the cold-junction temperature and the cold-junction temperature, for various types of thermocouples, are depicted in Fig. 3.18. From the analysis of the relationships of the absolute error of the compensation of the influence of the cold-junction temperature vs. the temperature (Fig. 3.18), it can be seen that the circuit described in [100] ensures the reproducibility of the thermo-emf of the cold-junctions with the reproducibility error less than 0.01°C for L-type thermocouples, and less than 0.04°C for K-type, R-type, S-type and N-type thermocouples.

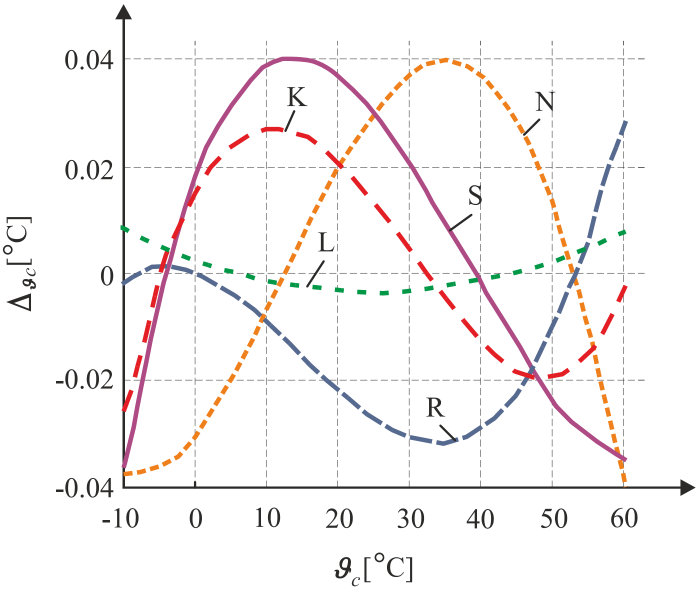

Figure 3.18. Relationships between the absolute error of the compensation of the influence of the cold-junction temperature and the cold-junction temperature for various types of thermocouples

3.2.4. Compensating circuit with temperature-dependent voltage divider

The effectiveness of the compensating circuits over a wide range of the cold-junction temperature change can be improved by employing additional temperature-dependent voltage dividers [22, 102].

The schematic of the resistor-based compensation bridge circuit with additional, temperature-dependent voltage divider built with the resistors R_4 and $R_{\vartheta 2}$, is shown in Fig. 3.19. In order to maintain equal temperatures of the resistance temperature sensors $R_{\vartheta 1}$ and $R_{\vartheta 2}$, and the cold-junction of the thermocouple, the passive thermostat with thermally conductive temperature equalisers can be employed.

A voltage source U_s or a current source I_0 can be used as the power supply of the compensating circuit.

If a voltage source U_s is employed, the output compensating voltage of the compensating bridge circuit with additional voltage divider can be expressed as:

$$U_c = U_s \frac{R_b}{R_d + R_b}\left(\frac{R_{\vartheta 1}}{R_1 + R_{\vartheta 1}} - \frac{R_3}{R_2 + R_3}\right) \cdot \frac{R_{\vartheta 2}}{R_{out} + R_4 + R_{\vartheta 2}}, \tag{3.28}$$

where $R_b = \dfrac{(R_1 + R_{\vartheta 1})(R_2 + R_3)}{R_1 + R_2 + R_3 + R_{\vartheta 1}}$ is the input resistance of the bridge circuit, and

$R_{out} = \frac{(R_3 + R_{\vartheta 1})(R_2 + R_1)}{R_1 + R_2 + R_3 + R_{\vartheta 1}}$ is the output resistance of the bridge circuit, assuming $R_b << R_d$.

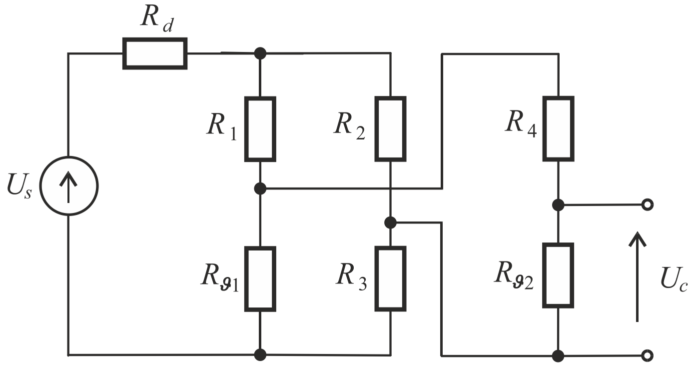

Figure 3.19. Schematic of the compensation bridge circuit with a temperature-dependent voltage divider

If a current source I_0 is employed, the output compensating voltage can be calculated as:

$$U_c = I_0 R_b \left(\frac{R_{\vartheta 1}}{R_1 + R_{\vartheta 1}} - \frac{R_3}{R_2 + R_3} \right) \cdot \frac{R_{\vartheta 2}}{R_{out} + R_4 + R_{\vartheta 2}}. \tag{3.29}$$

From the analysis of the formulas for compensating voltages (expressions (3.28) and (3.29)), it can be seen that the application of a temperature-dependent voltage divider involves the presence of additional nonlinear components in the formulas for the output voltage, which improve the accuracy of the function describing the dependence of the thermo-emf reproducibility of the thermo-emf on the cold-junction temperature.

The relationships between the absolute error of the compensation of the influence of the cold-junction temperature and the cold-junction temperature of the bridge circuit fed from voltage source, for the resistance temperature sensor Pt100 and various types of thermocouples, are shown in Fig. 3.20.

The relationships between the absolute error of the compensation of the influence of the cold-junction temperature and the cold-junction temperature of the bridge circuit fed from a current source, for Pt100 and various types of thermocouples, are shown in Fig. 3.21.

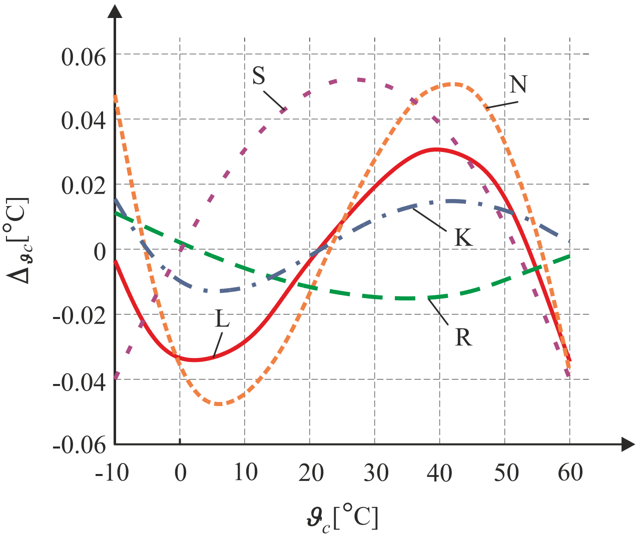

Figure 3.20. Relationships between the absolute error of the compensation of the influence of the cold-junction temperature and the cold-junction temperature of the resistor-based circuit fed from a voltage source, for Pt100 RTD and various types of thermocouples

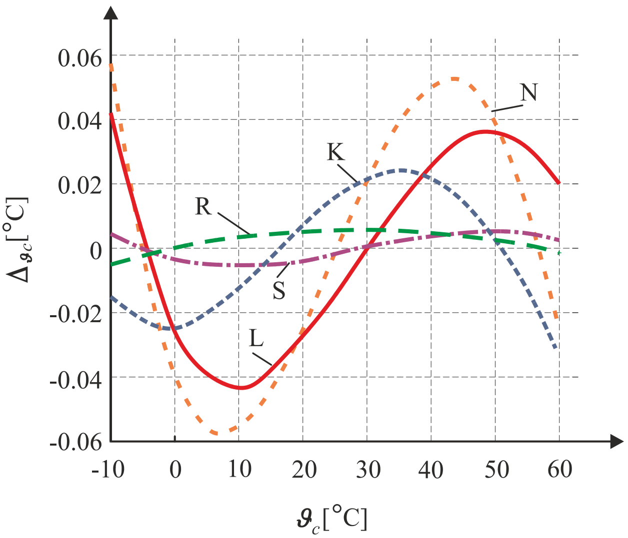

Figure 3.21. Relationships between the absolute error of the compensation of the influence of the cold-junction temperature and the cold-junction temperature of the bridge circuit fed from a current source for Pt100 RTD and various types of the thermocouples

The absolute error of the compensation of the influence of the cold-junction temperature versus the cold-junction temperature for the Cu100 RTD connected as R_t and the bridge circuit fed from a voltage source is plotted in Fig. 3.22a and for the bridge circuit fed from a current source is presented in Fig. 3.22b.

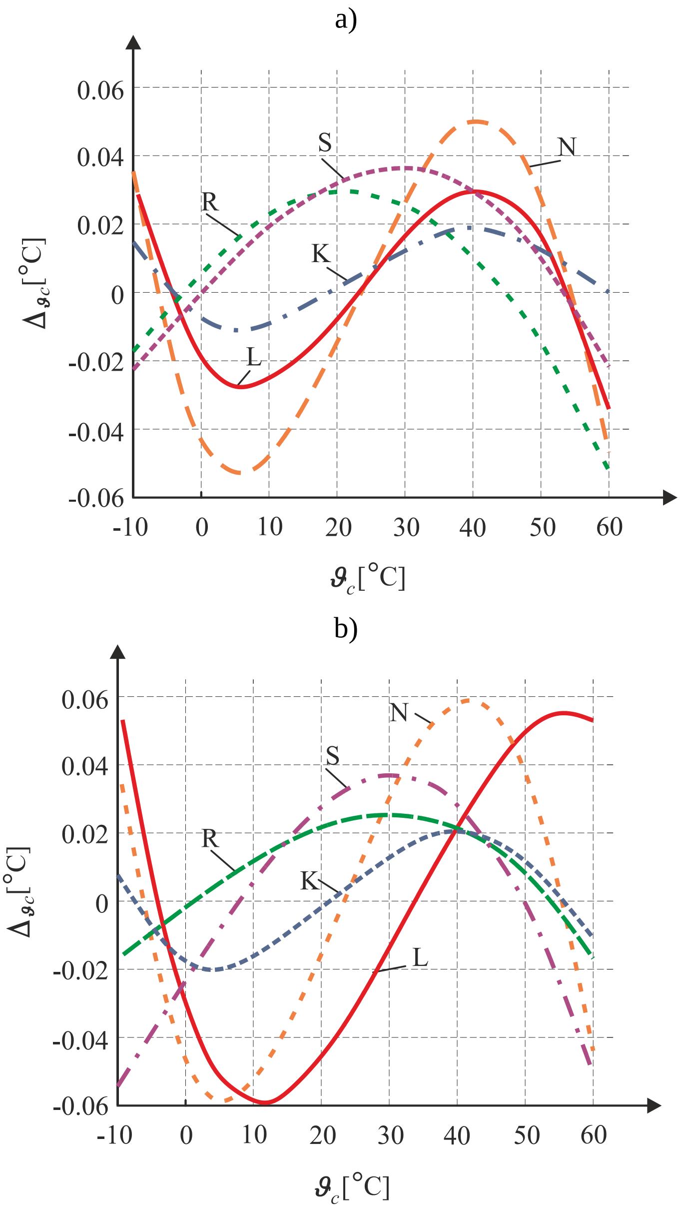

Figure 3.22. Relationships between the absolute error of the compensation of the influence of the cold-junction temperature and the cold-junction temperature for the bridge circuit fed (a) from a voltage source and (b) from a current source, for the Cu100 RTD and for various types of the thermocouples

From the analysis of the plotted relationships between the absolute error of the compensation of the influence of the cold-junction temperature and the cold-junction temperature (Figs. 3.20, 3.21, and 3.22), it can be seen that the abovementioned circuit (Fig. 3.19) ensures the reproducibility of thermo-emf of a cold-junction with an error less than 0.06°C for various types of thermocouples.

The reproducibility errors of the thermo-emf of cold-junction for Pt100 and Cu100 RTDs within the investigating temperature range are equal. Therefore, while designing the compensating circuits the Cu RTDs can be applied, since they are at lower cost than Pt RTDs and nevertheless, good enough to ensure the required metrological characteristics over the cold-junction temperature range –10°C…60°C. For driving the bridge circuit, both a voltage source and a current source can be applied, because in both cases the same compensation accuracy is achieved. In the case of long lead wires connecting the supply source to the bridge circuit, the current source should be employed.

3.2.5. Compensation of the influence of the cold-junction temperature and linearization of the thermocouple transfer function in multichannel temperature measuring devices

In many investigations of thermal processes, e.g. heat spreading in the tooth root, a set of thermocouples is used [64, 168]. In this case, the multichannel measuring devices are employed. Their accuracy depends on cold-junction temperature and nonlinearity of the emf versus temperature relationship.

The compensation of the influence of the cold-junction temperature can be either individual, in groups or general. In the case of the same type of thermocouples being used, the general compensation for all thermocouples should be done.

The structural scheme of a multichannel temperature-measuring device intended for performing the general analogue compensation of the influence of the cold-junction temperature change is shown in Fig. 3.23.

The temperatures of the cold junctions of the thermocouples and of the resistance temperature sensor R_ϑ of the compensating circuit are equalised by a temperature equilibrator. The negative legs of the thermocouples are connected at a common point and to the compensating circuit. The positive legs are connected separately to the inputs of the multiswitch. To the *i*-th input of the multiswitch, the following voltage is applied:

$$U_i = e_i(\vartheta) + U_c, \qquad (3.30)$$

where $e_i(\vartheta)$ is the emf of the *i*-th thermocouple, and U_c is the output voltage of the compensating circuit, i=1, ..., n; n – the number of thermocouples.

The voltage U_i is passed from the multiswitch to the input of the voltage amplifier. The amplifier's output voltage is equal to:

$$U_{a\,i} = k_a\left[e_i(\vartheta) + U_c\right], \tag{3.31}$$

where k_a is the transfer coefficient of the voltage amplifier.

At the digital output of the analogue-to-digital converter, the following code N_i is formed:

$$N_i = k_a k_c\left[e_i(\vartheta) + U_c\right], \tag{3.32}$$

where k_c is the conversion coefficient of the ADC.

Choosing certain values of k_a and k_c, one can establish the equivalence of the output code of the ADC to the value of the measured emf of the thermocouple.

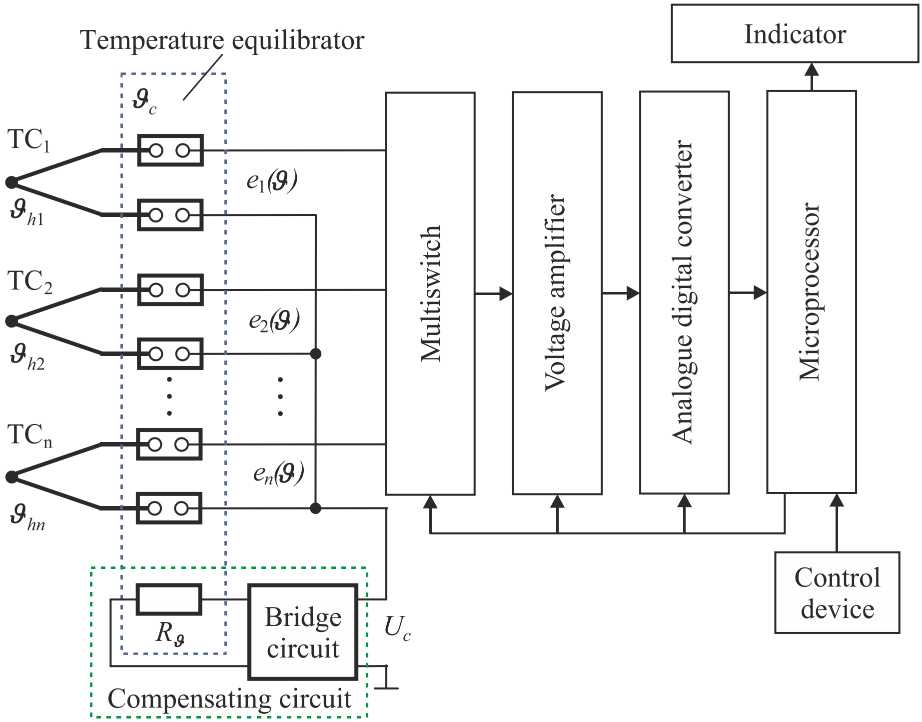

Figure 3.23. Structural scheme of a multichannel temperature measuring device

The output codes of the ADC are passed to the input of the microprocessor, which averages the results N_j of the conversion of the ADC at every channel, in order to reduce the normal noise:

$$N_{iav} = \frac{1}{m}\sum_{l=1}^{m} N_{il} \ , \qquad (3.33)$$

where N_{iav} is the output average code of the microprocessor, and m is the number of the measured values at every channel, l=1, ..., m.

The relationship between the output voltage of the thermocouple and the temperature is nonlinear. The linearization of the conversion function can be done in either analogue or digital form [97].

The analogue linearization can be done by changing the conversion function of the amplifier over certain conversion ranges. The use of an electronic circuit for linearization may add temperature drift.

For digital linearization, the calibration tables or functions approximating the table values, or neural networks should be used for determining the temperature value corresponding to the measured thermocouple voltage. The application of the calibration tables requires a large memory capacity for their storing. The size of the look-up table stored in the memory of microprocessor increases with the accuracy of the stored data. The use of the high power polynomials can negatively affect the measurement accuracy. Because of this, the piecewise-linear approximation is preferred. In this case, the error of nonlinearity depends on the thermocouple type and the temperature measurement range.

The equivalent temperature code N_{ϑ} is determined from the following expression:

$$N_{\vartheta} = k_{Lj} N_{iav} + a_{Lj} \ , \qquad (3.34)$$

where k_{Lj}, a_{Lj} are the multiplicative and additive coefficients of linearization (resp.), for certain temperature ranges.

The coefficients k_{Lj}, a_{Lj} are determined from the condition which requires the approximation function to pass through the endpoints of the linearization interval. The coefficients can be calculated from the following equations:

$$k_{Lj} = \frac{\vartheta_{2j} - \vartheta_{1j}}{k_a k_c (e_{2j} - e_{1j})\left(e_{2j} - e_{1j}\right)} \ , \qquad (3.35)$$

$$a_{Lj} = \vartheta_{1j} - \frac{\vartheta_{2j} - \vartheta_{1j}}{e_{2j} - e_{1j}} e_{1j} \ , \qquad (3.36)$$

where ϑ_{1j}, ϑ_{2j} denote the lower and upper endpoint values of temperature of the j-th interval, respectively, and e_{1j}, e_{2j} denote the initial and final emf of the j-th range of the thermocouple, respectively. The number of the approximation intervals is chosen according to the tolerated error of the measurement for a given type of thermocouple.

The microprocessor sets the given interval after checking the conditions: $\vartheta_{1j} \le N_{iav} \le \vartheta_{2j}$, and calculates the value of the temperature from the expression (3.34) using appropriate coefficients k_{Lj}, a_{Lj}, which are saved in the memory of the microprocessor and can be set from the control device.

In this case, the error of nonlinearity of temperature approximation in a given range is equal:

$$\Delta_{\vartheta n} = \frac{\vartheta_{2j} - \vartheta_{1j}}{e_{2j} - e_{1j}}\left(e_{rj} - e_{1j}\right) + \vartheta_{1j} - \vartheta_{rj}, \qquad (3.37)$$

where ϑ_{rj}, e_{rj} are the true values of the temperature and the emf of the thermocouple, respectively.

The relationship between the error of nonlinearity of the temperature piecewise-linear approximation and the temperature for K-type thermocouple, for 8 equal intervals and the temperature change from 0 to 800°C, is graphed in Fig. 3.24.

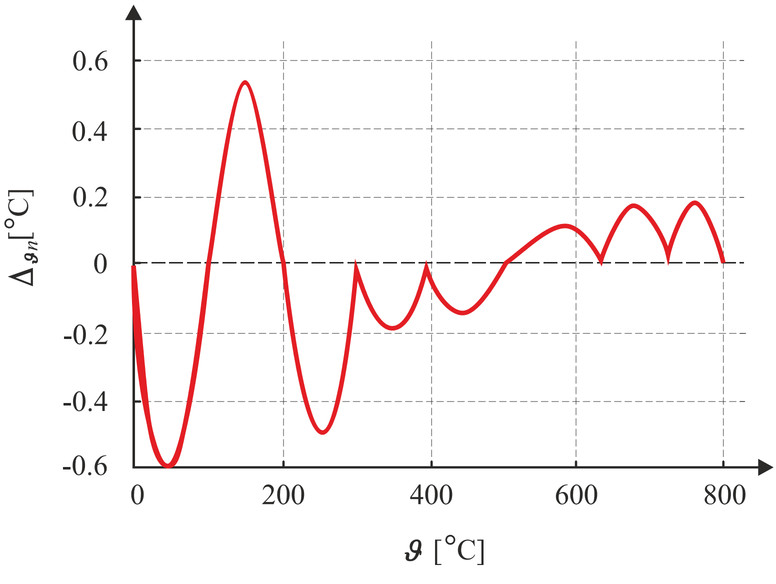

Figure 3.24. Error of nonlinearity of the temperature approximation vs. temperature for K-type thermocouple for 8 equal approximation intervals and the temperature range from 0 to 800°C

In order to improve the accuracy, the number of intervals within the temperature range with the highest error can be increased. The error of nonlinearity of the temperature piecewise-linear approximation vs. the measured temperature for K-type thermocouple for a doubled number of intervals (6 intervals) within the temperature range from 0 to 300°C is plotted in Fig. 3.25.

As it can be seen from the plots (Figs. 3.24 and 3.25), the piecewise-linear approximation of the conversion function of the thermocouple ensures the error of nonlinearity over the temperature range from 0 to 800°C less than 0.6°C for 8 equal approximation intervals, and less than 0.2°C for 11 intervals (6 intervals for temperatures from 0 to 300°C, and 5 intervals for temperatures from 300°C to 800°C).

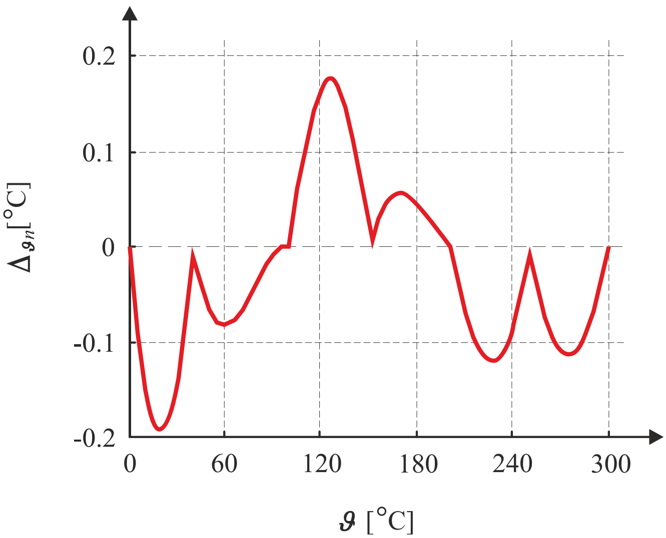

Figure 3.25. Error of nonlinearity of the temperature piecewise-linear approximation vs. temperature for K-type thermocouple for 6 intervals within the temperature range from 0 to 300°C

Summary

Thermocouples are the most popular temperature measurement transducers available. Because of their low cost and wide acceptable range of temperature measurement, one can employ thermocouples for a variety of applications in all industry fields. The cold-junction temperature of a thermocouple influences its measurement accuracy, especially in measurements of low temperatures. One of the more popular methods for eliminating the cold-junction temperature influence is the application of compensating circuits which form the voltage equal to the thermocouple voltage at cold-junction temperature but of opposite sign. The bridge compensating circuits fed from voltage or current source are mostly used. In this case, in order to compensate the influence of the cold-junction temperature, the equality of the cold-junction temperature and the compensating circuit temperature-dependent components should be ensured. The application of thin film technology for manufacturing process of the temperature-dependent resistance bridge circuits considerably increases the accuracy of the equalisation of the temperatures of the cold junction and the temperature-dependent resistors. If the compensating circuits based on resistive thin-film temperature sensors with both positive and negative TCR are employed, the error of the compensation of the cold-junction temperature is less than 0.15°C. The improvement in accuracy of reproducibility of the thermo-emf of thermocouples over a wide range of cold-junction temperature changes can be obtained using the temperature-dependent voltage source for bridge circuit supply. For the design of the temperature-dependent voltage sources, various resistive and semiconductor components can be employed. For example, if semiconductor transistors are employed, the absolute error induced by the influence of the cold-junction temperature change is less than 0.07°C for various types of thermocouples. Similarly, the compensating circuits with the temperature-dependent supply sources based on semiconductor diodes exhibits an error less than 0.06°C, and temperature-dependent resistors with operational amplifier ensure the error less than 0.04°C for different types of thermocouples.

In order to increase the effectiveness of the compensating bridge circuits over the wide range of cold-junction temperature change, also a circuit with additional temperature-dependent voltage divider can be proposed. An exemplary circuit comprising the Pt100 ensures the reproducibility of thermo-emf of a cold-junction with an error less than 0.06°C for various types of thermocouples. The same accuracy is also achieved for less expensive RTDs made of copper.

The nonlinearity of the output characteristic of the thermocouple also influences the measurement error. For example, the proposed piecewise-linear approximation of the transfer function of the thermocouple ensures the error of nonlinearity over the temperature range from 0 to 800°C less than 0.6°C for 8 approximation intervals, and less than 0.2°C for 11 intervals (6 intervals for temperatures from 0 to 300°C, and 5 intervals for temperatures from 300 to 800°C).

4. Fibre-optic temperature sensors

Conventional electric temperature sensors such as thermocouples, RTDs or thermoresistors are low-cost solution for majority of industrial measurement tasks. Nevertheless, they cannot meet some more demanding conditions, like:

- extremely high or low temperatures,
- the presence of high voltages or strong magnetic fields,
- harsh environment (aggressive chemicals, explosive substances sensitive to sparking,
- low mass,
- small dimensions (e.g. required in spacecrafts), etc.

In such cases, conventional electric temperature sensors can be replaced by more sophisticated, modern fibre-optic temperature sensors [16, 82, 166, 195].

The onset of fibre optics technology has begun with the invention of maser in 1953, which evaluated into optical maser, known as laser (1960). Shortly after the modern low-loss optical fibre was developed (1966), the era of fibre optic telecommunications has been opened. A few years later, in early 1970s, the first research on sensing applications of optical fibres has been started (although the first fibre optic sensor patent was filed in 1963 [153], and granted in 1967 [45]).

Up-to-date, optical fibre based techniques and sensors can deal with difficult measurements in some important niche areas, where conventional sensors do not fit. Such position of fibre-optic sensors is due to their numerous advantages [84, 141, 211, 225, 270, 274]:

– galvanic isolation,

– electromagnetic interference immunity to interference from external electric and magnetic fields,

– intrinsic safety laser power falls below the levels that can cause ignition,

– small size and lightweight, compactness,

– possibility of integrated telemetry: remote, multiplexed operation, the fibre itself is a data link,

– wide frequency bandwidth, larger than in the case of electric sensors,

– high sensitivity,

– no moving parts,

– immune to vibrations,

– design lives of 30 years and more,

– data transmitted in an optical format, no shielding required,

– savings in space and weight (aircrafts and spacecrafts),

– can withstand extreme temperatures better than electrical cables,

– robust to the presence of aggressive chemicals,

– provide perfectly separated electric potentials (e.g. in petrochemical installations), high electrical isolation of use in lightning protection, high-voltage and medical applications,

– biocompability, minimally invasive against surrounding tissues *in vivo*,

– can survive in different environments (e.g. stringent radiation test),

– main characteristics remain unaltered with high radiation doses: application in nuclear industry,

– high- and low-temperature capabilities,

– compatible with other optical devices,

– fibre-optic cables can be installed in the same cable tray with power cables, lowering installation costs,

– no electronics or power is required at the remote sensing point.

The drawbacks of the fibre-optic sensors are low mechanical strength of lightguides, the difficulties in launching light into the single-mode fibre lightguide, and the nonlinearity of the transfer functions.

At present, the fibre-optic temperature sensors are employed not only in medicine and biological investigations, but also in the conditions with aggressive vapours or potentially explosive gas mixtures, in the areas of high radioactivity and strong electromagnetic fields. These applications are connected with the possibility of separating the primary transducers from the secondary transducers by transmission lines of optical information over long distances. This allows the user to avoid placing the supply sources and other electronic devices in abovementioned areas. In this case, the system of optical signal transmission can include the amplifiers and other active elements of the optical path.

Over forty years of investigating and developing a variety of fibre optic sensing devices allow the users to measure with them most of basic mechanical, electrical, biomedical, and chemical quantities [187], such as: temperature (e.g. distributed sensing in rooms, hallways, offices), relative humidity, pressure, refractive index, displacement (e.g. in hydrophones), stress and strain, vibration, sound, flow, electric current, magnetic field, pH; blood glucose level, blood oxygen concentration, gas concentration (e.g. hydrogen sensing), blood CO_2 value. Moreover, such sensing devices can monitor creep and thermal stresses (in concrete or steel constructions), or detect onset and growth of cracks in civil engineering structures (non-destructive evaluation technique (NDE)) [161, 222].

The fibre-optic sensors of various physical quantities, including temperature, can be classified according to different criteria. Most popular is the sub-division into intrinsic (or direct) and extrinsic (or indirect) sensors; sometimes the third type, i.e. hybrid [254], is distinguished.

In the case of an intrinsic sensor, a part of the optical fibre interacts actually with the quantity to be measured, and one or more of the physical properties of the fibre undergo a change (Fig. 4.1). In extrinsic sensor, the sensing element (transducer) which is directly affected by the measurand, is external to the fibre. The sensing takes place outside the fibre which serves simply for coupling the light beam with the transducer where the light is influenced by environmental signal (Fig. 4.2).

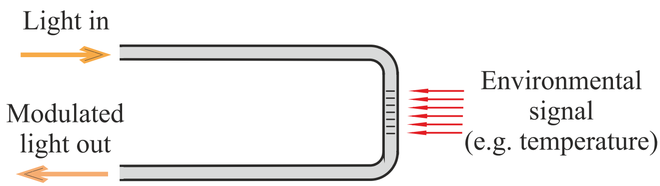

Figure 4.1. Fibre optic intrinsic sensor with Bragg grating

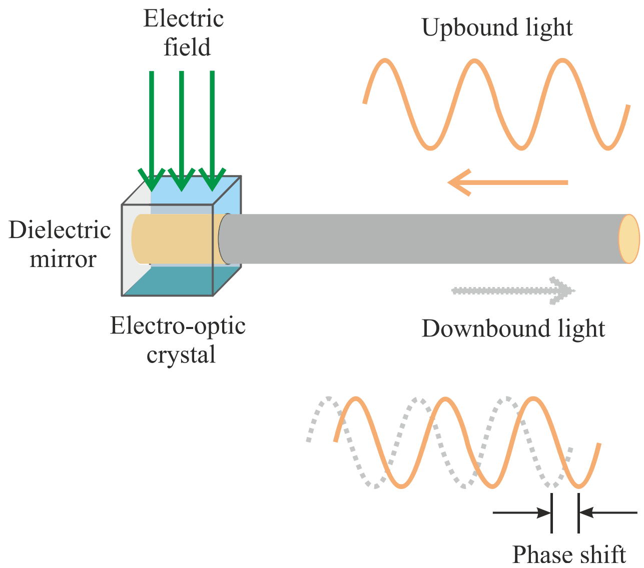

Figure 4.2. Fibre optic extrinsic sensor with electro-optic crystal

Another practically relevant classification is the subdivision of optical sensors into transmission and reflection sensors. The transmission sensors (Fig. 4.3) exhibit simpler structure because there is no need to use couplers for separating the forward and backward travelling light, which are necessary in the case of reflection sensors (Fig. 4.4). On the other hand, reflection sensors require access to only one of the optical fibre, which is more convenient design [195].

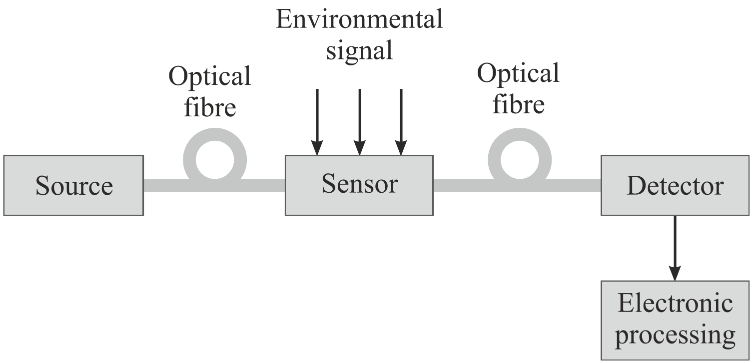

Figure 4.3. Fibre optic transmission sensor

Depending on the number of measurement points of a sensor system, three categories are distinguished. A point sensor is dedicated to a particular location; as a rule, only the fibre tip is sensitised, like in conventional sensors. An intrinsic distributed sensor can sense the distribution of the whole fibre, and a quasi-distributed sensor supplies the information collected at particular pre-determined points along the length of the fibre; then, the sensitised regions of the fibre are distributed in discrete pattern [82].

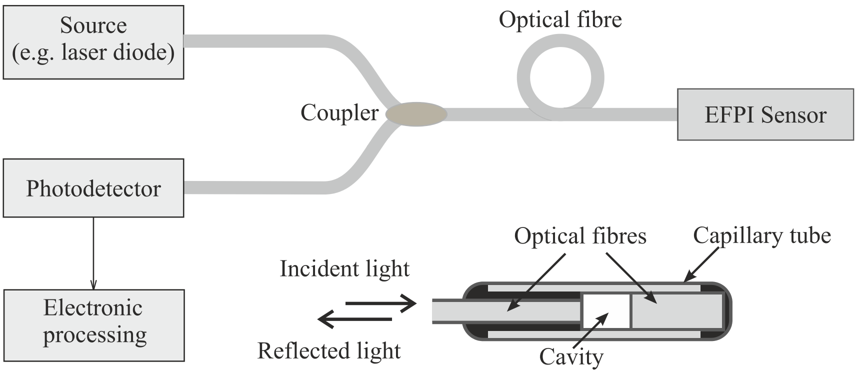

Figure 4.4. Fibre optic reflection sensor based on Fabry-Perot interferometer

The classification based on the light modulation and demodulation process distinguishes the amplitude (intensity) sensors, the phase sensors, the frequency sensors, and the polarisation sensors. The intensity sensors are incoherent and have simple design. The phase or frequency sensors demand optical interferometric technique of coherent detection; they have more complex construction, but better resolutions and sensitivities are achievable.

Depending on the physical principle of measurement, the following types of sensors for fibre optic temperature sensing are used [254]:

- the intrinsic temperature sensors, which in turn divide into:

- point measurement sensors: blackbody sensors, and interferometric sensors;

- distributed measurement sensors: Rayleigh scattering-based sensors, Raman scattering-based sensors, Brillouin scattering-based sensors, fibre Bragg grating-based sensors, and long-period grating-based sensors;

- the extrinsic temperature (point measurement) sensors, which can also be divided into: fluorescence-based (or lifetime-based) sensors, evanescent-type sensors, fibre optic pyrometers.

In the following sections, the most distinctive features of most of the dominant types of fibre-optic temperature sensors will be characterised. Some information on the photonic crystal fibre temperature sensing is also given.

4.1. Blackbody fibre optical thermometers

One of the niche areas where fibre optical thermometers (called also optical fibre thermometers, OFTs) compete successfully with conventional electric sensors, are the measurements in high temperature environments. The blackbody OFTs are devices design for very-high temperature measurements wherein the blackbody radiation physics can be utilised [140].

A typical blackbody OFT consists of a high-temperature optical fibre made of sapphire, of the diameter of tens μm. At the end of the fibre, a sensing tip is formed in the shape of a small (sharpened, cut at a 45^{o} angle) opaque isothermal cavity, covered with a refractory (e.g. iridium) metallic coating. The radiative flux emitted from the cavity is approximately equal to the emission from a blackbody, and related to the absolute temperature inside the cavity via Planck's law. At the other (flat) end face of the sapphire fibre, a detection system is processing the spectral radiative flux from the cavity (Fig. 4.5).

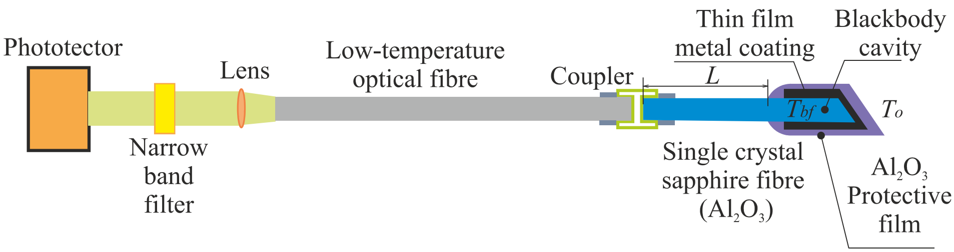

Figure .4.5. Typical configuration of a radiation-based sensor system

Despite of the thin film metallic coating and a sapphire cap on the tip, in temperatures above 1500^{o}C the impurities in the environment around the probe result in contamination and corrosion of the surface of the sapphire fibre. That causes scattering loss to the fibre. Another source of unstable optic losses is the coupler which splices the sapphire fibre with the low-temperature silica fibre.

The scheme in Fig. 4.5 illustrates the measuring circuit (arrangement) of the single-band method, which directly determines temperature T_0 by the intensity of one radiation signal. The low-temperature silica fibre is coupled through a lens and a narrow-band filter to a photodetector, which converts the radiation into an electrical signal. Because the equation relating the spectral intensity at the end of the fibre to the temperature of the sensing tip neglects the self-emission by the sapphire fibre, the measured temperature T_b is greater than the actual temperature T_0. The losses resulting from the contaminated surface of the sapphire fibre and from the coupler affect the measuring accuracy of the single-band method.

More accurate (but more costly) is the dual-band method (not depicted in Fig. 4.5), which determines the temperature T_b by the ratio of two radiations transmitted through the same optical arrangement.

The accuracy of the single-band method can be improved, if two measurements are made at two wavelengths λ_1 and λ_2. The estimated temperature T_b is expressed by the formula [138]:

$$T_b = \frac{c_2\left(\dfrac{1}{n_2\lambda_2} - \dfrac{1}{n_1\lambda_1}\right)}{\ln\left[\left(\dfrac{n_1}{n_2}\right)^2\left(\dfrac{\lambda_1}{\lambda_2}\right)^5 \dfrac{M_{e\lambda 1}\beta_{\lambda 1}e^{t_{\lambda 1L}}}{M_{e\lambda 2}\beta_{\lambda 2}e^{t_{\lambda 2L}}}\right]}, \tag{4.1}$$

where n_1 and n_2 are the refractive indices of the fibre at the wavelength λ_1 and λ_2, c_2 is radiation constant from Planck's law, $c_2 = hc/k_b$, $\beta_{\lambda 1}$ and $\beta_{\lambda 2}$ are calibration factors, $M_{e\lambda 1}$ and $M_{e\lambda 2}$ are the outputs from the detector, and $t_{\lambda 1L} = K_{a\lambda 1}L$, $t_{\lambda 2L} = K_{a\lambda 2}L$ are the optical depths of the fibre for the respective absorption coefficients $K_{a\lambda 1}$ and $K_{a\lambda 2}$ of the sapphire fibre.

Sapphire, which is an allotrope of aluminium oxide Al_2O_3, is rather uneasy material to deal with; however, silica fibre-based temperature sensor cannot work above 1000°C because of degradation of mechanical strength and the thermal out-diffusion of the germanium dopant. The right choice is a crystalline optical fibre, owing to compact size and very good optical and mechanical properties at elevated temperature [266]. Especially single-crystal fibres are preferred; a zirconium single-crystal fibre sensor is reported to operate at 2300°C, and Yb-doped single-crystal YAG optical fibre sensor can withstand 1600°C. The single-crystal sapphire fibre exhibits high melting point, ca. 2050°C, and is chemically inert, but its integration with silica fibre based systems is difficult [187].

4.2. Fibre-optic temperature sensors based on fluorescence lifetime measurement

The concept of optical fibres doped with materials possessing luminescent properties has emerged in the early 1960s, but then it was oriented on laser applications.

At present, most popular type of such sensors are fluorescence-based temperature sensors [187, 230]. Fluorescence is a form of photoluminescence; it happens when a substance has absorbed electromagnetic radiation [260]. A molecule, ion or atom of that substance has been promoted from the state of its lowest energy (ground state) to a state of higher energy (excited state). Then, the excited entities undergo a radiative transition to lower (usually ground) state, and a fluorescence emission is produced [55]. This is the operation principle of many intrinsic sensors based on rare-earth-doped fibres, e.g. fibres containing erbium, thulium, holmium, neodymium, praseodymium, or ytterbium. In commercial applications, most common are temperature sensors based on fluorescence decay in erbium-doped fibre (EDF).

The EDF sensor is placed into the oven inside a quartz sheath, and excited in the 800-nm region. For example, the 980-nm laser pump beam is launched through a plain optical fibre into Er-doped piece of fibre, via a wavelength division multiplexing coupler. Thus, the $^4I_{11/2}$ erbium level is excited, and the metastable erbium level $^4I_{13/2}$ is quasi-instantaneously populated due to the non-radiative transition. Then the population inversion between these levels occurs, and a fluorescence emission at around 1550 nm takes place. If the Er-doped fibre is pumped at a fixed rate, the fluorescence variations of lifetime reflect the changes in temperature. The lifetime is linear function of temperature with negative slope of approximately 9 μs/°C, which is the sensor's sensitivity within the 0÷200°C range. The lifetime reduction with temperature is attributed to the quenching of the erbium luminescence. The excitation becomes less efficient, and thus the absorption coefficient of erbium ions falls with temperature; therefore, the sensitivity decreases if the measurement temperature range is shifted towards higher temperatures [271].

An example of extrinsic fibre-optic temperature sensor based on the crystal of ruby is shown in Fig. 4.6. Crystalline ruby is Cr^{3+} (0.35 wt %) doped Al_2O_3 [4], and therefore it can be easily coupled mechanically with sapphire fibre (also, an allotrope of Al_2O_3) which exhibits very good transparency at the near IR-region. The operation principle is similar as for the EDF sensor: first, the crystal is pumped with an excitation pulse of 520 nm, and then the fluorescent emission of 698 nm takes place, so both excitation (green) and radiation (red) occur within the visible spectrum [134].

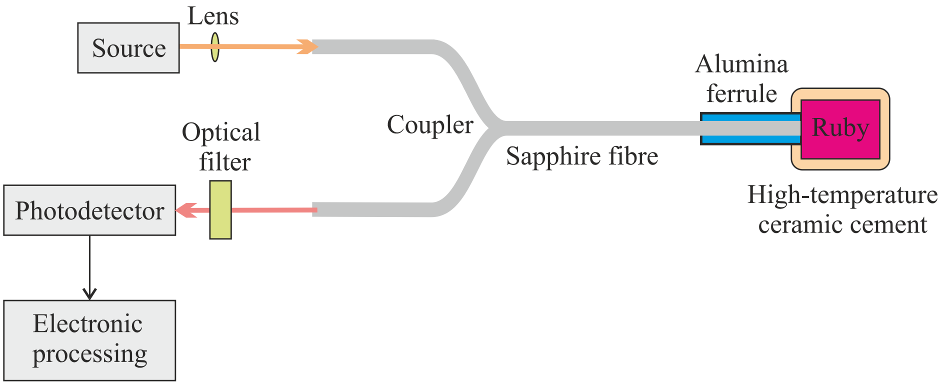

Figure 4.6. Schematic of fibre optic high temperature measuring system using ruby sensor head [3]

For lower temperature ranges (below 500 K), the most commonly found type of fluorescence decay, namely exponential dependence on time is valid:

$$J(t) = J_0 e^{-\frac{t}{\tau_0}}, \tag{4.2}$$

where $J(t)$ is the fluorescent radiation intensity at time t after the termination of the exciting radiant energy, J_0 is the fluorescent radiation intensity at t=0, and τ_0 is the lifetime of fluorescence decay at a given wavelength. For the ruby crystal-based temperature sensor, above ca. 500 K a second exponential component of faster fluorescence decay appears in the equation, which becomes double exponential:

$$J(t) = J_0 e^{-\frac{t}{\tau_0}} + J_1 e^{-\frac{t}{\tau_1}}, \tag{4.3}$$

where J_1 is the faster fluorescent radiation intensity component at t=0, and τ_1 is the lifetime of faster fluorescence decay component.

4.3. Interferometric fibre-optic temperature sensors

Although the main configurations of bulk-optic interferometry systems have been developed over a century ago, they are still very attractive for their exceptionally high accuracy of displacement sensing. From the early 1970s, several fibre-optic equivalents of bulk-optic interferometers are available, including the Michelson, Sagnac, Mach-Zehnder, and Fabry-Perot interferometer. Among them, the Sagnac interferometer implementation as a fibre-optic gyroscope (FOG) offers the sensitivity better than 10^{-7} radians [45]. The dual-path interferometers like Mach-Zehnder are easier to implement, but less accurate. For temperature sensing, the Fabry-Perot interferometer is preferable, as the most versatile, because of it extremely high spectral resolving power $\lambda/\Delta\lambda$ up to 10^7 for an optical wavelength λ [227].

An optical fibre itself can be exploited as a temperature sensor because it exhibits the thermo-optic effect. This effect is described by the thermo-optic coefficient which comprises two components. The major component accounts for the change of the refractive index of a fibre with temperature rise; the minor contribution is from the thermal expansion of the fibre. The resultant change in optical patch due to the rise of the fibre temperature is around 30-40 ppm/K for silica-core fibre [195].

The Fabry-Perot interferometry-based temperature sensors are realised in both extrinsic (EFPI) [66] and intrinsic (IFPI) implementations [225] (also, miniature EFPI, i.e. MEFPI, are reported [267]). In each case, the change in temperature to be measured should be converted into a change in optical thickness of a portion of the optical path.

In EFPI-based temperature sensors, a low-finesse Fabry-Perot cavity is formed outside the fibre [15], inside a thin silicon chip attached to the polished end face of a fibre. The opposite surface of the silicon chip is also polished and may be covered with metallic film for better reflection. The light travelling from a monochromatic source down the optical fibre partially reflects off on the optical interface fibre end/silicon chip. The remained amount of light arrives to the opposite face of the chip and then partially reflects off on the optical interface chip/air.

Passing back through the fibre, the reflected beams of light interfere with one another. The resulting interference pattern of fringes produced by constructive interfering beams is detected, and converted into an electrical signal. The signal can be demodulated to allow measuring the gap between the two interface surfaces acting as mirrors. The measured gap is equal to the thickness of the chip multiplied by its temperature-dependent refractive index. For high temperature measurement, the silica optical fibre would be replaced with a sapphire fibre [252], and the silicon chip with a sapphire wafer [276] or a silicon carbide chip. This would allow extending the range well above 1000^0C.

The technique of the temperature measurement using an intrinsic Fabry-Perot interferometer (IFPI) [167] is much the same as EFPI [233], only the Fabry-Perot cavity is inserted within the fibre. For this purpose, the fibre is cleaved, and the ends are coated with a thin dielectric or metallic coating. Then the end-coated fibres are fused to a portion of the fibre of the length L of the order of tens times fibre's diameter, producing two in-fibre reflective splices.

Some authors distinguish also the in-line fibre Fabry-Perot etalon based on Fabry-Perot interferometer [82]. In that design, the two parts of a cleaved fibre are fusion spliced to a section of a hollow-core fibre, a micro-tube, of the same outer diameter. This type of sensor is applied in order to monitor concrete or composite construction, especially for strain and temperature analysis.

The need of clear discrimination of strain and temperature contribution to the resulting phase-shift of the FP interferometer technique is met by strain- and pressure-free housing design of the temperature sensor, or a reference sensor is placed in a fixed temperature. The latter solution was adopted in classical dual-Fabry-Perot sensor, where one fibre Fabry-Perot interferometer was exposed to the temperature to be measured [167]. With respect to the light fed into the Fabry-Perot sensing element, the system can be configured for white light interferometry (or, more correctly, low-coherence interferometry) which allows the user to analyse the full reflectance spectrum to determine the absolute optical path difference, or for laser-based coherent light interferometry which relies on fringe counting.

A Fabry-Perot interferometer contains two exactly parallel planar reflecting surfaces (mirrors) separated by a distance L (e.g. 500÷1000 nm) [15]. The multiply reflected beams from the two reflecting surfaces interfere within the resonator cavity. The reflectance of the resonator is a strong function of wavelength and the optical length, nL, where n is the index of refraction of the medium between the two reflecting surfaces. The phase difference between two successive beams transmitted from the Fabry-Perot interferometer is given by:

$$\Delta\Phi_0 = \frac{4\pi v n L}{c}, \tag{4.4}$$

where v is the optical frequency, n is the unperturbated value for the effective refractive index of fibre mode, and c is the free space velocity of light.

A dual Fabry-Perot interferometry system belongs to tandem interferometry. The light source is a LED of low coherence, and the coherence length close to optical path difference between the Fabry-Perot interferometers. The spectral characteristics of the LED source are assumed to be Gaussian. The light from the LED passes through a fibre coupler into the sensing Fabry-Perot interferometer exposed to the change in temperature. The LED light is spectrally modulated in reflection inside the sensing interferometer, which acts as a spectrally selective reflector. This reflected light is, in turn, passed upon the reference Fabry-Perrot interferometer, and partly transmitted to a power meter, whereas the reflected light is detected with a photodetector module.

The sensing Fabry-Perot interferometer is assumed to be of a low-finesse type, i.e. the reflectances of its two mirrors R_s are equal and much less than 1. The same is assumed for the reference Fabry-Perot interferometer: R_r<<1. The phase shift $\Delta\Phi_p$ induced by the temperature change, adds to the shift $\Delta\Phi_0$; so the total phase shift in the sensing interferometer: $\Delta\Phi_s=\Delta\Phi_0+\Delta\Phi_p$. Next important assumption is that in the absence of temperature change, the sensing and reference interferometers are identical (i.e., their optical path lengths are equal).

Then the spectral power density of the power P_{Rr} reflected from the reference interferometer is equal to [167]:

$$\frac{dP_{Rr}}{dv} = 4R_s R_r \alpha_\gamma \frac{dP_{Is}}{dv}\left(1-\cos\Delta\Phi_0\right)\left(1-\cos\Delta\Phi_s\right), \tag{4.5}$$

where α_γ is a constant that represents optical losses on the path between the sensing and reference interferometers, and $dP_{Is}/d\nu$ is the spectral power density of the power dP_{Is} incident on the sensing interferometer.

After performing the integration over v under some simplifying assumptions, one obtains [167]:

$$P_{Rr} = 4R_s R_r \alpha_\gamma P_{Is}\left(1+0.5\cos\Delta\Phi_p\right). \tag{4.6}$$

This result shows that the power P_{Rr} reflected from the reference interferometer is a cosinusoidal function of the phase shift $\Delta\Phi_p$ introduced by the temperature change.

The reflectance spectra of both interferometers give a product which fringes location depends on the phase shift $\Delta\Phi_p$. That means that the sensing interferometer's output frequency spectrum of the light is modulated by the reference interferometer, and only then passed to the photodetector. From the formula (4.6) it can be inferred that P_{Rr} changes between the P_{max} value for $\Delta\Phi_p=2m\pi$ and the P_{min} value for $\Delta\Phi_p=(2m+1)\pi$, where m is an integer, $m=0, \pm1, \pm2, \ldots$. The visibility of the interference pattern is defined as [90]:

$$V_p = \frac{P_{\max} - P_{\min}}{P_{\max} + P_{\min}}. \tag{4.7}$$

Substituting the values of P_{max} and P_{min} for the discussed dual Fabry-Perot interferometer temperature sensor, one can obtain $V=0.5$ as the maximum ideal value of fringe visibility. For an experimental setup, the sensitivity of 1.57 rad/^{o}C has been achieved, and a linear relationship between the temperature and the phase shift was established for the temperature range 26÷108^{o}C; the respective phase interval was 40π radians (approximately a 2^{o}C change in temperature produced a π-radian half-fringe phase shift in the interference pattern [167].

The advantages of the Fabry-Perot interferometric sensors, such as high values of sensitivity, resolution, and accuracy still encourage the researchers for developing improved designs [162, 169]. An arrangement of a novel fibre-optic temperature sensor based on the difference between thermal expansion coefficient of fused silica core and metallic cladding is depicted in Fig. 4.7.

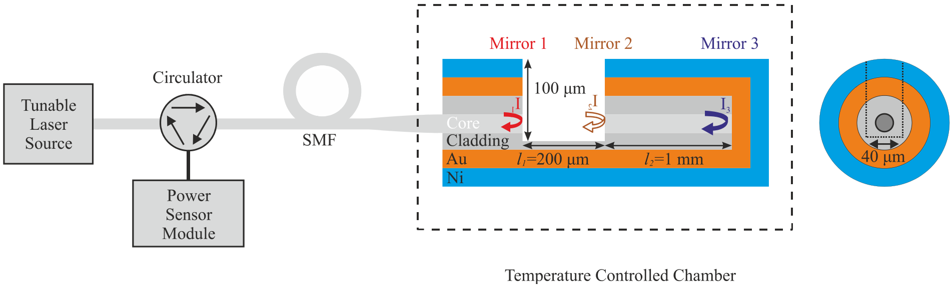

Figure 4.7. Configuration of a fibre Fabry-Perrot interferometric temperature sensor with a micromachined cavity and three mirror surfaces [169]

A detailed analysis shows that the dominant contribution to the modulation in reflection is from the mirror 1 (the interface silica core/air) and the mirror 3 (the reflective coating of gold). The thermal expansion coefficient of gold and nickel is about 20 times above pure silica within the range $-200^{o}C \div 1000^{o}C$. The cavity length changes with temperature, and the induced optical phase shift can be measured by quantifying the changes in the visibility of the interference fringes, using a power sensor module. There are also similar devices designed as cryogenic fibre optic temperature sensors (e.g. [154]).

Generally, the Fabry-Perrot interferometry-based temperature sensors require an analysis of light interference patterns performed with complex, delicate and costly interference analysis equipment [39]. However, the benefits of spectrally encoded signal from the interferometric sensing device are its high reliability and a nearly path-independent transmission along optical fibres over long distances.

4.4. Grating-based fibre-optic temperature sensors

Although diffraction gratings were invented at the end of XVIIIth century, the concept of creating grating into optical fibre emerged only about 30 years ago. After some technological improvements, grating-based sensors have become useful for many applications. Especially promising is the area of distributed sensing with arrays of sensors embedded in materials for creating so-called “smart structures” [222].

Fibre gratings are the most popular topic in fibre-optic sensor technology under investigation: almost half of papers addressing fibre-optic sensors concern this subject, and ca. 20% of them is linked to the temperature measurements [166]. During extensive research on fibre grating sensors, various types of fibre gratings have been developed: uniform fibre Bragg gratings, long-period fibre gratings, chirped fibre gratings, tilted fibre gratings, or sampled fibre gratings [141]. All the non-uniform structures can be tailored for special applications in sensing; but the most widely used type are the uniform fibre Bragg gratings (FBGs).

Grating-based sensors are useful for a variety of applications (e.g. [265]). In particular, the area of distributed embedded sensing in materials for creating "smart structures" is of primary interest.

The first fibre Bragg gratings were developed as laboratory prototype designs in 1978 by Canadian researchers Hill et al., but the real breakthrough was made at the late 1980s, when a new fabrication technique was devised by Meltz et al. [199].

The optical fibre that is to be perturbated by producing periodic variations in the refraction index along a given portion in the core, must be photosensitive. The property of photosensitivity in fibre optic silica (SiO_2) core is due to the germania (GeO_2) doping. The concentration of Ge can be up to 15%, although usually it is 3...5%. Inside the Ge-doped single-moded fibre core, the oxygen-deficient bonds Si-Ge cause the GeO defects in the silica matrix.

The defect bonds can be broken by single-photon absorption of 244-nm UV radiation from an excimer laser. In consequence, modifications in the glass structure can shift the absorption spectrum $\alpha_a(\omega)$. This, in turn, involves a change Δn of the refractive index adequately to the Kramers-Kronig equation [2]:

$$\Delta n(\omega) = \frac{c}{\pi} \int_0^{\infty} \frac{\Delta\alpha_a(\omega) d\omega}{\omega^2 - \omega'^2}, \tag{4.8}$$

where ω and ω' are complex variables unchanged, and changed, respectively.

The absorption shift occurs in the UV region, but the change in the refractive index can occur in the visible region, or even in the IR region. In the portions of the core where UV absorption takes place, an index grating appears as a periodic pattern of the UV radiation intensity. Typically, within the range from 1300 nm to 1600 nm, Δn is equal ca.10^{-4}, but for high Ge concentration it can attain 10^{-3}; unfortunately, this involves increased splice loss.

Another technique for enhancing the change Δn of the refractive index up to 10^{-2}, invented in 1993, is to soak the fibre in molecular hydrogen gas at 200 atm at room temperature. To preserve the photosensitivity, the fibre is stored at low temperature after the hydrogenation.

Such core material (Ge-doped, or hydrogen-soaked) can be subjected to the UV radiation which etches the grating into the core, either by using interferometric techniques or through a photomask [81]. Chronologically, the first was the single-beam interval technique, in which into the Ge-doped silica core a single beam from an argon-ion laser operating near 488 nm, is launched. Grating formation is started by the light reflected from the far end of the fibre, which propagates backward and interferes with the incident wave radiation. The two waves create a standing wave pattern with periodicity $\lambda/2n$, i.e. laser wavelength divided by double mode index at that wavelength. The initial far-end reflectivity is about 4%, but the light reflected from grating increases the feedback and after a few minutes the strengthened grating ensures 90% reflectivity. Unfortunately, such gratings exhibit the Bragg wavelength near the laser's wavelength, far from the technically important from 1300 nm to 1600 nm region [145].

More flexible is the dual-beam interferometric external technique, invented in 1989, similar to that used for holography, i.e. transverse-holographic method [199]. The radiation from an UV laser is split into two beams, which subsequently recombine at the fibre, the interference pattern of the beams is written through the side of the cladding into the optical fibre core. However, despite of the transverse access to the core, this technique is very sensitive to the alignment of the system, and to ambient vibration. Anyway, it was a breakthrough to use UV pulsed beam, which allows controlling the parameters of the grating by direct side writing, after the fibre's plastic buffer has been temporarily removed. The Bragg wavelength becomes also independent of the type of the writing laser. The reflection wavelength (Bragg wavelength) of the grating is selected by controlling the angle 2θ of incidence between the two interfering UV beams, or by tuning the wavelength of the UV radiation: $\lambda_B=\lambda_i n_{eff}/\sin\theta$, where λ_i is the UV wavelength used to generate the grating, and n_{eff} is the effective refractive index.

The phase-mask technique was first introduced in 1993, and the concept was borrowed from the photolithographic process utilized to fabricate integrated electronic circuits. The substrate of a phase mask is made of quartz or fused silica. A thin metallic layer can be deposited onto the substrate and periodic pattern is etched – or, most recently, femtosecond laser pulses are used for inscription of phase masks [47].

The phase mask plays role of a master grating, which should be transferred to the fibre. The mask is illuminated with the laser light, and the mask's corrugations produce periodic phase change of the light incident on the fibre core. The quality of the master phase mask determines the features of the grating: each mask's imperfection would be reproduced exactly.

The phase mask can also be used in an interferometric arrangement, in which the UV laser beam is incident normally on the phase mask. On the mask's corrugations, diffractive beams in the Raman-Nath regime are created [2]. The beam of direct transmission (the zeroth-order beam) is cancelled or blocked, so that most of the optical power is transmitted with the diffracted beams of the + 1 and −1 orders. These two first-order beams interfere on the fibre, placed very close to the mask (within micrometers), forming an intensity pattern. The period of the interference fringes is a half of the period of the phase mask. Because the fibre and the mask are separated by a very short distance (a few micrometers), the two interfering diffractive beams generated within the phase mask require a spatial coherence of the order of a few tens of micrometers, in order to produce visible interference pattern. The phase-mask method is less sensitive to the laser's beam lateral shift and beam-pointing instability than the dual-beam interferometric technique [2], as well as to vibrations and air fluctuations [84]. There was also a concept of so-called amplitude mask but that device turned out to be of lesser writing efficiency. The benefits of phase-mask fabrication method are exposed in so-called Talbot interferometer [47].

In his experiments, a century ago, William Bragg modelled a crystal as a set of discrete parallel planes, which reflect a beam of light of a selected wavelength. The same phenomenon occurs when a fibre Bragg grating is illuminated by a broadband light source. A set of beams, which differ in wavelength, reflect from a serial arrangement of partially reflecting quasi-planes formed in the fibre core by the periodic refractive index modulation. The reflected beams interfere with each other: most of them destructively, but some beams meet the in-phase condition of constructive interference [222]. The selected wavelength λ_B can be determined according to Bragg's law at normal incidence $\lambda_B=2n_{eff}\Lambda$, where n_{eff} is the effective index of refraction in the core, and Λ is the grating pitch of the index modulation [141]. From this equation it can be seen that the Bragg wavelength λ_B can be changed either with a change in the grating pitch Λ or in the effective refractive index n_{eff}. The Bragg's reflection is a consequence of the coupling resonance between a forward-propagating core mode and its coupled backward-propagating version. If the grating design is of high quality, this reflective coupling exhibits a narrow spectral band, even as small as 0.1 nm (100 pm). It should be noticed that λ_B is the centre wavelength of the reflected band.

Under phase matching conditions, the reflectivity R_B of the "Bragg signal" of a given mode at the centre wavelength λ_B is given by [222]:

$$R_B = \tan h^2 \Omega_B, \tag{4.9}$$

where $\Omega_B = \dfrac{\pi L \Delta n \eta(V)}{\lambda_B}$, L is the length of the grating, Δn is the magnitude of the index perturbation, and $\eta(V)$ is a function of the fibre V parameter that represents the fraction of the integrated fundamental mode density contained in the core (V is called "the normalized frequency of the fibre"). The formula for Ω_B is valid for a cosinusoidal distribution of the refractive index n along the propagation axis z [141]:

$$n(z) = n_o + \Delta n \cos\frac{2\pi z}{\Lambda}. \tag{4.10}$$

The magnitude of the index perturbation Δn is determined by the fibre exposure time and the power of the UV radiation; typically Δn=10^{-5}÷10^{-3}. It is worth noting that R_B increases with L and Δn.

The sensing properties of fibre Bragg gratings are modelled taking into account the change in geometry due to strains ε=$\Delta L/L$ caused by mechanical stress σ or by temperature change ΔT, i.e. the strain-induced change in the refractive index (the photoelastic effect), and the change in the refractive index due to the temperature change ΔT (the thermooptical effect). The resultant change $\Delta\lambda_B$ in the centre wavelength for isotropic and homogeneous properties of a silica fibre is given by [141]:

$$\Delta\lambda_B = 2\left(\Lambda\frac{\partial n_{eff}}{\partial L} + n_{eff}\frac{\partial\Lambda}{\partial L}\right)\Delta L + 2\left(\Lambda\frac{\partial n_{eff}}{\partial T} + n_{eff}\frac{\partial\Lambda}{\partial T}\right)\Delta T \qquad (4.11)$$

$$\Delta\lambda_B = 2\left(\Lambda\frac{\partial n_{eff}}{\partial L} + n_{eff}\frac{\partial\Lambda}{\partial L}\right)\Delta L + 2\left(\Lambda\frac{\partial n_{eff}}{\partial T} + n_{eff}\frac{\partial\Lambda}{\partial T}\right)\Delta T\ . \qquad (4.11)$$

This formula can be rewritten as:

$$\Delta\lambda_B = \lambda_B\left[(1-p_e)\varepsilon + (\alpha_T + \xi)\Delta T\right], \qquad (4.12)$$

where ε is the strain, $\alpha_T = \frac{1}{\Lambda}\frac{\partial\Lambda}{\partial T} = \frac{1}{\Lambda}\frac{\partial\Lambda}{\partial T}$ is the thermal expansion coefficient of the core material, $\xi = \frac{1}{n_{eff}}\frac{\partial n_{eff}}{\partial T}$ is the thermooptical coefficient, and $p_e = \frac{n_{eff}}{2}\left[p_{12} - v_p(p_{11} + p_{12})\right]$, where v_p is the Poisson's ratio and p_{11}, p_{12} are Pockel's (photoelasticity) coefficients.

The temperature sensitivity coefficient of a fibre Bragg grating sensor is equal to:

$$k_{TS} = \frac{\Delta\lambda_{BT}/\lambda_B}{\Delta T} = \alpha_T + \xi\,, \qquad (4.13)$$

and the temperature sensitivity

$$S_{\Delta T} = \frac{\Delta\lambda_{BT}}{\Delta T} = k_{TS}\lambda_B\,. \qquad (4.14)$$

For λ_B=1550 nm (laying within the 3rd transmission window of silica fibres, so called "erbium window"), calculated value is equal to $S_{\Delta T}$=14.2pm/^{o}C.

If the grating is uniform, a precisely defined wavelength from the incident light that is twice the spacing of the periodic index perturbation would be coupled into a reflected beam. This wavelength depends on the optical period of the grating. The grating's optical period is a function of the refractive index of the fibre n, and of the length Λ of the period. Both n and Λ depend on the temperature, the strain, and to a lesser extent on the pressure, acting on a particular fibre core containing an in-fibre Bragg grating. If the fibre is not exposed to changes in these physical quantities, the grating structure with high reflectivity (which can reach almost 100 %) on a selected centre wavelength λ_B and a narrow band around it, behaves as an optical filter [18].

The temperature monitoring FBG systems react on the shift in the Bragg's wavelength λ_B. Under temperature change, the refractive index and the spacing between the grating's index perturbances will change. In consequence, the reflected beam's wavelengths are shifted, especially the centre wavelength λ_B – and the shift in wavelength is proportional to the change in temperature.

As was described above, the temperature response of FBG depends on the value of the thermal expansion coefficient α_T for a given fibre (for the fused silica α_T=0.55·10^{-6}) and the thermooptical coefficient ξ (for the Germania-doped silica core ξ=8.3·10^{-6}) [225].

Around room temperature, the normalized temperature-induced wavelength change is predominantly dependent on the refractive index change (i.e. on ξ) which is about one order of magnitude greater than the effect of thermal expansion (or contraction). The typical temperature response is ca. 6.8 pm/^{o}C near 830 nm ("old" window), ca. 10 pm/^{o}C near 1300 nm (O-window) and ca. 13 pm/^{o}C near 1550 nm (C-window); exact values depend on the type of the FBG [222].

These data confirm the conclusion to be drawn from the formula above that greater temperature sensitivity can be obtained by going towards longer wavelengths.

The fibre-optic grating temperature sensors are relatively short (1 cm or less) uniform period gratings. That short length limits the reflectivity of the FBG temperature sensors.

Multi-point temperature sensing is possible with multiple gratings, multiplexed by an offset in the central reflected wavelength λ_{Bi}, all written into a single optical fibre. To avoid the errors introduced by non-temperature quantities (mainly strain), a reference grating should be placed in isothermal conditions near the sensing FBG [61-62]. The reference grating can be produced inside the same fibre as is the sensing grating [94].

Another technique is to apply chirped grating which allows measuring the temperature and the strain simultaneously. The chirped grating's response to strain gives a broadening of the shift in the Bragg condition, whereas the temperature affects only the location of the central wavelength through the thermooptical coefficient $\xi=(1/n)\mathrm{d}n/\mathrm{d}T$. The independent measurement of temperature and strain requires a careful calibration and measurement of the spectral shift and its broadening [82].

The fibre Bragg grating sensors possess all the advantages of the fibre-optic sensors; moreover, they offer some additional possibilities. Firstly, FBG sensors exhibit an inherent self-referencing capability. The information about the measured quantity (e.g. temperature change) is wavelength-encoded [82]. Therefore, the measurement results are insensitive to fluctuations in the irradiance of the light source, and the direct encoding in wavelength shift provides robustness to noise or losses in the connecting fibres and couples.

Secondly, the fibre Bragg gratings fabrication techniques provide versatility, because they are formed inside the fibre not changing its diameter, and the in-fibre writing does not depend on the laser's type [47]. Another advantage of FBG sensors is the easy multiplexing of the grating along a single fibre, which opens the possibility for multi-point temperature measurements using wavelength division multiplexing.

Such quasi-distributed sensors can be embedded in materials (e.g. in concrete) creating so-called "fibre-optic smart structures" [45]. That technology allows for monitoring strain and temperature distributions inside a structure without the wiring harnesses characteristic for electrical sensors.

4.4.1. FBG circuits

An ideal source for excitation of fibre Bragg grating sensor should offer a broad spectral range, around 3-4 nm per an FBG, with linear output optical power. After feeding the light from the source into the fibre, the grating modulates the incident light, and the information about the measurand encoded in form of a Bragg's wavelength shift should be detected and extracted. The wavelength shift can be measured either on reflection or transmission spectrum of the grating (Fig. 4.8). In the reflection spectrum, a narrow spectral component at the Bragg wavelength should be detected, and from the transmission spectrum the same component is missing.

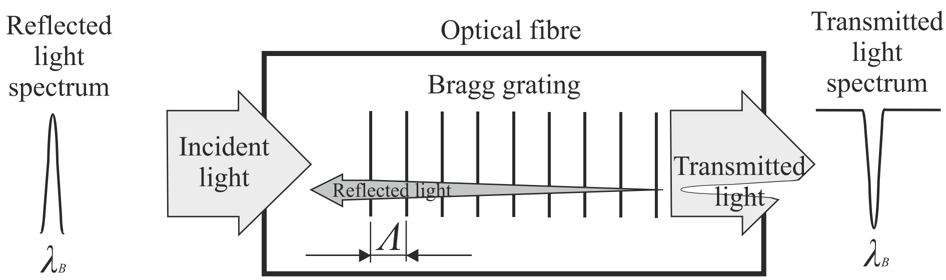

Figure 4.8. The concept of Bragg-grating based sensor system

There are many detection schemes, both passive and active. Most concepts of interrogation schemes for FBGs are based on analysing the power reflection spectrum of the sensor. The scheme is often supported with a peak finding algorithm which searches for the Bragg reflection peak, with the resolution well below a picometer [94]. In the case of temperature sensing, the respective resolution is about 0.1 K.

In order to monitor the wavelength shift of the central Bragg wavelength due to the change in externally applied temperature, high-resolution demodulation or interrogation systems are required for the FBG sensors. Optical spectrum analysers (OSA) are expensive, and the wavelength scanning speed can be too slow for real-time operation sensing systems. The simplest and most effective technique for monitoring fibre Bragg grating sensors is performed by measuring the optical power [18].

4.4.2. Long-period fibre-grating sensors

The long-period fibre grating (LPG) sensors have been developed in 1995, and initially were used as band-rejection filters in optical fibre communication systems, but soon (in 1996) it was discovered that these sensors exhibit temperature- and strain wavelength response coefficients different from those of fibre Bragg grating sensors. This is due the different operation mode of the LPG sensors when compared to that of the FBG. Long-period fibre gratings are fabricated using the "point-by-point" technology [2], which is similar to that employed to obtain FBG. This nonholographic scanning technique is based on the use of a high-intensity tightly focused femtosecond laser pulses. A micro-objective as an amplitude mask has replaced the costly phase mask required for FBG fabrication. The grating is written directly on the fibre, with the period 100-1000 μm [132], by exposing short sections to a single high-energy pulse. The fibre is translated by a period Λ, and the fraction of a higher refractive index is usually chosen to be $\Lambda/2$.

The length of a long-period grating (LPG) is typically a few centimetres, and the refractive index modulation is 10^{-4} or greater. This is related to the concept of coupling the fundamental fibre mode to a higher-order copropagating mode. For a single-mode fibre, that mode propagates inside the cladding as so-called "cladding mode". In terms of the coupled-mode theory [246], the grating period required to couple two copropagating modes can be determined from the condition imposed on the wave vectors $\vec{k}_i$ and $\vec{k}_d$: $\vec{k}_i - \vec{k}_d = m\vec{k}_g$, where m is the order of Bragg diffraction, $\vec{k}_i$ is the incident light wave vector, $\vec{k}_d$ is the diffracted light wave vector, and $\vec{k}_g$ is the grating vector of the magnitude $2\pi/\Lambda$. As $\Lambda=\lambda/\Delta n$, where Δn is equal to the difference of the refractive indices of the two copropagating coupled modes. Usually $\Delta n<0.01$, and Λ is much longer than the optical wavelength λ [2]. In this sense, the period of LPG is long. Both the fundamental and the cladding mode travel forward along the fibre axis, but the cladding mode(s) can quickly be lost due to scattering and absorption. As in the case of FBGs, only certain wavelengths are affected. The spectral scattering out light at a particular wavelength depends on the grating period Λ, the fibre refractive index, and the refractive index of the fibre environment. The coupling can be designed for a shift in wavelength caused by the change in the refractive index of environment related to a change in temperature. The temperature sensitivity can be either positive or negative, even -0.34 nm/^{o}C [131]. Usually, LPG sensor has much larger temperature response than the FBG; currently, the temperature range 20-200^{o}C is available [270]. The drawbacks of the LPG temperature sensors are: high sensitivity to bends in the fibre, and longer length than that of FBG, inconvenient for non-uniform temperature fields along a few centimetres of the grating.

4.5. Distributed temperature sensors

The optical fibre is sensitive to several external stimuli (like e.g. temperature) which affect the optical loss inside the fibre. This property offers an opportunity for sensing various physical quantities along the whole fibre, and both the location and intensity of the sensed stimulus can be assessed by the measurement of a localized loss in the core. Moreover, the fibre itself can be used as the sensor's connecting wire [142].

In 1981, the first distributed fibre-optic temperature sensor was shown publicly [255]. Since then, the concept of distributed temperature sensing optoelectronic devices (DTS) [255] has been considerably developed. Nowadays, an optical fibre working as a spatial linear temperature sensor can operate over long distances up to 30 km (even 100 km distances are mentioned), and DTS systems can locate the temperature to a spatial resolution of 1m. The measurement accuracy of 1^{o}C can be achieved at a resolution of 0.01^{o}C [255].

The focus of this section is the area of the light scattering-based distributed temperature sensors, because of their versality and broad field of applications.

A light wave propagating through a fibre interacts with atoms and molecules. If the wavelength of the incident beam of light is far from the resonance value, its electric field induces dipoles, which in turn generate a secondary wave in all directions. This phenomenon is called the scattering of light, and different types of scattering can be explained through several mechanisms [45]. The Rayleigh scattering is elastic, so no wavelength shift occurs – but the wavelength must be much longer than the inhomogeneities of the medium. Both the Raman and the Brillouin scattering are inelastic. The scattered light of wavelengths longer than the wavelength of the incident light is called the Stokes component, and the scattered light of shorter wavelength is the anti-Stokes component (Fig. 4.9). Therefore, in the spectrum of the spontaneous backscattered light, both the

Stokes and anti-Stokes Raman lines can be distinguished; the same is true for the Brillouin scattering [8].

More popular are the sensing methods based on the backscattered light, because the access to only one fibre end is required. However, the backscattered light signal is weak, and - in consequence of long integration time - the system's response is slow. On the contrary, the forward scattered light-based techniques need access to both ends of the fibre, but offer a much shorter response time [82]. For the spontaneous Rayleigh, Raman and Brillouin scatterings, the input light is linearly proportional to the scattered light and no strong changes within the fibre material occurs – but the backscattered signal of inelastic scattering is weak. However, if a threshold value of the incident light power is passed, the optical properties of the fibre can be modified, and the scattered light intensity rises proportionally to the incident light intensity taken to a power. Then the nonlinear effects dominate, and the stimulated scattering occurs [85].

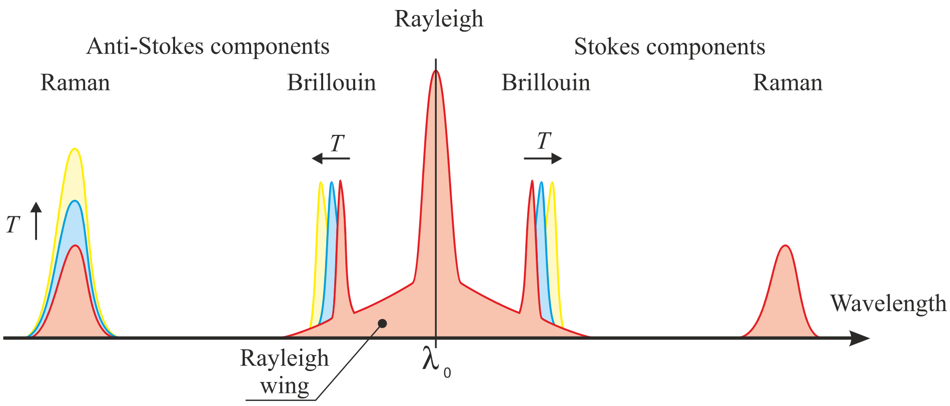

Figure 4.9. Spontaneous scattered spectrum for optical fibre (after [8])

The DTS are employed in many applications; for instance [8, 11, 45, 72, 92, 94, 231, 255-256]:

– in measurements of temperature distribution: in boilers or pressure vessels, in high voltage transformers, and generators;

– in monitoring the temperature of electric transmission cables, and gas pipelines;

– for fire detection in tunnels and buildings;

– in downhole performance monitoring oil and gas wells;

– to detect hot spots or cold spots;

– in engine health monitoring;

– for icing detection on large structures;

– for process control (e.g. diagnostics on a large reaction vessel);

– in long-term curing or drying processes;

– for automatic control of the heating conditions in a furnace;

– for measuring local heating conditions *in-situ* (small defects within an optical component can scatter light from the guiding core and induce local heating in the fibre and surrounding coating or packaging).

The distributed fibre-optic temperature sensors are easy to be embedded in large structures.

Optical fibres offer unique advantages for distributed sensing. If temperature measurements are required at many locations, such a distributed sensor may be more cost effective than individual sensors at each point, especially if installation costs are also considered. A distributed sensor can replace many point sensors, and weight and space efficient sensor systems are available [8]. It only requires one fibre capable of sending and receiving the signal from the same fibre, and only one monitor is adequate to display local changes in temperature [11]. Optical fibres, being a one-dimensional distributed measuring medium, offer the advantages of allowing line integrations and line differentiations to be performed over any closed path [155]. The line-integrating property enables the attainment of large sensitivities in measurements by means of a long path of optical interaction with the measurand [142]. The line-differential information enables a simultaneous determination of the spatial and temporal behaviour of the temperature field. Distributed sensors are also more reliable because they are not subject to the total system breakdown problem, which might occur when one element in a chain of individual sensors would fail [82].

4.5.1. Rayleigh scattering-based distributed temperature sensors

The Rayleigh scattering was discovered and described by Lord Rayleigh (John William Strutt) in 1871. In 1976, a method for determining the optical loss distribution along an optical fibre was developed. The concept is very similar to that adopted in radar systems, but the informative signal is extracted from Rayleigh backscattering light. The method, called optical time-domain refractometry (OTDR) is still used, often with some modifications. The spatial resolution of OTDR meter is the smallest distance between two scatterers for an input pulse width τ [8]:

$$\Delta z = \frac{c\tau}{2n_{eff}}. \qquad (4.15)$$

The Rayleigh scattering was chosen as the basic phenomenon, because it is an elastic scattering process, and no frequency shift is returned; moreover, the spectral width of the backward pulse lies in the range of MHz. Another reason for applying the Rayleigh scattering is the domination of this type of light scattering (96%) in the total optical loss within the fibre. Because of that overwhelming participation in losses and relatively strong backscatter signal, the spontaneous Rayleigh scattering is usually applied. More recently, Rayleigh-based OTDR systems are replaced by optical frequency-domain reflectometry (OFDR) systems [224], where a tunable laser is used for scanning a frequency range ΔF. Then, using Fourier transformation, a spatial resolution of:

$$\Delta z = \frac{c}{2n_{eff}\Delta F} \tag{4.16}$$

can be obtained.

In the formulae (4.15) and (4.16), z denotes the coordinate of the axis along the fibre, c is the speed of light, and n_{eff} is the effective refractive index of the fibre core.

In the process of fabrication of an optical fibre, the molten silica glass is processed in high-temperature and then cooled. The cooling from the melt involves thermally-induced nonequilibrium states. At the moment of vitrification, on the microscopic scale, the silica fibre exhibits localised disordered areas, which are “frozen” into the glass structure [142]. The random ordering of molecules and fluctuations of chemical composition (caused by the presence of dopants) result in small localised density variations, which in turn cause random fluctuations of the profile of the refractive index along the fibre, acting as distributed weak fibre Bragg gratings with a random period. Broadly speaking, such structure is related to entropy fluctuations.

If the intensity of the light that travels along the fibre core is low, and the wavelength λ of this light is long when compared to the spatial variations in the refractive index of the core, a spontaneous scattering process occurs (stimulated Rayleigh scattering can be employed in lasers [275]). The incident light excites the small-scale inhomogeneities in the fibre. The excited localised micro-areas act as secondary induced dipole emitters, which generate radiation in a wide angular spectrum. The light is scattered in all directions at random; this phenomenon is known as the spontaneous Rayleigh scattering. There is also another scatter mechanism called the Rayleigh wing scattering, but it arises from the fluctuations in the orientation of anisotropic molecules.

As the scattered Rayleigh light propagates in all directions, a part of it passes into the fibre cladding (the cladding modes) where it extincts, and another part of the light leaves the fibre altogether (the extracladding modes). The rest of the incident light, when passing through the localised variations intensity and the refractive index, gives rise to the Rayleigh scattering, which causes attenuation of the forward-propagating light [239]. Finally, the part of the incident light which is either reflected back inside the core or re-captured by the waveguide and sent in the backward direction, creates the backward-propagating wave.

The scattering loss is referred to as Rayleigh loss, and decreases monotonically with λ; for $\lambda \le 1.2$ μm the loss is proportional to λ^{-4} [72]. The most common formula describing the energy loss due to the scattered light is given by [85, 91]:

$$\alpha_\gamma = \frac{8\pi^3}{3\lambda^4} n^8 p^2 k_B T_f \beta \,, \tag{4.17}$$

where n is the refraction index, p is the average photoelastic coefficient of the glass, k_B is the Boltzmann's constant, β is the isothermal compressibility, and T_f represents the temperature at which the density fluctuations are "frozen" in the material; below T_f no further structural relaxation can occur in the glass. The changes of T_f depend on the glass viscosity and the cooling rate; for annealed pure silica, T_f=1170°C. A simplified formula [254]:

$$\alpha_\gamma = 8\pi^3 (n^2 - 1) k_B T_f \beta / 3\lambda^4 \tag{4.18}$$

can also be applied.

The Rayleigh scattering is a linear process in that the scattered power is simply proportional to the incident power. For a homogeneous fibre placed in uniform ambient conditions, the backscatter intensity due to intrinsic loss in the fibre exhibits an exponential decay with time. If a pulse of duration τ conveys the peak power P_0 fed into the fibre, the backscattered power $P(t)$ detected at a time delay t can be expressed as [254]:

$$P_\gamma(t) = P_0 \kappa (1-\kappa) D r_\gamma(z) \exp\left[-\int_0^2 2\alpha_\gamma(z) dz \right], \tag{4.19}$$

where $z = \frac{ct}{2n_g}$ is the coordinate of the forward-propagating pulse during generation of the detected backscatter signal $P_\gamma(t)$; $\alpha_\gamma(z)$ is the Rayleigh scattering coefficient, and n_g is the group refractive index of the fibre core; D is the length of the optical pulse in the fibre, and $r_\gamma(z)$ is the effective backscatter reflection coefficient per unit length (accounts for the Rayleigh backscattering coefficient and the numerical aperture of the fibre); κ stands for the power splitting ratio of the input fibre coupler.

A change in external temperature can thermally induce a change in the localized Rayleigh scattering, which in turn can cause a change in the locally reflected spectrum. Because the density variations are "frozen" inside the glass, the Rayleigh scattering varies very little with temperature of the glass; correspondingly, in conventional solid core silica fibres the temperature influence is poor. In liquids and liquid-core fibres, the temperature coefficient of Rayleigh scattering rises significantly from real-time thermodynamic fluctuation, and the refractive index is much more strongly dependent on temperature. The backscatter coefficient $r_\gamma(z)$ is temperature-dependent, but the microscopic variations in the refractive index of the core are essentially frozen in place. The first Rayleigh scattering-based distributed temperature sensor which was demonstrated in 1983, utilized the temperature-induced rise in the refractive index, as well as the increasing scattering loss $\alpha_\gamma(T)$ resulting from thermal agitation inside the liquid core (hexachlorobutadiene). The formula describing $\alpha_\gamma(T)$ in liquid core is identical with that for α_γ in solid core, except for substituting the T_f with the absolute temperature T of the liquid. The thermal agitation of liquid molecules results in much higher sensitivity [91].

In sensing local temperature with an optical fibre, the interference with the signal from reference fibre length is applied. Another technique is based on the coherent Rayleigh scatter patterns. Generally, the spatial accuracy of Rayleigh scattering-based DTS is below 1 m [82], and a 1^{o}C resolution can be achieved [70]. The Rayleigh scattering can also be used in temperature sensing system which employ Brillouin scattering [44].

4.5.2. Raman scattering-based distributed temperature sensors

The phenomenon called Raman scattering was predicted by C.V.Raman in 1922, and discovered in liquids only in 1928. The concept of the Raman scatter-based fibre-optic distributed temperature sensing was pioneered by the oil and gas industries in the mid-1980s [92], and developed into commercially available instruments adapted either to standard single-mode or multi-mode fibres, in the late 1980s.

The silica optical fibres are made from doped ultra-pure quartz glass, i.e. silicon dioxide SiO_2, with amorphous solid structure. The atoms and molecules of that structure are incessantly vibrating with their characteristic frequencies. Most of the photons of the light pulse of the frequency ν_0 propagating along the fibre are scattered elastically on the inhomogeneities within the fibre core structure. This Rayleigh scattered light is sent at random in all directions without any frequency shift. However, a small part of the scattered photons (one in ten million, in average) is subject to inelastic interaction with the thermally vibrating molecules and atoms of the core. The photons scattered on the molecules exhibit shifts in frequency, which can be explained by quantum mechanics [8].

The state of the molecules varies between two vibration energy levels, the occupation of which is governed by the Bose-Einstein phonon distribution. If an energy level of a molecule after the interaction with an incident photon is higher, the Raman Stokes scattering has occurred. The emitted Stokes photon has a lower frequency $\nu_0 - \Delta\nu$ because the vibration of the molecule increased by a phonon energy, which for vitreous SiO_2 is about 50 meV. Analogically, if the energy level of another molecule has dropped of about 50 meV after the inelastic interaction with another photon, a Raman anti-Stokes photon of the frequency $\nu_0 + \Delta\nu$ is emitted [84].

The Stokes transitions are more frequent than the anti-Stokes ones, and in consequence, the intensity of the Stokes line in the spectrum of spontaneous Raman scattering is higher than the anti-Stokes line – but the probability for the anti-Stokes transitions increases with temperature much stronger than for the Stokes transitions [58].

In fact, the Raman spectral band consists of many separated narrower bands due to the electronic vibrations resulting from the excited molecular rotation or reorientation [8]. The intensity of the spontaneous Raman scattering is linearly proportional to the intensity of the incident light, and is directed at random [170]. The magnitude of the Raman lines in the Ge-doped silica fibre is higher due to Raman scattering coefficient of the molecules of germanium. The central frequencies of the Raman Stokes and anti-Stokes lines can be assigned to the characteristic vibrational frequencies of the given molecules. For fused silica, the frequency shift $\Delta\nu$=13.2 THz, and the corresponding wavelength shift is $\Delta\nu/c$=440 cm^{-1} (c is the speed of light in vacuum); for high Ge-doped fibre, $\Delta\nu/c$=400 cm^{-1}.

In the single-end Raman reflectometry configuration, a short (10-15 ns) laser light pulse of a few watts power is launched into the fibre, and the returned signal is divided through a wavelength-division multiplexer to three receivers: of the Rayleigh, Raman up-shifted (Stokes) and Raman down-shifted (anti-Stokes) wavelengths, respectively [11]. The width of the reflected pulse is a few tens of microseconds, so the frequency of the pumping laser pulses can achieve several kilohertz. Because the received signals are relatively weak, long integration times up to 80 s are needed for large numbers of signal averaging cycles (ca. 10^5-10^6) to reduce the S/N ratio.

Because the Raman anti-Stokes component exhibits significant temperature dependence, and the Raman Stokes backscatter is much less sensitive, the ratio of the intensities R_I of these two components can be employed for determining the absolute temperature T in any portion of the optical fibre, from the formula [48]:

$$R_I(T) = \left(\frac{\lambda_S}{\lambda_{aS}}\right)^4 \exp\left(-\frac{h\Delta\nu}{k_B T}\right), \tag{4.20}$$

where λ_S and λ_{aS} are the measured Stokes and anti-Stokes wavelengths, $\Delta\nu$ is the frequency shift from the pump laser frequency, h is Planck's constant, and k_B is Boltzmann's constant.

Such ratiometric method is independent of common-mode factors such as optical fibre loss and splice loss (to the first order, at least), the laser power fluctuations, the launch conditions, and the composition of the fibre. However, when long lengths of fibre are involved, the result of measurement should be corrected for the differences in the fibre attenuation at λ_S and λ_{aS}. The extended formula taking into account the spatial distribution of temperature along the fibre (the z coordinate) and the abovementioned correction, is written as [241]:

$$R_I(T,z) = \left(\frac{\lambda_S}{\lambda_{aS}}\right)^4 \exp\left[-\frac{h\Delta\nu}{k_B T(z)} - \int_0^z \left(\alpha_{\gamma aS}(\zeta) - \alpha_{\gamma S}(\zeta)\right) d\zeta\right], \tag{4.21}$$

where $\alpha_{\gamma S}$ and $\alpha_{\gamma aS}$ are the respective fibre attenuation coefficients.

The explicit formula for the temperature distribution, including the term responsible for the differences in detector sensitivities, is given by [256]:

$$T(z,t) = \frac{\gamma}{\ln\left[\frac{P_S(z,t)}{P_{aS}(z,t)} + C(t) - \int_0^z \Delta\alpha(z')dz'\right]}, \tag{4.22}$$

where z is the distance along the fibre with z=0 at the DTS instrument. $P_S(z,t)/P_{aS}(z,t)$ is the measured ratio between the power of the Stokes and anti-Stokes backscatter reaching the instrument. The integral in the denominator is called "cumulative differential attenuation". The numerator γ (in K) is often treated as a constant for a given DTS system representing the shift in energy between a photon at the wavelength of the incident laser and the scattered Raman photon. The term $C(t)$ accounts for differences in effective detector sensitivities with respect to Stokes and anti-Stokes photons. The term $\Delta\alpha(z)$ represents the differential attenuation of the Stokes and anti-Stokes backscattering along the cable. The integral $\int_0^z \Delta\alpha(z')dz'$ simplifies to $\Delta\alpha \cdot z$ when the value of $\Delta\alpha(z)$ is constant, i.e. the differential attenuation is uniform along a cable. Then, for stationary signals, the formula takes a simplified form [92, 256]:

$$T(z) = \frac{\gamma}{\ln\frac{P_S(z)}{P_{aS}(z)} + C - \Delta\alpha \cdot z}. \tag{4.23}$$

An approach that omits partly the problem of discrepancies between $\alpha_{\gamma S}$ and $\alpha_{\gamma aS}$, is the evaluating of the temperature value from the ratio of the Raman anti-Stokes power P_{aS} over the Rayleigh-backscattering power P_{Ray}, which is proportional to the absolute temperature [17, 269]:

$$\frac{P_{aS}}{P_{Ray}} \propto \left[\exp\left(\frac{h\Delta\nu}{k_B T} \right) - 1 \right]^{-1}. \tag{4.24}$$

The accuracy of T measurements cannot be improved by stronger pump laser pulses, because there is a threshold optical power, which for single-mode fibres is given by [85]:

$$P_{ThR} = 5.9 \cdot 10^{-2} d^2 \lambda_p A, \tag{4.25}$$

where d is the fibre core diameter in μm, λ_p is the pump laser pulse wavelength in μm, and A is the fibre attenuation in dB/km. The power P_{ThR} is expressed in watts.

Above that threshold power R_{ThR}, the stimulated Raman scattering region begins, where temperature sensing cannot be performed, since the temperature signal is buried in the stimulated Raman signal, and the anti-Stokes energy is transformed to the Stokes signal.

4.5.3. Brillouin scattering-based distributed temperature sensors

Although this type of radiation scattering was predicted by Leon Brillouin in 1922, it was discovered experimentally only in 1930. In bulk silica the Brillouin scattering was first demonstrated in 1950, but the Brillouin scattering-based approach towards the temperature sensing was developed only in the 1990s.

On contrary to the Raman, the Brillouin scattering-based DTS are sensitive to both temperature and strain, and cross-sensitivity problems must be dealt with, because they change the band intensity and the Brillouin frequency shift.

In the distributed temperature sensing applications, both spontaneous and stimulated Brillouin regimes are applied. As in the case of the Raman scattering-based sensors, there is no requirement of special fibres, but the measuring devices are quite complex and expensive [142]. Distributed hybrid Raman-Brillouin sensing is also investigated [240].

Among others topics, Brillouin studied the propagation of monochromatic light wave and its interaction with acoustic waves, and concluded that such interaction must result in scattering of light with a frequency change. The physical causes of this are the collective acoustic oscillations of the fibreglass structure; these collective repeating cyclic motions of the molecule lattice are called acoustic phonons (and are analogous to oscillations of an imaginary moving grating). These microscopic movements of molecules about equilibrium positions can be described using macroscopic thermodynamic parameters: density, pressure, temperature, and entropy. Local changes of these parameters (mainly density and temperature) induce local variations in the dielectric constant related to the electrostriction constant. The adiabatic density fluctuations correspond to pressure waves, which are the same as acoustic waves. The acoustic wave can be described by a partial differential wave equation, which has a solution returning the values of the wave's resonance (i.e. constructive interference) frequencies [8].

The spontaneous Brillouin scattering has the advantage that single-end configuration of the DTS is sufficient, because access to only one end of the fibre is necessary [184]. The drawback of this type of scattering is weak backscatter signal, two orders of magnitude lower than the Rayleigh backscatter signal (but still one order higher than Raman backscatter intensity).

If thermal excitation of acoustic waves (i.e. phonons) in the fibreglass takes place, the scattered light undergoes a Doppler frequency shift and exhibits maximum scattering in the backwards direction. The frequency shift is expressed as [129, 141, 161]:

$$\nu_B = \frac{2n\upsilon_A}{\lambda_p}, \tag{4.26}$$

where n is the refractive index, υ_A is the acoustic velocity in the fibre, λ_p is the pump wavelength. This shift is approximately three orders of magnitude smaller than for Raman scattering, because the phonon frequencies involved in Brillouin scattering are much smaller (ca. 10 GHz). The range of Brillouin frequency shift is up to 500 MHz, and the sensed temperature values are within the range 180-600 K (broader than for Raman scattering-based systems) [184].

The Brillouin power P_B can be calculated as a function of temperature [212]:

$$P_B = \frac{A_p T}{\nu_B^2}, \tag{4.27}$$

where ν_B is the Brillouin frequency shift, and A_p is a constant which can be determined from a measurement made for the known temperature. This power is linearly dependent on temperature, but its values are small in comparison with the Rayleigh backscattered power; hence, the temperature measurements are usually based on the frequency shift vs. temperature relationship, which is expressed as [226]:

$$\nu_B(T) = \nu_B(T_{ref}) + C_T(T - T_{ref}), \tag{4.28}$$

where T_{ref} is a reference temperature, and C_T is the temperature coefficient of the Brillouin frequency shift (for conventional single-mode fibre, $C_T \cong 1.1$ MHz/^{o}C at the 1.5 μm wavelength range). The peak of the Brillouin anti-Stokes moves toward higher frequencies when temperature rises; simultaneously, the shape of Brillouin gain spectrum becomes narrower.

In order to improve the separation of the Brillouin from the Rayleigh signal, the stimulated Brillouin scattering is applied. That type of Brillouin scattering was first observed in 1964, and from the early 1990s has gained interest of DTS researchers. The stimulated Brillouin scattering (SBS) requires the access to both ends of the sensing fibre, or provision of an end-reflection. The second condition for operating the nonlinear backscatter regime is to increase the laser pulse power density above the threshold Brillouin power P_B, given by [84]:

$$P_B = 4.4 \cdot 10^{-3} d^2 \lambda^2 A \nu, \tag{4.29}$$

where d is the fibre core diameter (in μm), λ is the laser's wavelength (in μm), A is the fibre attenuation (in dB/km), and ν is the bandwidth of the injection laser (in GHz). The power P_B is expressed in watts. In the case of SBS, usually a few tens of milliwats is enough to considerably increase the intensity of the Brillouin Stokes. The typical configuration of a DTS system based on SBS comprises a pumping pulse light at one end of the fibre, and a CW probe light launched into the opposite fibre end [14].

The interaction between two counter-propagating optical fields and an acoustic field can provide the Brillouin Stokes peak in the returned spectrum as high as the Rayleigh peak. The stimulated Brillouin scattering-based DTS enables to determine the temperature profile with a spatial resolution of 5 m, and the temperature resolution of 1^{o}C, over a sensing fibre length of 22 km [226]. The stimulated Brillouin scattering can also be employed in lasers [65].

4.6. Photonic crystal fibre temperature sensors

Low-loss conventional optical fibres have appeared very attractive for telecommunications and sensing applications; however, the properties of silica impose some limitations on this technology, which hamper freely engineering of fibre's inherent losses, birefringence and other optical characteristics. Also, the manipulating on optical signals in standard optical fibres often requires an intermediate conversion into an electrical signal which after necessary transformations must be converted into optical form again [59].

The photonic crystal fibres (PCFs) with solid core at the centre were developed in 1996, and the structure with hollow core – in 1998. The microstructure of PCFs exhibits a periodic arrangement in form of (usually hexagonal) lattice of air holes over much of the cross-section of a silica fibre. The air holes run along the entire length of the fibre creating a kind of cladding around the fibre core (or several cores). The hollow-core PCFs exhibit a negative difference of the core-cladding refractive indices which rules out its operating via total internal reflection principle. Nevertheless, a thoroughly designed cladding of periodically distributed array of air holes can produce photonic gaps which allow the reflected modes to be guided along the entire length of the fibre [244].

Both physical and chemical PCF-based sensor designs are available, which enable sensing the curvature (bend), displacement, strain, electric and magnetic fields, temperature, pressure, torsion (twist) [208], refractive index, vibration, and gases like methane or acethylene. Also, hybrid fibre-optic sensor systems based partly on photonic crystal fibre are developed (e.g. [221, 273]). In recent research on PCF-based temperature sensors, the filling of the air holes with various liquids is applied: either of the cladding air holes (some of them) or the hollow core. The filling can be performed using pressure, or utilizing capillary action. The infiltrated segment of PCF is several centimetres long.

In high-temperature sensing applications up to 1000°C, the conventional Ge-doped optical fibres exhibit loss of properties because of the out-diffusion of Ge into the fibre cladding. Instead, short length of photonic crystal fibre can be spliced to a standard optical fibre creating a two-mode interferometer, because the PCF section undergoes multimode excitation. The wavelength shift about 0.01 nm/ °C is observed [42].

A similar design based on intrinsic Fabry-Perot interferometry is obtained by splicing a section of so-called endlessly single mode PCF to a conventional single mode optical fibre (SMF) (Fig. 4.10). The temperature sensing is based on the thermally-induced change in the length of the cavity formed within the PCF section, which is much longer than the cavity formed in the end cap of a short section of SMF. The reflectivity of all reflecting surfaces is assumed to be low; that simplifies the analytical description of that design as a low finesse intrinsic Fabry-Perot interferometer. The relationship of cavity length change vs. temperature is linear, with temperature sensitivity slightly over 4 nm/°C. This design allows simultaneous measurement of temperature and refractive index of the liquid into which the sensor is immersed [223].

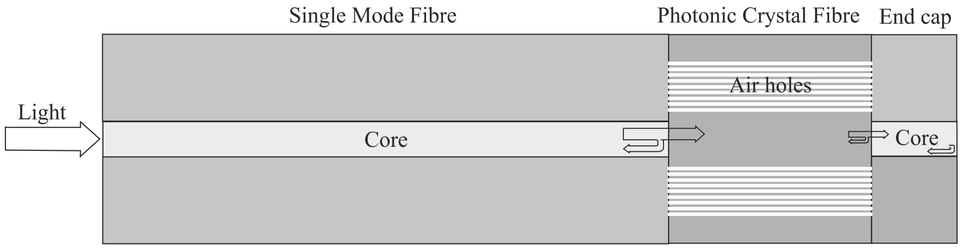

Figure 4.10. A PCF-based interferometric temperature sensor (after [223])

Another design of a high-temperature sensor based on modal interferometric technique is described in [207]. A 40 cm long portion of a nonlinear photonic crystal fibre was spliced between a multimode optical fibre on one side and a single mode fibre on the other. Then, broadband spectrum light was injected into the multimode fibre. Because of the core diameters mismatch, both core and cladding modes of the PCF are excited. These modes travel forward with different velocities and an interference pattern due to phase shift between the excited modes is transmitted through the SMF to an optical spectrum analyser.

The change in wavelength $\Delta\lambda$ per one degree Celsius is 0.073 nm, and $\Delta\lambda$ dependence on temperature is quasi-linear.

The concept of fabricating conventional optical fibre with a core filled with liquid is known for over two decades (e.g. [68]). However, since 2003, a new research trend has emerged; as the liquid medium to infiltrate the air holes in photonic crystal fibres, liquid crystal materials have been applied [127, 262]. This novel class of microstructured fibres is called photonic liquid-crystal fibres (PLCFs) and is expected to advance the tunability level of holey PCFs.

If the cylindrical tubes in the cladding along the PCF core are filled with liquid crystal (LC) material, the thermal, optical and electrooptical properties of the cladding can be controlled by influencing the alignment of the LC molecules. The details of handling with liquid crystal alignment configurations in capillaries within the diameter range 8-25μm are described in [38]. Recently, the principle of modal interferometric technique was applied in a PLCF-based modal interferometer [194], which is an improved version of the concept of the PCF-based modal interferometer with a coating made of an LC material. A 17 cm long section of a photonic crystal fibre was infiltrated with an LC material, firstly by employing capillary action, and then high pressure air was used to push the LC molecules along the full length of the microsized air channels in the PCF. Next, the obtained portion of PLCF was spliced between the end faces of two standard telecommunications single mode optical fibres. During the splicing process, at both ends of the PLCF piece small regions with fully collapsed air holes were produced.

When the light propagates through the SMF, it diffracts on the collapsed region, and in consequence, in the PLCF segment higher order modes are excited. The phase velocities of the higher order modes differ from the phase velocity of the fundamental mode because of the difference in the effective indices between the modes. A relative phase difference between the fundamental and higher order modes occurs, and an interference pattern related to this phase difference occurs at the interferometer end.

In the PLCF interferometer, the fundamental and the second order modes are the strongest and exhibit relative phase difference, which can easily be extracted from the interference pattern visible in the measured power spectrum.

The analysis of the power spectrum interference pattern is performed by tracking the value of the free spectral range (FSR), which is given by [141, 194]:

$$FSR = \frac{\lambda^2}{\Delta n_{eff} L_p}, \tag{4.30}$$

where λ is the length of the guided light, L_p is the length of the PLCF segment, and Δn_{eff} is the difference between the effective refractive indices of the fundamental mode and the second order mode: $\Delta n_{eff} = n_1 - n_2$.

FSR is interpreted as the spacing in wavelength between two successive transmitted maxima of the optical power, obtained using optical spectrum analyser connected to the second end face of the SMF segment guiding light from the PLCF.

The experiments have shown that the transmitted spectra from the PCF-based interferometer (without LC) obtained for different temperatures, do not exhibit any wavelength shift, whereas the transmitted spectra from the PLCF-based interferometer (with LC in holes) gives a wavelength shift into the lower wavelength region. The temperature sensitivity is 0.23 nm/ ^{o}C, and can be explained by the temperature-induced decrease of the initial planar alignment of the LC molecules; in consequence, the effective refractive index of the LC changes [194].

Summary

Over the past two decades, an immense progress in the field of fibre-optic temperature sensors has been made. Various types of new grating sensors (e.g. the long-period fibre grating-based [LPG] sensors) have emerged, parallel with improved constructions of sensing-oriented fibres (e.g., the sapphire fibre core for ultra-high temperature measurements), and of the components of fibre-optic temperature sensor systems: lasers, diodes, couplers etc. More recently, tendency to combine various types of fibre-optic sensors in hybrid systems, e.g. Bragg gratings with Fabry-Perot interferometers, can be observed. Another trend is to expand the measurement range of different types of fibre-optic temperature sensors, towards both ultra-high range and cryogenic temperatures. In the unique area of distributed fibre-optic sensing, research is focused on improving both the spatial and temperature resolution, simultaneously extending the length of the sensing fibre, and reducing the required time of measurement. Great expectations are connected to the newly emerged PCF-based temperature sensors, and especially to their modifications containing liquid crystal materials – the PLCF sensors.

5. Liquid crystal-based temperature sensors

The design of liquid crystal-based temperature sensors involves application of new liquid crystal (LC) materials, or new sensor constructions. In order to realize useful LC temperature sensors, LC materials have to possess appropriate material parameters. These parameters can be predicted if the properties of LCs and the influence of various factors on them are known. To understand the feasibility of employing certain LCs in the field of temperature sensors, the main types of LCs and their properties, parameters and characteristics should firstly be presented. The emphasis is put on describing these properties, which should be considered while designing an LC-based temperature sensor.

5.1. Liquid crystals: classification, properties and characteristics

The short historical note for the earliest investigations on liquid crystal materials is given below.

Julius Planer, Friedrich Reinitzer and Otto Lehmann are mentioned among the first researchers of liquid crystals. It should be noted that Planer worked at the Lviv (called Lemberg at that time) University, Ukraine [250].

1861 – Julius Planer, *Notiz über das Cholestearin*, Annalen der Chemie und Pharmacie 1861, 118, 25-27 (the first documented observation of the thermotropic liquid crystal and its phase behaviour).

1880 - Friedrich Reinitzer, *Beiträge zur Kenntnis des Cholesterins*, Monatshefte für Chemie, 1888, 9, 421-441 [Reinitzer investigated a derivative of cholesterol (cholesteryl benzoate)].

1889 - Otto Lehmann, *Über iessende Kristalle*, Zeitschrift fur Chemie, 462(4), 1889 462-472. (Lehmann first suggested the term “liquid crystals”; he performed systematic study of liquid crystals as the intermediate phase between solid and liquid states).

1922 – Georges Friedel**,** *Les états mésomorphes de la matière*, Ann. Phys. 18:273–474 (1922) [Friedel preferred to use the term “mesophase” (Greek: *mesos* ≡ *between*, and *phasis* ≡ *state*) but not “liquid crystal”. He classified liquid crystals into nematic, cholesteric and smectic].

Then, it is acknowledged that liquid crystal materials (or mesophases) were classified by G.Friedel into three main classes. The cholesteric phase now is also called “the spontaneously twisted” or “chiral nematic” phase. At present, more than fifty liquid crystal phases are known. In recent papers, the term “mesogen” is used for liquid crystal materials (e.g., of rod-like molecules materials).

LC phases occur both in natural and synthetic materials. Depending on the method of liquid crystal formation, the thermotropic and lyotropic LCs are distinguished. Thermotropic LC phases are obtained from pure material or mixtures by cooling or heating. Lyotropic (solvent-induced) LC phases are formed from crystals with amphiphile and solvent (by surfactant solutions). The nematic, chiral-nematic (cholesteric) and smectic liquid crystals belong to thermotropic LCs [83].

The thermotropic liquid crystals change their colour with temperature change. This peculiarity of liquid crystals can be applied for visualisation of the surface temperature changes. It is important in the cases when the other types of temperature sensors (e.g. thermocouples or infrared thermography) cannot be employed. The thermal field visualisation can be qualitative (observing the colour change) or quantitative (calibrating the thermal field with a thermocouple operating over a given range of temperatures) [7]. Although the measurements are relatively fast, the accuracy of the temperature measurements using liquid crystals is strongly dependent on the calibration. One of the advantages of liquid crystal application for thermal visualisation is the possibility of mapping the temperature field (on contrary to thermocouples, where measurements are conducted in a single point) [196]. In the application of the LCs for thermal measurements, the factors of external influence should be considered.

Contrary to liquids, the crystals may be characterised by some degree of orientational (the molecular axes are oriented in specific directions) or positional (molecules occupy specific states in a lattice) orders (or by the absence of the latter). LCs can be classified not only by orientational and translational orders, but also by bond-orientational order (the degree of parallelism of axes over large distance), chirality and dipolar order [158]. To characterise the displacement of the molecules in LC, a unit vector $\vec{n}$ is applied. The vector $\vec{n}$ is known as a "director" because it defines the direction of the dominating orientation of the long molecular axes. The investigated parameters of LCs are marked by subscripts || (means "parallel to director direction") and $\perp$ (means "perpendicular to director direction").

In order to characterise the orientational order of molecules, the order parameter S is used:

$$S = \frac{1}{2}\left\langle 3\cos^2\theta - 1 \right\rangle, \tag{5.1}$$

where θ is the angle between the long axis L of individual molecule and the director's $\vec{n}$ direction; the angle brackets $\langle\ \rangle$ denote "average". The parameter S ranges from 0 to 1; S=0 corresponds to the complete orientational order when the directions of long axes of molecules and director are the same θ=0 (for ideal crystals); S=0 when $\left\langle \cos^2\theta \right\rangle = 1/3$ which corresponds to orientational chaos (for isotropic liquid).

Liquid crystalline order is very attractive for obtaining new functional materials. In these materials, the liquid crystal-generated permanent order can be made via polymerization, gelation or glass formation. For example, thermotropic liquid crystals can be applied as templates for developing a solid, either by polymerizing the liquid crystalline phase or by polymerizing another material inside the liquid crystal. Also the liquid crystalline sample such as a regular array of defects, which can then be used for e.g. the positioning of nano- or microparticles over large areas, can be prepared [163].

According to their molecular structures, LCs can be divided into different types, for example, calamitics (from ellipsoid rod-like molecules), or discotics (from disk-shape molecules). The calamitics may be nematic or smectic LCs; discotics may be nematic discotic or columnar discotic LCs. The materials composed of the molecules which exhibit a rod- or disk-like shapes, are characterised by both calamitic and discotic phases, and are known as phasmidic.

The schematic representation of molecular arrangement and director orientation in nematic (N), smectic (S) and cholesteric (Ch) phases is shown in Fig. 5.1. From this picture it can be seen that in the nematic phase exists only orientational order, and no sign of translational (positional) order can be noticed. The smectic phase exhibits mainly orientational, and some translational order (in the direction perpendicular to the layers). There are many smectic phases, which are characterised by varying degrees of bond-orientational and translational order (for example, SmA, SmB, SmC). In cholesteric liquid crystal, the molecular orientation repeats for 0.5 pitch length (the helical pitch p, i.e. the period of the twist, corresponds to the director rotation through full angle (2π).

The chiral-nematic (cholesteric) phase can be formed in liquid crystal containing chiral (without mirror symmetry) molecules, and in nematic liquid crystal with small concentrations of chiral additive. One can distinguish a few types of chiral-nematic (cholesteric) materials: the cholesteryl derivatives, the chiral nematics and nematic-chiral mixtures (i.e. nematic-cholesteric mixtures: nematic+cholesteryl derivative, the nematic-chiral nematic mixtures, the induced cholesterics: nematic+optically active additive). The chirality is the necessary condition for the appearance of cholesteric phase. Chirality can be defined as $2\pi/p$, where p is the pitch. The degree of molecular chirality depends on the helical pitch, which can vary from about 0.1 μm to values close to infinity. For cholesteric LCs, the pitch lengths are in the range of 100 nm...100 μm. The helical structures may be left-handed or right-handed, depending on the molecular stereochemical structure. It should be noted that a mixture composed of two cholesterics of opposite sign of helical twist forms a nematic phase. In order to form undistorted helical structures, the surface influence on the structures should be considered. The low values of the surface energy and elastic constants K_{22}/K_{33} are required for formation of such helical structures [120]. The helical structure can be stabilised using polymers.

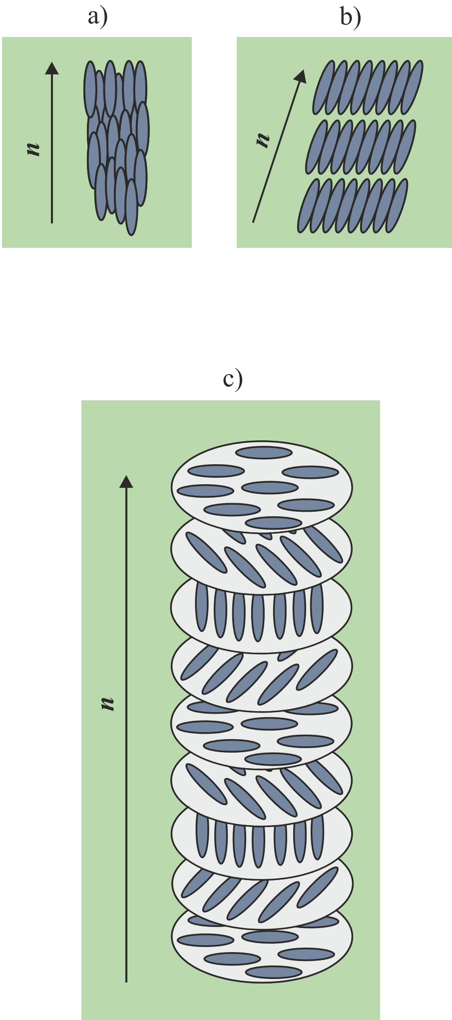

Figure 5.1. Schematic representation of molecular arrangement of rod-like molecules in the (a) nematic, (b) smectic (SmA), and (c) cholesteric phase

Let us consider one more example of mesophases - the blue phases, which possess distinguishing properties. The scientist who first described blue phases was Friedrich Reinitzer. These phases are called “blue” because of the transient blue colour of the isotropic liquid of cholesteryl esters. The temperature span in which the blue phases exist is narrow, and covers a range of a few degrees Celsius. For example, the BPIII temperature range is very narrow ($\leq$0.05 ^{o}C). The blue phases are the transient phases between the isotropic and chiral nematic (cholesteric) phases of sufficiently small pitch, and can occur in highly chiral liquid crystals. The pitch of cholesterics is important for the existence of the blue phase: it should not exceed a critical value p_c, in order to allow the blue phase to occur. As chirality increases, the three blue phases appear in the sequence: BPI, BPII, and BPIII. It should be noted that the phase BPII occurs only over a limited chirality range in the materials of a very short helical pitch [40-41, 237], while the phases BPI and BPIII have no such limitation (Fig. 5.2). The helix pitch has a direct influence on the stability of the blue phases [237, 263]. The critical pitches of the liquid crystal material are dependent on its molecular structure and composition. The schematic phase diagram showing the variation of blue phase polymorphism is depicted in Fig. 5.3.

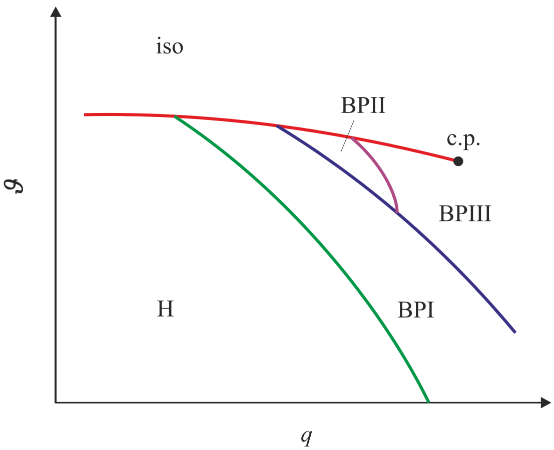

Figure 5.2. Generic phase diagram showing temperature ϑ versus chirality q for blue phases [43]

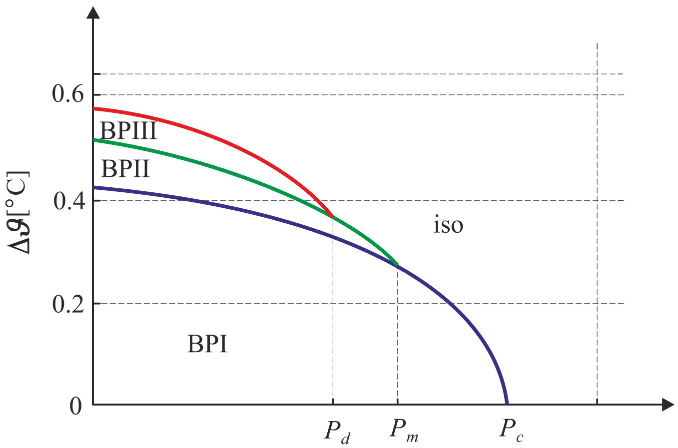

Figure 5.3. Schematic phase diagram showing the variation in blue phase polymorphism [237]

The chiral phases exhibit a helical structure of the director field. The director twist can be oriented in one direction (as in cholesteric phase) or in two mutually perpendicular directions (as in blue phase). The double director twist is related to the appearance of defects in the director field. The blue phases exist if the energy cost of double twist is higher than the energy needed for defect formation.

The blue phases are thermodynamically stable, ordered defect structures. The phases BPI and BPII have body-centered-cubic and simple cubic symmetry (defect structure), respectively. The phase BPIII has the same symmetry as the isotropic phase: amorphous with a local cubic lattice structure. In order to observe the blue phases, one can employ the polarized reflection microscopy with precise temperature control of the LC. It should be pointed out that the colour of the blue phases should not only be blue; for example, phases BPI and BPII are brightly coloured, and the phase BPIII is dull gray coloured.

Since blue phases have three-dimensional cubic structure with lattice periods, they are characterised by the selective light reflection within the range of visible light at certain temperatures. The blue phases can be considered as anisotropic photonic crystals, which exhibit small value of the refractive index contrast. During the phase transition between the cholesteric phase and the blue phase, the phenomenon of thermal hysteresis can be observed. It should be mentioned that the cholesteric and blue phases could stably coexist at room temperature [258].

Liquid crystals are characterised by anisotropic mechanical, electrical, magnetic and optical properties [163]. Let us now consider these properties.

There are three types of deformations in LCs: the splay, the twist, and the bend, which can be characterised by elastic constants of LCs (Fig. 5.4). The elastic constants K_1, K_2 and K_3 correspond to these deformations (the splay, the twist, and the bend, respectively). The elastic constants are proportional to the order parameter. The elastic parameters of LCs in both splay and twist relaxation modes are not only temperature depend but also depend on pretilt angle [126]. The elastic constants for LC materials (e.g. cholesteric-nematic mixtures) can be determined using the method described in [159].

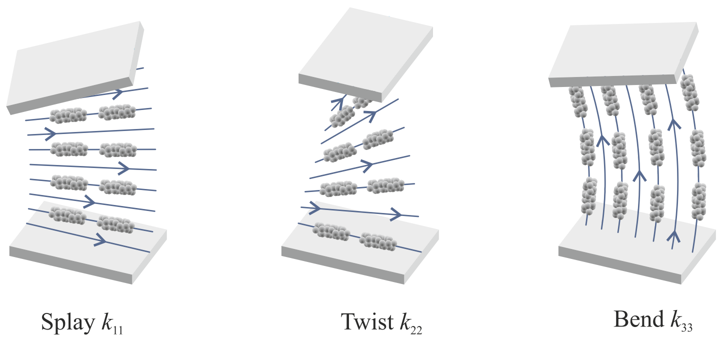

Figure 5.4. Illustration of the splay, torsion (twist), and bend deformations in LCs

The dielectric anisotropy $\Delta\varepsilon$ of LCs is given by the following expression:

$$\Delta\varepsilon=\varepsilon_{II}-\varepsilon_{\perp}, \tag{5.2}$$

where ε_{II} and $\varepsilon_{\perp}$ are dielectric permittivities in the directions parallel or perpendicular with respect to the director direction. The dielectric anisotropy can be positive ($\Delta\varepsilon>0$, the molecules of LC are oriented along the direction of the electric field strength vector), or negative ($\Delta\varepsilon<0$, the molecules of LC are oriented perpendicularly to the direction of the electric field strength vector). The parallel or perpendicular orientations are caused by the dielectric torque acting on the director, which depends on the electric field strength and the electric dipole moment induced in the LC.

Thus, one should consider the influence of both dielectric and elastic properties of LCs if the electric field is applied. Depending on the electric field strength, the initial director orientation may be stable (in weak fields, the most important are the elastic properties, which do not allow the director orientation to change) or may as well be changed (in strong fields the main contribution to the director orientation is from dielectric properties).

The expression for the magnetic anisotropy is similar to that for dielectric anisotropy:

$$\Delta\mu=\mu_{II}-\mu_{\perp}, \tag{5.3}$$

where μ_{II} and $\mu_{\perp}$ are magnetic permeabilities in the directions parallel and perpendicular with respect to director.

The optical anisotropy (birefringence) Δn of LCs is expressed as follows:

$$\Delta n = n_e - n_o, \tag{5.4}$$

where n_e and n_o are the indices of the extraordinary and ordinary refraction, respectively. These indices characterise the light wave spreading when electrical vector is perpendicular (n_e) or parallel (n_o) to the optical axis. In nematics, the optical axis and the director are oriented in the same direction. The anisotropy in nematics can be described in the form:

$$\Delta n=n_e-n_o=n_{II}-n_{\perp}. \tag{5.5}$$

An important question is the alignment of LC molecules in the sample; it depends on the surfaces of the cell, and can be homeotropic (when $\vec{n}$ is perpendicular to the substrates) or planar orientation (when $\vec{n}$ is parallel to the substrates). The LC material is investigated in the cell placed between crossed polarisers; all areas where director is parallel to one of the polarisers become black. The optical methods for investigation of oriented structures using crossed polarisers are called optical conoscopy [12, 27, 209]. In this method, the conoscopic pattern is seen after passing of the convergent (cone-shaped) light beam through the LC cell placed between the crossed polarisers. The information obtained from conoscopic investigations can be used for designing new devices [174, 177] or for developing new techniques for structure orientation identification in anisotropic environment [175, 268]. In [25] the use of optical conoscopy to discriminate between different phases (for example, uniaxial and biaxial LC phases) is described.

Temperature is the main factor affecting all abovementioned LCs properties. It should be mentioned that the LC phase exists only within a certain temperature range characteristic for a given LC material. For the thermotropic LC considered in this book, one should differentiate such phase transition temperatures as the melting point T_m of the crystalline solid, the clearing point T_c, the transition into an isotropic liquid (when LC scatters light, and the isotropic liquid is clear), and the liquid crystal-isotropic phase transition T_i temperature. For the temperature range within which LCs exist, one should know the relationships between the LCs parameters and the temperature because of their importance for LCs applications in sensor design.

5.2. Electro-optical effects in liquid crystals for temperature sensor design

The use of electro-optical effects in liquid crystals is one of the modern trends in thermometry. The electro-optical effects are due to the director reorientation under an applied electric field. This reorientation is related to the electrical and magnetical anisotropies (in dielectric and diamagnetic susceptibilities, and in electrical conductivity), the elastic properties, and the initial molecular orientation with respect to the field in liquid crystal. In consequence of the director reorientation, the optical properties of the liquid crystal are changed because of its optical anisotropy. The process of director reorientation occurs in the majority of electro- and magneto-optical effects. The degree of structural order, dielectric and optical anisotropy, and elastic properties are closely related to the mesophase state nature which is defined by the physical processes within the narrow temperature range (where the mesophase appears), and are temperature dependent.

For temperature sensor design, the electro-optical effects are used. These effects can be related to optical transmission or scattering change during different types of transitions, such as: transitions between different textures of certain type of mesophase, phase transitions between different mesophases, transitions of mesophase-isotropic liquid, or transition with selective reflection (when the wavelength of reflected light depends on the temperature of the LC).

The change in light transmission due to change in temperature can be employed as the working principle of temperature sensor design. The transmission can be practically constant when temperature rises up to the critical temperature above which the transmission increases abruptly. This tendency can be observed not only for LC materials, but also for other materials which include LC components [51]. The LC component influences the properties of the host material containing it, and the temperature dependence of the material is similar to that which characterises the given LC alone.

For temperature sensors, the response time of the LC sample (i.e. the time that elapsed during the process of transition from the transparent to opaque state, and vice versa) is of great importance; e.g. for the polymer-dispersed LC it can be of the order of a few milliseconds only. It should be noted that the rise time (the time required for a change in transmittance from 10 to 90% upon turning-on the electric field) and the decay time (the time required for the transmittance to change from 90 to 10% upon turning-off) are different. This difference may be connected with not only the value of the electric field strength, but also with the molecular characteristics of the LC.

It is known that for realization of most electro-optical effects in nematic LCs, the initial homogeneous non-defective texture of LC should be formed. Interesting results were obtained for highly defective texture of LC with positive dielectric anisotropy [108]. The increase of applied electric field strength leads to the appearance of two transmittance minima; the second minimum corresponds to maximum light scattering. The location of the minimum depends on the wavelength of the incident radiation and on the temperature. The possibility of appearance of abovementioned electro-optical effect in highly defective LC materials should be considered when designing a temperature sensor.

In the LC-based temperature sensors, the cholesteric LC materials are mostly applied. The cholesteric LCs are the most attractive LCs from the point of view of their unique properties. Different electro-optical effects can be observed in these materials, depending on the surface treatment (the boundary conditions), the helical pitch p, the ratio d/p (d is the cell thickness), the value and the sign of dielectric anisotropy, and the amplitude and frequency of an applied electric field [34]. In order to understand the electro-optical properties of cholesteric LCs and to employ them in temperature sensors design, let us consider the major factors - especially the temperature and the electric field strength - influencing the properties of LCs and the processes in LCs.

The cholesteric LCs have the property of selective light reflection. The optical properties of the cholesteric LCs such as reflection, or scattering (and others) are related to Bragg optics. The scattering of induced cholesteric LCs can be explained by Bragg scattering in the local order helical structure regions [204]. The incident unpolarised light can be splitted into left- and right-handed circularly polarised components. In the case of the opposite handedness of the component with respect to the LC material, such component passes through the LC material, and the other component (of the same handedness as the LC material) is reflected.

The helical pitch is one of the important parameters influencing the electro-optical properties of the cholesteric LC. The design of LC-based temperature sensors requires the cholesteric LC materials to be characterised by the predetermined helical pitch. The pitch of the cholesteric LC can be controlled by the amount and strength of the chiral component. As mentioned above, the pitch can be changed by the temperature, electric and magnetic fields, and mechanical deformations. The pitch of the cholesteric LCs ranges from 0.1 μm up to several hundred μm.

There are both strong and weak temperature dependencies of the helical pitch for different LC materials. Attempts were made to describe the temperature dependencies of the pitch, but it is difficult to obtain one generalised expression, which would describe correctly the temperature dependence of the helical pitch [5, 71, 146, 216, 264]. Some studies that consider temperature dependencies of the helical pitch are reported in [35].

For the majority of cholesterol derivatives, the pitch decreases as temperature increases, and the wavelength of the selective reflection is shifted towards shorter wavelengths. The change in the helix pitch involves the change in colour if the Bragg's reflection occurs in the visible spectral range. The wavelength of the reflected light that corresponds to the maximum sensitivity can be chosen using two or more component mixtures.

The pre-transitional effects cause the changes in the helical pitch, the untwisting of the helical structure and then the cholesteric-smectic transition. The change in colour of the cholesteric LC with temperature can be due to the smectic-cholesteric transition. The temperature dependence of the helical pitch near the smectic(A)-cholesteric transition is given in [278].

In some cases, the thermal hysteresis can appear; that means that different temperature values for opposite processes, such as heating and cooling, result in the same colour of the cholesteric LC material [54]. The examples of difference in colour response (i.e. the hue vs. temperature relationship) of thermochromic LCs depending on the cooling or heating cycle, are given in [53].

According to the value of the pitch p with respect to the wavelength of light λ, two cases can be considered. The first one takes place for low chiral LCs with long pitch ($p \gg \lambda$). In this case, when the light propagates in parallel to the helical axis it can be described by the superposition of two eigenwaves with electric field vectors parallel and perpendicular to the director. For short-pitch LCs of high chirality, when the pitch p and the wavelength λ are of the same order, the eigenwaves can be either elliptical or circular. In the last case, there is a selective reflection (reflected light is circularly polarised) due to Bragg diffraction at the following wavelength:

$$\lambda_B = \frac{n}{m} p \cos\theta_{in}, \tag{5.6}$$

where n is the average refractive index of the ordinary n_o and extraordinary n_e indices, m is the diffraction order, and θ_{in} is the incident angle of light.

In the case of light propagating along the helical axis, only first-order Bragg reflection is possible. Then for θ_{in}=0 and m=1 the maximum reflection occurs at the wavelength λ_B=np. The width of the selective reflection band is equal to $\Delta\lambda$=Δnp, where Δn is the difference between the refractive ordinary and extraordinary indices n_e and n_o. Depending on the wavelength of the incident light, there appear areas with strong rotation of the plane of polarisation of light: the rotation is large for λ close to λ_B. At $\lambda = \lambda_B$, the optical rotation changes its sign.

In the case when the incident light is perpendicular to the helical axis, one can consider cholesteric liquid crystal as material with the periodic (period equals 0.5p) change of the refractive index (between n_e and n_o).

As can be concluded from the abovementioned cases, the pitch should be taken into account when one chooses the wavelength of LC illumination.

The optical properties of the cholesteric liquid crystal (the selective reflection in cholesteric liquid crystal for visible light, and the polarisation state of the light transmitted through the cholesteric liquid crystal with different optical pitch) can be described using Jones matrix, in which each matrix element is a complex exponential [32, 60]. The cholesteric liquid crystal is considered to be a multilayer structure, which consists of many uniaxial thin films, and the orientation of optical axes of these films changes from layer to layer. It can be shown that depending on the type of the circular polarisation (left-hand or right-hand), the polarised light of the wavelength equal to the helical pitch which propagates in the direction of the helical axis is totally reflected or simply transmitted.

The intensity of transmitted light may be employed to identify the phase transition temperature. The light transmission through the samples as well as the cholesteric pitch depends on the electric field strength and the presence of dopants in the cholesteric matrix. For example, for the doped compound (the azo-derivatives are utilized as the dopants), the electric field has less influence on the transmitted light intensity versus temperature characteristics [248].

Under electric field, the helices of the cholesteric LC materials can be deformed by changing the texture (texture transition), or destructed. The destruction of the cholesteric helix under the electric (or magnetic) field, and formation of the homeotropic nematic phase is known as the cholesteric-nematic transition. The transmittance of the LC materials depends on both the electric field and the temperature. Under the influence of temperature, different LC textures may appear, and depending on the type of the texture, different changes in transmittance occur. An example of the transmittance intensity-voltage characteristics for cholesteric LCs is presented in Fig. 5.5. The transmittance of the LC is high for planar texture, if no electric field is applied, and decreases as the electric field rises from zero, because of the scattering which occurs when the planar texture changes into the focal ones. The value of the electric field strength $E_{c'c}$ at which the maximum scattering occurs, is the threshold of the focal-conic deformation (texture transition). In this texture, the helical axes are oriented in parallel to the LC cell plates. The results of the investigation of the texture transitions and the peculiarities of the scattering by focal texture are described in [9-10, 206]. As the electric field increases further ($E > E_{cn}$), the helix untwists and the focal structure transforms into the homeotropic one (which is transparent). The E_{cn} value is the threshold of the cholesteric-nematic transition. The type of the texture depends not only on the value of the pitch, but also on the thickness-to-pitch ratio, the direction of the change in applied voltage, and the boundary conditions.

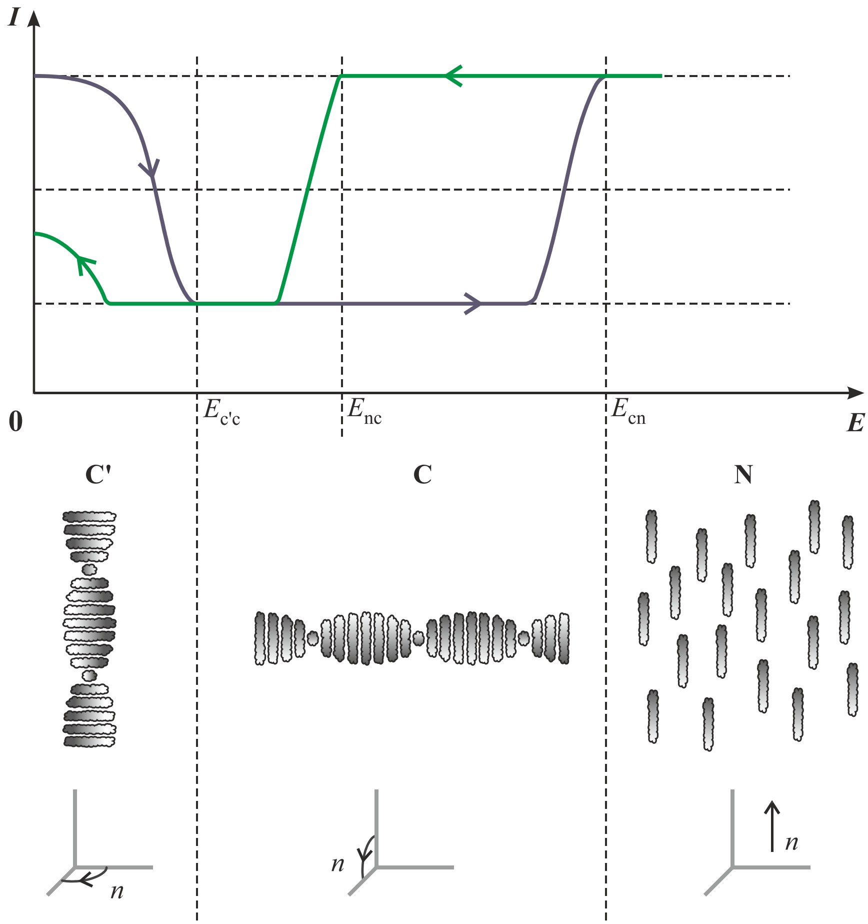

Figure 5.5. Typical dependence of optical transmission of an LC cell on the applied electric field, and the orientation of molecules and the director

In LC materials, the field hysteresis can occur [202]. Among the factors that strongly influence the value of the field hysteresis loop, the temperature should be mentioned [191]. The properties of cholesteric-nematic transition can be applied not only in temperature sensors, but also in other practical applications, e.g. light modulators [201].

The twist effect in the induced cholesterics can be investigated using the cholesteric-nematic transition effect theory [122]: the twist effect can be considered as a simple case of the cholesteric-nematic effect in thin LC layers. The application of this theory is related to the d/p_0 ratio. For certain d/p_0 ratios the chiral texture of the induced cholesteric is destructed without previous texture transition (without formation of the scattering focal-conic textures), because the threshold voltage of the cholesteric-nematic transition is lower than the threshold voltage of texture transition. Above a certain critical value of d/p_0 ratio, for which the voltage of the cholesteric-nematic transition becomes higher than the voltage of the texture transition, the cholesteric-nematic transition occurs through the formation of scattering focal-conic texture. The critical value of d/p_0 can be determined by the correlation of the values of surface energy densities corresponding to the director states F_{sc} and F_{sn}, taking into account the value of K_{22}. In order to determine the value of d/p_0 ratio for which the cholesteric-nematic transition occurs, one can equate the expressions for threshold field values of the texture ($E_{c'c}$) and the cholesteric-nematic (E_{cn}) transitions.

For thick LC layers one can use the expression for E_{cn} in which the boundary conditions can be neglected, but for thin LC layers the boundary conditions should be taken into account [257]. The value of E_{cn} depends on the elastic constant K_{22}, the pitch p, the LC layer thickness d, the surface free energy, and the dielectric anisotropy. The ratio d/p and the substrate treatment necessary to obtain the required boundary conditions should be considered in investigations of the cholesteric LCs in the cells of thickness d [238]. If the thickness d of the LC is comparable with the helical pitch p, the hysteresis appears.

The novel approach to determinate the threshold cholesteric-nematic transition voltages using the conoscopic images is described in [121]. It is shown that from the analysis of the conoscopic images one can accurately determine the threshold cholesteric-nematic transition voltages for different types of cholesteric liquid crystals.

Let us consider the plot of the light transmission intensity versus the applied rising and falling voltage for nematic-cholesteric mixture, shown in Fig. 5.6. The points in the figure correspond to the conoscopic images shown in Photos 5.1a-h. In these photos, the conoscopic images of the liquid crystal mixture SP-92+1% HDN-1, obtained using the conoscopic method at the wavelength λ=0.63 μm, are shown. In Photo 5.1a the initial planar cholesteric structure is illustrated. It can be noticed that there are no conoscopic images. As the voltage increases, the initial planar structure of the liquid crystal material changes into the homeotropic one. The conoscopic images are formed as the voltage increases. Photos 5.2b, 5.3c, and 5.4d show the homeotropic alignment of the liquid crystal layer. A further increase in the threshold voltage is related to the increase of the brightness of isochromic circles of the conoscopic image (Photos 5.3c, 5.4d, and 5.5e). The maximum resolution of the conoscopic image with isochromic circles corresponds to the cholesteric-nematic transition voltage (Photo 5.5e). It should be noted that this method of determining of the cholesteric-nematic threshold voltage allows obtaining the values of the threshold voltage visually, using a photodetector; i.e. this method is simple and convenient for application.

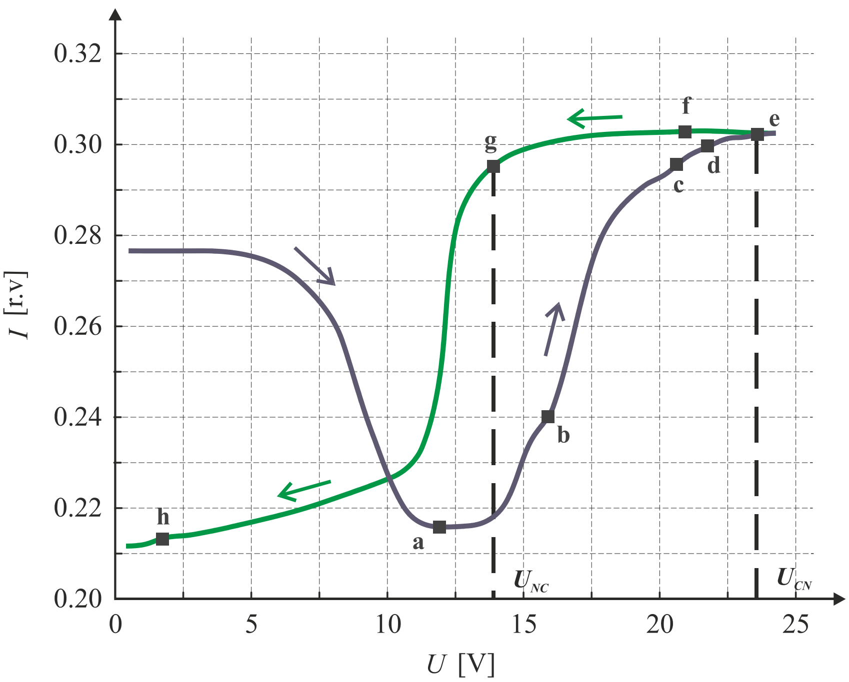

Figure 5.6. Light transmission intensity versus the applied rising and falling voltage for SP-92+1% HDN-1

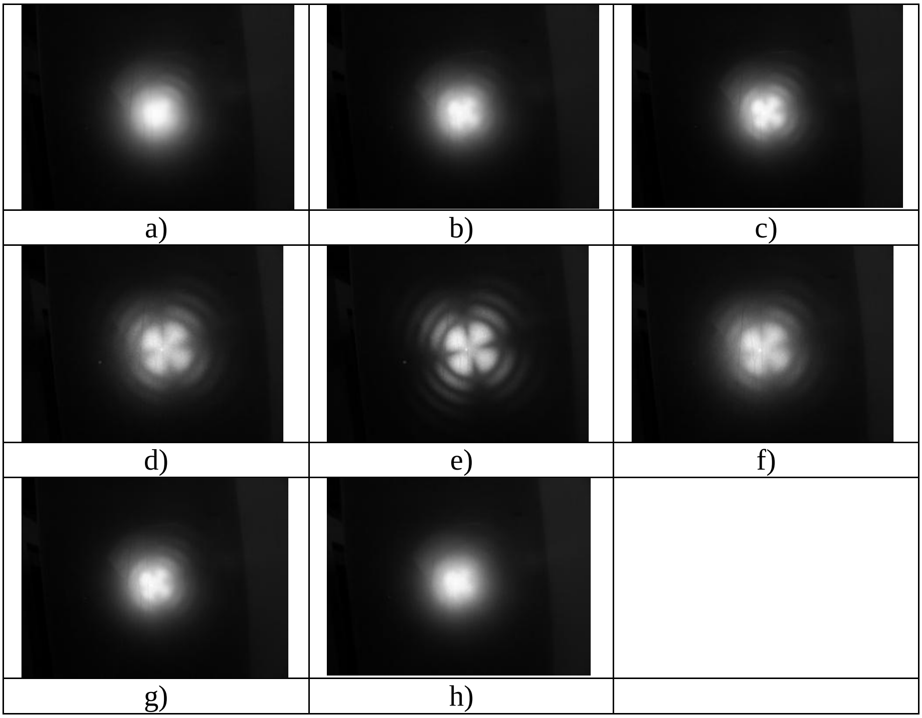

Photo 5.1. Conoscopic images (liquid crystal layer thickness is 50 μm) in corresponding points in Fig. 5.6

As shown in Table 5.1, the known methods currently used to determine the values of threshold voltage give different values of the threshold voltage for different wavelengths. However, the values of the threshold voltage determined by the aforementioned conoscopic method are the same for different wavelengths, as one can see from Table 5.1.

The conclusion to be drawn is that the conoscopic methods can be applied not only to investigate the structure of liquid crystals and the changes due to the influence of different factors on these crystals, but also as an alternative to known methods for the determination of some characteristic parameters of liquid crystal materials.

It is important to know the threshold voltages of the cholesteric-nematic transition voltages because the operating principle of one type of temperature sensors described in this chapter is based on that transition.

Table 5.1. Threshold cholesteric-nematic transition voltages for different wavelengths at temperature T=300 K

Matrices	λ=337 nm		λ=444 nm		λ=630 nm		λ=1150 nm		Proposed method (λ=337 nm, λ=444 nm, λ=630 nm, λ=1150 nm)	
	U_{cn} [V]	U_{nc} [V]	U_{cn} [V]	U_{nc} [V]	U_{cn} [V]	U_{nc} [V]	U_{cn} [V]	U_{nc} [V]	U_{cn} [V]	U_{nc} [V]
20%5CB+80%LC-440+1% cholesterylpropionat	25.5	14	24	13.5	18	10,5	22.5	12.5	23	13
20%5CB+80%LC-440+1.5% cholesterylpropionat	31	22.7	29.5	21.5	25.5	20	27.5	23	28	23.5
40%5CB+60%LC-440+1% cholesterylpropionat	18.5	19.3	17.7	18	15	15.7	17.5	17	18	17.6
40%5CB+60%LC-440+1,5% cholesterylpropionat	27.7	23.6	26.5	22	20.5	18	24	20	24.5	20.7
60%5CB+40%LC-440+1% cholesterylpropionat	19.6	16.5	18	15	12.7	11.3	15	13.5	15.6	14
60%5CB+40%LC-440+1.5% cholesterylpropionat	20.3	19.5	19.8	17.7	14.5	13.4	16.5	15.5	17	16
80%5CB+20%LC-440+1% cholesterylpropionat	19.4	16	18	14.5	14.8	10.4	16	12.5	16.5	13

Table 5.1. Threshold cholesteric-nematic transition voltages for different wavelengths at temperature T=300 K (cont.)

Matrices	λ=337 nm		λ=444 nm		λ=630 nm		λ=1150 nm		Proposed method (λ=337 nm, λ=444 nm, λ=630 nm, λ=1150 nm)	
	U_{cn} [V]	U_{nc} [V]	U_{cn} [V]	U_{nc} [V]	U_{cn} [V]	U_{nc} [V]	U_{cn} [V]	U_{nc} [V]	U_{cn} [V]	U_{nc} [V]
80%5CB+20%LC-440+1.5% cholesterylpropionat	27	21	26	19.7	22.5	16	24	18	24.7	18.5
20%5CB+80%LC-440+0.4% cholesterylpelargonat	12.7	2.3	11	1.9	8	1.2	9.5	1.3	10.2	2.3
20%5CB+80%LC-440+1% cholesterylpelargonat	24.4	10.3	23.5	8.9	21.4	6.3	22	7.5	22.5	8
40%5CB+60%LC-440+0.4% cholesterylpelargonat	15.8	2.1	14	1.6	10	1	12	1	12.3	1.3
40%5CB+60%LC-440+1% cholesterylpelargonat	21.3	17.9	20	16.4	29.5	16.7	31	18	31.4	18.4

5.3. Liquid crystal-based optoelectronic temperature sensors

Liquid crystals are employed in different types of temperature sensors, e.g. LC-based optoelectronic and fibre-optic temperature sensors [113]. In addition, we should note the new possibilities for temperature measurements, e.g., the application of cholesteric LC laser as an optic fibre-based temperature sensor [198]. Many LC-based sensors are multifunctional: they can measure not only the temperature but also other parameters (e.g. pressure, or electric and magnetic field strength) which can influence the parameters of the LC material [74, 192-193, 203].

Let us consider one of the constructions of the LC-based optoelectronic sensors. The main components of the optoelectronic temperature sensor are: the prism that is employed for dispersion of light, and the temperature dependent LC cell material placed between the prism and the glass plate (Fig. 5.7) [119]. The LC material is an induced cholesteric. The light beam is dispersed by the prism into its full spectrum, and then passes through the LC cell. Only the light of the wavelength corresponding to the maximum of the selective reflection of LC does not pass the LC cell and is reflected back. In the place of the light component thrown back because of selective reflection, a dark strip appears. The selective reflection of LCs is temperature dependent; the temperature change involves the selective reflection of a certain wavelength. Because of the selective reflection of the spectrum wavelengths passed through the LC cell, the strip position changes. Thus, the temperature can be visualized. The sensor operates within the temperature range of the LC mesophase.

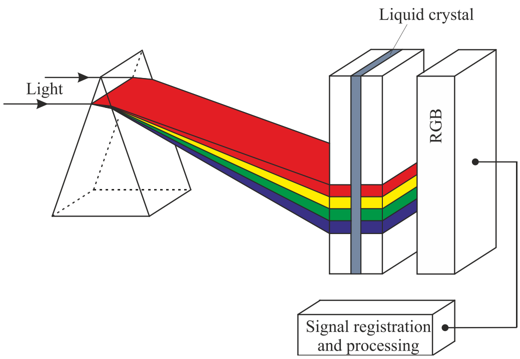

Figure 5.7. Schematic of the optoelectronic temperature sensor based on prism and LC cell

The block diagram of the LC-based temperature sensor based on the prism with LC analogue indicator, is given in Fig. 5.8. The dark strip can be registered by the RGB photodetector. The signal from the photodetector can be formed into a signal carrying information to an analogue indicator, in order to visualize the temperature value. This signal is amplified and converted by the multiplexer from the three-channel into one-channel signal, which is passed to the analogue-to-digital converter (ADC). The main processor of the microcontroller processes the signals and forms the control signals for the analogue LC indicator by means of a digital-to-analogue converter. The microcontroller controls the supply of the light diode and the multiplexer. The value of the voltage formed inside the block for output signals corresponds to the determined temperature.

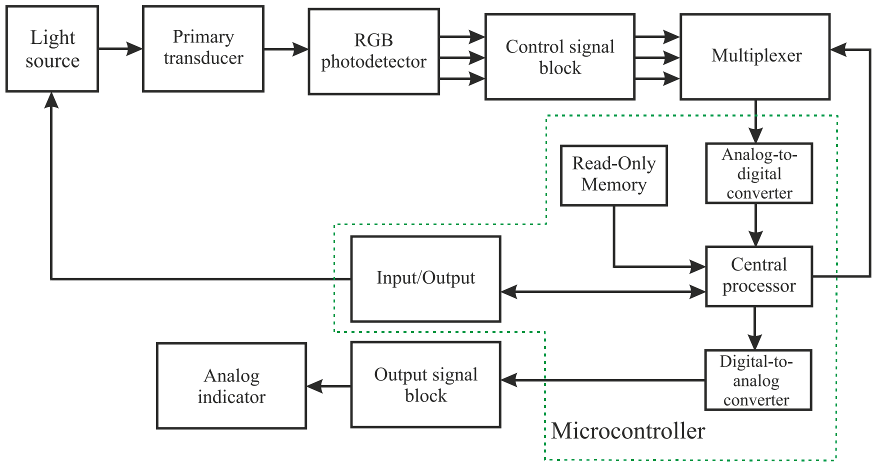

Figure 5.8. Block diagram of the LC temperature sensor based on the prism, with analogue LC indicator

The applications of LC indicators are related to their advantages over other types of indicators, such as low power consumption (from a few to a few tens of μW/cm^2), low control voltages (from a few volts to 10…20 V), low cost, high manufacturability, and durability.

In order to facilitate making the choice of an appropriate LC indicator, the possible constructions of the LC analogue indicators and their attributes are described below. The choice of the type of the LC analogue indicator depends on the required visualisation design.

In these LC analogue indicators, the change in input quantity (voltage) is visualized. The peculiarities of the LC indicators consist in the formation of a voltage gradient across the indicator with varying thickness of the transparent conductive electrode, or by variable doping concentration of the transparent electrode [114-116]. The peculiarity of the LC indicator described in [78, 117] consists in the creation of the reflecting cover with transparent areas shaped like symbols. If reflecting covers are used, the light losses at the glass substrate-transparent electrode boundary can be reduced [79]. The LC analogue indicator without the reference voltage source is described in [76, 95, 112]. The results calculated for the LC analogue indicators, without supply elements for sensor devices, are given in [214-215]. The mathematical model of the LC analogue indicator is described in [125].

Let us consider another construction of the LC-based optoelectronic sensor employing the selective reflection in LCs. For the design of the temperature sensors based on the helical structure LC materials, more attractive are the materials exhibiting selective reflection band laying within the visible spectrum. The investigation of the temperature influence on these materials is a current issue. We investigated the temperature dependencies of the transmission spectra of the cholesteric LC sample KET90600 (HCCH Jiangsu Hecheng Chemical Materials Co, Ltd.) over the temperature range from 20°C up to 80°C. The temperature dependencies of the selective reflection wavelength maximum for the given LC material are plotted in Fig. 5.9. As it can be seen from Fig. 5.9, the selective reflection wavelength maximum is shifted toward longer wavelengths with an increase in temperature. The registered characteristics are useful for designing an LC-based optoelectronic temperature sensor.

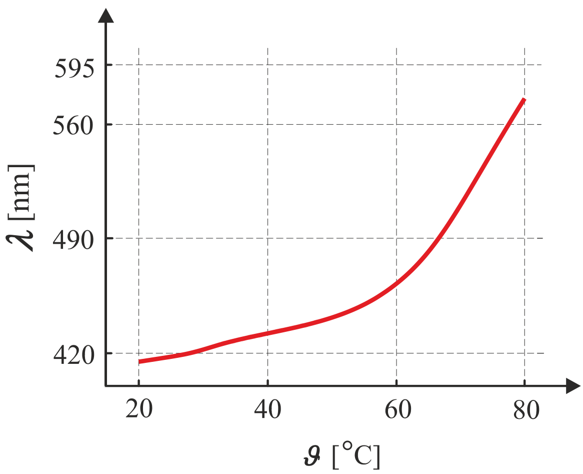

Figure 5.9. Relationship between the selective reflection wavelength maximum and temperature for LC sample KET90600

The radiation passed through or reflected from the LC cell causes a change in the helical pitch under the influence of temperature. The operating of such LC-based optoelectronic sensor is based on the registration of the change in the radiation spectral characteristics. The block diagram of the LC-based optoelectronic sensor is shown in Fig. 5.10.

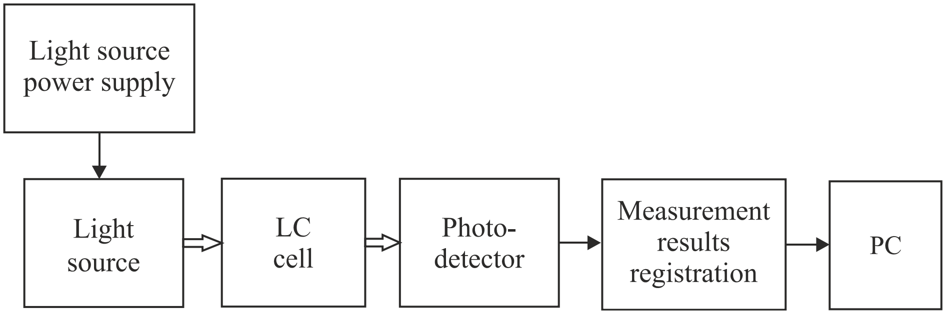

Figure 5.10. Block diagram of the LC-based optoelectronic temperature sensor

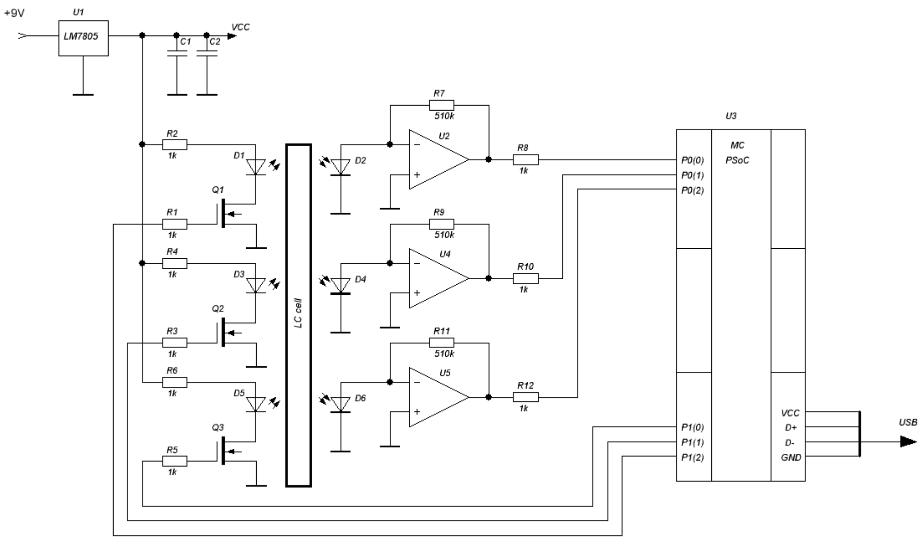

Figure 5.11. Circuit schematic of the LC-based optoelectronic temperature sensor

The circuit schematic of the LC-based optoelectronic temperature sensor is given in Fig. 5.11. As the source of radiation, the RGB LED RL81-S3B7G746/I6 (EXCEED) with peak wavelengths 645 nm (GaAlAs/GaAs), 465 nm (InGaN/GaN), and 520 nm (InGaN/GaN) was employed. The temperature sensor is supplied from an external network adapter; the output voltage of the adapter is kept constant using the integrated voltage stabiliser LM 7805. For the registration of the spectral characteristics of the radiation, the three-channel (RGB) silicon photodiode S9702 (Hamamatsu) was used. The spectral characteristic of this photodiode corresponds to the visual bands of three colours ($\lambda_B = 400\ldots540$ nm, $\lambda_G = 480\ldots600$ nm, $\lambda_R = 590\ldots720$ nm).

The LEDs are driven through the transistor switches (VT1÷VT3), which in turn are controlled by the digital outputs of the microcontroller PSoC (Cypress) and provide the diode operation in both continuous and pulsed regime. The pulsed regime allows setting the required level of the light intensity and synchronising the input signals for the sensor’s noise immunity improvement. The light passed through the LC cell is received by the RGB photodiode. The level of the input signals required for sensor’s operating is set using the operational amplifiers. The outputs of the amplifiers are connected to the analogue inputs of the microcontroller. The built-in ADC converts analogue signals into 14-bit code words, which are used in further program analysis. The internal software compares the digital codes of the input signals with the corresponding codes of the values stored in the built-in database. A given value of the measured parameter corresponds to a given input combination. The formed output value is transmitted through the built-in interface circuitry to the PC for the visualisation on the screen in a user-friendly way. The representation of the measured quantity can be visualised in both analytical and graphical form. The measured results are used to create databases, and for the calibration purposes. The measurement accuracy is limited by the sensitivity of the primary transducer (LC cell) and the number of bits of the internal ADC.

The abovementioned circuit scheme of the LC-based optical temperature sensor is versatile. The range of the measured temperatures and the measurement accuracy are determined by the properties of the LC material used in the LC cell. For the KET90600 LC material, the measured temperature ranges from 20^{o}C up to 80^{o}C, and the sensitivity is 0.25^{o}C/nm. The built-in 14-bit ADC provides the level of temperature measurement accuracy 0.01^{o}C which does not influence the sensor’s accuracy.

The abovementioned properties of the cholesteric-nematic transition can be employed in the threshold-based temperature sensors [106, 107, 109]. The operating principle of the threshold-based temperature sensor is based on the registration of the change in an LC cell transparency under the temperature influence. In this case, at the threshold voltage for a certain temperature, the cholesteric-nematic transition occurs, changing the transparency of the LC cell. Before the start of sensor’s operating, one should fix the required threshold voltage for the sensor. At the moment of registration of an LC transparency (light intensity) change, the temperature can be determined.

The threshold-based temperature sensor consists of the light source, the primary transducer (LC cell), the photodetetor and the circuit forming the output signal. The block diagram of the threshold-based temperature sensor is shown in Fig. 5.12.

The light from LED GNS-0603URC (GaAlAs) with peak sensitivity at 660 nm is sent on the LC cell (primary transducer). The nematic-cholesteric mixtures can be used as the active material of the sensor. The relationships between the threshold voltage and the temperature for the cholesteric mixtures applied in the sensor are shown in Fig. 5.13. The photodiode S1787-12 with peak sensitivity at 650 nm was used as photodetector.

The electric scheme of the control block comprises the stabilisator of the input voltage, the control circuit of the LC cell supply voltage, the microcontroller, and the interface block through which the signals are transferred to PC. The functional scheme of the threshold-based temperature sensor employing LC is shown in Fig. 5.14.

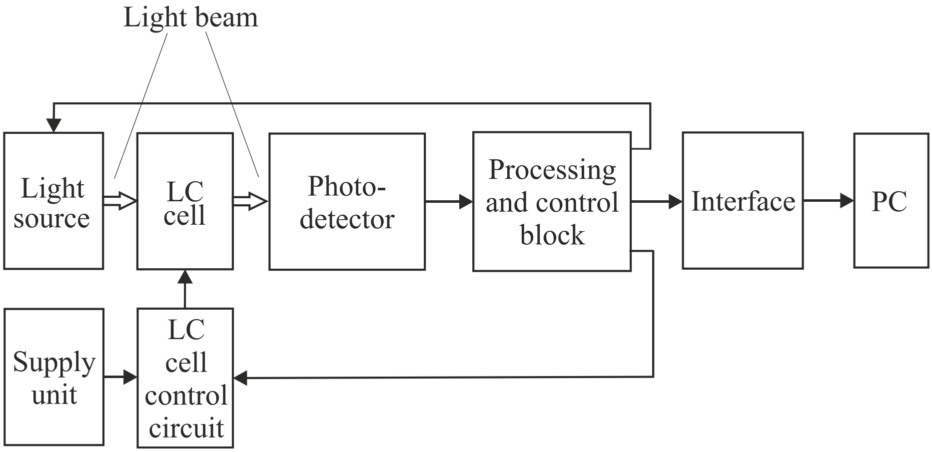

Figure 5.12. Block diagram of the LC threshold-based temperature sensor

The secondary transducer is based on the microcontroller PSoC (Cypress). The use of such microcontroller allows creating a compact and convenient to use control device with the possibility of information exchange with PC.

The architecture of PSoC consists of four main blocks: PSoC Core, digital system, analogue system, and functional blocks including fast USB ports. All the functional blocks are integrated in one complete system. The PSoC CY8C24x94 devices can have up to seven I/O ports. The digital system of the PSoC microcontroller CY8C24x94 (DAC) consists of four digital PSoC blocks. Each block is an 8-bit device, which can be employed separately, or with other blocks as 16-, 24- or 32-bit periphery devices. A D/A converter is applied for the conversion of the binary code into the voltage or current value, which are proportional to the value of digital code.

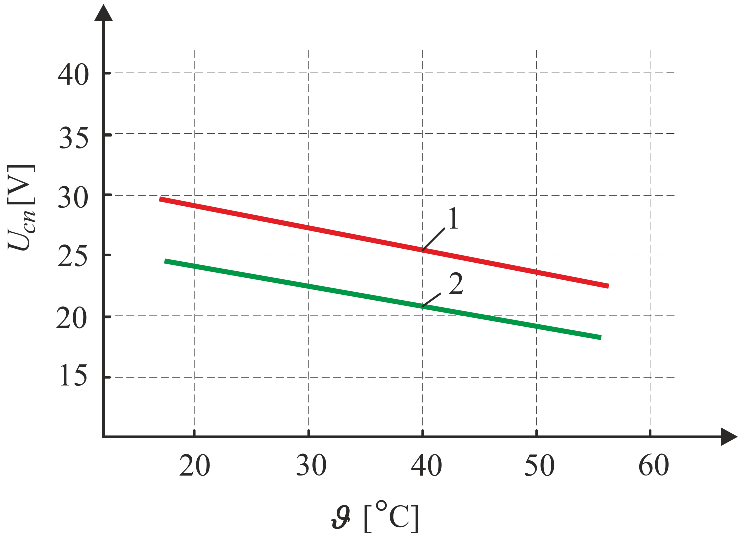

Figure 5.13. Temperature dependencies of the threshold voltage U_{cn} for the cholesteric mixtures: 1 – 80%5CB+20%LC-440+1.5% cholesterylpropionat; 2 – 20%5CB+80%LC-440+1.5% cholesterylpropionat

The LED is supplied through the transistor switch (Q3) which is controlled by the digital output of the PSoC microcontroller (Cypress). The light passed through the LC cell is received by the photodiode D2.

Before starting the registration and processing of the signals from the photodiode, one should set the required threshold voltage for the sensor (Fig. 5.5, block 1). It can be done using the voltage divider (built with the resistors *R3*, *RV1* and *R10*). For further amplification, the signals are put through the operational amplifier U1:B on the transistor switch Q2. In order to protect the sensor's operation from the influence of frequency noise, the capacitors *C2* and *C3* are used. Through the transistor switch Q1, the signals are put on the LC cell. The device creates an array of consecutive voltage values. The minimum value of the voltage (and the voltage step change) across the LC cell is limited by the number of the ADC bits. The built-in ADC converts the analogue signal into digital 14-bit code, which is used in further program analysis. Further operations aimed at obtaining the value of the measured temperature are the same as have been described for the optoelectronic temperature sensor (Fig. 5.11). The measured temperature range and the measurement accuracy are determined by the properties of the LC material used in the LC cell, in particular by the slope of the contrast vs. voltage characteristic, which is different for various materials; e.g. for the 20%5CB+80%LC-440+1.5% cholesterylpropionat and 80%5CB+20%LC-440+1.5% cholesterylpropionat, the measured temperature ranges from 17°C to 57°C. The temperature measurement accuracy is equal to 0.05°C.

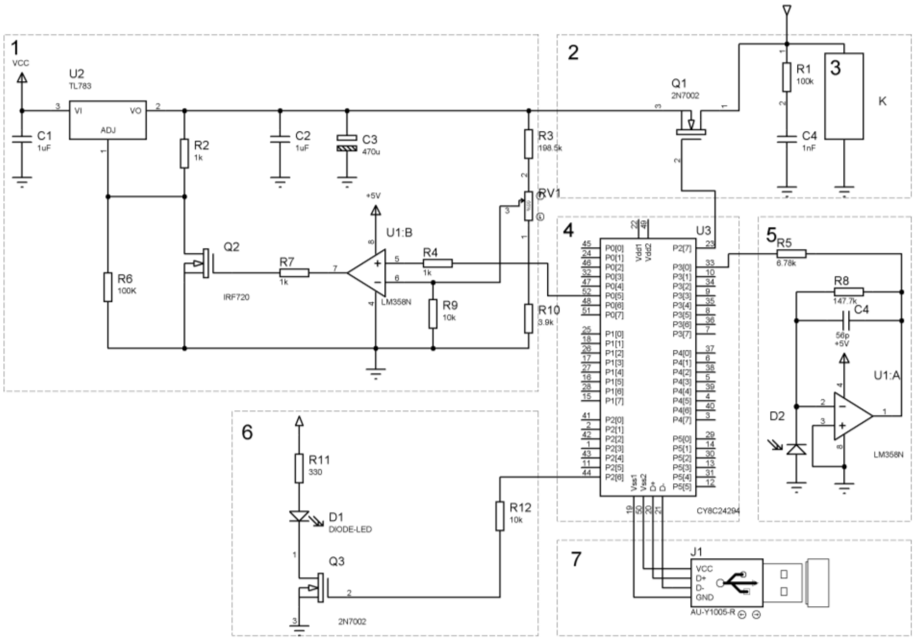

Figure 5.14. Functional scheme of the threshold-based temperature sensor employing LC: 1 - the programmable power supply block, 2 – the block of the LC cell threshold voltage control, 3 - the LC cell, 4 - the microcontroller PSoC CY8C24x944, 5 - the photodiode (S1787-12) control block, 6 - the LED (GNS-0603URC) control block, 7 - USB interface

5.4. Liquid crystal-based fibre-optic temperature sensors

Liquid crystals can be applied not only as the sensing elements in fibre-optic temperature sensors, but a liquid crystal cell can be also employed as an optical control element for lightguides [189]. The light propagation in optic fibre with LC cell is analysed in [205] and on the basis of this analysis, a mode selector is elaborated. Moreover, on the basis of three optic fibres with LC cells, a spectral selector which can be applied in the temperature sensors, was elaborated [204]. The other possibilities of use of liquid crystals and optic fibres are described in [123].

Liquid crystal-based fibre-optic temperature sensors consist of an LC and a fibre-optic cable. Usually the LC material is the sensitive element of the sensor, and the fibre-optic cable is used for light transmission. The transmission of information about temperature dependent properties of the sensing material allows determining the temperature value. Under the influence of temperature, the changes in intensity of light reflected from LC material, or in optical rotatory power (in binary LC mixtures) appear [50]. In order to understand the operating of LC-based sensors, the changes in the electro-optic properties of LCs (e.g. transmittance) under various factors (including temperature) acting on LCs, were described above. Further on, let us consider only the constructions and the principle of work of some LC-based fibre-optic temperature sensors.

The earlier LC-based fibre-optic temperature sensors are described in [69, 135-137, 228-229]. The liquid crystal-based fibre-optic temperature probe consists of an LC and an optical fibre. The LC is placed between two glass or teflon cups as the temperature-sensitive element of the temperature probe. The thin film of an LC is spaced 0.5-1.0 mm from the distal tip of a sheathed fibre-optic bundle containing 5-15 fibres of 0.125 mm in diameter. As an LC material, the LC mixture of three cholesterol compounds was applied.

The fibre-optic cable is used for the light transmission to the LC, and for receiving the back scattered light from the LC. About half of the optical fibres are employed for illuminating the LC film by LED light (0.685 μm, gallium-arsenide-phosphide LED). The current through the LED is pulsed with a pulse width of about 10 ms at 100 pulses per second. The current pulses of about 1-3 A are put through the LED. The other half of the optical fibres is used for the transmission of the back scattered light from the LC to a phototransistor. The reflected light pulses are amplified, and as a voltage signal are put into the sample-and-hold circuit where they are stored.

The sizes of the probe are as follows: the diameter is about 2 mm, and the length can be up to 1 meter or more.

For obtaining the required parameters of the temperature probe, the following factors should be considered: the temperature range of the LC, the illuminating light wavelength, the purity of the LC, and the temperature probe configuration.

The aforementioned temperature probe can measure temperature differences to within 0.1°C accuracy. Such temperature probe can be useful for a range of medical and biological applications, because it perturbs the electromagnetic field in the tissue only minimally and gives a large variation of red reflectance in the 30-45°C range. The application field of such temperature probe is wide; for example, measurement of the rectal temperature of animals, temperature measurements in the chambers of excised animal hearts in cardiac studies, temperature monitoring in the tissues, etc.

Let us consider one more LC-based temperature probe [261]. The LC material is placed inside the cell between the heat-treated glass plates (1 mm in diameter), with a dielectric mirror on the outer surface of one plate. The LC cell is put together with the polariser at the well-polished tip of the optic fibre. The LC cell is protected by the epoxy resin, in which it is dipped. The linearly polarised beam passes through the LC, and its temperature dependent rotation occurs. Then the beam is reflected from the mirror, and additional rotation takes place. A difference in light intensities exists between the incident and reflected beams. To compare these intensities, the beam splitter is applied.

The relationship between the intensity of the reflected beam and the temperature can be expressed as follows:

$$\Gamma(T) = \Gamma_0 \cos^2 \Psi(T), \tag{5.7}$$

where $\Psi(T)$ is the temperature-dependent total rotation, and Γ_0 is a constant that depends on the attenuations due to reflection from the mirror and the passage through the glass plates, the liquid crystal, and the polarising material. The range of reflected intensities corresponds to a given temperature range. By proper choice of liquid crystal composition, cell thickness, and illumination wavelength one can obtain the required range of reflected intensities, which corresponds to the required temperature range.

An important parameter is the inversion wavelength λ_0:

$$\lambda_0 = np, \tag{5.8}$$

where n is the average refractive index. The inversion wavelength may be roughly approximated as the effective pitch.

Depending on the wavelength (far from, or close to the inversion wavelength) the LC is either transparent or opaque to the incident light. In the region far from the inversion wavelength, the liquid crystal transmits the linearly polarised light without significant attenuation. At the inversion wavelength, one of the circular components of the linearly polarised incident beam is entirely reflected while the other is transmitted.

The device geometry for LC-based temperature probe described in [173] is shown in Fig. 5.15. The LC is placed between two glass lenses attached to the distal end of a fibre-optic catheter. As the LC material, an LC mixture of three-component cholesteric LC was used. The catheter comprises eight optical fibres. One half of the fibres transmits the light from the LED to the LC; the other part of the fibre bundle transmits the light scattered from the LC to a photodetector. At higher temperatures, the greater part of the incident light is reflected. This reflected light is registered by the photodetector and converted into electric signal (the voltage output on the digital panel of the meter). A narrow thermal hysteresis loop (0.1^{o}C or lower) can be observed. Hysteresis and aging of the LC material are disadvantages of such temperature probe, but the recalibration of the temperature probe at periodic intervals allows solving the drift problems. This temperature probe was employed for temperature monitoring in studies of microwave-induced hyperthermia in mice and the interaction of this treatment with ionizing radiation, for investigation of biological effects of microwaves on isolated hearts of mammalia and rats, and for basic studies on the bioeffects of microwave radiation at the cellular level.

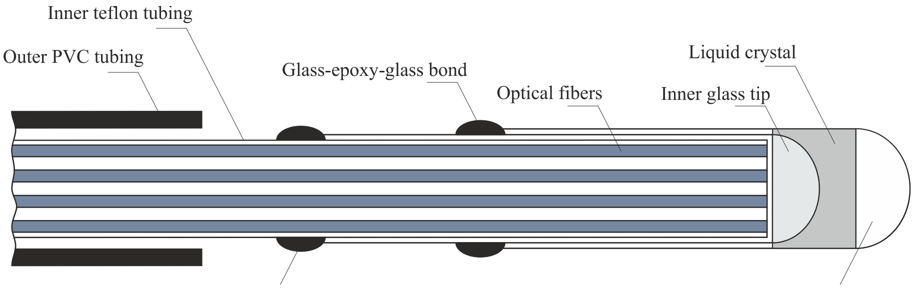

Figure 5.15. Liquid crystal fibre optic temperature probe (after [173])

The benefits of LC-based fibre optic temperature probe for biological and tissue investigations are as follows:

- construction transparent and non-perturbing to electromagnetic fields (because it is completely non-metallic),
- probes relatively small in size (1-2mm in diameter; can be easily implantable into biological tissues),
- probes provide temperature versatility and retain thermal sensitivity for many months,
- probes can be surface sterilized and used under aseptic conditions,
- probes provide continuous monitoring of tissue temperature response to irradiation with 0.1^{o}C accuracy.

The disadvantage is a slight but significant decay in response to repeated temperature cycling. For the drift compensation, periodic calibrations are required. Therefore, that temperature probe is employed in relatively short-term experiments.

The operating of the other LC-based fibre-optic temperature sensors is similar to the probe described above. The LC cell (with cholesteric) is illuminated by the light beam from a light source. Because of the LC selective reflection in the direction of the detector, the light (the wavelength of which is directly related to the environment temperature) is spread. The temperature change involves the change in helical pitch, and the selective reflection is registered by the detector. It should be noted that LC-based sensors can be used not only for temperature measurement, but also for pressure measurement, as well as for the magnetic and electric field measurement. The required range of the measured values is determined by the choice of the LC mixtures. In order to construct the LC-based fibre-optic sensors, both the LC materials and fibre lightguides should be researched carefully [77, 192]. Depending on the type of LC material, different requirements should be fulfilled. In the case of the nematic materials, the initial orientation of LC should be homeotropic, and the refractive index of the core should lie within the following interval: $n_o < n_c < n_e$. In the case of the induced cholesteric, the initial texture should be planar, the wavelength of the radiation spread in the lightguide should be commensurable with the helical pitch, and the refractive index of the core should be less than that of the induced cholesteric. The refractive index of LC material should be constant in the LC layer, and should lie within the range from n_{min} to n_{max} [190].

The block diagram of an LC-based fibre-optic temperature sensor is shown in Fig. 5.16.

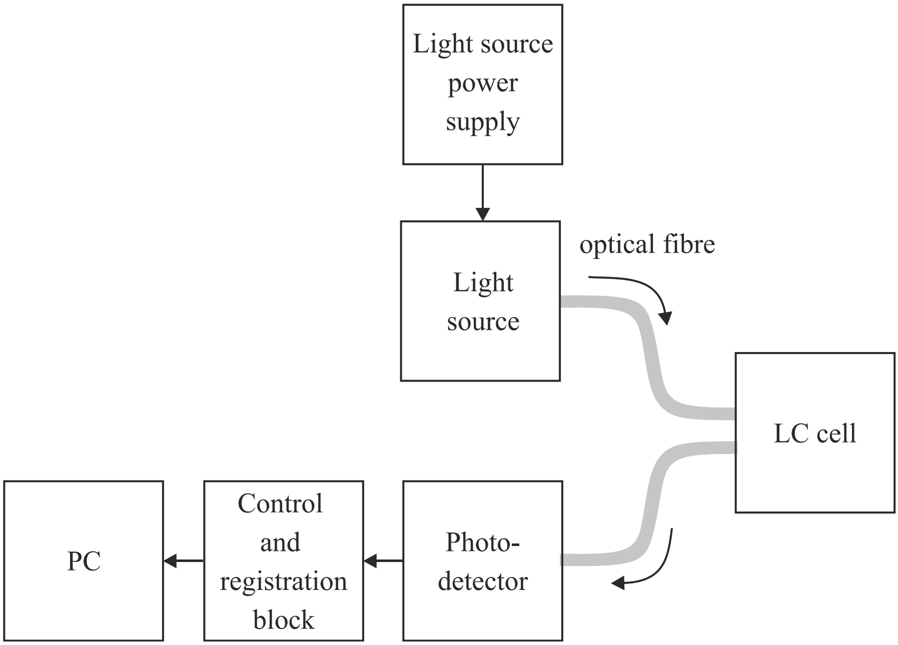

Figure 5.16. Block diagram of an LC-based fibre-optic temperature sensor

The electronic circuit of that temperature sensor can be the same as for the temperature sensors described above (Fig. 5.11 and Fig. 5.14). The use of the optical fibre does not require any redesigning of sensor's electronic circuitry. Only the algorithm of signal processing should be modified, since the sensor's operation is controlled by the algorithm implemented in the microprocessor. Such modification is caused by the difference in spectral characteristics between the light passed through and reflected from the LC cell. The sensor parameters remain unchanged.

The abovementioned electronic circuits of the temperature sensors can be employed with the LC-based sensors shown in Figs. 5.17 and 5.18. In these cases, the temperature sensors do not require the reference voltage source which supplies the primary transducer (the LC cell). The measured temperature is determined by the LC mesophase existence. In the sensor's construction shown in Fig. 5.17, the application of the spacers allows to obtain an unfilled area. This area is filled with the LC material [74].

The multifunctional fibre-optic sensor shown in Fig. 5.18 can be applied not only for temperature measurement, but also for pressure, electric and magnetic field measurements, etc. [77, 118].

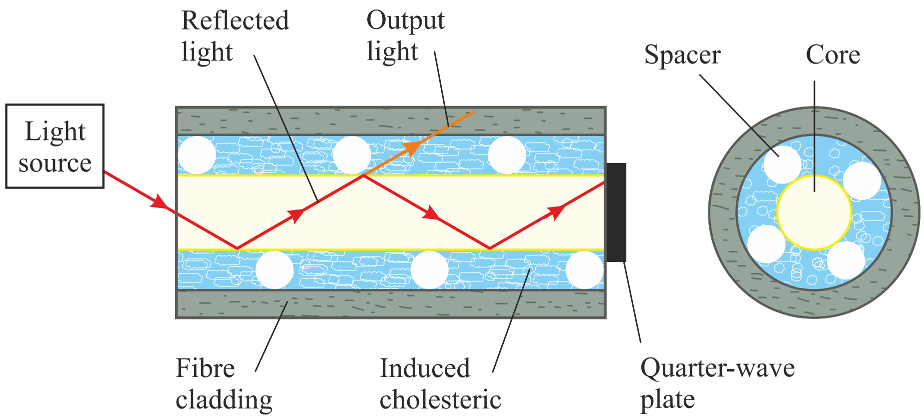

Figure 5.17. The LC-based temperature sensor with LC cladding

The sensor consists of the lightguide with the capsule containing LC inserted into the cladding. The light from the laser is fed into the end of the lightguide and spread inside the fibre's core. The value of the refractive index of the induced cholesteric is close to the refractive index of the cladding; thus, the condition of full internal reflection is fulfilled. If no temperature influence occurs, there is no external light radiation in the place of the LC inserting, because the selective reflection of the LC involves the return of the light beam back into the lightguide. Under the temperature influence, the helical pitch and the refractive index are subject to change.

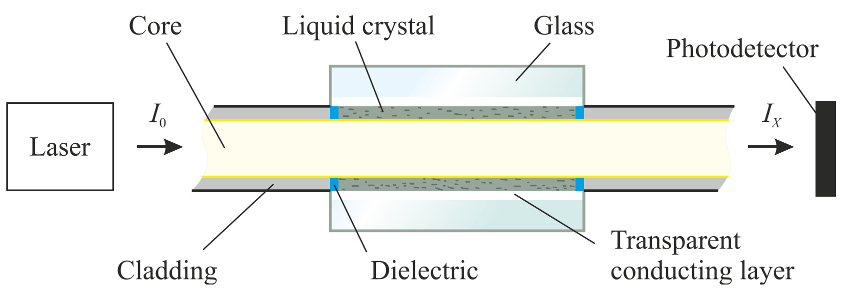

Figure 5.18. Fibre-optic temperature sensor with a capsule containing LC material

The condition of selective reflection is not met, and an external light radiation in the place of the insertion of the LC capsule appears; the light is modulated. After passing through the lightguide containing the LC capsule, the light is registered by the photodetector. The photodiode current vs. temperature relationships for different LC materials are depicted in Fig. 5.19.

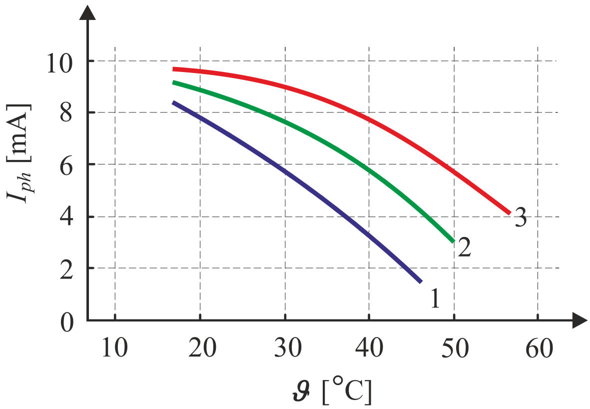

Figure 5.19. Relationships between the photodiode current and temperature for 5 CB+10% LC-440 with 0.5% cholesteric derivatives: 1 – cholesterylpropionat, 2 –cholesterylcaprilate, 3 – cholesteryllaurate

The sensitivity of such sensor is dependent on the birefringence value and the length of the capsule. The relationship between the sensor sensitivity and the length of the LC capsule is shown in Fig. 5.20.

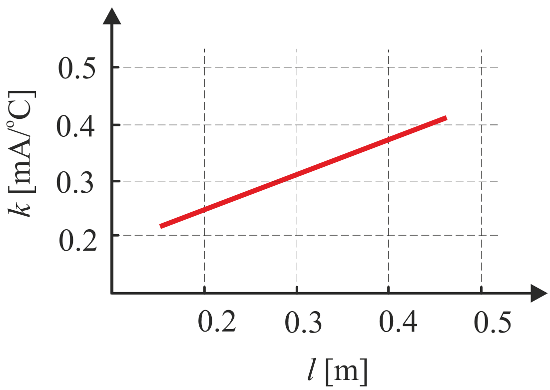

Figure 5 .20. Relationship between the sensor sensitivity and the length of the capsule containing LC (5 CB+10% LC-440 with 0.5% cholesterylpropionat)

Another construction of an LC-based temperature sensor is shown in Fig. 5.21 [144].

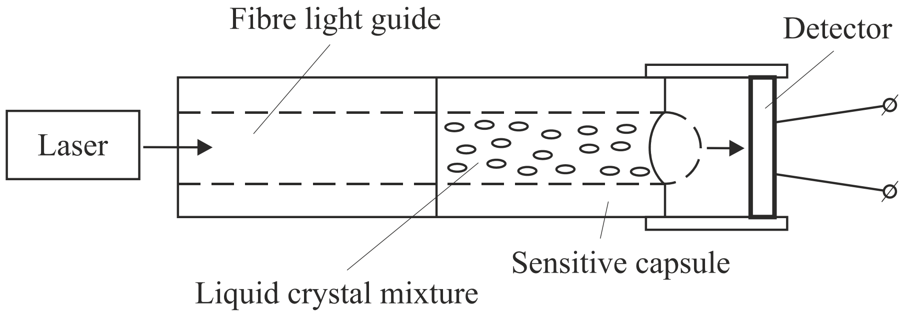

Figure 5.21. Design of an LC-based temperature sensor

The sensitive element of the sensor is the capsule filled with the LC material. The refractive index of the LC material is lower than that of the capsule. The influence of the temperature involves the change in the output beam intensity, which is registered by photodetector.

5.5. Liquid crystal-based colour-changing temperature sensors

The peculiar properties of the blue phase (BP) and the narrow blue phase temperature range can be applied for temperature registration, e.g. temperature sensor design. The narrow temperature range of BP implies sensor's high sensitivity to temperature change, i.e. fixation of given temperatures. In order to choose the given Bragg wavelength, one should use the liquid crystal materials with appropriate helical pitch.

The use of the liquid crystals containing blue phases as temperature sensitive material in temperature sensors allows visualizing the attainment of certain temperatures of the objects. The chosen liquid crystal material should exhibit the same temperature of the cholesteric-blue phase transition as the fixed temperature of the object to be measured. During the phase transition, there is the wavelength step change in the selective light reflection, which results in the colour step change. The human eye can distinguish the colour changes corresponding to the temperature changes. In some cases, it offers sufficient accuracy for revealing the fixed temperature of an object.

The operating principle of the sensors using the blue phase properties is based on the colour change in areas where the temperature exceeds the given value. In areas where the temperature is critical, blue-phase selective reflection occurs. These sensors can be employed for the visualisation of the points or areas of the investigated object where the fixed temperature is exceeded, and also where the temperature has exceeded the fixed temperature for only a short time, and then has decreased a bit to lower values. The latter application is based on the effect of blue phase overcooling, i.e. that the temperature of the cholesteric-blue phase during heating-induced transition can be a few degrees higher than at cooling.

The construction of LC-based colour-changing temperature sensor is shown in Fig. 5.22 [80, 124]. It consists of two polyethylene terephthalate (PET) films (one transparent, and the other blackened) with liquid crystal material between them. To define the thickness of the gap between the films, different structures (shown in Fig. 5.22) can be used: the grid, crimped, capsulated or scantling (metal or polymer) structure, in order to ensure even thickness of the LC layer between the films.

The liquid crystal material used in this type of temperature sensor can be a chiral nematic in which the blue phase with selective reflection exists in the visible part of the spectrum. It allows visualising the areas of the object under investigation over which the temperature has achieved some fixed values, in form of isotherms (the strip of the colour corresponding to Bragg wavelength of the blue phase). The temperature sensor is attached to the object of investigation making close contact of the blackened film with the object. In the areas where the temperature exceeds the cholesteric-blue phase temperature transition and does not exceed the temperature of the transition to the isotropic phase, the colour corresponds to the wavelength of the selective reflection of the blue phase. The colour of these areas differs from the areas of lower temperatures. In the areas where the temperature is higher than the temperature of the transition to the isotropic phase, there will be no light reflection, and their colour will be black.

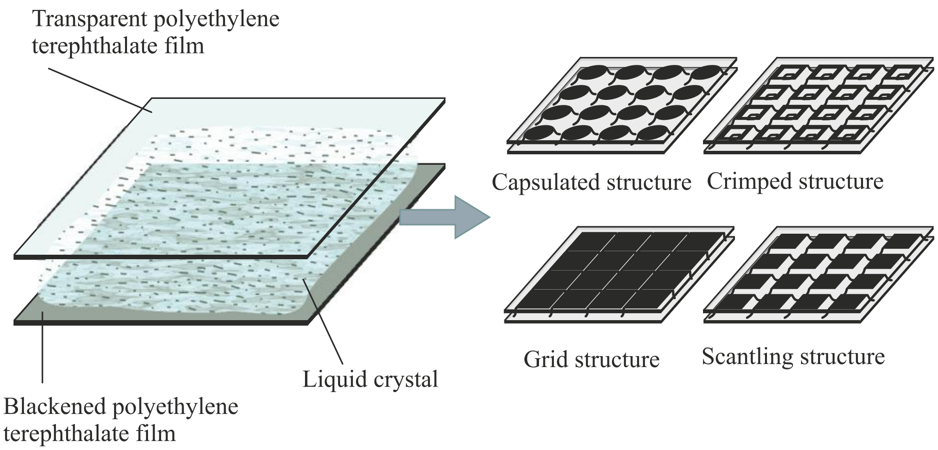

Figure 5.22. Construction of LC-based colour-changing temperature sensor

Another application of the colour-changing sensor is related to the visual indication of the temperature deviation from the fixed temperature when the temperature should be stable, for example for biological objects, where the temperature rise of the microorganisms or cells higher than 0.1°C leads to their overheating and death. Therefore, it is very convenient to use colour-changing sensors in the case of simultaneous temperature monitoring of many objects. Such application of temperature sensors is simple, low cost, and provides sufficient accuracy.

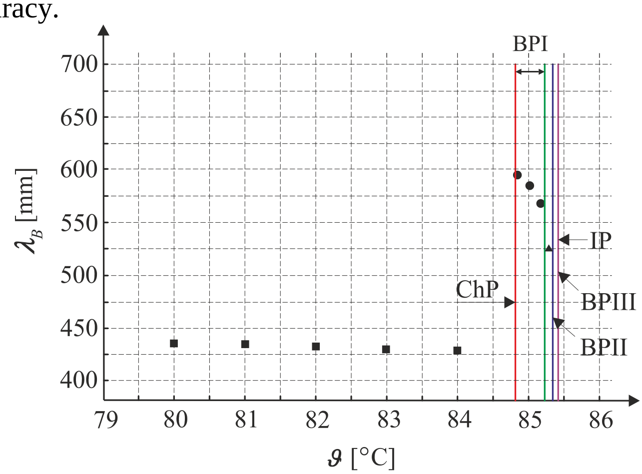

Figure 5.23. Relationship between the Bragg wavelength and temperature for the mixture of 15 weight % cholesteryl chloride – 85 weight % cholesteryl pelargonate

BPI and BPII are characterised by highly selective reflection at different wavelengths. Therefore, when choosing the liquid crystals mixtures with different component concentrations, one can obtain two-colour strips representing the fixed temperature. For example, the relationship between the Bragg wavelength in the cholesteric and blue phases for the mixture of 15 wt. % cholesteryl chloride + 85 wt. % cholesteryl pelargonate confirms the possibility of BPs application for the visualisation of the areas with fixed temperatures (Fig. 5.23). The temperature colour sensor can be realized using such mixture because it does not disturb the temperature field of the object under investigation. The response time (0.1...0.2 s) to changes in temperature of the sensor is determined by the duration of the change of the cholesteric helix into the helix with another twist pitch during the cholesteric-BP phase transition. The investigations of this mixture revealed that its use in temperature sensors is reasonable.

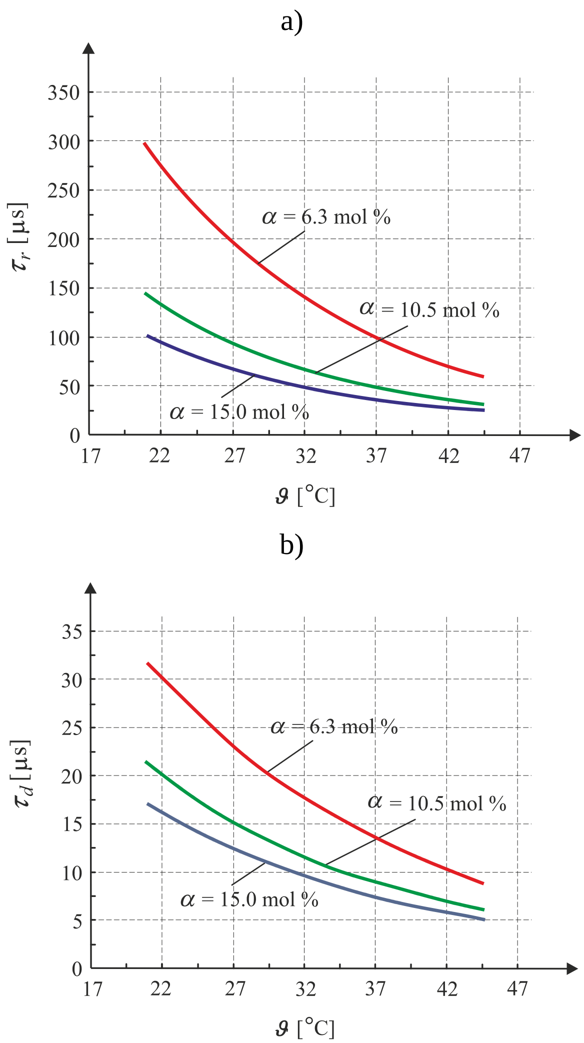

Figure 5.24. Temperature dependence of the electro-optical response time for the polymer stabilised blue phases (polymer fraction: α = 6.3, 10.5, 15.0 mol %): (a) for the rise process and (b) for the decay process [93]

The the polymer-stabilised and polymer-dispersed LCs can also (like the abovementioned LCs) be applied in the "on-off" type temperature sensors [52]. The investigations of electro-optical effect in polymer-stabilised blue phases [93, 148-149] have shown that the response times of polymer-stabilised blue phases (in the order of microseconds) are shorter than for the nematic liquid crystals (of millisecond order) (Fig. 5.24). This property can be taken into account during temperature sensor design.

Summary

LC-based temperature sensors are an alternative to contacting sensors and can be employed in operating conditions where the use of thermocouples or resistance temperature sensors is not reasonable. The parameters of the LC-based temperature sensors depend on the properties and characteristics of the applied LC materials. Therefore, in order to predict and to modify the parameters of new LC materials, the thorough study of LC materials is a topical issue. An accurate knowledge of the properties of LCs allows the researcher to find practical applications of LC materials in temperature sensors. In designing LC-based temperature sensors, the electrooptical effects in LCs are frequently employed.

The proposed LC-based temperature sensors employ the selective reflection in LCs (the designs based on prism, and the fibre-optic designs), the cholesteric-nematic transition (threshold-based temperature sensor employing cholesteric-nematic transition), or properties of the blue phase (liquid crystal-based colour-changing temperature sensor). The temperature measurement range of the LC-based temperature sensors is limited to temperature interval of the existence of the LC phase. The temperature measurement accuracy depends on the type of the used LC material. For temperature sensors based on the selective reflection in liquid crystals (e.g. the KET90600 material), the measured temperature ranges from 20^{o}C up to 80^{o}C, and the sensitivity is 0.25^{o}C/nm. For the threshold-based temperature sensor employing cholesteric-nematic transition, the measured temperature ranges from 17^{o}C to 57^{o}C and the temperature measurement accuracy is equal 0.05 ^{o}C for given LC materials.

In designing LC-based temperature sensors, two current issues emerge: the use of the new LC materials, and the elaboration of the new constructions of sensors. Selected solutions proposed by the author can broaden the field of the LC-based temperature sensor designs.

6. Metrological instrumentation for temperature sensors

The modern industrial facilities are characterised by world-wide use of both local and global automation systems based on the control devices, and on measurements of technological parameters of a process, using various sensors (including temperature sensors). The reliability and proper functioning of industrial facilities, in particular of control systems which are responsible for security, should be as high as possible. Although the measuring devices are periodically verified in specialised laboratories, it does not guarantee the lack of random failures, or not immediately noticeable noise.

In order to improve the reliability of the automation systems of technological process control, the reliable metrological equipment necessary for proper operation of the measuring and sensoring devices is required. The technical surveillance of all elements of the automated system should be carried out both continuously (during operation) and periodically (also in off-line) mode [217]. Taking into account the large number of potential influence factors and wide range of their changes, there is a need to conduct regular metrological supervision of the measuring equipment used in industrial facilities in the course of their operating, without stopping the process.

For metrological checking of the measuring devices which comprise thermoresistive or thermoelectric sensing elements, the code-controlled multi-value standards of resistance, voltage and current are required.

The construction concept of an electric circuit used as a resistance standard for which the equivalent resistance value R_{eq} (or capacitance C_{eq}, or impedance Z_{eq}) seen by the meter inserted between the standard's terminals differs from the true value of the "real" resistance R_{tr} (C_{tr} or Z_{tr}, resp.) physically present inside the box, is a well-known technical solution of working resistance standards (e.g. [87, 179-180, 183]). Such devices are termed "resistance simulators" [242], or "resistance substituters" [89], or "impedance synthetizers" [172], or "resistance imitators" [105]; the latter term is used throughout this chapter.

Resistance imitators can be divided into two classes: passive, made of a circuit with switched resistors, e.g. "wye-delta" (also termed: "star-triangle" or "star-delta") circuits [33, 89, 165], incapable of providing accurate regulation – and active resistance imitators comprising a digitally-controlled voltage calibrator [86, 88] or switched capacitors [253], for which the code-controlled regulation of the value of the imitated resistance in very small steps can be performed.

As the advancement in the IC circuits manufacturing technology has evolved, it has opened the possibility of building code-controlled dividers of current [157] or voltage [200]. Such dividers have much in common with the D/A converters; they allow setting the divider's step output voltage in very small increment of regulation. Precision resistance imitators are commercially available (e.g. [282-283]). A special field of application of resistance imitators are the simulators of the RTD resistance temperature sensors [67, 290].

6.1. Improvement of the code-controlled multi-value resistance standards

Traditional resistance decade boxes have a number of disadvantages, such as difficulties with automation, insufficient resistance resolution per step and complexity of the realisation due to the use of considerable number of resistors of different nominal precision. The current issue is to design the code-controlled multi-value standards based on the active imitators of resistance, voltage and current.

The best place to connect a code-controlled standard is a commutator switch box situated close to the connection between the primary transducer and the measuring channel, since in this case the secondary transducer is checked including its lead wires. However, to put the standard of measurement in this place is often impossible because of the peculiarities of the construction of certain objects, and the influence of destabilising factors such as temperature, humidity, radioactive radiation, emissions from chemical processes, etc. Moreover, in order to organise the checking of metrological characteristics of measuring devices, the simultaneous check of the standard of measurement and the observation of the output signal of the measuring channel should be provided. Therefore, the standard of measurement should ensure the possibility of transmitting a given value of the electrical resistance standard over distance to certain points of the checked device with the required level of accuracy.

A possible solution to the problem is the use of the two-pair wire imitators of resistance. In Fig. 6.1 the structural scheme of an active resistance imitator comprising an auxiliary voltage divider is shown [98]. In that scheme, the influence of the lead wire resistances R_{L2}, R_{L3} and R_{L4}, can be neglected. Only the resistance of the lead wire R_{L1} influences the accuracy of the reproduction of the resistance value. The auxiliary resistive voltage divider inserted between the output of the code-controlled voltage divider and the input of differential amplifier DA2 is applied for ensuring the required accuracy and the resolution per step of resistance imitation.

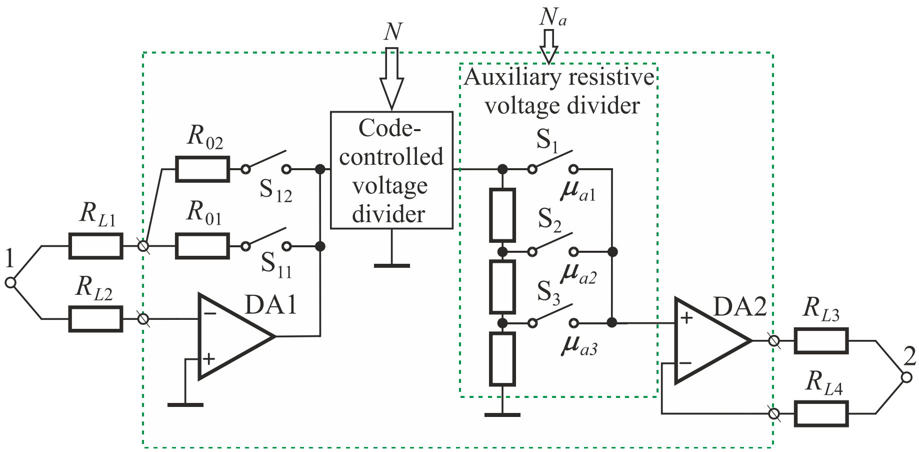

Figure 6.1. Structural scheme of an active resistance imitator with two selector switches for combined range selection [98]

The value of the absolute resistance error due to the resistance of connecting wires is equal to:

$$\Delta R_{im\,j}(R_L) = R_{L1} \cdot \mu\mu_{aj}, \tag{6.1}$$

where R_{L1} is the resistance of connecting wire, μ is the actual division ratio of the code-controlled voltage divider, μ_{aj} is the j-th division ratio (j=1, 2, 3) of the auxiliary voltage divider which can be calculated as follows:

$$\mu_{a\,j} = \frac{R_{im\,max\,j}}{\mu_{max} R_{0i}}, \tag{6.2}$$

where $R_{im\max j}$ is the maximum imitation resistance for μ_{aj}, μ_{max} is the maximum code-controlled divider's voltage ratio for the maximum code value, R_{0i} is the resistance of the i-th standard resistor; in compliance with the scheme in Fig. 6.1, i=1 or 2.

In order to reduce the resistance imitation error, the standard resistor value should be increased according to the following condition:

$$R_{0i} \leq \frac{U_{a\,max}}{I_{l\,max}}, \tag{6.3}$$

where $U_{a\,max}$ is the maximum output voltage of the differential amplifier DA1 (Fig. 6.1), and $I_{l\,max}$ is the maximum value of the input current for the l-th range of imitated resistance, equal to the maximum allowable current of the standard resistor of the l-th selected range.

From mentioned above, the conclusion to be drawn is that the required range of imitated resistance can be selected by switching in a given standard resistor and setting a given division ratio of the auxiliary voltage divider.

The effectiveness of the lead wire configuration of the active resistance imitator can be evaluated compared to the common two-wire connection of a resistance standard. For a two-wire connection, the lead wire resistances R_L introduce an error because they add to the standard resistance value. In the case of two pairs of connecting wires used for the active resistance imitator, the error due to lead wire resistances is largely reduced. Hence, the lead wire error reduction ratio K_r can be determined by the following expressions:

$$K_r = \frac{2R_L}{\Delta R_{im\,j}(R_L)} , \tag{6.4}$$

or in decibels:

$$K_r = 20\lg\frac{2R_L}{\Delta R_{im\,j}(R_L)} = 20\lg\frac{2}{\mu\mu_{a\,j}} . \tag{6.5}$$

The relationships between the lead wire error reduction ratio K_r and $R_{im\,max}$, for the combined range selection of the resistance imitation (according to Table 6.1) and the common range selection with one selector switch, are plotted in Fig. 6.2. The common range selection is performed by change of nominal resistance value of the standard resistor; the values fit a geometric progression, e.g. 10-100-1000-10000 Ω (Fig. 6.2).

Table 6.1. Nominal resistance values of the standard resistor R_{0i}, and division ratios $\mu_{a\,j}$ of the auxiliary voltage divider for combined range selection

Number of the range	$R_{im\,max}$ [Ω]	R_{0i} [kΩ]	$\mu_{a\,j}$	$I_{i\,max}$ [mA]
1	10	1	0.01	10
2	100	1	0.1	10
3	1000	10	0.1	1
4	10000	10	1.0	1

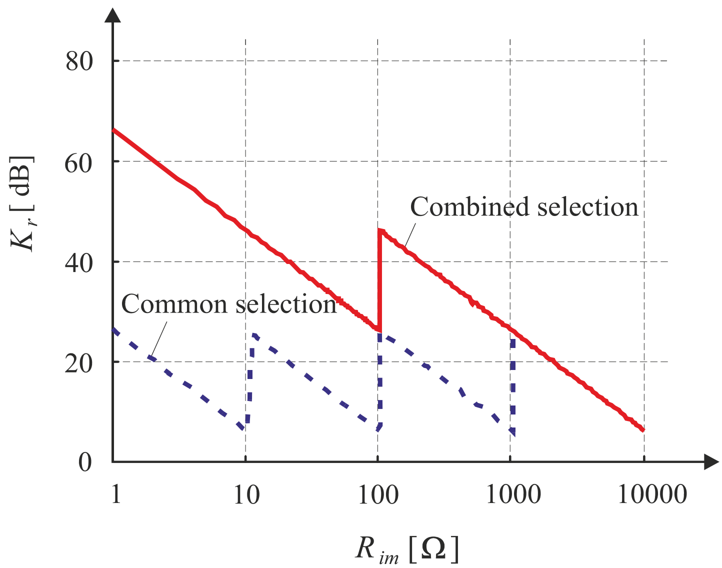

Figure 6.2. Relationships between the lead wire error reduction ratio K_r and the resistance R_{im}, for different range selection of the resistance imitator: 1) combined selection, 2) common selection

The use of combined range selection in the active imitator results in lower number of required high accuracy standard resistors. On the other hand, the resistors of the auxiliary voltage divider can be less accurate because the accuracy of the voltage divider depends on the accuracy of divider's resistance ratio (and not on the accuracies of the individual resistances of the divider's resistors, of which the divider is made up). That can be achieved using resistors fabricated by hybrid planar technology.

In multi-range resistance imitator design, the electronic switches are employed to commute between the resistances of the standard resistors, but the switches' on-state residual resistances significantly influence the accuracy of the resistance imitation. The structural scheme of the active resistance imitator in which the influence of lead wires resistance R_{L1} and of the residual resistances of the commutating switches is reduced, is shown in Fig. 6.3.

The compensating circuit designed to compensate for the influence of lead wires resistance R_{L1} and the residual resistances of the commutating switches S_{11}, S_{12} contains the differential amplifiers DA2, DA3 and DA4. The input of DA2 is connected to a given standard resistor R_{01} or R_{02} through the switches S_{21} or S_{22}, respectively.

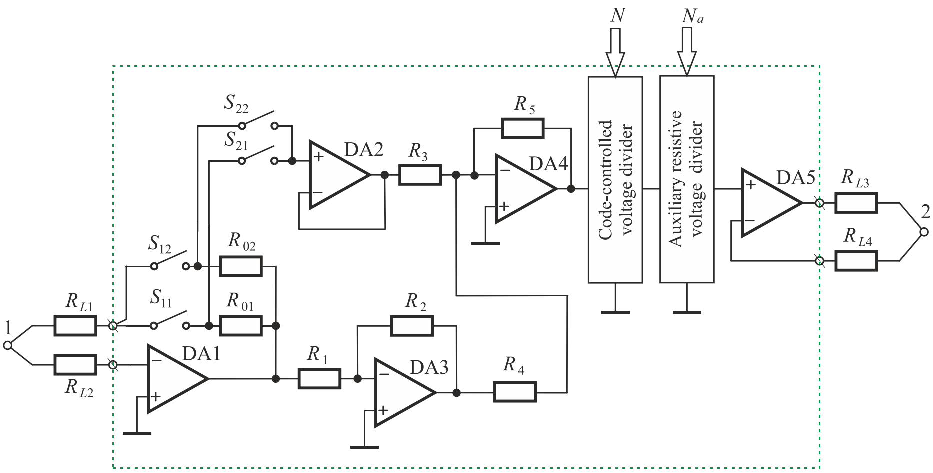

Figure 6.3. Structural scheme of the multirange active resistance imitator

The residual resistances of the switches S_{21}, S_{22} are connected in series to the high-impedance input of DA2. Therefore, their contribution to the value of the imitated resistance can be ignored.

The imitator output voltage between points 1 and 2 is equal to:

$$U_{12} = \left[I_{in}\left(R_{0i} + R_{L1} + r_{1i}\right)\frac{R_2}{R_1}\cdot\frac{R_5}{R_4} - I_{in}\left(R_{L1} + r_{1i}\right)\frac{R_5}{R_3} \right]\mu\mu_{a\,j}\,, \tag{6.6}$$

where I_{in} is the value of input current, and r_{1i} is the on-state resistance of the switch S_{1i}.

If the following condition is met:

$$R_2 R_3 = R_1 R_4\,, \tag{6.7}$$

then the imitator resistance between points 1 and 2 is equal to:

$$R_{im} = R_0 \frac{R_5}{R_3}\mu\mu_{a\,j}\,. \tag{6.8}$$

It can be seen from (6.8) that the circuit depicted in Fig. 6.3 provides the compensation of the influence of lead wire resistances and residual resistances of commutating switches.

6.2. Reduction of the influence of noise on the error of the resistance imitation

To maintain the required metrological characteristics of the active resistance imitators when conveying the values set on the resistance standard over long distances from the device, it is necessary to overcome the influence of the resistances of the lead wires and the influence of both external and internal noise. The increase in global power consumption by industrial equipment − both electromechanical and technological – involves rapid rise in intensity of industrial noise. During the active resistance imitator operation under industrial conditions, the internal and external noise is generated, both inside and outside the electronic circuit. That noise causes erratic changes of the voltage values between the points 1 and 2 of the resistance imitator; in this case, an additional error appears. The value of this error may be higher than the tolerated basic absolute error and sometimes it can exceed the imitated resistance value. The noise can interfere into the measuring circuits, to which the imitator is connected, through the galvanic connections between the parasitic noise source and the measuring circuits, and as the noise induced electromagnetically and electrostatically into lead wires and some parts of the electric circuits of the active resistance imitators.

The equivalent noise voltages interfering in the respective lead wires 1 to 4: e_{n1}, e_{n2}, e_{n3}, and e_{n4} are caused by various parasitic noise sources. The wires 1÷4 are galvanically connected with these noise sources. Thus, in each lead wire a different level of normal mode noise intensity can exist.

For equalisating the noise level between the first and the second wire, the compensating current formation circuit can be employed (Fig. 6.4).

The transfer function of the active resistance imitator can be expressed as follows:

$$R_{im} = R_0\mu + \frac{e_{n4} - e_{n2}}{I_{in}} + \left(\frac{e_{n2} - e_{n1}}{I_{in}} + \frac{I_c R_0}{I_{in}}\right)\mu + \frac{e_{n3}}{k_a I_{in}} \ , \tag{6.9}$$

where e_{n1}, e_{n2}, e_{n3}, e_{n4} are the noise voltages in respective wires, μ is the division ratio of the code-controlled voltage divider, I_{in} is the value of the input current, I_c is the value of the compensating current, R_0 is the value of the resistance of standard resistor, and k_a is the gain of the differential amplifier DA3.

The current formation circuit supplies the compensating current I_c equal to:

$$I_c = \frac{e_{n1} - e_{n2}}{R_0} \ . \tag{6.10}$$

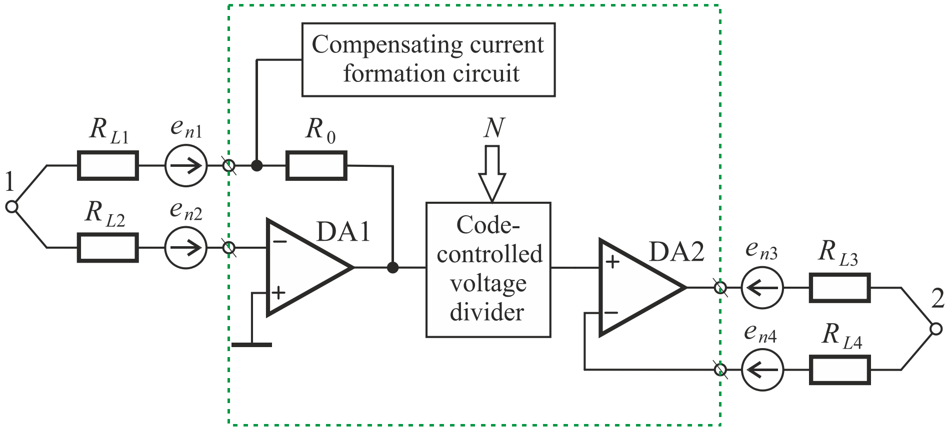

Figure 6.4. Equivalent structural scheme of active resistance imitator with normal mode noise compensation in the first and the second lead wires

Assuming that the formation error is negligible, the transfer function of the resistance imitator is found as:

$$R_{im} = R_0\mu + \frac{e_{n4} - e_{n2}}{I_{in}} . \tag{6.11}$$

The absolute error of the resistance imitator caused by noise is equal to:

$$\Delta_{Rim\,n} = \frac{e_{n4} - e_{n2}}{I_{in}} . \tag{6.12}$$

The noise in the third wire (Fig. 6.4) is reduced due to the negative feedback branch connected around the amplifier DA2 placed in the circuit containing this wire. Thus, the efficient noise reduction depends only on the amplification factor of the differential amplifier DA3.

For equalising the noise level between the second and the fourth wire, two additional capacitors have been inserted into the circuit [105]. The capacitor C_1 is connected between points 1 and 2, and the capacitor C_2 is connected around the differential amplifier DA1. That ensures equal potentials of the variable component between the second and the fourth wire. The equivalent structural scheme of the active resistance imitator with normal mode noise compensation in all connecting wires is shown in Fig. 6.5.

The compensating current formation circuit is built using the differential amplifier DA3 and the resistors R_1, R_2 and R_3. In order to compensate the noise picked upon the first lead wire, the following condition should be met:

$$R_0 R_2 = R_1 R_3 . \tag{6.13}$$

In this case, the influence of the resistance of the first lead wire can be compensated. The resistances of the load wires R_{L2}, R_{L3} and R_{L4} also do not influence the resistance imitation error.

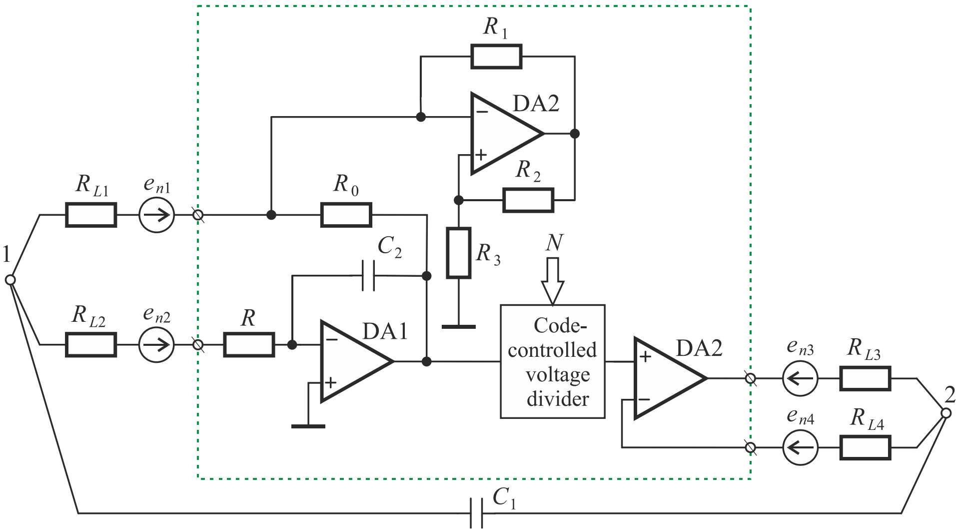

Figure 6.5. Structural scheme of the active resistance imitator with normal mode noise compensation in all connecting wires [105]

The equivalent noise voltage between points 1 and 2 − when neglecting the errors caused by limited amplification factor of op-amps and formation error of I_c − can be expressed as:

$$U_{12n} = \left(e_{n4} - e_{n2}\right)\left[1 - \frac{R_0\left(R_{L2}+R\right)}{R_0\left(R_{L2}+R\right) - \dfrac{1}{\omega^2 C_1 C_2} - j\dfrac{R_0}{\omega C_1}}\right], \qquad (6.14)$$

where ω is the angular frequency of the noise voltage.

The noise reduction coefficient K_n (also: NRC, in decibels) is equal to:

$$K_n = 20\lg \frac{\left[R_0(R_{L2}+R) - \dfrac{1}{\omega^2 C_1 C_2}\right]^2 + \left[\dfrac{R_0}{\omega C_1}\right]^2}{\dfrac{1}{\omega C_1}\sqrt{\left[\dfrac{1}{\omega^3 C_1 C_2^{\,2}} + \dfrac{R_0^{\,2}}{\omega C_1} - \dfrac{R_0(R_{L2}+R)}{\omega C_2}\right]^2 + \left[R_0^{\,2}(R_{L2}+R)\right]^2}}. \qquad (6.15)$$

The noise reduction coefficient depends on the values of R_0, R, C_1 and C_2. The relationships between the noise reduction coefficient K_n and R, C_1 and C_2 are graphed in Figs. 6.6, 6.7 and 6.8, respectively.

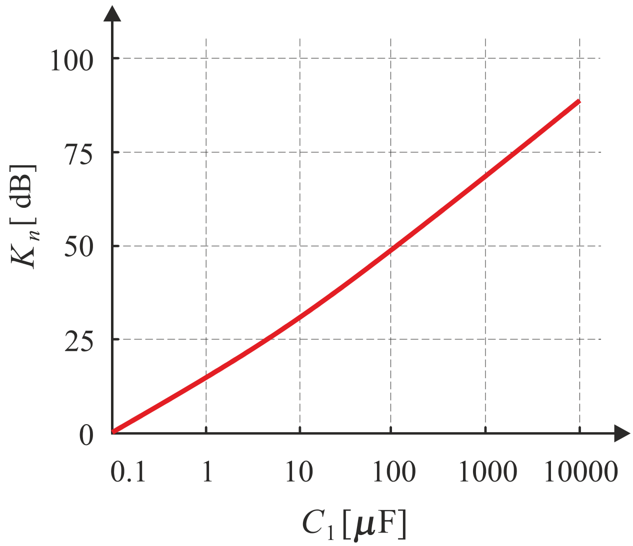

Figure 6.6. Relationship between the noise reduction coefficient K_n and the capacitance C_1, at C_2=10 µF and R=10 kΩ

From Fig. 6.8 it can be seen that the noise reduction coefficient increases by 20 dB when either the capacitance C_1 or the resistance R increases 10 times. The increase in value of C_1 and R is limited: firstly, by the transition time of the input signal; secondly, by the differential amplifier input resistance; and finally, by the size and residual resistance of the capacitor. The optimal value of the capacitance C_2 is 10 µF (Fig. 6.8).

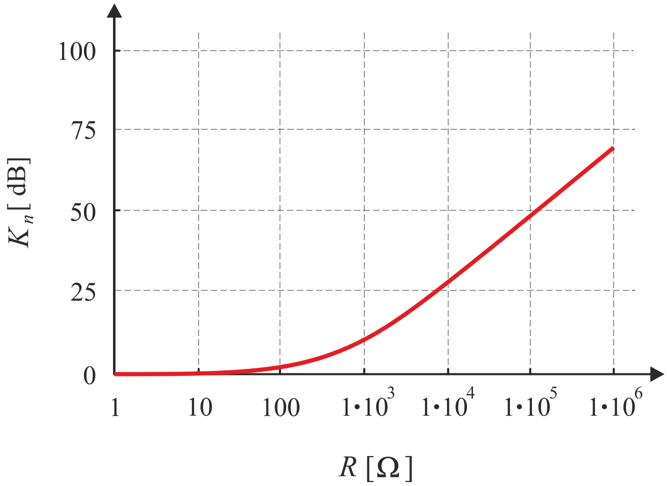

Figure 6.7. Relationship between the noise reduction coefficient K_n and the resistance R, at C_1=10 μF and C_2=10 μF

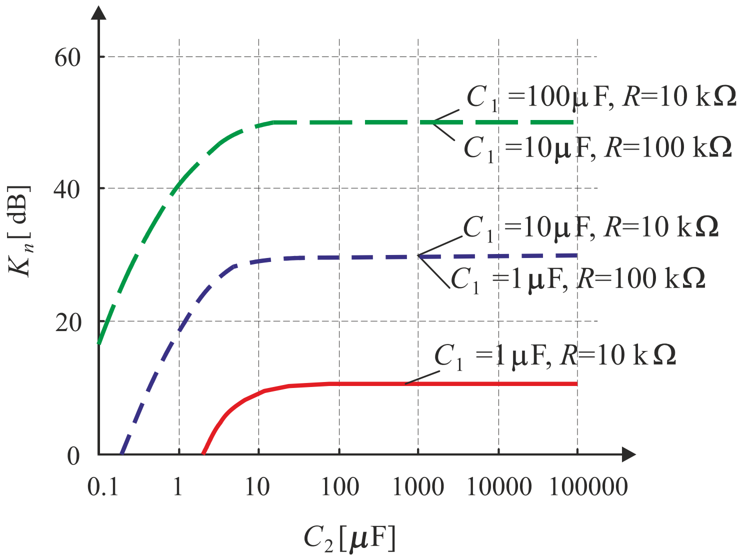

Figure 6.8. Relationship between the noise reduction coefficient K_n and the capacitance C_2 at various C_1 and R

6.3. Multi-range resistance standard fabricated by thin film hybrid technology

The semiconductor technology does not ensure the manufacturing of analogue devices with high metrological characteristics. This is due to the difficulties encountered when designing the precision passive components. The application of the thin film hybrid technology allows achieving high metrological parameters of the resistance, voltage and current standards. Especially high metrological parameters are achieved for the resistors and resistive dividers. The deposition of the resistors on a single dielectric substrate during one technological process ensures the same temperature and time changes of the nominal values for the resistors. Therefore, the influence of the temperature and time changes of the resistor values on the divider's voltage ratio is compensated. For the design of high stability resistors, it is reasonable to use the double-layer resistive structures with the same absolute values of TCRs but of opposite sign [24].

As the result of investigations of technical parameters of the components fabricated using thin film hybrid technology, the following structural scheme of active resistance imitator was proposed (Fig. 6.9) [101]. The scheme consists of the analogue and the digital section. The analogue section of the active resistance imitator comprises a current-to-voltage converter, a pulse-to-voltage converter, and an output cascade.

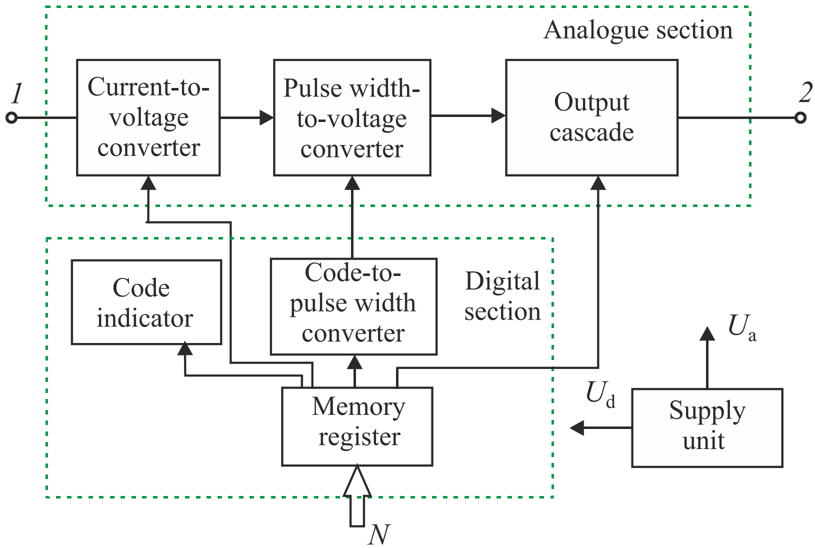

Figure 6.9. Functional scheme of the active resistance imitator

The digital section of the active resistance imitator consists of a memory register, an indicator of the memory register code, and a code-to-pulse converter. The memory register and the code-pulse width converter are based on serial digital ICs. The indicator of the memory register code is based on LEDs. The code-pulse width converter is based on two pulse counters, one of which forms the period T_p and the other forms the time interval τ proportional to the digital input code N.

The principle scheme of the input current-to-voltage converter is shown in Fig. 6.10. It is based on the differential amplifier DA1 with the standard resistor R_{0i} in the feedback loop. The resistors R_{0i} are applied for selecting different ranges of the resistance imitation. The resistors R_{01}, and R_{02} are connected through the switches S_{11}, and S_{21}, respectively. In order to eliminate the residual resistances of the switches, the supplementary differential amplifier DA2 is applied. The amplifier's input is connected through the switches S_{12} or S_{22} to the respective standard resistor R_{0i}, depending on the chosen range.

The output voltages of the differential amplifiers DA1 (U_1) and DA2 (U_2) can be expressed as follows:

$$U_1 = I_{in} \cdot \left(R_{L1} + R_{0i} + r_{i1}\right), \tag{6.16}$$

$$U_2 = I_{in} \cdot \left(R_{L1} + R_{0i}\right), \tag{6.17}$$

where I_{in} is the input current, R_{L1} is the first lead wire resistance, R_{0i} is the resistance of the standard resistor of the respective range, r_{i1} is the on-state resistance of the switch S_{i1}.

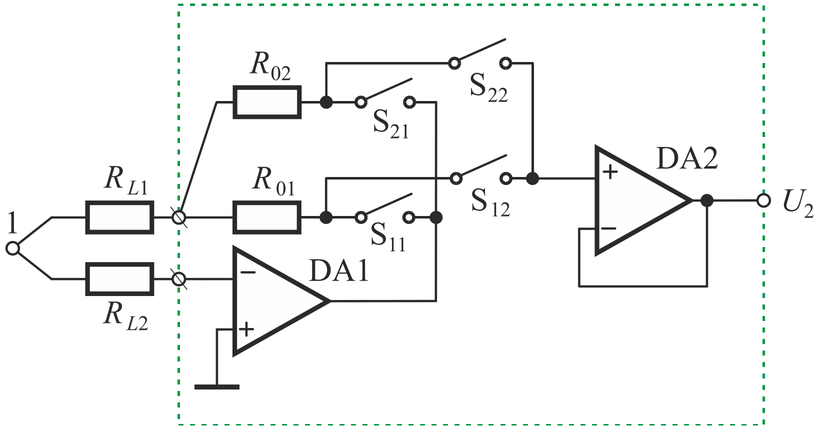

Figure 6.10. Principle scheme of the input current-to-voltage converter

The resistances of the switches S_{i2} do not influence the accuracy of the voltage formed using the current-to-voltage converter because they are connected to the high-ohmic input of the differential amplifier DA2.

The output voltage of the differential amplifier DA2 is put on the input of the pulse-to-voltage converter. The principle scheme of the pulse-to-voltage converter, comprising the additional divider and the voltage follower, is shown in Fig. 6.11.

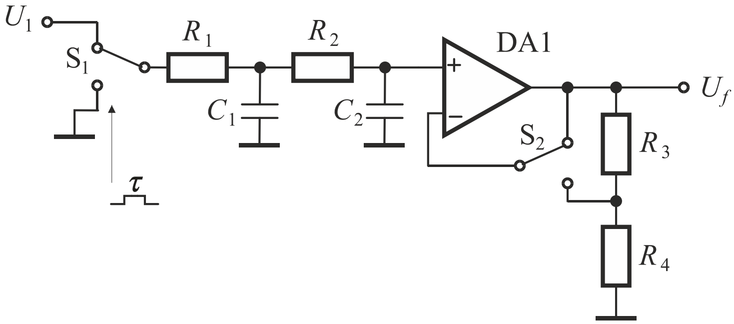

Figure 6.11. Principle scheme of the pulse-to-voltage converter

The input signal of the code-pulse width converter is passed through switch S_1. This voltage signal is averaged within *RC*-filter and put into the input of the differential amplifier DA1, which can operate either as voltage follower or an amplifier. The operating mode is chosen using the switch S_2. The gain k_d is determined by the resistors R_3 and R_4. The amplification mode of the differential amplifier DA1 ensures the resistance imitation with the values higher than the nominal resistance values over the selected range.

The output voltage of the pulse-to-voltage converter is equal:

$$U_f = U_1 \frac{\tau}{T_p} = k_d I_{in} \left(R_{L1} + R_{0i} \right) \frac{\tau}{T_p}, \tag{6.18}$$

where τ denotes the width of the output pulse of the code-to-pulse converter, and T_p is the pulse repetition period.

In order to ensure high linearity of the output voltage of the pulse-to-voltage converter, and hence to obtain better metrological parameters of the active resistance imitator, the time constant of charging τ_c and of discharging τ_d the *RC*-filter should be equal.

The output voltage of the pulse-to-voltage converter is put on the input of the output cascade, the scheme of which is shown in Fig. 6.12.

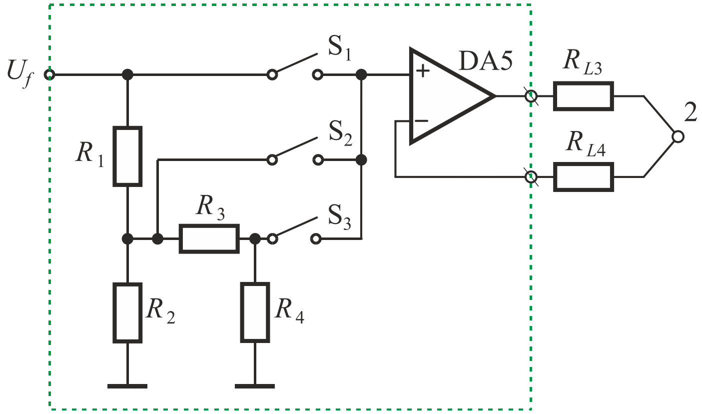

Figure. 6.12. Principle scheme of the output cascade

The output cascade consists of the two-stage resistive voltage divider and the differential amplifier DA5. The two-stage resistive divider is employed in order to reduce the influence of the instability of the low value thin film resistors.

The value of the imitated resistance is equal to:

$$R_{im} = k_d \mu_2 \left(R_{L1} + R_{0i}\right)\frac{\tau}{T_p}, \tag{6.19}$$

where μ_2 is the two-stage resistive divider's voltage ratio.

For τ=N and T_p=N_{max}, where N is the input code, equivalent with the imitator resistance value, and N_{max} is the maximum value of the input code, the following expression can be obtained:

$$R_{im} = k_d \mu_2 \left(R_{L1} + R_{0i}\right)\frac{N}{N_{\max}}. \tag{6.20}$$

It can be seen from the expression (6.20) that for reducing the influence of the wire resistance R_{L1}, the following high resistance R_{0i} ($R_{L1} \ll R_{0i}$) should be chosen. The influence of the wire resistances R_{L2}, R_{L3} and R_{L4} is fully compensated.

The proposed circuit of the active imitator allows the user to select certain ranges using standard resistor and the resistive divider's voltage ratio, depending on the required accuracy of the imitation of the resistance, and the output current value. The expansion of the range of the imitation of the resistance is obtained by the gain of the output cascade of the differential amplifier of the pulse-to-voltage converter.

6.4. Multi-value resistance, voltage and current standards for temperature sensors

At present, many designs of combined calibrators of voltage, current and resistance are available (e.g. [56, 279, 288]); some calibrators are also equipped with the built-in function of RTDs simulation[210, 295].

It is expedient to design the combined multi-value standard of voltage, current and resistance on the base of the active resistance imitator [19]. In this case, the main components of the active resistance imitator are fully exploited when the multi-value standard operates in the mode of the voltage or current calibrator. The supplementary units in the voltage or current calibrator operating mode are the reference voltage or current source, and the commutating elements for selecting the respective operating mode.

The combined microelectronic multi-value standard of voltage, current and resistance used for imitating the signals of the resistance temperature sensors, thermocouples, and measuring transducers is shown in Fig. 6.13. The structural scheme of the standard consists of a reference voltage source, a current-to-voltage converter, an operating mode selector, a code-controlled voltage divider, an auxiliary voltage divider, an output voltage follower, a control device, a code converter, an indicator of the zero voltage level, and a power supply unit.

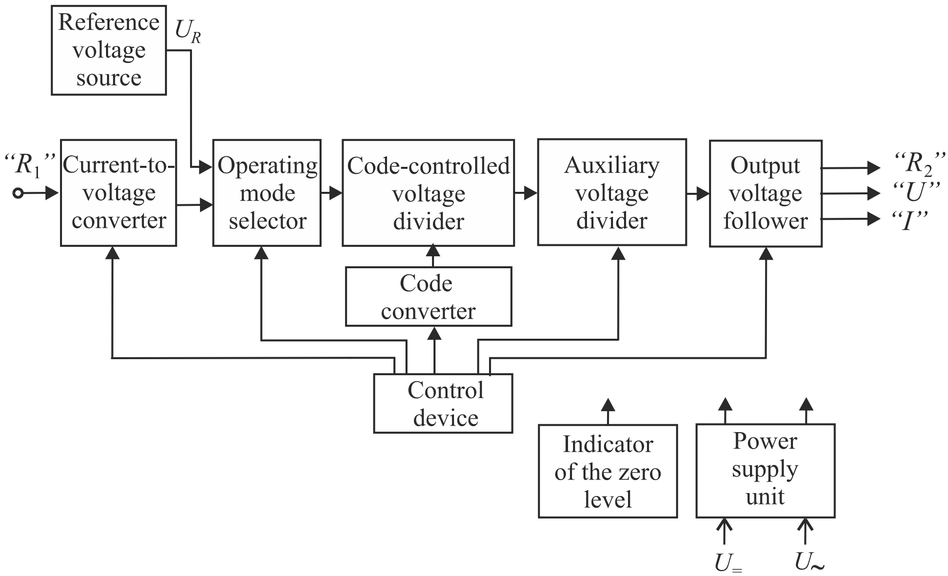

Figure 6.13. Structural scheme of the calibrator-imitator of the voltage, current and resistance

In the resistance imitator mode, the input terminal "R_1" is connected to the current-to-voltage converter, which in turn is connected through the operating mode selector switch to the input of the code-controlled voltage divider. The principle scheme of the current-to-voltage converter (Fig. 6.14) is based on the differential amplifier DA1 with bipolar emitter follower built with two transistors Q1 and Q2. The resistors R_5, R_6 and R_7 are applied for protecting the differential amplifier and the transistors Q1 and Q2 against current overloads. In order to protect the inverting input of the differential amplifier against voltage overloads, the limiter based on the resistor R_2 and the diodes D1 and D2, is employed. The resistors R_1, R_3 and R_4 are applied for setting the zero voltage level at the output of the current-to-voltage converter.

The output voltage of the current-to-voltage converter U_1 is determined by the following expression:

$$U_1 = I_{in}\left(R_{0i} + R_{L1}\right), \tag{6.21}$$

where I_{in} is the input current between the input "R_1" and the output "R_2"; R_{0i} is the resistance of the standard resistor of the i-th range.

The maximally tolerated input current I_{max} is determined by the resistance value of the standard resistor R_{0i} and the output voltage range U_{max} of the differential amplifier placed inside the current-to-voltage converter.

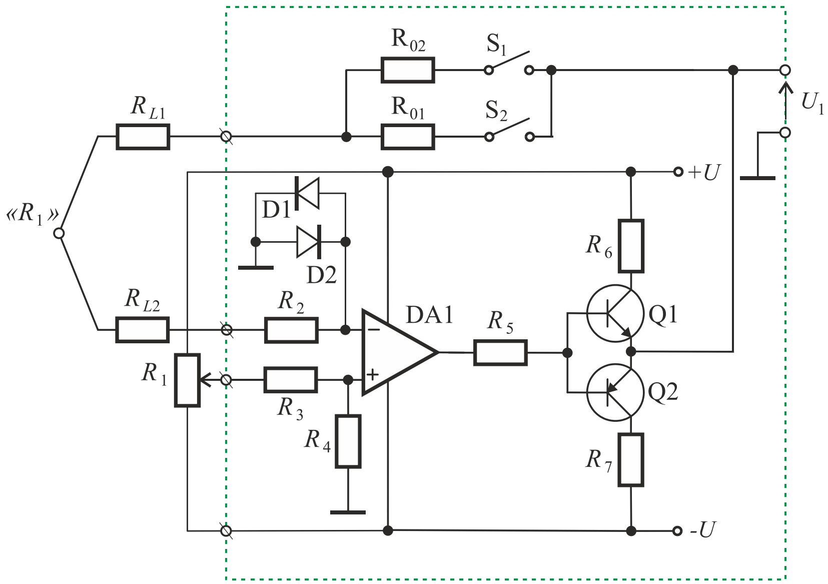

Figure 6.14. Principle scheme of the current-to-voltage converter

The code-controlled voltage divider is based on the *R*-2*R* binary resistive ladder. The resistors *R* and 2*R* are fabricated using the film hybrid technology, and are characterised by high metrological parameters. The resistor's nominal value *R* is made by placing a pair of 2*R* in parallel. Therefore, the process of the resistor adjusting is simplified because only the resistors of the same nominal value are employed. The required value of the imitating resistance is set in the decimal code by 10-position switches, which are included in the control device, using decimal code numbers. That decimal-code number is converted by the decimal-to-binary code converter into a binary code. The binary output code is used to control the switching of the appropriate resistors of the *R*-2*R* binary ladder between the output of the current-to-voltage converter and the ground bus. In this case, the output voltage of the code-controlled voltage divider is equal to:

$$U_2 = I_{in} R_{0i} \sum_{q=1}^{N} a_q \cdot 2^{-q} , \qquad (6.22)$$

where a_q is the coefficient equal 0 or 1 depending on the connection of the appropriate resistors either to the common ground bus or to the output of the current-to-voltage converter, respectively; *q* is the binary place of the bit in the binary output code, *N* is the number of the binary digits.

The increase of the number of measuring ranges of the resistance imitation is achieved by the use of the auxiliary decade voltage divider with the division ratios in decade progression. The division ratio of the auxiliary decade voltage divider is obtained by connecting additional resistors in series configuration to the output of the code-controlled voltage divider. The resistances of these resistors are determined by the following expression:

$$R_{aj} = \frac{R_{out}}{k_{aj} - 1} , \qquad (6.23)$$

where R_{out} is the output resistance of the resistive ladder of the code-controlled voltage divider, and k_{aj} is the value of the auxiliary divider's division ratio of the respective measuring ranges.

The division ratio of the auxiliary voltage divider is equal to:

$$\mu_{a\,j} = \frac{1}{k_{aj}} = \frac{R_{aj}}{R_{out} + R_{aj}} . \qquad (6.24)$$

The output voltage follower is applied for providing the output voltage of the auxiliary voltage divider U_a to the terminal "R_2". For example, an output voltage follower circuit can be based on the differential amplifier DA1 with bipolar emitter follower built with transistors Q1 and Q2 (Fig. 6.15).

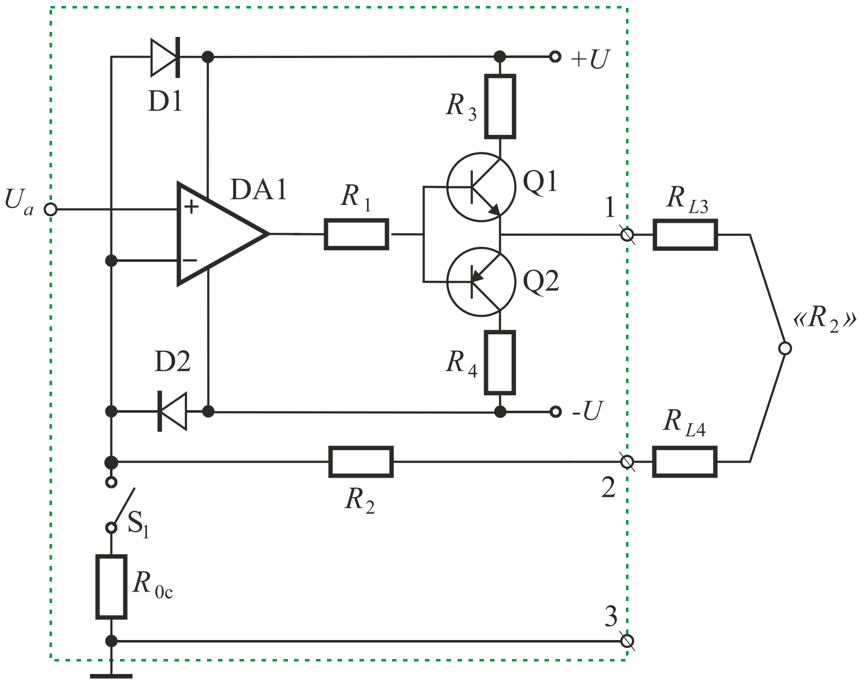

Figure 6.15. Principle scheme of the output voltage follower

In order to reduce the influence of lead wires, the input terminal "R_2" of the resistance imitator is connected with the terminals "1" and "2" of the output voltage follower by a pair of wires. The resistance R_{L4} is connected in series with the high-ohmic input of the differential amplifier DA1; hence, its influence can be neglected. The resistance R_{L3} is inserted in the feedback loop, and its contribution decreases g times (g is the gain of the differential amplifier DA1).

The output voltage of the output voltage follower can be determined by the following expression:

$$U_3 = I_{in} R_{0i} \mu_{ai} \sum_{q=1}^{N} a_q \cdot 2^{-q} . \quad (6.25)$$

The value of the imitated resistance is equal to:

$$R_{im} = R_{0i} \mu_{ai} \sum_{q=1}^{N} a_q \cdot 2^{-q} . \quad (6.26)$$

If the combined standard operates in the mode of the voltage calibrator, the output voltage of the reference voltage source through the operating mode selector switch is put on the input of the code-controlled voltage divider. The output voltage of the output voltage follower is equal to:

$$U = U_R \mu_{ai} \sum_{q=1}^{N} a_q \cdot 2^{-q}, \quad (6.27)$$

where U_R is the value of the output voltage of the reference voltage source.

The reference voltage signal is taken between the terminals "1" and "2", and the common bus (point "3"). Depending on the load resistance and lead wire resistance, the one-wire or two-wire connections can be used. If one-wire line is employed, the points "1" and "2" are short-circuited.

In the operating mode of the current calibrator, the resistor R_{0c} is connected through the switch S_1 to the inverting input of the differential amplifier DA1. The output voltage follower operates in the mode of the voltage-to-current converter, and the load resistance is connected to the points "2" and "3". In this case, the output current of the output voltage follower is determined by the following expression:

$$I = \frac{U_R}{R_{0c}} \mu_{ai} \sum_{q=1}^{N} a_q \cdot 2^{-q}, \quad (6.28)$$

where R_{0c} is the resistance of the standard resistor of the output voltage follower operating in the mode of the voltage-to-current converter.

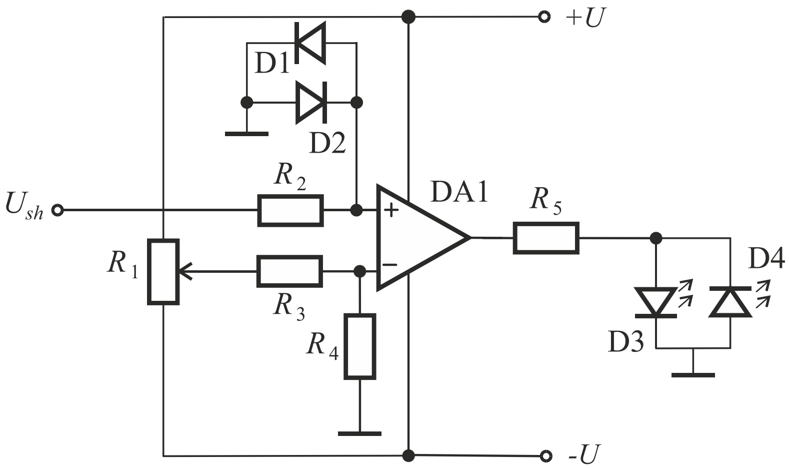

Figure 6.16. Principle scheme of the indicator of the zero voltage level

The indicator of the zero voltage level (Fig. 6.16) is used for correction of the voltage level shift from the zero voltage level, for either the current-to-voltage converter or output voltage follower. The main component of the indicator is the differential amplifier DA1, the output of which is connected through the resistor R_5 with the indicator's LEDs: D3 and D4. The voltage level shift from the zero voltage level is corrected as follows: at first, the voltage shift from the zero voltage level of the differential amplifier of the indicator is corrected; then the same is done with the differential amplifier of the current-to-voltage converter; and (finally) with the differential amplifier of the output voltage follower.

Summary

For metrological support of the secondary measuring devices which are used in conjunction with thermoresistive or thermoelectric sensors, the code-controlled multi-value standards of resistance, voltage and current are required. In order to improve the metrological reliability of measuring channels, it is reasonable to conduct the checking of the secondary measuring devices including its connection wires. In this case, the two-pair wire resistance imitators, invariant to the lead wire resistance and to the resistance of switching elements, that allow the transfer of resistance value with high accuracy over required distance can be applied. In these imitators three of the four lead wires are inserted in the negative feedback loops of respective differential amplifiers, therefore, their influence can be neglected. For the compensation of the lead wire connected in series with the standard resistor, the compensating circuit is used. The voltage compensation circuit based on differential amplifiers selects the voltage drop in the lead wire, and subtracts it from the output voltage of the input amplifier.

Commonly, the selection of the resistance imitation range is accomplished by commutation of the appropriate standard resistor. For further reduction of the influence of the lead wire resistances, the selection of the resistance imitation range can be performed by combined selection of the standard resistor value and of the division ratio of the auxiliary voltage divider. Consequently, the number of the high precision standard resistors and commutation elements is reduced.

Since the noise influences the resistance imitation accuracy, the technique for equalising the noise voltages in lead wires by means of a compensation circuit and additional capacitors can be employed. The compensation is based on the formation of a compensating current proportional to the noise-induced voltage drop in lead wire. The application of this technique reduces the influence of the normal mode noise by 30-50 dB.

Summary and conclusions

Thermocouples and resistance temperature sensors are the most widely used sensors for industrial applications. Therefore, the improvement of the accuracy of temperature measurement with these sensors is an important issue at present.

The circuit design methods proposed by the author allow remarkably improving the accuracy of temperature measurement with RTDs by the reduction of the error of nonlinearity and the lead wires influence. In that case, the error of nonlinearity does not exceed 0.1% over the temperature measurement range from 0°C to 500°C, and less than 0.05% over the temperature measurement range from 0°C to 350°C. The proposed circuit for temperature measuring based on current stabiliser, in the case of equalising of the resistance values of the lead wires allows complete compensation of lead wires influence.

In temperature measurements with thermocouples, the accuracy improvement was achieved by the compensation of influence of the cold-junction temperature, and by the linearization of the temperature-to-voltage conversion. In order to increase the effectiveness of the compensating bridge circuits over a wide range of cold-junction temperature change, the bridge circuits with temperature-dependent supply sources and additional temperature-dependent voltage divider have been evolved. The most effective is the compensating circuit containing temperature-dependent resistors and operational amplifier. That circuit provides the error less than 0.04°C for different types of thermocouples. Piecewise-linear approximation of the transfer function of the thermocouple allows achieving the error of nonlinearity less than 0.2°C over the temperature range from 0°C to 800°C.

For the metrological instrumentation of the secondary measuring devices which operate with thermoresistive and thermoelectrical sensors, the designs of the imitators of resistance, voltage and current are proposed. These structures are invariant to the influence of the lead wires resistances and commutating elements; as a consequence, that allow reproduction of the standard values over required distances with improved accuracy.

In the cases when the application of the thermocouples or resistance temperature sensors is impossible, the fibre optic temperature sensor or the liquid crystal-based temperature sensors can be employed. The designs of liquid crystal-based temperature sensors analysed in this book are original, simple in use and can be employed in the cases when the highest accuracy is not necessarily required, e.g. in biology and medicine.

The directions for further research will be related to the elaboration of new methods for the improvement of accuracy of the known sensors, and the design of the new constructions of temperature sensors.

References

1. Abdelaziz Y.A., Megahed F.M., Halawa M.M., *Stability and calibration of platinum/palladium thermocouples following heat treatment*, “Measurement”, 2004 vol. 35, p. 413-420.
2. Agraval G.P., *Applications of non-linear fiber optics*, Burlington, Academic Press, Elsevier Inc., 2008.
3. Aisawa H. et al., *Characteristics of sapphire fiber connected with rubby sensor head for the fiber-optic thermometer applications*, “Sensors and Actuators”, 2002 vol. 101, p. 42-48.
4. Aizawa H. et al., *Fiber-optic thermometer for high temperature measurement*, SICE-ICASE International Joint Conference, 2006, p. 1899-1902.
5. Alben R., *Theory of pitch change near the smectic-cholesteric transition point*, “Molecular Crystals and Liquid Crystals”, 1973 vol. 20, p. 231-239.
6. Al-Hawari T., Al-Bo'ol S., Momani A., *Selection of temperature measuring sensors using the analytic hierarchy process*, “Jordan Journal of Mechanical and Industrial Engineering”, 2011 vol. 5, no. 5, p. 451-459.
7. Balasubramaniam V. M. Sastry S. K., *Use of liquid crystals as temperature sensors in food processing research*, “Journal of Food Engineering”, 1995 vol. 26, p. 219-230.
8. Bao X., Chen L., *Recent progress in distributed fiber optic sensors*, “Sensors”, 2012 vol. 12, p. 8601-8639.
9. Batbayaryn D., Gotra O., Mikityuk Z., Semenova J., *Wybrane aplikacje wyswietlaczy cieklokrystalicznich na bazie przejscia teksturowego*, 6 Konferencja naukowa “Technologia Elektronowa”, ELTE’97, 1997 vol. 1, p. 112-115.
10. Batbayaryn D., Gotra O., Mikityuk Z., Semenova J., *Wyswietlacze cieklokrystaliczne na bazie przejscia teksturowego*, 6 Konferencja naukowa “Technologia Elektronowa”, ELTE’97, 1997 vol. 1, p. 108-111.
11. Batchellor C.R., Edge C., *Some recent advances in fibre-optic sensors*, “Electronics Communication Engineering Journal”, 1990 vol. 2, no. 5, p. 175-184.
12. Baur G., Wittwer V., Berreman D. W., *Determination of the tilt angles at surfaces of substrates in liquid crystal cells*, “Physics Letters”, 1976 vol. A56, p. 142-144.
13. Bentley R. E., *Handbook of Temperature Measurement Vol. 2: Resistance and Liquid-In-Glass Thermometry*, New York, Springer, 1998.

14. Bernini R., Minardo A., Zeni L., *Accuracy enhancement in Brillouin distributed fiber-optic temperature sensors using signal processing techniques*, “IEEE Photonics Technology Letters”, 2004 vol. 16, no. 4, p. 1143-1145.
15. Berthold J.W., Jeffers L.A., *Extended range fiber-optic temperature sensor*. Patent 6,270,254 B1. Date of Patent: 07.08.2001.
16. Betta G., Pietrosanto A., *Temperature measurement by multifiber optical sensor*, “IEEE Transactions on Instrumentation and Measurement”, 2000 vol. 49, no. 5, p. 1004-1007.
17. Bolognini G., Soto M.A., Pasquale F.D., *Fiber-optic distributed sensor based on hybrid Raman and Brillouin scattering employing multiwavelength Fabry-Perot lasers*, “IEEE Photonics Technology Letters”, 2009 vol. 21, no. 20, p. 1523-1525.
18. Bosiljevac M., Komljenovic T., Babic D., Sipus Z., *Interrogating FBG based temperature sensors - practical issues*, “54th International Symposium ELMAR-2012”, 2012, p. 305-308.
19. Boyko O. Hotra O., *Mikroelektronna bagatoznachna mira oporu, naprugy ta strumu*, Visnyk Nacionalnogo Universytetu “Lvivska Politechnika” “Electronics”, 2001 vol. 423, p. 31-35.
20. Boyko O., Hotra Z., Hotra O., Kostiv N., *Prystrij kompensaciji temperatury vilnukh kinciv pervynnykh termoelektrychnykh peretvoriuvachiv*, Mizhvidomchuj naukovo-technichnyj zbirnyk “Measuring Technique and Metrology”, 2010 vol. 71, p. 120- 124.
21. Boyko O., Hotra Z., Hotra O., Kostiv N., *Temperature measuring device*. Patent 54329 A. Date of Patent: 10.11.2010.
22. Boyko O., Hotra Z., Hotra O., Kostiv N., *Temperature measuring device*. Patent 54676 A. Date of Patent: 25.11.2010.
23. Boyko O., Hotra O., Hotra Z., Lopatynskyj I., *Device for temperature measurement*. Patent 34039 A. Date of Patent: 15.02.2001.
24. Boyko O., Hotra O., Hotra Z., Lopatynskyj I., *Temperature measuring device*. Patent 34184 A. Date of Patent: 15.02.2001.
25. Braga W.S., Santos O.R., Sampaio A.R., Kimura N.M., *An optical conoscopy study of a reentrant discotic nematic—Biaxial nematic phase transition*, “Journal of Molecular Liquids”, 2012 vol. 170, p. 72-75.
26. Brajlovski V.V., Ilarionov O.J., Kalynjuk V.V., *Tekhnologija vygotovlennia tonkoplivkovykh termoperetvoriuvachiv oporu*, Visnyk Cherniveckogo Derzhavnogo universytetu "Fizyka", 1998 vol. 32, p. 86-88.

27. Brett L. H., Winter H. H., *Analysis of the conoscopic measurement for uniaxial liquid-crystal tilt angles,* “Applied Optics”, 2001 vol. 40, no. 13, p. 2089-2094.

28. Budjak J., *New approach in the kinetic theory of crystal properties*, “International Conference on Statistical Physics and Phase Transitions”, 1993, p. 22-27.

29. Budjak J., Frejik D., Hotra O., Nykyruj L., Mezhylovska L., *Do teorii kinetychnykh javushch u napivprovidnykovykh krystalakh*, “Physics and Chemistry of Solid State”, 2001 vol. 2, no. 1, p. 77-85.

30. Budjak J., Hotra O., *About the nature of the main parameters of temperature sensors,* 6th International Symposium “Microelectronics Technologies and Microsystems, MTM-2002”, 2002, p. 238-241.

31. Budjak J., Hotra O., Lopatynskyj I., *Elementy teorii termodynamichnykh ta kinetychnykh vlastyvostej materialiv*, Visnyk Nacionalnoho Universytetu “Lvivska Politechnika” “Electronics”, 2000 vol. 397, p. 108-113.

32. Chen T., Feng S.M., Xie J.N., *The new matrix the polarization state of the transmitted light through the cholesteric liquid crystal*, “Optik”, 2010 vol. 121, p. 253-258.

33. Chernov A.M., Kibenko V.D., *Apparatus for imitating great values of electric resistance*. US Patent 3,596,224. Date of Patent: 27.07.1971.

34. Chilaya G., *Cholesteric Liquid Crystals: Optics, electro-optics, photo-optics*, [In]: Chirality in liquid crystals, New York, Springer-Verlag, 2001, p. 159-185.

35. Chilaya G., *Effect of various external factors pretransitional phenomena on structural transformations in cholesteric liquid crystals*, “Crystallography Reports”, 2000 vol. 45, no. 5, p. 871-886.

36. Childs P., *Practical Temperature Measurement*, Oxford, Butterworth-Heineman, 2001.

37. Chung G.-S., Kim C.-H., *RTD characteristics for micro-thermal sensors*, “Microelectronics Journal”, 2008 vol. 39, p. 1560-1563.

38. Chychlowski M., Yaroshchuk O., Kravchuk R., Wolinski T., *Liquid crystal alignment in cylindrical microcappillaries*, “Opto-Electronics Review”, 2012 vol. 20, no. 1, p. 47-52.

39. Cloutier M., Pronovost J., Cloutier M., *Fiber optic temperature sensor,* US Patent 8,277,119 B2. Date of Patent: 02.10.2012.

40. Collings P.J., *Optical Rotatory Dispersion Measurements in the Third Cholesteric Blue Phase*, “Physical Review A”, 1984 vol. 30, no. 4, p. 1990-1993.

41. Collings P.J., *Optical Rotatory Dispersion of Single Crystals in the Cholesteric Blue Phase*, “Molecular Crystals Liquid Crystals”, 1984 vol. 113, p. 277-289.

42. Coviello G., Finazzi V., Villatoro J., Pruneri V., *Encapsuled coated photonic crystal fiber sensor for temperature measurements up to 1000°C*, European Conference on Lasers Electro-Optics; European Quantum Electronics Conference, 2009, p. 1.

43. Crooker P. P., *Cholesteric Liquid Crystals: The Blue Phases*, [In]: Encyclopedia of Materials: Science and Technology, Elsevier Science, 2001, p. 1223-1227.

44. Cui Q. et al., *Distributed temperature sensing system based on Rayleigh scattering BOTDA*, “IEEE SENSORS JOURNAL”, 2011 vol. 11, no. 2, p. 399-403.

45. Culshaw B., Kersey A., *Fiber-optic sensing: a historical perspective*, “Journal of Lightwave Technology”, 2008 vol. 26, no. 9, p. 1064-1077.

46. Curtis D. J., *Process Control Instrumentation Technology*, New York, Prentice Hall, 2006.

47. Cusano A., Cutolo A., Albert J., *FBG sensors: recent advancements*, Bentham, Science Publishers, 2011.

48. Dakin J.P., Pratt D.J., Bibby G.W., Ross J.N., *Distributed optical fibre Raman temperature sensor using a semiconductor light source detector*, “Electronics Letters”, vol. 21, 1985 no. 13, p. 569-570.

49. Danisman K., Dalkiran I., Celebi F.V., *Design of a high precision temperature measurement system based on artificial neural network for different thermocouple types*, “Measurement”, 2006 vol. 39, p. 695-700.

50. de Gennes P. G., *The Physics of Liquid Crystals*, London, Oxford University Press, 1974.

51. Deshmukh R.R., Malik M. K., *Effect of Temperature on the optical electro-optical properties of poly(methyl methacrylate)/E7 polymer-dispersed liquid crystal composites*, “Journal of Applied Polymer Science”, 2008 vol. 109, p. 627-637.

52. Diankov G., Naradikian H., Angelov T., *Polymer-stabilized liquid crystal indicator used in thermometry*, “Journal of Materials Science: Materials in Electronics”, 2003 vol. 14, p. 831-832.

53. Dixon V.U., Lock G.D., Wilson M., Owen J.M., Mayhew J.E., *Accurate heat transfer measurements using thermochromic liquid crystal. Part 1: Calibration characteristics of crystals*, “International Journal of Heat Fluid Flow”, 2009 vol. 30, p. 939-949.

54. Dixon G., Scala I., *Heat hysteresis of colour response of cholesteric liquid crystals*, “Molecular Crystals and Liquid Crystals”, 1970 vol. 10, p. 317-326.

55. Djeu N.I., *Fiber-optic high temperature sensor*. US Patent 6,045,259, Date of Patent: 04.04. 2000.

56. Eccleston L.E., *Apparatus for method of internally calibrating an electrical calibrator*. US Patent 5,012,181. Date of Patent: 30.04.1991.

57. Fang A., Ye X., Chen A., Xu X., Yu R., *Using operational amplifiers to realize the compensation of thermocouples*, ISECS International Colloquium on Computing, Communication, Control, and Management, vol. 1, 2008, p. 774-777.

58. Farahani M.A., Gogolla T., *Spontaneous Raman scattering in optical fibers with modulated probe light for distributed temperature Raman remote sensing*, “Journal of Lightwave Technology”, 1999 vol. 17, no. 8, p. 1379-1391.

59. Farnell J., *Selective infiltration of photonic crystal fibres for waveguide arrays*, “ANU Undergraduate Research Journal”, 2009 vol. 1, p. 7-15.

60. Feng S.M., Chen T., *Study of polarization state of the transmitted light through the cholesteric liquid crystal*, “Displays”, 2009 vol. 30, p. 195-198.

61. Fernald M.R. et al., *Pressure-isolated Bragg grating temperature sensor*. US Patent 6,452,667 B1. Date of Patent: 17.09.2002.

62. Fernald M.R. et al., *Pressure-isolated Bragg grating temperature sensor*. US Patent 6,813,013 B2. Date of Patent: 02.11.2004.

63. Fernicola V.C., Iacomini L., *Approximating the ITS-90 Temperature Scale with Industrial Platinum Resistance Thermometers*, “International Journal of Thermophysics”, 2008 vol. 29, p. 1817-1827.

64. Floren J.W., Weller R.N., Pashley D.H., Kimbrough W.F., *Changes in root surface temperatures with in vitro use of the system B heat source*, “Journal of Endodontics”, 1999 vol. 25, p. 593-595.

65. Frazao O., Marques J.M., Santos J.L., Marques M.B., Baptista J.M., *Brillouin fibre laser discrete sensor for simultaneous strain temperature measurement*, “Applied Physics”, 2007 vol. 86, p. 555-558.

66. Galarneau P., Levesque M., Fougeres A., Labranche B., *Fiber-optic temperature sensor assembly*. US Patent 8,170,832 B2. Date of Patent: 01.05.2012.

67. Gaussa W., Theriault D., Wassel W., Skoncey J., *Process sensor simulators*. US Patent 4,922,194. Date of Patent: 01.05.1990.

68. Geddes J.J., Hocker B., *Fiber optic temperature sensor using liquid component fiber*. US Patent 4,201,446. Date of Patent: 06.05.1980.

69. Ghi O.P., Rozzell T.C., *Liquid crystal fiberoptic RF probes-Part II: A microwave power probe,* "Microwave Journal", 1975 vol. 18, no. 8, p. 58-59.

70. Gifford D.K., Solier B.J., Wolfe M.S., Froggatt M.E., *Distributed fiber-optic temperature sensing using Rayleigh backscatter*, 31th European Conference on Optical Communication (ECOC2005), 2005 vol. 3, p. 511-512.

71. Goosens W., *Molecular theory of the cholesteric phase optical rotatory of optical molecules in nematic*, "Molecular Crystals and Liquid Crystals", 1971 vol. 12, p. 237-241.

72. Gornostaev G.F., Frolov G.A., Pasichnyi V.V., Tkachenko G.V., *Fiber-optic thermometry its application*, "Journal of Engineering Physics and Thermophysics", 2007 vol. 80, no. 2, p. 403-408.

73. Gotra O., Kalita W., Slosarcik S., Pietrikova A., *Thermosensitive IC for relative temperature determination*, "Radioengineering", 2002 vol. 11, no. 2, p. 31-34.

74. Gotra O., Mykytyuk Z., Lichkovskij E., *Multifunction light guide fibre sensor with cholesteric liquid crystal envelope*, 4th International Symposium on Microelectronic Technologies and Microsystems, 2000, p. 22-26.

75. Gotra O., Potenski J., *Method of temperature measurement with signal conversion in differential block*, XXIII International Conference of IMAPS Poland Chapter, 1999, p. 325-329.

76. Gotra O., Sopilnyk L., *Analog liquid crystal indicator*, Selected Papers from International Conference on Optoelectronic Information Technologies, SPIE, 2000 vol. 4425, p. 374-376.

77. Gotra Z., Gotra O., Mikityuk Z., Zayats R., Stadnyc B., *Fibre optic sensors on the base of liquid crystals*, "Lightguides and their Applications", SPIE, 2000 vol. 4239, p. 76-81.

78. Gotra Z., Gotra O., Senyuk B., *Colour liquid crystal indicators*, 6th International Symposium "Advanced Display Technologies", 1997, p. 69-71.

79. Gotra Z., Gotra O., Smalyukh I., Senyuk B., *Liquid crystal devices with antireflecting coatings*, 6th International Symposium "Advanced Display Technologies", 1997, p. 59-62.

80. Gotra Z., Yu. Nastishin, I. Smalyukh, Gotra O., *Liquid-crystalline temperature sensor*, 3rd International Symposium on Microelectronic Technologies and Microsystems, 1999, p. 93-97.

81. Grattan K.T.V., Meggitt B.T., *Optical fiber sensor technology, advanced applications – Bragg gratings and distributed sensors*, vol.5, Boston, Kluwer Academic Publishers, 2000.
82. Grattan K.T.V., Sun D.T., *Fiber optic sensor technology: an overview*, "Sensors and Actuators", 2000 vol. 82, p. 40-61.
83. Gray G.W., *Liquid Crystals: Overview*, [In]: Encyclopedia of Materials: Science and Technology, Elsevier Science Ltd., 2001, p. 4570-4579.
84. Gupta B.D., *Fiber Optic Sensors: Principles Applications*, New Delhi, New Delhi Publishing Agency, 2006.
85. Gupta S.C., *Textbook on Optical Fiber Communication and Its Applications*, New Delhi, PHI Learning Prt. Ltd., 2012.
86. Guzik J., *Aktywny imitator rezystancji do wzorcowania megaomomierzy*, "Pomiary, Automatyka, Kontrola", 2009 vol. 55, no. 9, p. 766-768.
87. Guzik J., *Imitator dużych rezystancji do wzorcowania megaomomierzy*, VI Konferencja Naukowo-Techniczna PPM'8, 2008, p. 141-146.
88. Guzik J., Pilśniak A., Rochiński P., *Uogólniony model matematyczny imitatora dużych rezystancji*, VIII Konferencja Naukowo-Techniczna PPM'11, 2011, p. 160-163.
89. Guzik J., Rochiński P., *Imitatory dużych rezystancji – porównania własciwości*, IX Konferencja Naukowo-Techniczna PPM'12, 2012, p. 286-289.
90. Hariharan P., *Basics of Interferometry*, San Diego, Academic Press, Elsevier Inc., 2007.
91. Hartog A.H., *A Distributed Temperature Sensor Based on Liquid-Core Optical Fibers*, "Journal of Lightwave Technology", 1983 vol. LT-1, no. 3, p. 498-509.
92. Hausner M.B. et al., *Calibrating single-ended fiber-optic Raman spectra distributed temperature sensing data*, "Sensors", 2011 vol.11, p. 10859-10879.
93. Hisakado Y., Kikuchi H., Nagamura T., Kajiyama T., *Large electro-optic Kerr effect in polymer stabilized liquid crystalline blue phases*, "Advanced Materials", 2005 vol. 17, p. 96-98.
94. Hoffmann L. et al., *Applications of fibre optic temperature measurement*, "Proceedings of Estonian Academy of Sciences, Engineering", 2007 vol. 13, no. 4, p. 363-378.
95. Hotra O., *Analogue liquid crystal indicator*. UA Patent 43016 A. Date of Patent: 15.11.2001.
96. Hotra O., *Cold-junction temperature compensation of thermoelectric transducers*, "Przegląd Elektrotechniczny", 2010 vol. 10, p. 24-26.

97. Hotra O., *Microprocessor temperature meter for dentistry investigation*, “Przegląd Elektrotechniczny”, 2010 vol. 7, p. 63-65.
98. Hotra O., *Multirange code-controlled active resistance imitator*, “Przegląd Elektrotechniczny”, 2010 vol. 7, p. 60-62.
99. Hotra O., *Termorezystyvni vymirjuvalni prystroji*, Mizhvidomchuj naukovo-technichnyj zbirnyk “Measuring Technique and Metrology”, 2000 vol. 56, p. 46-51.
100. Hotra O., *The device for cold-junction temperature compensation of thermoelectric transducers with temperature-dependent voltage source*, “Przegląd Elektrotechniczny”, 2013, in press.
101. Hotra O., Boyko O., *Active simulator of standard resistance with time-pulse transformation in hybrid film performance*, XXV International Conference of IMAPS Poland Chapter, 2001, p. 305-308.
102. Hotra O., Boyko O., *Compensation bridge circuit with temperature-dependent voltage divider*, “Przegląd Elektrotechniczny”, 2012 vol. 4a, p. 169-171.
103. Hotra O., Boyko O., *Temperature measuring device based on thin film thermoresistors*, “Prace Instytutu Elektrotechniki”, 2012 vol. 260, p.207-217.
104. Hotra O., Boyko O., *Tranzystorowo-rezystancyjny układ kompensacji wpływu temperatury wolnych końców termopary*, “Prace Instytutu Elektrotechniki”, 2011 vol. 249, p. 21-27.
105. Hotra O., Bojko O., Majewski J., *Influence of methods for noise reduction on dynamic characteristics of active resistance imitators*, “Pomiary, Automatyka, Kontrola”, 2008 vol. 54, no. 10, p. 733-736.
106. Hotra O., Cherpak V., *Volokonno-optychni sensory temperatury na osnovi efektu KhNFP v ridkukh krystalakh*, 5th International Conference “Problems of Industrial Heat and Engineering”, 2007, p. 330-331.
107. Hotra O., Fechan A., Mykytyuk Z., Cherpak V., Lopatynskyj I., *Ridkokrystalichnyj material dla porohovoho sensora temperatury*, Visnyk Nacionalnogo Universytetu “Lvivska Politechnika” “Elements of the theory and devices of solid-state electronics”, 2003 vol. 491, p. 64-69.
108. Hotra O., Lopatynskyj I., Yavorskyj B., *New electro-optical effect in nematic liquid crystal for integrated optics elements*, “Optoelectronic and Electronic sensors V”, SPIE, 2003 vol. 5124, p. 112-114.

109. Hotra O., Mykytyuk Z., Fechan A., Cherpak V., *Porohovuj sensor temperatury na bazi efektu kholesteryko-nematychnoho perekhodu*, Mizhvidomchuj naukovo-technichnyj zbirnyk "Measuring Technique and Metrology", 2003 vol. 63, p. 67-69.

110. Hotra O., Semerak M., *Heat properties of microelectronic heat flux sensors on the base of AgCuSe*, "Optoelectronic and Electronic sensors V", SPIE, 2003 vol. 5124, p. 108-111.

111. Hotra O., Stadnyk B., Timchishin M., *Plivkovi sensory dla vymirjuvannja temperatury ta teplovoho potoku*, Visnyk Nacionalnoho Universytetu "Lvivska Politechnika" "Electronics", 2000 vol. 397, p. 37-42.

112. Hotra O., Stadnyk B., Yavorsky B., *Analogovuj ridkokrystalichnuj indykator dla vumiriuvannia naprugy*, "Automatics, Measurement and Control, 2001 vol. 420, p. 95-98.

113. Hotra O., Wojcik W., Skoczylas M., Cherpak V., *Modern state trends of temperature sensors on the basis of integrated optics*, 4th International Conference "Problems of Industrial Heat and Engineering", 2005, p. 270-271.

114. Hotra Z., Hotra O.; Batbayaryn D.; Petriv O.; Senyuk B.; Smalukh I., *Analogue liquid crystal indicator*. UA Patent 29718 A. Date of Patent: 15.11.2000.

115. Hotra Z., Hotra O. Batbayaryn D.; Petriv O.; Senyuk B.; Smalyukh I., *Analogue liquid crystal indicator*. UA Patent 29717 A. Date of Patent: 15.11.2000.

116. Hotra Z., Nevmerzhitska O., Petriv O., *Analogue liquid crystal indicator*. UA Patent 20372 A. Date of Patent: 15.07.1997.

117. Hotra Z., Hotra O., Senyuk B., Smalyukh I., *Liquid crystal indicator*. UA Patent 32774 A. Date of Patent: 15.02.2001.

118. Hotra Z., Hotra O., Zayats R., Mykytyuk Z., *Fibre-optic sensor*. UA Patent 34182 A. Date of Patent: 15.02.2001.

119. Hotra Z., Hotra O., Zayats R., Mykytyuk Z, Sushynskyy O., *Optoelectronic sensor*. UA Patent 34241 A. Date of Patent: 15.02.2001.

120. Hotra Z., Mykytyuk Z., Hotra O., *Vpluv poverkhni na parametry ridkykh krystaliv*, "Technical news", 1998 vol. 1(6), 2(7), p. 73-76.

121. Hotra Z., Mykytyuk Z., Hotra O., Fechan A., Sushynskyy O., Yasynovska O., Kotsun, V., *New method of the threshold voltages determination of a cholesteric-nematic transition*, "Molecular Crystals and Liquid Crystals", 2011 vol. 535, p. 225-232.

122. Hotra Z., Mykytyuk Z., Hotra O., Fechan A., Sushynskyy O., Yasynovska O., Kotsun V., *The cholesteric-nematic transition in thin layers of nematic-cholesteric mixtures*, “Molecular Crystals and Liquid Crystals”, 2011 vol. 534, p. 32-40.

123. Hotra Z., Mykytyuk Z., Sushynskyy O., Hotra O., Yasynovska O., Kisala P., *Sensor systems with optical channel of information transferring*, “Przegląd Elektrotechniczny”, 2010 vol. 86, no. 10, p. 21-23.

124. Hotra Z., Smalyukh I., Nastishin Yu., Hotra O., *Colour liquid crystal temperature indicator*. UA Patent 31816 A. Date of Patent: 15.12.2000.

125. Hotra Z., Ubizskyj S., Hotra O., Senyuk B., *Matematychna model analogovoho ridkokrystalichnoho indykatora*, “Technical News”, 1998 vol. 1(6),2(7), p. 76-79.

126. Huang Y.-X., Tu M., *Dependence of viscoelastic parameters of nematic liquid crystals on pretilt angle temperature*, “Current Applied Physics”, 2010 vol. 10, p. 561-564.

127. Hu D.J.J. et al., *Fabrication and characterization of a highly temperature sensitive device based on nematic liquid crystal-filled photonic crystal fiber*, “IEEE Photonics Journal”, 2012 vol. 4, no. 5, p. 1248-1255.

128. Hyde D., *Evaluating thin film RTD stability*, “Sensors-Peterborough-”, 1997 vol. 14, no. 10, p. 79-81.

129. Iten M., *Novel applications of distributed fiber-optic sensing in geotechnical engineering*, ETH-Dissertation, 2012 vol. 19632.

130. Jahan F., Ballico M., *Stability studies of a new design Au/Pt thermocouple without a strain relieving coil*, “International Journal of Thermophysics”, 2007 vol. 28, p. 1822-1831.

131. James S.W., Khaliq S., Tatam R.P., *Enhanced sensitivity fibre optic long period grating temperature sensor*, Optical Fiber Sensors Conference Technical Digest, IEEE, 2002 vol. 1, p. 139-142.

132. James S.W., Tatam R.P., *Optical fibre long-period grating sensors: characteristics and application*, “Measurement Science Technology”, 2003 vol. 14, p. R49-R61.

133. Jeong J.W., Won C.S., Chung W.S., Son S.H., Cho K.R., *A low-cost resistance-to-time converter for resistive bridge sensors*, International Technical Conference on Circuits/Systems, Computers Communications (ITC-CSCC), 2008, p. 1137-1140.

134. Jinling W., Junhai Y., Zhanhua H., *A Fluorescence optic-fiber Temperature Sensor Based on Ruby*, Fifth International Conference on Intelligent Computation Technology Automation, 2012, p. 623-625.

135. Johnson C.C., Durney C.H., Lords J.L., *Liquid crystal fiberoptic temperature probe for the measurement of electromagnetic power absorption in tissue*, Microwave Symposium Digest, S-MTT International, 1974 vol. 74, no. 1, p. 32-34.

136. Johnson C.C., Durney C.H., Lords J.L., Rozzell T.C., Livingston G.K., *Fiberoptic liquid crystal probe for absorbed radio-frequency power temperature measurement in tissue during irradiation*, "Annals of the New York Academy of Sciences, Biological effects of Nonionizing Radiation", 1975 vol. 247, p. 527-531.

137. Johnson C.C., Rozzell T.C., *Liquid crystal fiberoptic RF probes-Part I*, "Microwave Journal", 1975 vol. 8, p. 55-57.

138. Jones M.R., Barker D.C., *Use of blackbody optical fiber thermometers in high temperature environments*, Thermal Fluids Analysis Workshop NASA, 2001, p. 1-16.

139. Julsereewong P., Julsereewong A., Rerkratn A., Pootharaporn N., *Simple resistance-to-time converter with lead-wire-resistance compensation*, International Conference on Instrumentation, Control, Information Technology and System Integration (SICE Annual Conference), 2011, p. 2760-2763.

140. Jurca M., Urs C., *Novel noncontact temperature fiber sensor for multispot field measurements*, International Symposium on Optoelectronic Technologies, 2010, p. 1-4.

141. Kaczmarek Z., *Światłowodowe czujniki i przetworniki pomiarowe*, Warszawa, Agenda Wydawnicza PAK, 2006.

142. Kai P., Ko Yiu, Demokan M. S., Tam H., *Distributed temperature sensing with erbium-doped fiber amplifiers*, "Jounal of Lightwave Technology", 1996 vol. 14, no. 10, p. 2236-2244.

143. Kalantar-zadeh K., Fry B., *Nanotechnology-Enabled Sensors*, New York, Springer Science+Business Media, 2008.

144. Kalita W., Gotra O., Sushynsky O., Ivanytskiy V., *The multifunctional sensor with an analog indicator*, Selected Papers from International Conference on Optoelectronic Information Technologies, SPIE, 2001 vol. 4425, p. 465-471.

145. Kashyap R., *Fiber Bragg Gratings*, San Diego, Elsevier Inc., 2010.

146. Keating P., *Theory of cholesteric mesophase*, "Molecular Crystals and Liquid Crystals", 1969 vol. 8, p. 315-326.

147. Kerlin T.W., *Practical Thermocouple Thermometry*, North Carolina, Instrument Society of America, Research Triangle Park, 1999.

148. Kikuchi H., *Liquid Crystalline Blue Phases*, “Structure Bonding”, 2008 vol. 128, p. 99-117.

149. Kikuchi H., Hisakado Y., Uchida K., Nagamura T., Kajiyama T., *Fast electro-optical effect in polymer-stabilized blue phases*, “Liquid Crystals VIII”, SPIE, 2004 vol. 5518, p. 182-189.

150. Kim Y.-G., Gam K. S., Kang K.H., *An investigation of the thermoelectric properties of type S thermocouples from different manufacturers*, “Measurement”, 2002 vol. 31, p. 131-137.

151. Kim H., Chung W.S., Kim H.J., Son S.H., *A resistance deviation-to-pulsewidth converter for resistive sensors*, “IEEE Transactions on Instrumentation and Measurement”, 2009 vol. 58, no. 2, p. 397-400.

152. Kim J., Shin Y., Yoon Y., *A study on the fabrication of an RTD (resistance temperature detector) by using Pt thin film*, “Korean Journal of Chemical Engineering”, 2001 vol. 18, no. 1, p. 61-66.

153. Kissinger C.D., *Fiber optic proximity probe*. US Patent 3,327,584. Date of Patent: 27.06.1967.

154. Kochergin V., *Cryogenic fiber optic temperature sensor method of manufacturing the same*. US Patent 8,303,176 B2. Date of Patent: 06.11.2012.

155. Ko P.K.Y., Demokan M.S., Tam H., *Distributed temperature sensing with Erbium-doped fiber amplifiers*, “Journal of Lightwave Technology”, 1996 vol. 14, no. 10, p. 2236-2245.

156. Komuri R., Hou Z.B., *A review of the experimental techniques for the measurement of heat temperatures generated in some manufacturing processes tribology*, “Tribology International”, 2001 vol. 34, p. 653-682.

157. Kononenko Ya.M., Sushko A.F., *Possibility of constructing highly accurate code controlled current dividers*, “Measurement Techniques”, 1987 vol. 30, no. 3, p. 271-274.

158. Kumar S., Kang S.-W., *Liquid Crystals*, [In]: Encyclopedia of condensed matter, ed. by G. Bassani, G. Liedl, P. Wyder, Oxford, Elsevier Ltd., 2005 vol. 3, p. 111-120.

159. Kurik M., Mikityuk Z., Fechan A., Vistak M., Nevmerzhitska O., *Determination of elastic constants of nematic-cholesteric mixtures*, “Molecular Crystals Liqiud Crystals”, 1997 vol. 293, 1-6.

160. Kwok K., *Complete Guide to Semiconductor Devices*, New York, John Wiley & Sons, 2002.

161. Kwon Il-Bum, *Distributed measurements of structures by fiber optic sensors*, "KSCE Journal of Civil Engineering", 2003 vol. 7, no. 6, p. 659-666.

162. Lagakos N., Bucaro J.A., *Miniature fiber optic temperature sensor with edge reflector*. US Patent 8,322,919 B. Date of Patent: 04.12.2012.

163. Lagerwall J.P., Scalia G., *A new era for liquid crystal research: Applications of liquid crystals in soft matter nano-, bio-microtechnology*, "Current Applied Physics", 2012 vol. 12, p. 1387-1412.

164. Lampasi D.A., Podesti L., *A measurement system exploiting non-linearity of thermocouples for cold junction compensation*, Instrumentation Measurement Technology Conference, IMTC 2004, p. 2170-2175.

165. Lebedev S.N., Kaminskii V.Ju., *Cheking the R4085 apparatus using transitional electric resistance measures*, "Measurements Techniques", 1987 vol. 30, no. 7, p. 719-721.

166. Lee B., *Review of the present status of optical fiber sensors*, "Optical Fiber Technology", 2003 vol. 9, p. 57-79.

167. Lee C.E., Taylor H.F., *Fiber-optic Fabry-Perot temperature sensor using a low-coherence light source*, "Journal of Lightwave Technology", 1991 vol. 9, no. 1, p. 129-134.

168. Lee F.S., Van-Cura J.E., Begole E.A., *A comparison of root surface temperatures using different obturation heat sources*, "Journal of Endodentistry", 1998 vol. 24, p. 617-620.

169. Li X. et al., *Fiber-optic temperature sensor based on difference of thermal expansion coefficient between fused silica and metallic materials*, "IEEE Photonics Journal", 2012 vol. 4, no. 1, p. 155-162.

170. Liu D., Liu S., Liu H., *Temperature performance of Raman scattering in data fiber its application in distributed temperature fiber-optic sensor*, "Frontiers of Optoelectronics in China", 2009 vol. 2, no. 2, p. 159-162.

171. Liu J., Ma L., Yang J., *Methods techniques of temperature measurement*, ICECE, IEEE Conference Publications, 2011, p. 5332-5334.

172. Liu J.C.P., Tse C.K., Poon F.N.K., Pong M.H., Lai Y.M., *General impedance synthesizer using minimal configuration of switching converters*, European Conference on Circuit Theory Design, 2005, p. I/173-I/176.

173. Livingston G.K., *Thermometry and dosimetry of heat with specific reference to the liquid crystal optical fiber temperature probe*, "Radiation Environmental Biophysics", 1980 vol. 17, p. 233-243.

174. Loiko V.A., Konkolovich A.V., *Focusing of light by polymer-dispersed liquid-crystal films with nanosized droplets*, “Journal of Experimental Theoretical Physics”, 2006 vol. 103, no. 6, p. 935-943.
175. Loiko V.A., Konkolovich A.V., *Polarization of light transmitted through a polymer film with nanosized droplets of liquid crystal*, “Journal of Experimental Theoretical Physics”, 2004 vol. 99, no. 2, p. 343-351.
176. Love J., *Process Automation Handbook: A Guide to Theory and Practice*, London, Springer, 2007.
177. Lucchetta D.E., Karapinar R., Manni A., Simoni F., *Phase-only modulation by nanosized polymer-dispersed liquid crystals*, “Journal of Applied Physics”, 2002 vol. 91, p. 6060-6065.
178. Lutsyk Ja., Huk O., Lach O., Stadnyk B., *Vymirjuvannja temperaturni: teorija ta praktyka*, Lviv, Beskyd Bit, 2006.
179. Madej P., *Wzorzec dużej rezystancji w układzie T. Zastosowanie i niepewność*, “Prace naukowe Instytutu Maszyn, Napędów i Pomiarów Elektrycznych Politechniki Wrocławskiej”, 2006 vol. 59, no. 26, p. 310-322.
180. Madej P., *Analiza niepewności pasywnego wzorca imitującego bardzo duże rezystancje*, “Pomiary, Automatyka, Robotyka”, 2006 vol. 10, no 10, p. 72-77.
181. Maiti T.K., *A novel lead-wire-resistance compensation technique using two-wire resistance temperature detector*, “IEEE SENSORS JOURNAL”, 2006 vol. 6, no. 6, p. 1454-1458.
182. Maiti T.K., Kar A., *A new low cost lead resistance compensation technique for resistive sensor*, “Measurement”, 2010 vol. 43, p. 735-738.
183. Maschera D., Dario D., *Active impedance synthesis circuit, for example for XDSL splitters*, US Patent 2007/0009051 A1. Date of Patent: 11.01.2007.
184. Maughan S.M., Kee H.H., Newson T.P., *Simultaneous distributed fibre temperature strain sensor using microwave coherent detection of spontaneous Brillouin backscatter*, “Measurement Science Technology”, 2001 vol. 12, p. 834-842.
185. Megahed F.M., Abdel-Aziz Y.A., *Assessment of Temperature Measurements Using Thermocouples at NIS-Egypt*, “International Journal of Thermophysics”, 2010 vol. 31, p. 601-611.
186. Meijer G.C.M. (Ed.), *Smart Sensor Systems*, Chishester, John Wiley & Sons, Ltd., 2008.
187. Mendez A., Morse T.F. (eds.), *Specialty optical fibers handbook*. Burlington, Elsevier Academic Press, 2007.
188. Michalski L., Eckersdorf K., Kucharski J., McGhee J., *Temperature Measurement*, New York, John Wiley & Sons, 2001.

189. Mikityuk Z., Gotra Z., Nevmerzhytska O., Zayats R., *Liquid crystal optical elements for fibre lightguides*, Symposium on Microelectronics Technologies Microsystems, 1997, p. 113-118.

190. Mikityuk Z., Lopatynskiy I., Gotra O., Dalambayar B., *Liquid crystal using in optical sensors*, Selected Papers from International Conference on Optoelectronic Information Technologies, SPIE, 2001 vol. 4425, p. 472-477.

191. Mikityuk Z., Nevmerzhitska O., Zaremba P., Vistak M., *Temperature dependence of field hysteresis loop in nemato-cholesteric mixtures*, "Molecular Crystals and Liquid Crystals", 1996 vol. 275, p. 3-14.

192. Mikityuk Z., Zayats R., Gotra O., *Multifunctional sensor with a liquid crystal probe*, 2nd International Symposium on Microelectronics Technologies Microsystems, 1998, p. 221-224.

193. Mikityuk Z., Zayats R., Gotra O., Kamuda K., Maślanka P., *Liquid crystal materials for multifunctional optoelectronic sensors*, XXII International Conference of IMAPS Poland Chapter, 1998, p. 359-362.

194. Milenko K., Wolinski T.R., Shum P.P., Hu D.J.J., *Temperature-Sensitive Photonic Liquid Crystal Fiber Modal Interferometer*, "IEEE Photonics Journal", 2012 vol. 4, no. 5, p. 1855-1860.

195. Mitscke F., *Fiber Optics*, Berlin, Heidelberg, Springer-Verlag, 2009.

196. Moffat R.J., *Some experimental methods for heat transfer*, "Experimental Themal Fluid Science", 1990 vol. 3, p. 14-32.

197. Moiseeva N.P., *The prospects for developing standard thermocouples of pure metals*, "Measurement Techniques", 2004 vol. 47, no. 9, p. 915-919.

198. Moreira M.F. et al., *Cholesteric liquid-crystal laser as an optic fiber-based temperature sensor*, "Applied Physics Letters", 2004 vol. 85, no. 14, p. 2691-2693.

199. Morey W.W., Meltz G., Glenn W.H., *Fiber optic Bragg grating sensors*, "Fiber Optic and Laser Sensors VII", SPIE, 1989 vol. 1169, p. 98-107.

200. Muratov V.A., Wiktor W., *Code-controlled voltage divider*, US Patent 6,937,180 B1. Date of Patent: 30.08.2005.

201. Mykytyuk Z., Fechan A., Hotra O., Semenova J., *Ridkokrystalichnyj material dla prostorovo-chasovukh modulatoriv svitla system avtomatyzovanogo keruvannja na osnovi kholesteryko-nematychnogo fazovogo perekhodu*, "Elektroenergetychni ta elekromekhanichni systemy", 1997 vol. 334, p.68-72.

202. Mykytyuk Z., Fechan A., Nevmerzhitska O., Vistak M., *The field hysteresis of the cholesteric-nematic transition of the phase*, "Liquid Crystal Materials, Devices and Applications", SPIE, 1993 vol. 1988, p. 211-222.

203. Mykytyuk Z., Hotra O., Cherpak V., Ivanytskyy V., Dalanbayar D., *Bagatofunkcionalnyj ridkokrustalichnuj sensor*, Visnyk Nacionalnogo Universytetu "Lvivska Politechnika" "Elements of Theory and Devices of Solid-State Electronics", 2001 vol. 427, p. 143-149.

204. Mykytyuk Z., Gotra O., Fechan, A., Cherpak V., Dalanbayar B., Ivanytskyy V., *Wave guide spectral analysers on the base of induced cholesteric liquid crystal*, XXV International Conference of IMAPS Poland Chapter, 2001, p. 135-138.

205. Mykytyuk Z., Gotra O., Semenova Yu., Ivanytskyy V., Dalanbayar B., Cherpak V., Smaluch I., *Mode switching by using the LC cell*, 5th International Symposium on Microelectronic Technologies and Microsystems, 2001, p. 37-42.

206. Mykytyuk Z., Semenova J., Hotra O., Fechan A., *Osoblyvosti rozsijuvannja vyprominjyvannja konfokalnoju teksturoju v shari indukovanogo kholesteryka dla svitlorozsijujuchukh elementiv*, "Elektroenergetychni ta elekromekhanichni systemy", 1997 vol. 334, p. 72-76.

207. Nalawade S.M., Thakur H.V., *Photonic crystal fiber strain-independent temperature sensing based on modal interferometer*, "IEEE Photonics Technology Letters", 2011 vol. 23, no. 21, p. 1600-1602.

208. Nalawade S. M., Harnol S. S., Thakur H. V., *Temperature and strain independent modal interferometric torsion sensor using photonic crystal fiber*, IEEE SENSORS JOURNAL, 2012 vol. 12, no. 8, p. 2614-2615.

209. Nastishin Yu.A., Dovgyi O.B., Vlokh O.G., *Optical conoscopy of distorted uniaxial liquid crystals: computer simulation experiment*, "Ukrainian Journal of Physical Optics", 2001 vol. 2, no. 2, p. 98 -106.

210. Oomura H., Sakamaki Y., Aizawa S., Tajima K., *Model CA100 "Compact CAL" calibrator*, "Yokogawa Technical Report/English Edition", 1997 no. 24, p. 15-19.

211. Pal B.P.(Ed.), *Fundamentals of Fibre Optics in Telecommunication Sensor Systems*, New Delhi, New Age International Ltd., 1992.

212. Parker T.R., Farhadiroushan M., Herek V.A., Rogers A.J., *A fully distributed simultaneous strain temperature sensor using spontaneous Brillouin backscatter*, "IEEE Photonics Technology Letters", 1997 vol. 9, no. 7, p. 979-981.

213. Park J.M., Jun S.I., *A resistance deviation-to-time interval converter for resistive sensors*, IEEE SOC Conference, 2008, p. 101-103.

214. Petrovich I., Kalita W., Volodin Ph., Lychkovsky E., Gotra O., *The mathematical simulation of voltage measurement device on liquid crystal,* 3rd International Symposium on Microelectronic Technologies and Microsystems, 1999, p. 81-87.

215. Petrovich I., Stadnyk B., Volodin Ph., Gotra O., *Analogue liquid crystal display device*, 3rd International Symposium on Microelectronic Technologies and Microsystems, 1999, p. 78-80.

216. Pindak R., Ho J., *Cholesteric pitch of cholesteryl decanoate near the smectic-A transition,* "Physics Letters", 1976 vol. 59A, p. 277-281.

217. Podgornik T., Bojkovski J., Batagelj V., Drnovsek J., Automation of Resistance Bridge Calibrator, International Journal of Thermophysics, vol. 29, p. 403-413, 2008.

218. Post J.W., Bhattacharyya A., Imran M., *Experimental results a user-friendly model of heat transfer from a thin film resistance temperature detector*, "Applied Thermal Engineering", 2009 vol. 29, p. 116-130.

219. Pradhan S., Sen S., *An improved lead compensation technique for three -wire resistance temperature detectors,* "IEEE Transactions on Instrumentation and Measurement", 1999 vol. 48, p. 903-905.

220. Priest J., *Temperature and Its Measurement*, [In]: Encyclopedia of Energy, ed. by C.J.Cleveland, Oxford, Elsevier Science, 2004 vol.6, p. 45-54.

221. Rajan G. et al., *A photonic crystal fiber and fiber Bragg grating-based hybrid fiber-optic sensor system*, "IEEE Sensors Journal", 2012 vol. 12, no. 1, p. 39-42.

222. Rao Y., *In-fibre Bragg grating sensors*, "Measurement Science & Technology", 1997 vol. 8, p. 355-375.

223. Rao Y.-J., Deng M., Duan D.-W., Zhu T., *In-line fiber Fabry-Perot refractive-index tip sensor based on endlessly photonic crystal fiber*, "Sensors and Actuators A: Physical", 2008 vol. 148, p. 33-38.

224. Rathod R., Pechstedt R.D., Jackson D.A., Webb D.J., *Distributed temperature-change sensor based on Rayleigh backscattering in an optical fiber*, "Optics Letters", 1994 vol. 19, no. 8, p. 593-595.

225. Rice T. et al., *Fiber Optic Temperature Sensors - A New Temperature Measurement Toolbox*, [In]: Temperature: Its Measurement and Control in Science and Industry, ed. by D.C. Ripple, Melville, American Institute of Physics, 2003 vol. 7, p. 1015-1020.

226. Rossetto J.F., Lisboa O., Ferreira E.C., *Measurement of the temperature coefficient for the Brillouin frequency shift in an optical fibre*, Optics-XXV ENFMC Annals, 2002, p. 1-4.

227. Roychoudhuri C., Manzur T., *Demonstration of the evolution of spectral resolving power as a superposition of higher order delayed beams*, Proceedings SPIE, 1995 vol. 2525, p. 28-44.

228. Rozzel T.C., Johnson C., Durney C., Lords J., *Optical temperature probe*. US Patent 4,016,761. Date of Patent: 12.04.1977.

229. Rozzell T.C., Johnson C.C., Durney C.H., Lords J.L., Olsen R.G., *A nonperturbing Temperature sensor for Measurements in Electromagnetic Fields*, "Journal of Microwave Power", 1974 vol. 9, no. 3, p. 241-249.

230. Salour M.M., *Multiple sensing tip optical fiber thermometer*. US Patent 8,206,030 B1. Date of Patent: 26.07.2012.

231. D. Sarchi, R. Gaspari, G. Colletta, G. Villani, *Method and system for fiber-optic monitoring of spatially distributed components*. US Patent 8,184,980 B2. Date of Patent: 22.05.2012.

232. Sarma U., Boruah P.K., *Design and development of a high precision thermocouple based smart industrial thermometer with on line linearisation and data logging feature*, "Measurement", 2010 vol. 43, no. 10, p. 1589-1594.

233. Sawatari T., Gaubis P.A., *Fiber optic temperature sensor*. US Patent 6,141,098 A. Date of Patent: 31.10.2000.

234. Sen K., *An improved lead wire compensation technique for conventional two wire resistance temperature detectors* (*RTDs*), "Measurement", 2006 vol. 39, p. 477-480.

235. Sen S.K., Pan T.K., Ghosal P., *An improved lead wire compensation technique for conventional four wire resistance temperature detectors* (*RTDs*), "Measurement", 2011 vol. 44, p. 842-846.

236. Sifuentes E., Casas O., Reverter F., Pallas-Areny R., *Direct interface circuit to linearise resistive sensor bridges*, "Sensors and Actuators", 2008 vol. A 147, p. 210-215,.

237. S. Singh, *Phase transitions in liquid crystals*, "Physics Reports", 2000 vol. 324, p. 107-269.

238. Smalyukh I.I. et al., *Electric-field-induced nematic-cholesteric transition three-dimensional director structures in homeotropic cells*, "Physical Review, E: Statistical, Nonlinear, and Soft matter physics", 2005 vol. 72(1), no. 6, p. 061707.1-061707.16.

239. Soller B.J. et al., *Measurement of localized heating in fiber optic components with millimeter spatial resolution*, Optical Fiber Communication Conference and Exposition and the National Fiber Optic Engineers Conference, 2006 vol. Technical Digest Paper, OFN3.

240. Soto M.A., Bolognini G., Di Pasquale F., *Enhabced distributed hybrid sensor based on Brillouin and Raman scattering combining Fabry-Perot lasers and optical pulse coding,* IEEE Conference on OFC/NFOEC, 2010, p. 1-3.
241. Soto M., Signorini A., Nannipieri T., Faralli S., Bolognini G., *High-performance Raman-based distributed fiber-optic sensing under loop scheme using anti-Stokes light only*, "IEEE Photonics Technology Letters", 2011 vol. 23, no. 9, p. 534-536.
242. Springl V., Jaikla W., Siripruchyanan M., *Floating positive/negative resistance simulators employing single dual-output OTA*, International Symposium on Communications and Information Technologies, 2006, p. 352-355.
243. Stankovic S.B., Kyriacou P.A., *The effects of thermistor linearization techniques on the T-history characterization of phase change materials*, "Applied Thermal Engineering", 2012 vol. 44, p. 78-84.
244. Swirniak G., Mroczka J., *Wybrane zagadnienia pomiaru średnicy włokna optycznego w procesie produkcji z wykorzystaniem światła laserowego*, [In]: Problemy metrologii elektronicznej i fotonicznej, ed. by J. Mroczka, Wrocław, Oficyna Wydawnicza Politechniki Wrocławskiej, 2008.
245. Tanaka K., *Compensating circuit for a cold junction of a thermocouple*. US Patent 3956686. Date of Patent: 11.05.1976.
246. Thevenaz L., *Advanced fiber optics: concepts and technology*, Lausanne, EPFL Press, Taylor & Francis Group, 2011.
247. Timchishin M., Yavorsky B., Gotra O., *Miniature gauges of a thermal flow on the basis of thin films of a system Ag-Cu-Se*, 2nd International Symposium on Microelectronics Technologies and Microsystems, 1998, p. 175-179.
248. Topala C.M., Iacobescu G., Oprescu B., Ducu C., *Optical and thermo-electrical effects in newly synthesised cholesteric compounds*, "Materials Science and Engineering C", 2007 vol. 27, p. 1171-1173.
249. Trofimenkoff F.N., Nordquist A.E., *Signal amplifier resistance bridges with feedback linearization*, "IEEE Transactions on Instrumentation and Measurement", 1984 vol. IM-33, no. 1, p. 60-63.
250. Trokhymchuk A., *On Julius Planer's 1861 paper Notiz ¨uber das Cholestearin in Annalen der Chemie und Pharmacie*, "Condensed Matter Physics", 2010 vol. 13, no. 3, p. 37002: 1-4.
251. Trump B., *Analog linearization of resistance temperature detectors*, "Analog Applications Journal", 2011 vol. 4Q, p. 21-24.

252. Tuma M.L., Sawatari T., Lin Y., Elam K.A., *Flight tests on a fiber optic temperature sensor*, 17th Digital Avionics Systems Conference, 1998 vol. 1, p. D15/1-D15/7.

253. Tyman Z., Guzik J., *Model matematyczny wzorca dużych rezystancji wykonanego w technice SC*, "Pomiary, Automatyka, Kontrola", 2008 vol. 54, no. 9, p. 646-649.

254. Udd E., Spillman W.B., *Fiber Optic Sensors: An Introduction for Engineers and Scientists*, Hoboken, John Willey & Sons, 2011.

255. Ukil A., Braendle H., *Distributed temperature sensing: review of technology and applications*, "IEEE SENSORS JOURNAL", 2012 vol. 12, no. 5, p. 885-892.

256. Van de Giesen N. et al., *Double-ended calibration of fiber-optic Raman spectra distributed temperature sensing data*, "Sensors", 2012 vol. 12, p. 5471-5485.

257. Van Sprang H.A., van de Venne J.L.M., *Influence of the surface interaction on threshold values in the cholesteric-nematic phase transition*, "Applied Physics", 1985 vol. 57, no. 2, p. 175-179.

258. Wang C.-T., Jau H.-C., Lin T.-H., *Bistable cholesteric-blue phase liquid crystal using thermal hysteresis*, "Optical Materials", 2011 vol. 34, p. 248-250.

259. Wei G., Wang X., Sun J., *Signal processing method with cold junction compensation for thermocouple*, International Instrumentation Measurement Technology Conference I2MTC, 2009, p. 1422-1426.

260. Wickersheim K.A., Sun M.H., *Optical system using a luminiscent material sensor for measuring very high temperatures*. US Patent 4,859,079. Date of Patent: 22.08.1989.

261. Windhorn T.H., Cain C.A., *Optically active binary liquid crystal thermometry*, "IEEE Transactions On Biomedical Engineering", 1979 vol. BME-26, no. 3, p. 148-152.

262. Woliński T., *Photonic liquid-crystal fibers: new sensing opportunities*, [In]: Optical waveguide sensing and imaging ed. by Bock W.J., Gannot I., Tanev S., Dordrecht, Springer Science + Business Media B. V., 2008, p. 51-73.

263. Wright D.C., Mermin N.D., *Crystalline liquids: the blue phases*, "Reviews of Modern Physics", 1989 vol. 61, no. 2, p. 385-432.

264. Wulf A., *Model representation of cholestric twist*, "Journal of the Chemical Society", 1973 vol. 59, no. 3, p. 1487-1493.

265. Wu J., Tsao S., *Highly accurate temperature sensor using two fiber Bragg gratings*. US Patent 6,024,488. Date of Patent: 15.02.2000.

266. Xiao Y.W., Gao W., *Investigation on sapphire fiber blackbody sensor*, International Conference on Computer Application and System Modeling, 2010, p. V13/452-V13/455.

267. Xu J., Wang X., Cooper K.L., Pickrell G.R., A. Wang, *Miniature fiber optic pressure and temperature sensors*, "Fiber Optic Sensor Technology Applications IV", SPIE, 2005 vol. 6004, p. 600403/1-600403/6.

268. Yablonskii S.V. et al., *Accurate method for determining tilt bias angles in thin films of nematic liquid crystals*, "Journal of Experimental and Theoretical Physics Letters", 1998 vol. 67, no. 6, p. 409-415.

269. Yamate T., Schroeder R.J., Ramos R.T., Mullins O.C., *Method for measuring using optical fiber distributed sensor*. US Patent 7,215,416 B2. Date of Patent: 08.05.2007.

270. Yasin M., Harun S.W., Arof H. (eds.), *Fiber optic sensors*, Rijeke, InTech, 2012.

271. Yasin M., Harun S.W., Arof H. (eds.), *Optical Fiber Communications and Devices*, Rijeke, InTech, 2012.

272. Yeager J., Courts S.S., *A review of cryogenic thermometry and common temperature sensors*, "IEEE SENSORS JOURNAL", 2001 vol. 1, no. 4, p. 352-360.

273. Zhang Y.F., Chan C.C., Chia M.X.A., Zu P., *Temperature effect of liquid crystal in photonic bgap fiber-based Sagnac loop*, "IEEE SENSORS JOURNAL", 2012 vol. 12, no. 5, p. 1609-1610.

274. Zhang Z.Y., Grattan L.S., *Fiber Optic Fluorescence Thermometry*, London, Chapman & Hall, 1995.

275. Zhu T., Bao X., Chen L., *A single longitudinal-mode tunable fiber ring laser based on stimulated Rayleigh scattering in a nonuniform optical fiber*, "Journal of Lightwave Technology", 2011 vol. 29, no. 12, p. 1802-1807.

276. Zhu Y., Wang A., *Fabrication of miniature fiber-optic temperature sensors*. US Patent 7,762,720 B1. Date of Patent: 27.07.2010.

277. Zlatanovic M., Djukic M., Popovic I., Zirojevic Z., *Compensation of thermocouple reference junction temperature variation by a silicon temperature sensor*, 21st International Conference on Microelectronics MIEL'97, 1997 vol. 2, p. 557-560.

278. Żmija J., Kłosowicz S., Borys W., *Cholesteryczne ciekłe kryształy w detekcji promieniowania*, Warszawa, WNT, 1989.

279. *1017 Voltage/Current/Resistance Calibrator*, [accessed 11.02.2013]. Available from World Wide Web: http://www.timeelectronics.com/assets/upload/download_centre/documents/1017-ds_v1c.pdf.

280. *AN-225 IC Temperature Sensor Provides Thermocouple Cold-Junction Compensation* Texas Instruments Application Report, 2004, [accessed 11.02.2013]. Available from World Wide Web: http://www.ti.com/lit/an/snoa663a/snoa663a.pdf.

281. B. Baker, *Precision Temperature-Sensing With RTD Circuits*, Application Note 687, 2008, [accessed 11.02.2013]. Available from World Wide Web: http://ww1.microchip.com/downloads/en/appnotes/00687c.pdf.

282. *HARS-LX-9-0.001 Laboratory Standard Decade Resistance Substituter*, User and Service Manual, [accessed 11.02.2013]. Available from World Wide Web: http://www.ietlabs.com/pdf/Manuals/HARS-LX_im.pdf.

283. *High Precision Manual or SCPI Programmable Decade Resistance Substituters* (*IEEE-488.2 or RS232*), Operation Manual, [accessed 11.02.2013]. Available from World Wide Web: http://www.ietlabs.com/pdf/Manuals/PRS-200_IEEE.2_im.pdf.

284. IEC 584-1. Thermocouples. Part 1: Reference tables 1995-09.

285. IEC 60751:2008. Industrial Platinum Resistance Thermometers and Platinum Temperature Sensors.

286. *Implementing Cold-Junction Compensation in Thermocouple Applications*, Application Note 4026, Mar. 2007, [accessed 11.02.2013]. Available from World Wide Web: http://www.maximintegrated.com/app-notes/index.mvp/id/4026.

287. PN-EN 60584-1 Termoelementy - Charakterystyki.

288. *Portable Multi-Function Calibrator Model CEP 6000*, WIKA Data Sheet CT 83.01, 10/2010, p.1-6, [accessed 11.02.2013]. Available from World Wide Web: http://www.mensor.com/upload/DS_CT8301_GB_8126.pdf.

289. *Positive Analog Feedback Compensates PT100 Transducer*, Application Note 3450, 2005, [accessed 11.02.2013]. Available from World Wide Web: http://www.maximintegrated.com/app-notes/index.mvp/id/3450.

290. *Precision RTD simulator Model 4530*, [accessed 11.02.2013]. Available from World Wide Web: http://burster.de/en/products/calibration-instruments.html?RTD%20 simulators%20and%20temperature%20metal%20block%20calibrators/ RTD%20simulators%20and%20temperature%20metal%20block% 20calibrators/4530/135.

291. *Resistance thermometry theory*, [accessed 20.08.2012]. Available from World Wide Web: http://www.pentronic.se/Theory/Pt100sensor/tabid/188/language/en-GB/Default.aspx.

292. *Resistance thermometry*, [accessed 11.02.2013]. Available from World Wide Web: http://www.tempsens.com/thermometry_article.html.

293. *Temperature Sensor Market, A Study of major Sensor types (ICs, Thermostat, Thermistor, Resistive Temperature Detectors (RTDs), Thermocouple) & Applications, Global Forecast & Analysis 2011 – 2016*, [accessed 22.02.2013]. Available from World Wide Web: http://www.marketsandmarkets.com/Market-Reports/temperature-sensor-market-522.html

294. *The RTD*, [accessed 20.08.2012]. Available from World Wide Web: http://www.omega.com/temperature/z/pdf/z033-035.pdf.

295. *User's Manual Model CA51/71 HANDY CAL Calibrators*, *IM CA71-E*, p. 1-108, 2002, [accessed 11.02.2013]. Available from World Wide Web: http://aspzone.us.yokogawa.com/downloads/MI/Instruction%20Manuals /Calibrators/IM_CA71-CA51.pdf